

Helium cooling of Silicon Pixel Detector for Mu3e Experiment

Master Thesis



University of Applied Sciences and Arts Northwestern Switzerland
Institute of Thermal and Fluid Engineering, ITFE
Master of Science FHNW in Engineering
Specialisation in Energy and Environment
4th March, 2019

Student

Marin Deflorin

marin.deflorin@students.fhnw.ch

marin.deflorin@gmail.com

Project supervision

Prof. Dr. Beat Ribi

Prof. Dr. Peter Stuber

Prof. Dr. Daniel Weiss

Project partner

Mu3e

Dr. Frank Meier Aeschbacher

Acknowledgements

This master thesis was written during my studies for the Master of Science in Engineering at the University of Applied Sciences and Arts Northwestern Switzerland. From September 2018 to February 2019 I worked on the helium cooling system of the Mu3e experiment. At this point I would like to thank all involved people and friends for their support. This work would not be feasible to such an extent without the countless aids. Special thanks goes to:

- Frank Meier Aeschbacher and Mu3e collaboration
- Beat Ribl, Peter Stuber and Daniel Weiss
- Patrick Lüscher
- Edgar Brodmann
- Raphael Brunner
- Nino Degiampietro, Katharina Domnanich, Elias Mai, Sebastian Schmid, Elias Waldvogel
- Soraya Bonvin

March 2019, Marin Deflorin

Abstract

The Mu3e experiment is searching for the rare decay of a muon into two positrons and an electron. This would provide evidence of a new physics beyond the standard model of particle physics. The Mu3e experiment consists of three different detectors. A tracker made of thin silicon chips is used for vertex and momentum measurements and combined with two separate timing detectors. The thin silicon chips have an expected heat dissipation of $250 - 400 \text{ mW/cm}^2$ and their temperature should not exceed 70°C . Several cooling flows with an inlet temperature of 4°C are planned to stay in within this temperature limit. The optimal fluid for the experiment is helium, as it minimises the scattering of charged particles and is an excellent coolant.

In this thesis, the cooling of the silicon chips (MuPix) with helium was investigated in detail. At first, estimations were performed to determine an appropriate modelling approach for the simulation, and also to a first results of the occurring temperature.

A thermo-mechanical mockup of the Mu3e detector was experimentally investigated. The mockup was instrumented to measure the mass flows, temperatures, pressure drops, displacement of the detector as well as some other quantities. For the first measurements air was used as a coolant at a similar Reynolds number and temperature increase. Later the tests were repeated with helium to get the desired results.

CFD simulations were used to investigate the flow fields and determine the potential for improvement of the cooling system. Several iterations with optimised flow geometries were carried out until a geometry was found which ensures a more uniform cooling.

The comparison between the experimental results and the simulation proves that the cooling of the silicon chips can be performed in the specified range. Additionally, a simulation of the system was performed to investigate the placement of the control valves. The results were summarised at the end of the report including suggestions for improvements and possible further steps are described.

Contents

Nomenclature	vi
Acronyms	ix
1 Introduction	1
1.1 Mu3e Experiment	2
1.2 Progression of cooling system	2
1.3 Goal	3
1.4 Approach	4
2 Cooling system	7
2.1 Experiment components	7
2.2 Coolant	9
2.3 Helium cooling	9
2.4 Material properties	14
3 Theoretical fundamentals and analytical study	17
3.1 Joule-Thomson Effect	17
3.2 Passage of charged particles through matter	18
3.3 Cooling	19
3.4 Dimension analysis	21
3.5 Estimation of physical parameters	22
3.6 Cooling analysis	25
3.7 Conclusions of analytical study	31
4 CFD Simulation	33
4.1 Overview	33
4.2 Layers 1 & 2	43
4.3 Layers 3 & 4	58
4.4 V-folds layer 3 & 4	61
4.5 Gap layer 3 & 4	65
4.6 Gap layer 3 & SciFi	69
4.7 Layers 3 & 4 coupled	72

5	Measurements	83
5.1	Measurement model	83
5.2	Mockup of layers 1 & 2	86
5.3	Equipment and setup	93
5.4	Data evaluation	112
5.5	Diverse observations	113
5.6	Results	124
6	System simulation	133
6.1	Approach	133
6.2	Layer 1 & 2	134
6.3	Cooling plant concept	139
7	Comparison of results	141
7.1	Simplifications	141
7.2	Wall heat transfer coefficient	141
7.3	Temperature distribution	142
7.4	Dimensionless temperature	144
7.5	Discussion	145
8	Summary and Outlook	147
8.1	Outlook	149
8.2	Goal	152
8.3	Review	153
	List of Figures	157
	List of Tables	160
A	Project management	162
B	Simulation	189
C	Measurements	192
D	Digital appendix	198

Nomenclature

Symbols

A	Area	m^2
c_p	Specific heat capacity at constant pressure	$\text{J}/\text{kg} \cdot \text{K}$
D	Diameter	m
g	Gravitational acceleration of Earth	m/s^2
k	Extended uncertainty factor	—
l	Length	m
\dot{m}	Mass flow	g/s
\dot{Q}	Total heat load	W
\dot{q}	Heat load per surface	mW/cm^2
\dot{q}	Heat load per volume	W/m^3
R	Resistance	Ω
T	Temperature	$^{\circ}\text{C}$ or K
U	Perimeter	mm
w	Velocity	m/s
x	Position along layer	mm
z	Distance from midplane	mm

Greek symbols

α	Temperature coefficient of resistance	$1/\text{K}$
α	Wall heat transfer coefficient	$\text{W}/\text{m}^2 \cdot \text{K}$
Δ	Difference	—
ϵ	Emissivity coefficient	—
γ	Coefficient of thermal expansion	$1/\text{K}$
λ	Thermal conductivity	$\text{W}/\text{m} \cdot \text{K}$
μ	Dynamic viscosity	$\text{kg}/\text{m} \cdot \text{s}$

μ_{JT}	Joule-Thompson coefficient	K/bar
ν	Kinematic viscosity	m ² /s
ρ	Density	kg/m ³
ρ	Specific resistance	$\Omega\text{mm}^2/\text{m}$
σ	Stefan-Boltzmann-constant	W/m ² · T ⁴

Dimensionless numbers

Bi	Biot number	—
Ma	Mach number	—
Nu	Nusselt number	—
Π	Dimensionless number	—
Pr	Prandtl number	—
Re	Reynolds number	—
Ri	Richardson number	—
y^+	Dimensionless wall distance	—

Indices

0	Inlet
∞	Temperature far away from wall
a	Araldite
cor	Corrected
d	Divider
f	Fluid
g	Annular gap
h	Hydraulic
I	Current
i	Inlet
Mesh	Mesh
MuPix	Mupix
ov	Overlap
o	Outlet
p	Polymide
q	Constant heat flux on wall
R	Resistance

r	reduced
s	Solid
TC	Thermocouple
Th	Thermal
U	Voltage
w	Wall
x	Local

Particle Physics

βc	Velocity of incident particle	m/s
e^+	Positron	
e^-	Electron	
μ^+	Muon	
p	Momentum of incident particle	kg · m/s
x	Mass per unit area	g/cm ²
X_0	Radiation length	g/cm ²
z	Charge number of incident particle	—

Acronyms

CAD	Computer-aided design
CFD	Computational Fluid Dynamics
CLFV	charged lepton flavor violating
DAQ	Data acquisition
E+H	Endress + Hauser
EA	Elektro-Automatik
FHNW	University of Applied Sciences and Arts Northwestern Switzerland
GUM	Guide to the Uncertainty in Measurement
ITFE	Institute of Thermal and Fluid Engineering
G12	gap flow between layers 1 & 2
G34	gap flow between layers 3 & 4
G3S	gap flow between layer 3 & SciFi
G3T	gap flow between layer 3 & tile detector
NI	National Instruments
POM	Polyoxymethylen
PSI	Paul Scherrer Institute
SciFi	Scintillating Fibre
SM	Standard Model
V3	V-fold of layer 3
V34	V-fold of layers 3 & 4
V4	V-fold of layer 4

1 Introduction

The Mu3e experiment goal is to search for the decay of a muon into two positrons and one electron, which would give evidence of new physics beyond the Standard Model (SM) of particle physics. This fundamental physics experiment is a big challenge as most of the parts are new developments. Such a complex experiment is not only connected with scientific challenges in the field of physics, moreover the construction and assembly of components as well as the setup of the cooling system require tremendous engineering skills. The Mu3e experiment requires minimal material use, as otherwise the particles are deflected and therefore the required precision could not be achieved. One of the most crucial questions is the establishment of a gaseous helium cooling for ultra thin silicon detectors, encompassing a total surface of about 1 m^2 .

Mu3e is a collaboration which started in 2012 and currently consists of several European institutes which are based in Bristol, Genève, Heidelberg, Karlsruhe, Liverpool, London, Mainz, Oxford, Villigen and Zürich. The experimental setup will be commissioned at the premises of Paul Scherrer Institute (PSI) and currently entered phase I of the building stage. To realise further development and a functional evaluation of the cooling system, the Mu3e collaboration and especially Frank Meier Aeschbacher approached the University of Applied Sciences and Arts Northwestern Switzerland (FHNW) and the Institute of Thermal and Fluid Engineering (ITFE) for a cooperation. The first results of this mutual effort are summarised in this thesis, whereby the main focus was laid on the technical realisability of the helium cooling. For people interested into the muon decay and the experiment, detailed information can be found on www.psi.ch/mu3e/.

The focus of this thesis is the development of a cooling system for the MuPix chips of the Mu3e experiment, which are basically silicon chips with a thickness of $50 \mu\text{m}$ on a polyimide layer. These chips have a heat dissipation of up to 400 W/m^2 and must be cooled below $70 \text{ }^\circ\text{C}$ with a medium fulfilling the following requirements, low atomic number, good cooling properties and be inert. Helium was chosen because it best meets all the prerequisites.

In the next sections, the basic concept of the Mu3e experiment will be briefly explained, followed by a summary of previous projects on the helium cooling system. Then the goals as well as the approach will be discussed and finally an outlook over the whole thesis will be given.

1.1 Mu3e Experiment

The Mu3e experiment intends to search for the charged lepton flavor violating (CLFV) decay $\mu^+ \rightarrow e^+e^-e^+$. The goal is to either detect the decay or set a new branching ratio limit of 10^{-16} at a confidence level of 90 %. This would be four orders of magnitude lower than the previously performed search by the SINDRUM experiment [1]. In the Standard Model of particle physics the decay is suppressed with branching ratio under 10^{-54} , so any observation of the decay would be a sign for New Physics beyond the Standard Model. Different new physics models postulate the CLFV within the achievable limits of the Mu3e Experiment. The currently most intense source of low-energy muons is situated at PSI with a maximum muon rate of $1 \cdot 10^8$ Hz envisaged to be used during phase I of the project. A beam with higher intensity is currently under development and will probably be only available after 2025 for phase II experiments. In order to reach the aimed branching ratio, one year of data collection with a muon rate of $2 \cdot 10^9$ Hz will be required. Besides a high intensity muon beam, other crucial parameters, such as excellent timing, vertex and momentum resolution of the electrons and positrons are mandatory. The newly developed detector technology necessitates an extensive testing and improvement of the experimental setup and facilitates the collection of data within the next two years.

There are three different detectors with different functions which are described in section 2.1. The experimental setup is inside of a large superconducting magnet with an inner diameter of 1 m and a field intensity of 1 T which is required to keep the particle on a circular track. The detectors are positioned in a way to track as many particles as possible.

1.2 Progression of cooling system

The cooling system has already been analysed by a number of projects mainly performed at the University of Heidelberg. Most of them analysed the possibility of cooling the MuPix chips with helium with the then current version of design and specification. Their combined efforts led to the development of the current cooling concept Zimmermann [2] has first investigated the possibilities of a helium cooling for the Mu3e experiment. This included Computational Fluid Dynamics (CFD) simulation over one MuPix chip as well as measurements of a single silicon chip. Huxold [3] followed with an experimental setup with heatable mockup with accurate dimensions but only one global flow over all layers. Ng [4] has analysed and simulated both the inner and outer detector part and introduced the V-folds thereby increasing the stability of the outer layer and enabling a local cooling channel. The simulation model of Ng has been further developed by Herkert [5] and enhanced by adding a heatable model with the present geometry. The final geometry of the detector was designed after this works and was mostly finalised at the beginning of 2018. Tormann [6] used this geometry for new CFD simulations which showed that

there are some backflow regions which are causing high temperature especially on layers 1 & 2. Without this previous project, the helium cooling system would not be in such an advanced state.

This project is the first one where a heatable mockup with the final geometry of layers 1 & 2 is available. This mock-up has some little simplifications as there are aluminium heaters used, instead of the MuPix chips. The mock-up of layers 3 & 4 is not available until now due to production delays.

1.3 Goal

The following goals are a summary from the project clarification which can be found in appendix A.2. Main goals of the project are to analyse the helium cooling of the MuPix chips, optimise parts which could affect the experiment and create a concept for the control and regulation system. In the following list the sub-goals can be found:

Temperature	The temperature of the MuPix chip should not exceed 70 °C with a heat dissipation of 400 mW/cm ² .
Verification	Verification of the cooling results of the Layer 1/2 and 3/4 obtained in previous works.
Instrumentation	Instrumentation of the mockup for validation of the CFD and flow system-simulations.
Validation	Validation of the simulation results with measurements on the mockup.
Optimisation	Optimise the cooling of the Layer 1/2 and 3/4 if the temperature is too high or if other unacceptable states occur, e.g. oscillations that may trigger mechanical vibrations or stress.
Thermal deformation	Thermal deformation of the flexprint has to be investigated and the influence of it onto the cooling behaviour.
Flow system	Characterisation of helium flow through the whole system with the pressure drop and system behaviour.
Control concept	Develop a control concept for the helium cooling circuit with focus on start-up and shut-down phases.

The project task can be found in appendix A.1.

1.4 Approach

Based on these goals, which were agreed upon at the beginning of the project, different tasks were defined and are listed in figure 1.1. There are three main work packages which are investigating the helium cooling system of the Mu3e experiment. At the beginning, CFD simulations have been planned as the geometrical data were available and could also be compared with the results of Tormann [6]. The second package includes the measurements with the instrumentation. As the mockup was still in manufacturing process this was set after the simulation. The last package is to analyse the helium cooling system behaviour which includes the regulation of the different flow and determine whether control elements must be placed inside the magnet or not.

5

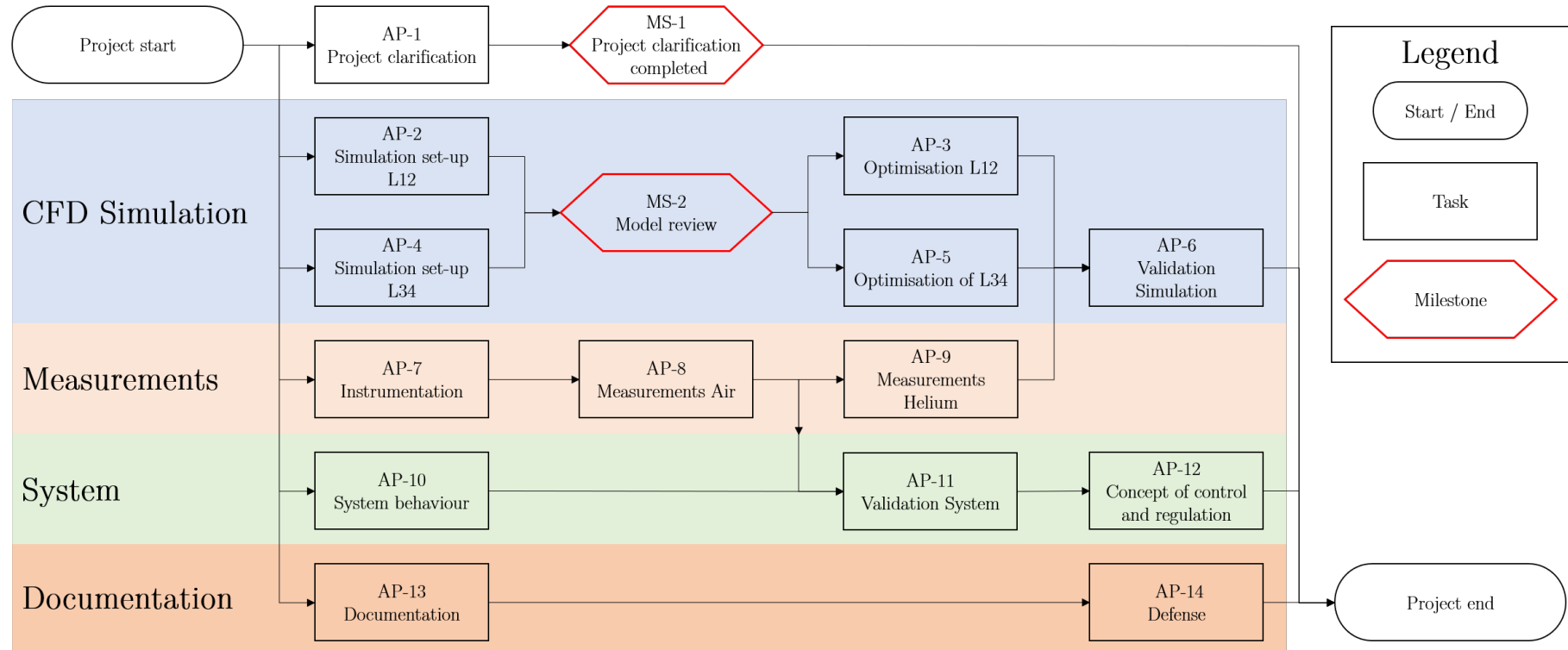


Figure 1.1: Task structure diagram.

In this thesis the cooling concept for the Mu3e pixel detector has been investigated using CFD simulation, measurements on a full-scale model of one part of the detector and some system analysis for the overall cooling circuit. The results of the simulations have been compared with the measurements. Chapter 2 gives an overview of the cooling system, the relevant components as well as material properties which are used in the following chapters. In chapter 3 theoretical fundamentals used for this thesis and analytical study of the cooling behaviour are explained. Chapter 4 describes the CFD simulation and optimisation of different geometries to obtain a more regular flow and cooling. In chapter 5 the measurement setup and results are shown. The system analysis which is looking on the control concept is described in chapter 6. The results of the simulations and the experiment are then compared and discussed in chapter 7. Finally, chapter 8 is concluding this thesis with an overall summary, open tasks and thoughts for the further development of the cooling system.

2 Cooling system

In this chapter, general information about the cooling system is given to provide an overview. Later, this knowledge will be used for the simulation, measurement and system modelling. A short browse through this chapter is recommended as it gives information common to all subsequent chapters. Furthermore, it gives an understanding of the cooling system and the components included. The whole experiment is explained in section 1.1, which describes the goals of the Mu3e experiment.

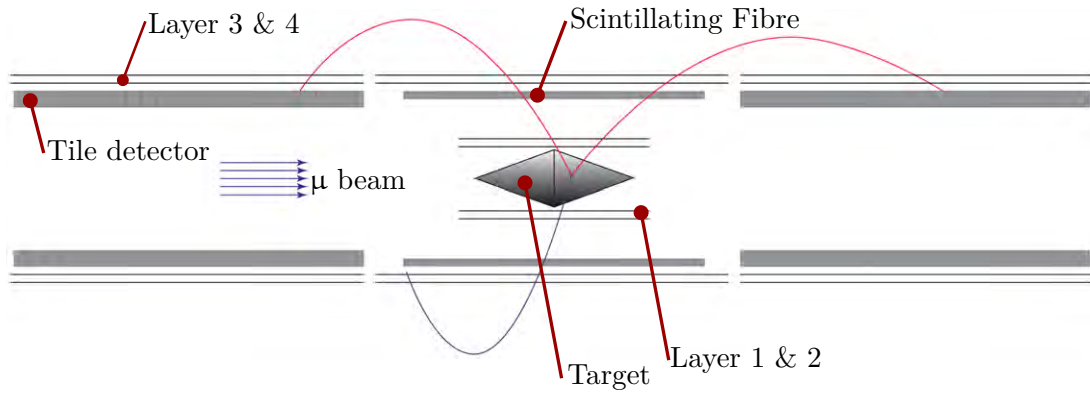
2.1 Experiment components

The relevant components for the helium cooling are the MuPix¹ chips which allow the detection of charged particles (here: electrons and positrons). The MuPix chips provide a high vertex and momentum resolution but insufficient timing resolution, which is important for distinguishing tracks from different decays occurring at almost the same time. Therefore, there are two different sensors with high time resolution but low spacial resolution. Figure 2.1a shows a sketch of all detectors as well as the target and the μ beam. One theoretical muon decay into two positrons (red) and one electron (blue) is displayed. The particles are first passing the layers 1 & 2 followed by the Scintillating Fibre (SciFi) detector, layers 3 & 4 of the central part. Due to the magnetic field, the particles are recurling and optimally passing the up- or downstream layers 3 & 4 and finally hitting into the tile detector. The MuPix layers as well as the SciFi must be made of very thin material to reduce the scattering of the charged particles². For the tile detector there is no such requirements as it is placed at the end of the recurling particle trajectories.

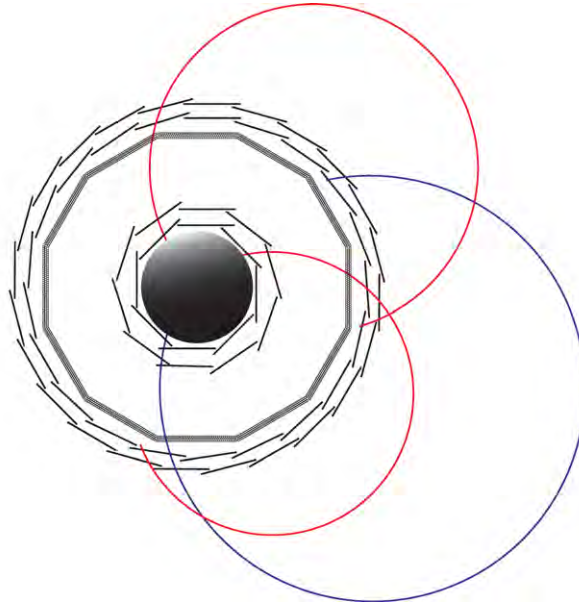
For the track reconstruction data from all three detectors are combined. The reconstruction itself is using graphics processing units and only interesting events are stored for later analysis to reduce data volume.

¹Silicon detector which is further described in section 2.3.2.

²(Charged particles passing through matter are deflected, which is dependent on the passed matter, see also section 3.2.)



(a) Cut through all detectors and target.



(b) Cut through the target and parts of the central detector.

Figure 2.1: Detector used for the Mu3e experiment with the MuPix sensor on the layers 1-4, Scintillating Fibre and the tile detector. Additionally, a theoretical particle track of a muon decay into two positrons and one electron is shown. [7]

2.1.1 Deviation of charged particles

The electrons and positrons fly through the different detectors and should optimally collide with as few matter as possible to enable a precise tracking of the trajectories. In section 3.2 the deflection angle of a charged particle passing through matter is explained. Therefore, it is required to have small radiation length³ for all parts which are passed by the particles. The MuPix chips have a radiation length of $x/x_0 \approx 0.115\%$ and the particles fly through a maximum of six layers. The SciFi detector has a thickness of under $100\ \mu\text{m}$ and a radiation length of $x/x_0 < 0.2\%$ which is a little higher than the one of the MuPix layer but is less critical as only one detector is present.

³Indicator of the deflection angle of charged particles passing this matter. Further information in section 3.2.

2.2 Coolant

The limitations restricting the detector in terms of layer thickness are also valid for the coolant. It can mainly be influenced by the used fluid which should have a good cooling capacity, low chemical reactivity as well as a small radiation length. Assuming the flight length of one particle from target to the tile detector to 1 m and that the coolant is filling all cavities, the radiation length of coolant can be evaluated. Nitrogen has then a radiation length of $x/x_0 \approx 0.3\%$. A lighter element such as helium has a radiation length of 0.019% which increases the accuracy of the experiment and is therefore preferred.

Additionally, helium is a good coolant with high heat conductivity compared to other gases and is chemically stable. There is only Hydrogen which has better cooling properties than helium. It has a 20% higher heat conductivity and a 2.7 times higher heat capacity. But hydrogen is explosive in combination with air which would require high safety precaution for the whole experiment. Therefore, helium is the best available coolant for the Mu3e experiment.

2.3 Helium cooling

The experiment has mainly two different cooling circuits. Parts that are passed by the electrons and positrons require a small radiation length to minimise the multiple coulomb scattering. Therefore, these parts are cooled by gaseous helium. Other parts as the tile detector or readout parts of the SciFi can be cooled with liquid water as these parts are not passed by the tracked particles. In this thesis only the helium flows are considered which are shown in figure 2.2. The parts A & C (up- & downstream) are principally the same just mirrored on the midplane. They are consisting of two MuPix layers (3 & 4) which are cooled with three helium flows. The part B (centre) has additionally to the outer layers 3 & 4 the inner MuPix layers 1 & 2 which are cooled with one gap flow. Those layers consists of several segments which are described in the next section.

The V-folds flow is flowing inside of a polyimide fold glued onto the layers 3 & 4 and provides directly a cooling flow to the chips. The gap flows is flowing in between two layers or between a layer another detector.

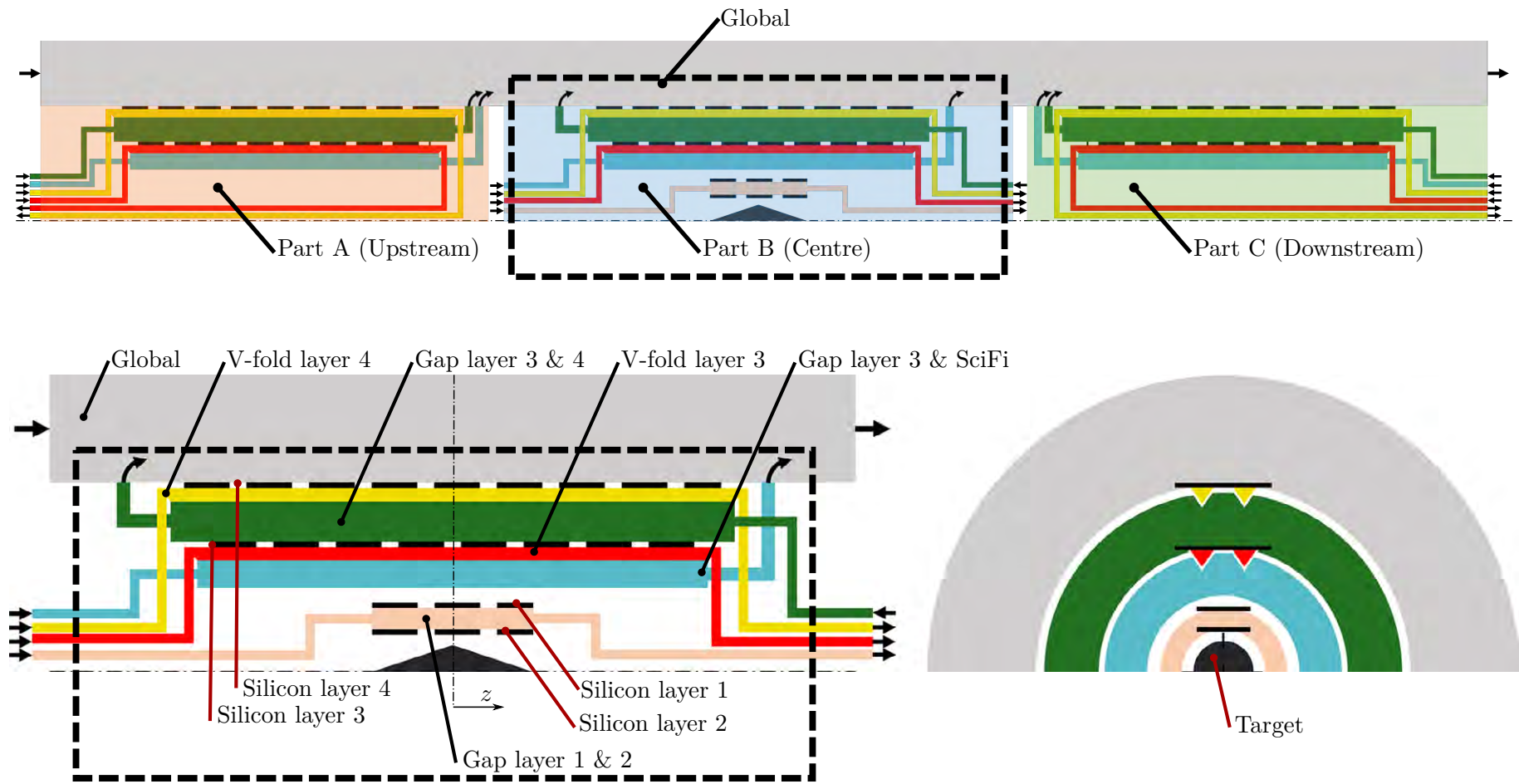


Figure 2.2: Helium cooling system of the silicon chips with detail of the centre part.

2.3.1 Layer segments

Each of the four layers consists of several segments. One segment of the mockup is shown in figure 2.3. One segment consists of multiple MuPix chips which are aligned next to each other. The number of chips over the segment length and the number of segments per layer are shown in table 2.1. The diameter is the distance of two segments on the opposite side. For the layers 1 & 2 6 chips are aligned, while the layers 3 & 4 have a total of 17 or 18 chips in row.

Table 2.1: Dimensions of the different layers and segments.

Layer	1	2	3	4
Number of segments per layer	8	10	24	28
Number of chips per segment	6	6	17	18
Layer "diameter" [mm]	46	59	144	170
Layer length [mm]	120	120	340	360

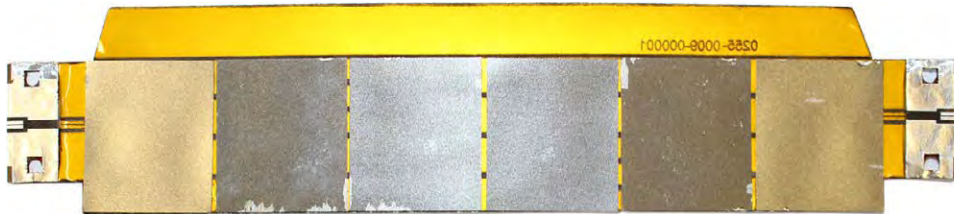


Figure 2.3: One segment of MuPix chips of layers 1 & 2 with 6 Mupix chips.

2.3.2 MuPix Chips

The MuPix chips are the part which have to be mainly cooled with helium. These chips are detecting passing electrons and positrons and have a high vertex and momentum resolution which is needed for the trajectory reconstruction. They are still in development and therefore the final heat dissipation of the chips is not available until now. It is expected that the chips will have a heat dissipation of 250 mW/cm^2 but the cooling system should be designed to keep the chip temperature under 70°C with a heat dissipation of 400 mW/cm^2 . This is representing the worst case scenario.

The chips have a dimension of $20 \times 23 \text{ mm}^2$ with a sensitive area which is only $20 \times 20 \text{ mm}^2$. This part is called detector area. The $3 \times 20 \text{ mm}^2$ area consists of digital read out and power lines. This inactive part is called periphery and has a higher heat dissipation as the detector area. The share of the heat has been estimated to be equal in terms of total heat for both parts which means that the periphery has a higher heat dissipation per surface than the detector. This is further explained in section 4.1.5.

The mockup which is used for the experiment has tape heater⁴, where only a constant heat load can be applied. As the simulation will be compared with the experimental results, the simulation will be performed with and without the high heat dissipation of the periphery.

In previous works both heat dissipations (250 & 400 mW/cm^2) have been simulated and then compared. As the temperature increase is mainly dependent on the heat dissipation, only the worst case with 400 mW/cm^2 will be simulated. To evaluate the temperature with another heat dissipation it can be linearly scaled, as long as the heat dissipation is smaller or in the same range as the worst case. Figure 2.4 shows the maximal and average temperature of the MuPix chips from a simulation which is in good agreement with a linear approximation.

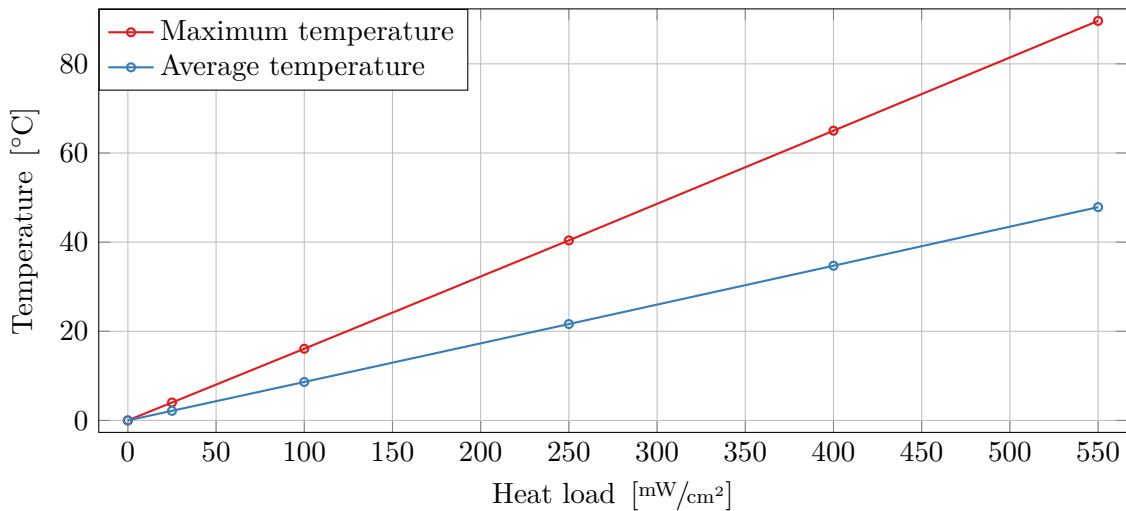


Figure 2.4: Temperature of MuPix chips depending on different heat dissipations.

The layers 1 to 4 showed in figure 2.2 have all different number of MuPix chips on them. Table 2.2 shows the number of chips per layer as well as the heat dissipation of each layer with the two different heat loads. The total heat dissipation with 400 mW/cm^2 of all MuPix chips is approximately 5.5 kW.

Table 2.2: Absolute heat load per layer.

Layer	Total heat load [W] (250/400)	
1 (48)	54.9	87.9
2 (60)	68.7	109.9
3 (408)	466.9	747.0
4 (504)	576.7	922.7
Total Centre (B)	1162.8	1866.6
Total (ABC)	3416.6	5484.5

⁴Segments with inactive steel plates and aluminium resistance to emulate the heat dissipation of MuPix chips.

2.3.3 Flows

For all the flows short names have been used, especially in the CFD simulation chapter. The gap flow as code G with the included layers, so the G12 is the gap flow between layers 1 & 2, G3S between layer 3 and SciFi etcetera. The following list shows the most used acronyms for the flows and parts:

V3	V-fold of layer 3
V4	V-fold of layer 3
G34	gap flow between layers 3 & 4
G3S	gap flow between layer 3 & SciFi
G3T	gap flow between layer 3 & tile detector
Part A	Upstream layers 3 & 4
Part B	Center layers 3 & 4
Part C	Downstream layers 3 & 4

The flows which have been shown in figure 2.2 have different mass flows through their volume. For most flows the average velocity has been set to 10 m/s which has been taken from the previous project. The V-fold of layers 3 & 4 (V34) flow velocity has been set to 20 m/s as the area is quite small. The global flow has only a velocity of 0.5 m/s but increases over the length of the detector as all gap flows of the outer layers are merged into the global flow. The inner diameter of the magnet is around 1 m which would result in a high mass flow with the specified velocity without essentially increasing the cooling capacity. Therefore, a mylar tube with a diameter of 0.3 m is proposed for the global flow to obtain a smaller area with helium flow.

Table 2.3 shows the different flows with the mass flows and also the required pressure at the in- & outlet. The striked global flow shows the required mass flow without a mylar tube which would double the total required mass flow. The indicated pressure drops have been taken from simulation, which were only performed until the end of the straight 3D printed in- & outlet geometries. The pressure drop of the tubing which lead out of the magnet as well as the change in diameter and bending in the tube is not considered in the pressure drop. Therefore, the required pressure drop will be higher.

Table 2.3: Helium mass flow through different cooling sections. Pressure levels are taken CFD simulation with the optimised parts which have higher drops than the original ones.

Flow	#	Inlet mass flow [g/s]	Inlet pressure [mbar]	Outlet pressure [mbar]	Velocity [m/s]
G12	1	2.0	40	-40	10
G3S	1	6.9	25	0	10
G3T	2	5.7	28	0	10
G34	3	7.6	25	0	10
V3	3	1.3	90	-90	20
V4	3	1.5	80	-80	20
Global ($D = 0.3$ m)	1	4.0	0.3	0	0.5
Global ($D = 1$ m)	0	62.4			0.5
Total		55.5			

2.4 Material properties

The material properties shown here are used for all following chapter.

2.4.1 Gas

Properties of helium are relatively constant with differing pressure in the used range but show some dependency on the temperature. The pressure is around atmospheric pressure for all parts of the cooling system which were analysed. In the range of 0 – 100 °C the viscosity and thermal conductivity of helium are changing up to 35 %. The viscosity and thermal conductivity have therefore been approximated with a linear function in this region. The largest deviation from the linearisation is 0.25 %. Same has also been applied for air which has a similar deviation due to the linearisation. The used standard conditions are 20 °C and 1 bar. This linear approximations were used for the CFD simulations.

2.4 Material properties

Table 2.4: Properties of helium and dry air used for simulations and estimations [8].

Property	Helium	Air	Unit
Molar mass	4.0	28.96	[g/mol]
Thermal conductivity	0.154	0.026	[W/m · K]
Dynamic viscosity	$19.6 \cdot 10^{-6}$	$18.2 \cdot 10^{-6}$	[kg/m · s]
Specific heat capacity	5193.2	1006.1	[J/kg · K]
Density	0.164	1.19	[kg/m ³]
Velocity of sound	1016	346	[m/s]
Temperature and pressure dependency			
Thermal Conductivity	$0.14 + 3.5 \cdot 10^{-4} \cdot T$	$0.024 + 7.3 \cdot 10^{-5} \cdot T$	[W/m · K]
Dynamic viscosity	$18.7 \cdot 10^{-6} + 4.5 \cdot 10^{-8} \cdot T$	$17.2 \cdot 10^{-6} + 4.7 \cdot 10^{-8} \cdot T$	[kg/m · s]
Density	Ideal gas	Ideal gas	[kg/m ³]

2.4.2 Air humidity

The air properties from table 2.4 are for dry air but in the experiment the laboratory air has a relative humidity between 35 and 60 % RH which gives a mass fraction of around 0.4 – 0.9 %. This increases the specific heat capacity by less than 1 % as well as the other quantities and is therefore neglected in this thesis.

2.4.3 Solid

The solid properties are less temperature dependent than the one of the gases. For the range used in this thesis the properties have been set to a constant value.

Table 2.5: Properties of silicon [9], polyimide [10], steel (1.4310) [11] and araldite [12] used for simulations and estimations.

Property	Silicon	Polyimide	Steel	Araldite	Unit
Molar mass	28.086				[g/mol]
Thermal Conductivity	149	0.12	15	0.22	[W/m · K]
Specific Heat Capacity	783.3	1090	500		[J/kg · K]
Density	2.33	1.42	7.9		[kg/m ³]
Thermal expansion	2.56	30-60	16		[10 ⁻⁶ K]

3 Theoretical fundamentals and analytical study

This chapter is describing most used theoretical fundamentals together with analytical study of the cooling system. This is not including the fundamentals of the Mu3e experiment which would go far over the knowledge of a mechanical engineer and is not necessary for the understanding of the cooling system which is analysed here.

3.1 Joule-Thomson Effect

The Joule-Thomson effect is a real gas behaviour of adiabatically expanding gases. The molecules of the gas at low temperatures are attracted by each other and while expanding they move away from each other. This requires energy, which is taken from the kinetic energy of the molecules, which become cooler as a result. On the other hand, at high temperatures the molecule try to repulse from each other. The separation releases energy, which is converted into kinetic energy of the molecules. Therefore, the behaviour during an expansion is a function of the current temperature but also of the current pressure as this defines the distance between the molecules. This behaviour is called the Joule-Thomson effect which is described with the Joule-Thomson coefficient μ_{JT} with the unit K/bar . At room-temperature and 1 bar only 3 gases have a repulsion of the molecules which gives them a negative Joule-Thomson coefficient, namely hydrogen, helium and neon. Figure 3.1 shows the μ_{JT} depending on the temperature for different gases. Helium has the lowest inversion temperature at 34 K, where the attraction forces is equal to repulsion. For ideal gases the Joule-Thomson coefficient is zero.

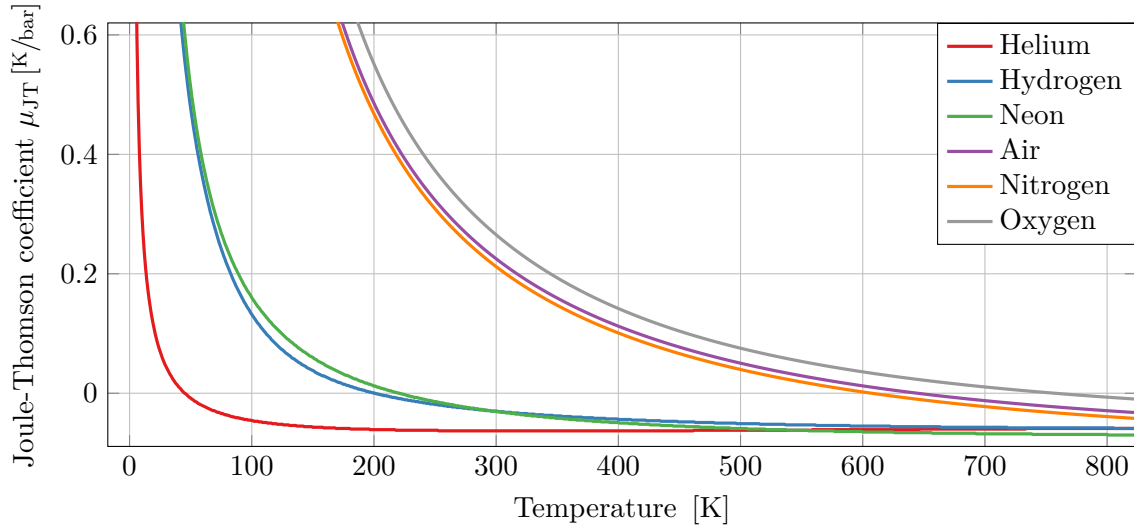


Figure 3.1: Joule-Thomson coefficient of different gases at 1 bar depending on the temperature. [8]

3.2 Passage of charged particles through matter

Charged particles like electrons or positrons passing through matter are deflected by many small-angle scatters, the nuclei and the electrons of atoms. The net scattering resulting of this multiple small-scatter follows a distribution that can be approximated by a Gaussian curve. This distribution is disturbed by "hard" scatters which produces a deviation at the far end of the curve. Figure 3.2 shows a charged particle passing through matter and the quantities used to describe the deviation. For a thin detector as used in the Mu3e experiment the y and z displacement can be neglected and only the angle deviation θ must be considered.

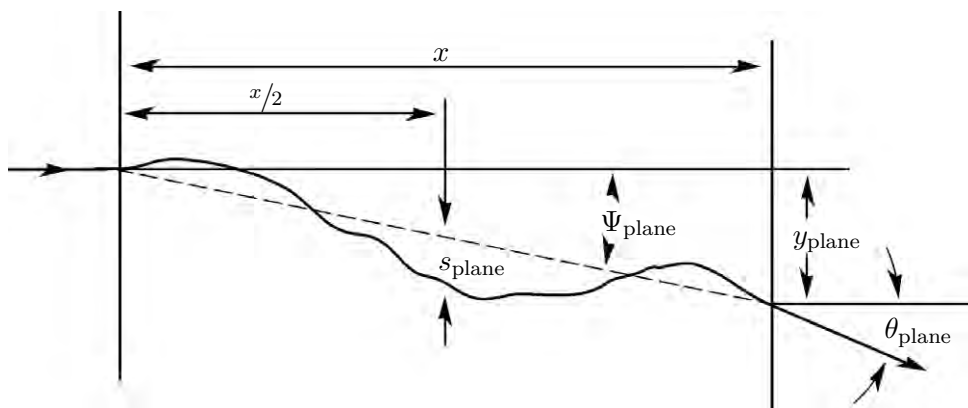


Figure 3.2: Used quantities used for multiple Coulomb scattering modified from [13].

The width of the Gaussian distribution of the deviation angle can be estimated as

$$\theta_0 = \frac{13.6 \text{ MeV}}{\beta c \cdot p} z \sqrt{\frac{x}{X_0}} \left[1 + 0.038 \cdot \ln\left(\frac{x \cdot z^2}{X_0 \cdot \beta^2}\right) \right] \quad (3.1)$$

where p , βc and z are the momentum, velocity and charge number of the incident particle. The radiation length X_0 describes the mean distance over which a high energy electron loses all but $1/e$ of its energy by bremsstrahlung. The radiation length is dependent on the atomic number. Light materials have a higher radiation length which leads to less scatters and lower deviation angle. For experiments observing the trajectories of charged particle a high radiation length is crucial to increase the precision.

This section has been summarised out of “Review of Particle Physics” [13].

3.3 Cooling

The analytical study of the cooling system is only performed for the gap flow between layers 1 & 2 as it only contains one cooling flow. Layers 3 & 4 have several cooling flows which make an analytical study more complex and less accurate.

3.3.1 Illustration of the system

The cooling system of the MuPix chips is simplified here for the analytical study. Figure 3.3 shows the inflow geometry in red as well as the gap flow between layers 1 & 2 (G12) in transparent grey. After the gap flow the outflow geometry follows which is not displayed here. The in- and outflow are neglected in this chapter as it causes some irregular flow which can hardly be considered.

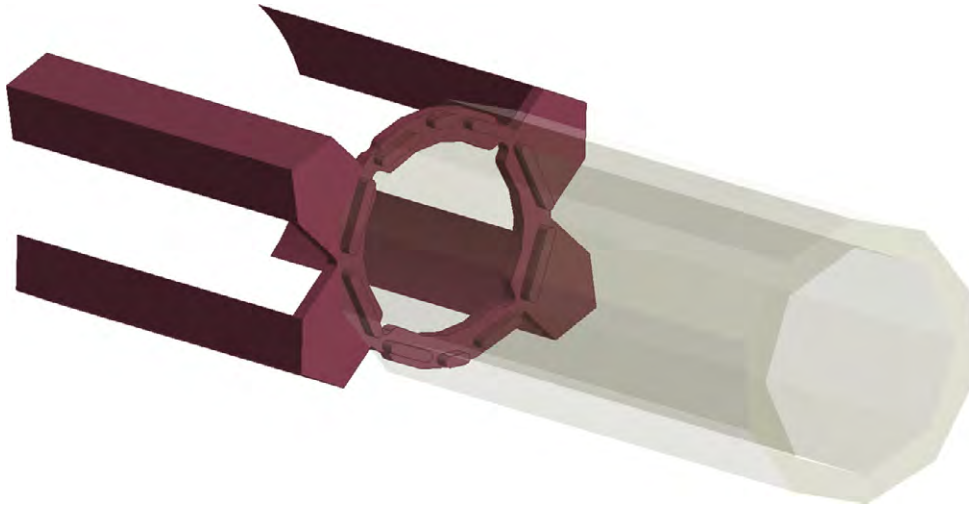


Figure 3.3: Inflow geometry and gap flow between layers 1 & 2.

The octagons and decagons of layers 1 and 2 are simplified by a tube with diameters corresponding to the edge distances illustrated in figure 3.4. For a tube there are analytical approximations which can be used for a first estimation as well as a reference for the simulations. Two MuPix chips are also shown, which are overlapping the outer decagon and the inner octagon.

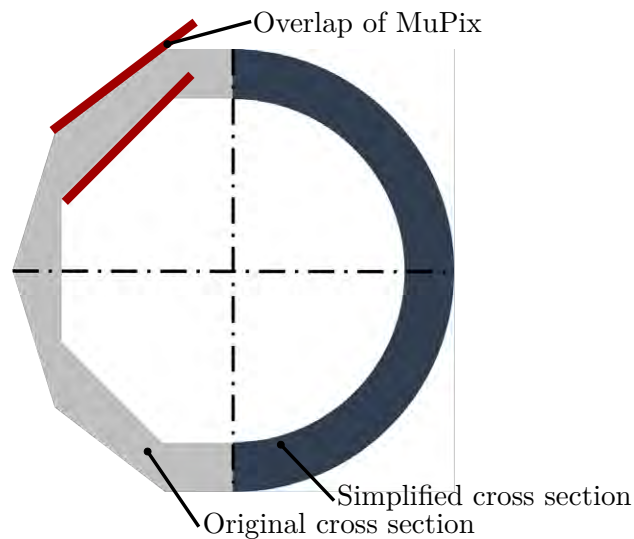


Figure 3.4: Simplified cross section of gap flow between layers 1 & 2 for analytical study.

The simplified geometry is a tube with a length of 120 mm, inner diameter of $D_i = 46$ mm and outer diameter of $D_o = 59$ mm. The heat dissipation of the chip is applied onto the whole wall but corrected to obtain the total heat which is emitted by the MuPix chips.

3.4 Dimension analysis

With a dimensional analysis of the simplified case the relevant non-dimensional number can be identified. Figure 3.5 shows the dimensions that have been evaluated to be relevant for the cooling process. There are in total 13 dimensions and 4 physical units ($[K, kg, s, m]$). As the specific heat capacity is only used together with the density this two are combined. The heat dissipation \dot{q} is not considered for the non-dimensional analysis. This gives a total of six non-dimensional numbers which can be found with Buckingham- Π theorem.

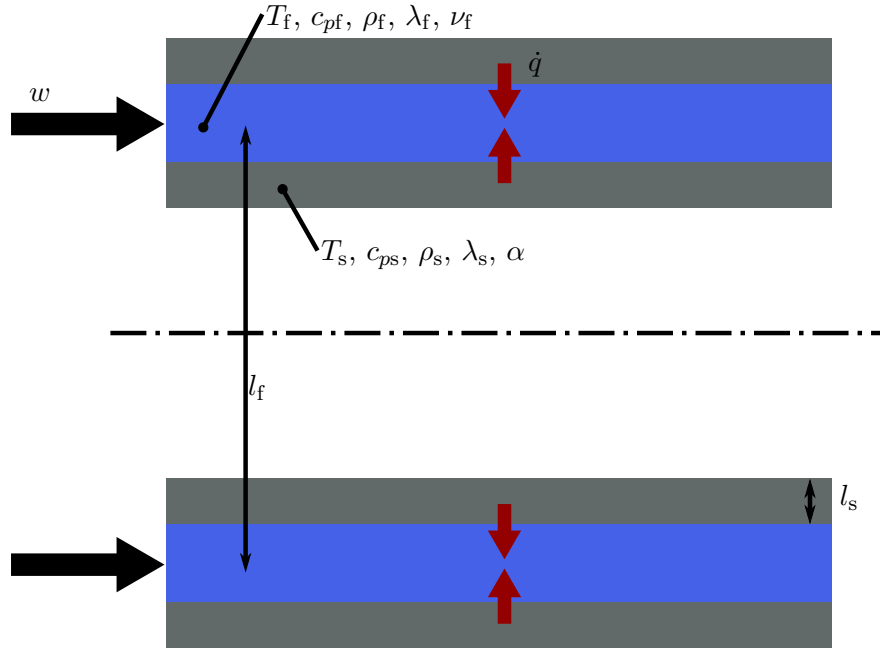


Figure 3.5: Annular flow considered for the analytical study of the gap flow between layers 1 & 2.

The six non-dimensional numbers are shown below. Not all these numbers have been used in this thesis. Π_{3-6} have been used for the estimation followed in the next sections.

$$\Pi_1 = \frac{T_f}{T_s} \quad (3.2)$$

$$\Pi_2 = \frac{c_{pf} \cdot \rho_f}{c_{ps} \cdot \rho_s} \quad (3.3)$$

$$\Pi_3 = \text{Nu} = \frac{\alpha \cdot l_f}{\lambda_f} \quad (3.4)$$

$$\Pi_4 = \text{Pr} = \frac{\nu \cdot \rho_f \cdot c_{pf}}{\lambda_f} \quad (3.5)$$

$$\Pi_5 = \text{Re} = \frac{l_f \cdot w}{\nu} \quad (3.6)$$

$$\Pi_6 = \text{Bi} = \frac{\alpha \cdot l_s}{\lambda_s} \quad (3.7)$$

3.5 Estimation of physical parameters

For the cooling analysis, CFD simulations and measurements it is important to know the present physical conditions. This includes mainly flow conditions and thermal properties.

Table 3.1: Data used for the estimation of non-dimensional number.

Property	Value	Unit	Source
Length scale l	13	[mm]	$D_o - D_i$
Velocity w	10	[m/s]	
Wall temperature T_w	70	[°C]	
Fluid temperature T_0	0	[°C]	
Coefficient of thermal expansion Helium γ	$3.41 \cdot 10^{-3}$	[1/K]	[8]
Mach number	0.06 – 0.15	[–]	
Reynolds number	1090 – 2350	[–]	
Richardson number	$3.04 \cdot 10^{-4}$	[–]	

3.5.1 Mach number

The Mach number is used to estimate if compressible effects can be expected. The Mach number for the high velocity (60 m/s) in the inflow tubes of G12 is $Ma = 0.06$. The inflow slots, where the fluid is directed into the gap has the highest velocity which goes up to 150 m/s which is still far away from $Ma = 0.3$. For layers 3 & 4 the velocities are quite similar. Therefore, compressible effects of the fluid is not expected and will be neglected in this thesis.

$$Ma = \frac{w}{c} \quad (3.8)$$

3.5.2 Reynolds number

The Reynolds number is computed to give an idea if the flow is rather laminar, turbulent or in a transitional region. The critical Reynolds number for circular tubes and similar forms is $Re_{crit} \approx 2300$. Under Re_{crit} the flow stays always laminar. The transition region is between $2300 < Re < 10^4$ where the flow is influenced by the inflow conditions. A flow with a Reynolds number over 10^4 is certainly turbulent. For an annular gap flow the critical Reynolds number is the same when using as characteristic length the difference of the diameters. [14]

$$Re = \frac{D_h \cdot \rho \cdot w}{\mu} \quad (3.9)$$

Here only the Reynolds number of G12 are estimated but are characteristic for all flows, which are in a similar range. In chapter 4 the Reynolds number of every flow is evaluated. There are

two main regions which have different Reynolds number which are shown in figure 3.3. The red inflow region has a smaller area and has therefore higher velocity, whereas the grey transparent gap flow has lower velocities.

Inflow tubes

For the inflow tubes the hydraulic diameter (see equation (3.10)) is used for the characteristic diameter which is 4.7 mm. The average flow velocity is 60.4 m/s which results in a $Re = 2350$. This is just above Re_{crit} and therefore in the transition region. The flow will probably stay laminar in the inflow tubes.

$$D_h = \frac{4 \cdot A}{U} \quad (3.10)$$

Annular gap flow

The length scale in the gap is defined following VDI-Wärmeatlas [14] which is the difference of the diameters (see equation (3.13)). The hydraulic diameter of the annular gap flow is therefore 13 mm and has an average flow velocity of 10 m/s. This results in a Reynolds number of 1090 which is clearly under the critical Reynolds number. The annular gap flow will stay laminar.

3.5.3 Richardson number

Another relevant number is the Richardson number (see equation (3.11)) which is basically comparing the natural convection to the forced convection. With small Richardson numbers the natural convection can be neglected and with high numbers the forced convection.

For gap flow between layers 1 & 2 the Richardson number is small and is therefore indicating that the natural convection can be neglected and therefore also the gravitation and thermal expansion of the gas. For the other flows and air as fluid the Richardson number is in a similar range.

$$Ri = \frac{g \cdot \gamma \cdot (T_w - T_0) \cdot l}{w^2} \quad (3.11)$$

3.5.4 Heat radiation

All bodies with a temperature higher than the absolute zero is emitting thermal radiation. This radiation has mostly wavelength in the infrared region. When a body is in thermal equilibrium with its surroundings, the thermal radiation emitted is approximately equal to the radiation absorbed. This is also depending on the emissivity and absorptivity of the surface.

As the MuPix chips are heated and have a higher temperature than the surrounding, there is a heat radiation which is given to the environment. With the expected maximal temperature of 70 °C the heat radiation \dot{Q}_{rad} can be computed with the Stefan-Boltzmann law (see equation (3.12)). The different material used for the measurement and the simulation have different emissivity ϵ . For the measurement with the thermal camera a black coating (NEXTEL) has been applied with an emissivity of 0.98.

Comparing the resulting radiation emitted by the heated chips without a coating it is neglectable compared to a heat dissipation of 1.8 W. With the NEXTEL coating the radiation is around 6 % of the total heat dissipation. This estimation is neglecting the heat absorption from the environment, which would even more decrease the heat loss from radiation. Therefore, the heat radiation is mostly neglected for the simulation and the measurements. During the measurements this was verified using an aluminium foil with the bright side over the mockup to reflect the radiation.

$$\dot{Q} = \epsilon \cdot \sigma \cdot A \cdot T^4 \quad (3.12)$$

Table 3.2: Data used for the heat radiation estimation.

Property	Value	Unit	Source
Area	4.6	[cm ²]	
Temperature	343.15	[K]	
Emissivity Steel ϵ	0.07	[-]	[11]
Emissivity Silicon ϵ	0.1	[-]	[15]
Emissivity NEXTEL ϵ	0.98	[-]	[16]
Stefan-Boltzmann-constant σ	$5.67 \cdot 10^{-8}$	[W/m ² T ⁴]	
Radiation Steel \dot{Q}	$25.3 \cdot 10^{-3}$	[W]	
Radiation Silicon \dot{Q}	$36.2 \cdot 10^{-3}$	[W]	
Radiation NEXTEL \dot{Q}	$108.5 \cdot 10^{-3}$	[W]	

3.6 Cooling analysis

The relevant non-dimensional numbers for the cooling estimations are Nusslet, Prandtl, Reynolds and to some extent the Biot number. The Reynolds number has already been analysed and emphasises a laminar flow through the gap. With this information the Nusselt number can be computed with the help of literature which finally gives the wall heat transfer coefficient α . The Prandtl number can be computed in dependence of the temperature and is easily obtained.

3.6.1 Heat transfer

The VDI-Wärmeatlas [14] has a large base of estimation for heat transfer for different cases. For an annular gap flow there is a section, which is only considering constant wall temperatures. For a tube there are approximations given for constant heat flux from the wall. Both cases give a similar wall heat transfer coefficient with less than 10% deviation. Still in this section the approximation with a constant heat flux is shown which is following [14, Chapter G4].

For the diameters the definition for an annular gap flow is

$$D_{h,g} = D_o - D_i. \quad (3.13)$$

The local Nusselt number approximation for a constant heat flux with thermal and hydrodynamic run-up for a laminar flow is

$$\text{Nu}_{x,q} = \left(\text{Nu}_{x,q,1}^3 + 1 + (\text{Nu}_{x,q,2} - 1)^3 + \text{Nu}_{x,q,3}^3 \right)^{1/3} \quad (3.14)$$

which consists of three Nusselt numbers

$$\text{Nu}_{x,q,1} = 4.364 \quad (3.15)$$

$$\text{Nu}_{x,q,2} = 1.302 \left(\text{Re} \cdot \text{Pr} \frac{D_{h,g}}{x} \right)^{1/3} \quad (3.16)$$

$$\text{Nu}_{x,q,3} = 0.459 \cdot \text{Pr}^{1/3} \left(\text{Re} \frac{D_{h,g}}{x} \right)^{1/2}. \quad (3.17)$$

With equation (3.4) and equation (3.18) the wall heat transfer coefficient can be computed.

$$\alpha = \frac{1}{l} \int_0^l \alpha_x dx \quad (3.18)$$

The temperature for the fluid properties have been considered with a middle temperature of $T = 30^\circ\text{C}$. The influence of the material data is around 0.15% and could be neglected as other simplification made before have higher uncertainties.

The heat dissipation of the MuPix chips is indicated as heat dissipation per surface of the chip. The total heat \dot{Q} is equal to 198.7 W which gives with the area of the cylinders a corrected heat load of $\dot{q}_{cor} = 499.4 \text{ mW/cm}^2$ for helium. For air similar conditions were chosen to obtain a similar behaviour as with helium. The Reynolds number and the temperature increase of the air has been set to the same value as with helium. The resulting properties are shown in the following table 3.3.

Table 3.3: Data used for the estimation of the G12.

Property	Helium	Air	Unit
$D_{h,g}$		13	[mm]
w	10	1.28	[m/s]
\dot{m}	2	1.87	[g/s]
\dot{Q}	198.7	35.8	[W]
\dot{q}	400	72.1	[mW/cm ²]
\dot{q}_{cor}	499.4	90.0	[mW/cm ²]
$\Delta T_{i,o}$	19.1	19.1	[K]
$\text{Re}(T = 30^\circ\text{C})$		1088	[-]
$\text{Pr}(T = 30^\circ\text{C})$	0.66352	0.7067	[-]
$\text{Nu}_{x,q,1}$		4.364	[-]
$\text{Nu}_{x,q,2}(T = 30^\circ\text{C})$	$2.695 \cdot x^{-1/3}$	$2.748 \cdot x^{-1/3}$	[-]
$\text{Nu}_{x,q,3}(T = 30^\circ\text{C})$	$1.4636 \cdot x^{-1/2}$	$1.4913 \cdot x^{-1/2}$	[-]
$\text{Nu}(T = 30^\circ\text{C})$	10.71	10.96	[-]
$\alpha(T = 30^\circ\text{C})$	126.87	21.91	[W/m ² K]

The global α value shown in table 3.3 shows the magnitude of the heat transfer coefficient for helium and air. The one of helium is around six times higher than the one of air. Figure 3.6 shows the local heat transfer coefficient computed with the local Nusselt number Nu_x . Around $x = 0$ the local heat transfer coefficient goes to infinity due to the inexistent thermal boundary layer. The integral of this curve gives the global heat transfer coefficient.

The wall temperature can be computed with

$$T_w = \frac{\dot{q}_{cor}}{\alpha_x}. \quad (3.19)$$

This temperature is also shown in figure 3.6 with the temperature increase being equal for helium and air. The wall temperature is higher for air as the heat transfer coefficient is proportion of the helium to air is 5.8 which is a little higher than the one of the heat capacities which is

5.16. Still the temperature difference is under 5 K which makes the helium and air measurement comparable. The expected temperature with helium and a heat flux of 400 mW/cm^2 is around 70°C which is just in the set boundaries. But there are some simplification as the overlap which will probably cause higher temperatures.

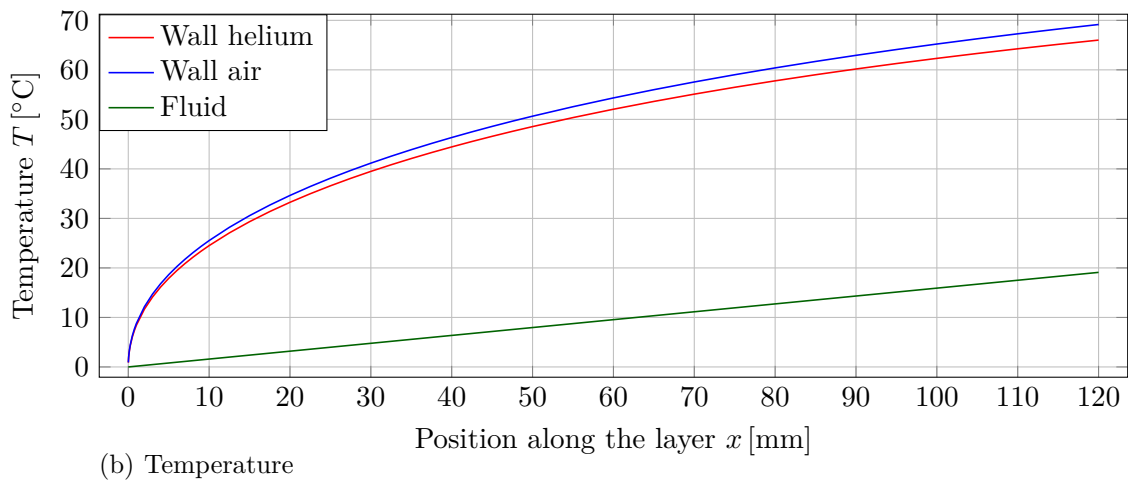
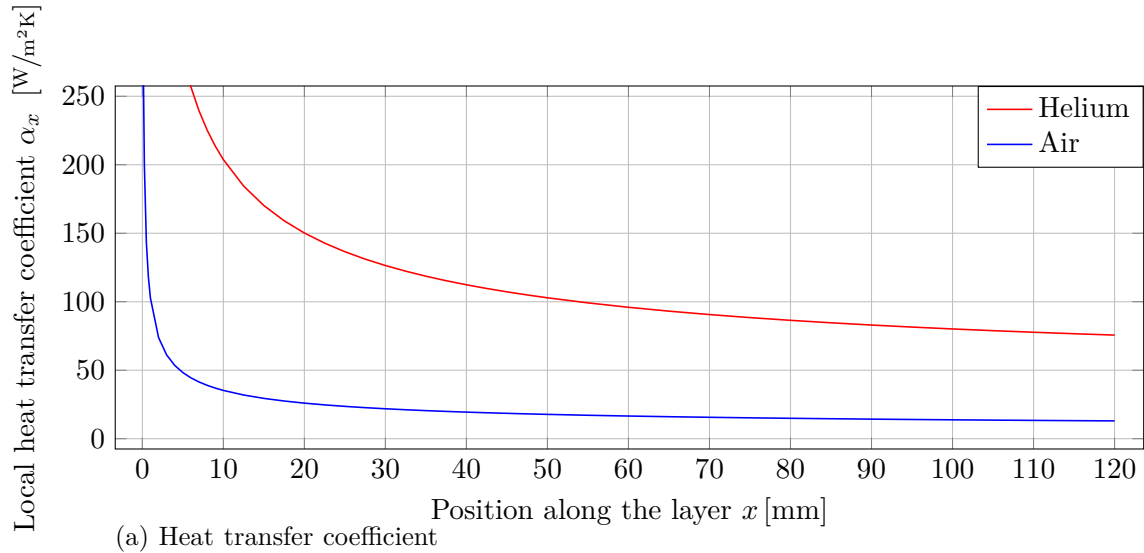


Figure 3.6: Local heat transfer coefficient and resulting temperature from uniform wall heating.

3.6.2 Heat conduction in chip

In the previous section the heat transfer of an annular flow was estimated for both fluids. The chips were completely neglected and will be analysed in this section. At first the temperature increase through only one chip will be estimated followed by a heat transfer through the polyimide foil. Some parts of the chip are not directly cooled and therefore the temperature is increasing compared to the cooled part of the chip. The Biot number with silicon is around $4 \cdot 10^{-5}$ which shows that the heat conduction in the chip is nearly irrelevant compared to the heat transfer of

the fluid. The internal temperature could be assumed constant.

Figure 3.7a shows one silicon chip insulated on one side and cooled from a flow on the other side. The temperature at the wall can be obtained with

$$T_1 = T_\infty + \frac{\dot{q}_{\text{gen}} \cdot l_s}{\alpha} \quad (3.20)$$

and the temperature at the interface to the insulation with

$$T_0 = T_1 + \frac{\dot{q}_{\text{gen}} \cdot l_s^2}{2 \cdot \lambda}. \quad (3.21)$$

As predicted with the Biot number the temperature over the thickness inside of the chip is nearly constant.

If the polyimide and araldite are also considered as shown in figure 3.7b, the temperature of the chip should increase. The wall temperature is still the same as the flow conditions are assumed to be constant. The temperature between the sheets can be computed following

$$T_x = T_{x+1} + \frac{\dot{q}_{\text{gen}} \cdot l_s \cdot l_x}{\lambda_x}. \quad (3.22)$$

Figure 3.8 shows the temperature profile of both cases, with and without the araldite and polyimide over the silicon chip. The difference between both cases is quite small. The major cause of temperature increase is the wall heat transfer coefficient. The polyimide foil is causing a temperature increase of ~ 1.5 K. The temperature profile of the fluid has been scaled for better visualisation.

All dimensions used for computation and the resulting temperature are shown in table 3.4.

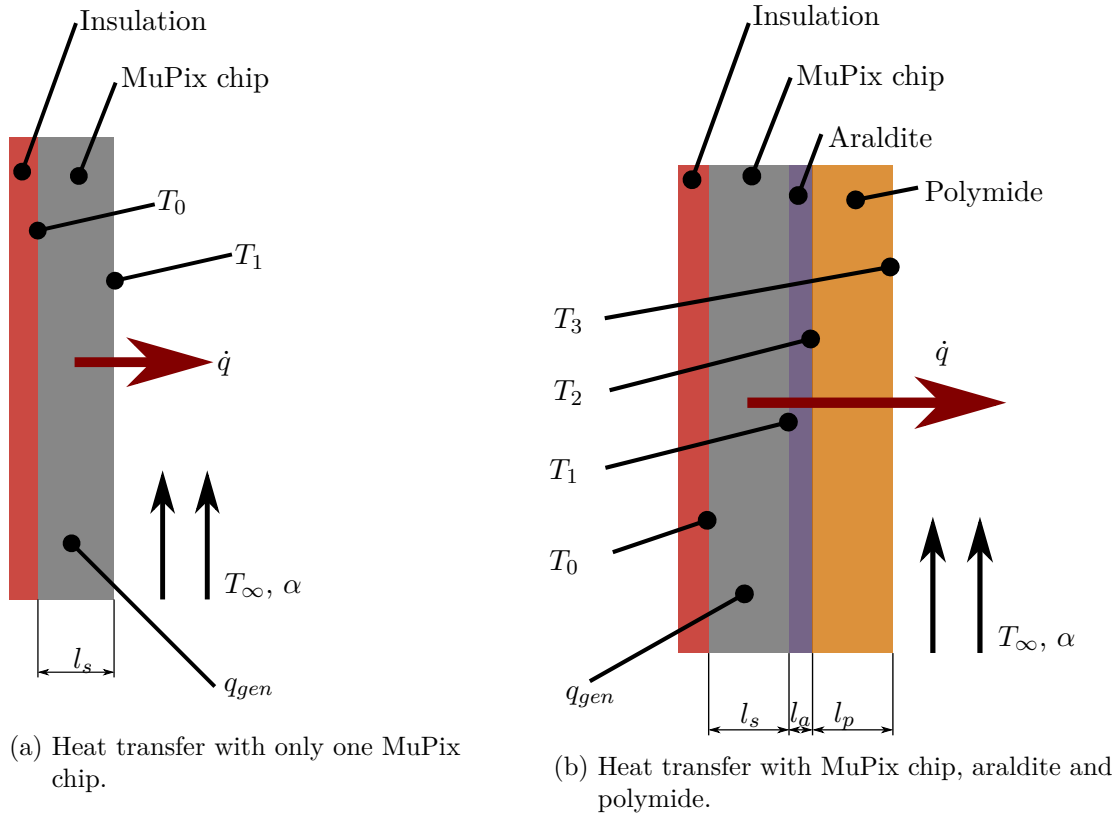


Figure 3.7: Heat generation inside the MuPix chip and heat transfer through the solid parts to the fluid.

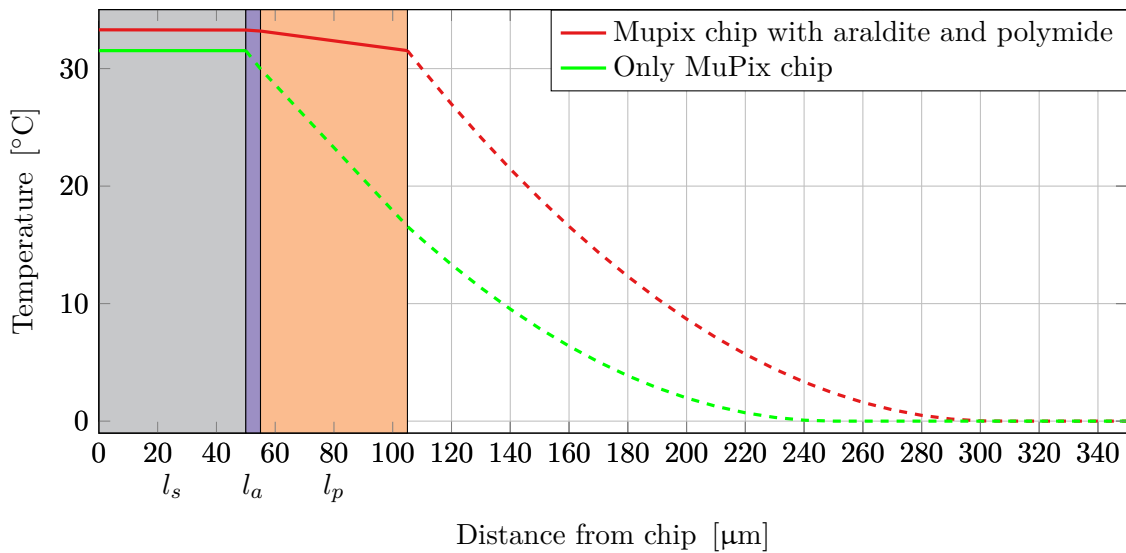


Figure 3.8: Temperature profile through the MuPix (silicon) chip and other solids as well as a visualisation of the fluid temperature (scaled).

Table 3.4: Properties of the conjugated heat transfer of the silicon chip.

Case	Properties	Silicon	Steel	Unit
	l_s	50		[μm]
	l_a	5		[μm]
	l_p	50		[μm]
	α	126.87		[$\text{W}/\text{m}^2\text{K}$]
	T_∞	0		[$^\circ\text{C}$]
	\dot{q}_{gen}	$8 \cdot 10^7$		[W/m^3]
	λ	149	15	[W/mK]
	$\text{Bi}(l_s)$	$4.2 \cdot 10^{-5}$	$4.2 \cdot 10^{-5}$	[$-$]
Only chip	T_1	31.528		[$^\circ\text{C}$]
	T_0	31.529	31.535	[$^\circ\text{C}$]
Chip, araldite and polyimide	T_3	31.528		[$^\circ\text{C}$]
	T_2	33.195		[$^\circ\text{C}$]
	T_1	33.286		[$^\circ\text{C}$]
	T_0	33.286	33.299	[$^\circ\text{C}$]

Temperature increase in overlap

Over the thickness of the MuPix chip the temperature is nearly constant for silicon and steel. But there are parts of the MuPix chip on layer 2 which are not directly cooled. This is only present on layer 2 where there is one cooling flow on the inner side. The geometry is described in section 4.2.2. Figure 3.9 shows a simplification of one MuPix of layer 2 with the green part as overlap which is not directly cooled by the flow. Assuming a constant temperature of the grey part the maximum temperature of the overlap can be computed following

$$T_{\text{ov}} = T_{\text{MuPix}} + \frac{\dot{q}_{\text{gen}} \cdot l_{\text{ov}}^2}{2 \cdot \lambda}. \quad (3.23)$$

The temperature increase is higher with steel due to worse heat conduction. With silicon there is still a temperature increase of 4K while have a constant heat load. Later it will be seen that the heat dissipation in the overlap is even higher as for the grey part, causing even higher temperatures in the overlap.

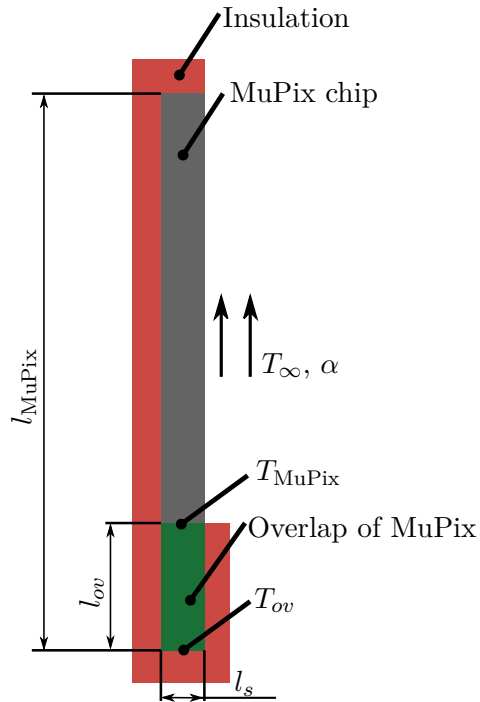


Figure 3.9: Estimation of the temperature increase in the overlap of the MuPix chip with different materials.

Table 3.5: Properties for temperature increase in the overlap of layer 2.

Properties	Silicon	Steel	Unit
l_s	50		[μm]
l_{MuPix}	23		[mm]
l_{ov}	4		[mm]
\dot{q}_{gen}	$8 \cdot 10^7$		[W/m ³]
λ	149	15	[W/mK]
$\text{Bi}(l_{\text{ov}})$	$3.4 \cdot 10^{-3}$	$3.4 \cdot 10^{-2}$	[–]
T_{MuPix}	33.286	31.535	[°C]
ΔT	4.30	42.67	[K]
T_{ov}	37.58	76.20	[°C]

3.7 Conclusions of analytical study

The results of the analytical study enhanced the understanding of the physical processes occurring during the cooling the MuPix chips. The knowledge could be used to build the CFD simulation model and also an estimation of the expected results for measurements and simulations. The estimation of non-dimensional numbers showed that the flow will mostly be incompressible and laminar. The convection is driven by forced convection and heat radiation is neglectable with steel or silicon chips, as it is less than one percent of the total heat dissipation.

The estimation of heat transfer showed that under the assumption of a tube flow, laminar flow and constant heat dissipation, the temperature of the wall goes up to 66°C for helium and with comparable conditions to 69°C with air. The heat conduction analysis of the MuPix chips finally showed that a modelling of the chip with heat conduction has a major influence on the occurring temperatures as not every part has the same cooling conditions.

4 CFD Simulation

The CFD simulations of the cooling system are shown in this chapter. As there are different cooling parts which were simulated independently, the first section is giving an overview of the geometry of the different parts, the modelling and simplifications made. Furthermore, the simulation and optimisation of layers 1 & 2 is shown in section 4.2, followed by an overview of the layers 3 & 4 in section 4.3. Since the mesh of layers 3 & 4 is large, the different flows were first optimised independently and then a combined simulation of all flows with heat transfer was performed. Section 4.4 shows the optimisation of the V-folds, followed by section 4.5 and section 4.6 which are showing the optimisation of the gap flows and finally in section 4.7 the combined simulation is shown.

4.1 Overview

Figure 4.1 shows the fluid geometry of part B (centre) of the helium cooling system. There is one flow in the middle for layers 1 & 2 which are shorter compared to the layers 3 & 4. For layers 3 & 4 four different flows are displayed. Two of them flow between the layers or other detectors and are exiting into a global flow which is not shown here. Additionally, there are two flows in the V-folds. The V-folds and the G12 are not exiting into the global flow but sucked out through tubes. The pressure difference between those flows and the surrounding can therefore be controlled with the outlet pressure level. The whole cooling scheme is shown in figure 2.2 on page 10 which additionally to part B (centre) is also displaying the up- and downstream part A & C. The mass flow through the different sections is shown in table 2.3.

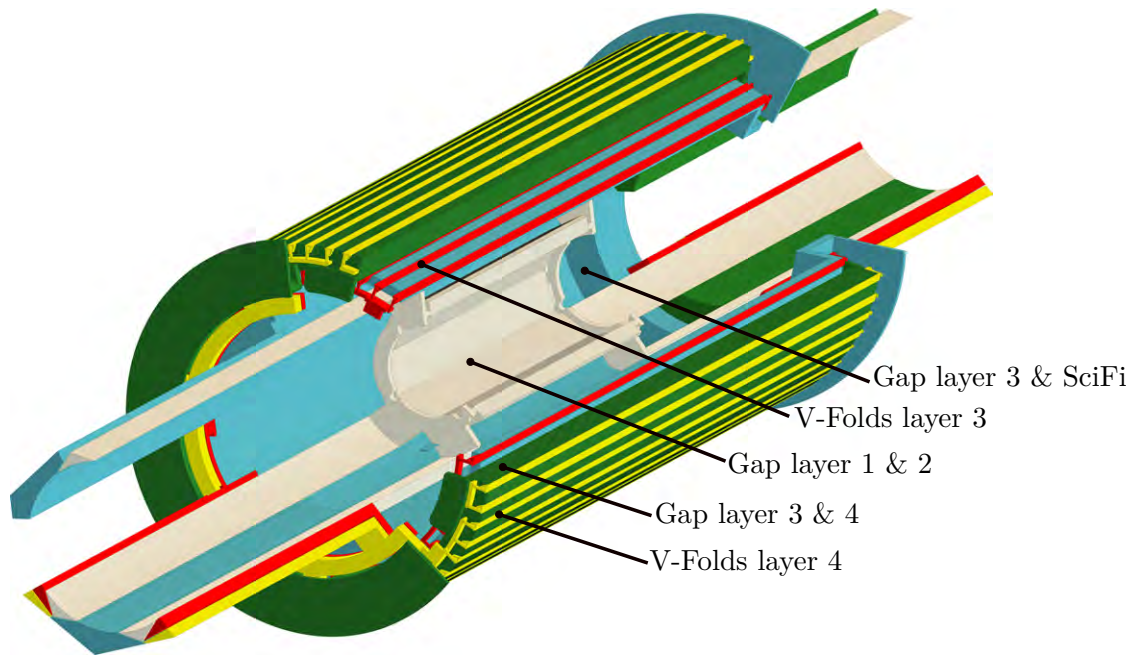


Figure 4.1: Fluid geometries of layer 1 to 4 in the centre part.

In this chapter many acronyms are used to describe the different flows and are summarised here:

V3	V-fold of layer 3
V34	V-fold of layers 3 & 4
V4	V-fold of layer 3
G12	gap flow between layers 1 & 2
G34	gap flow between layers 3 & 4
G3S	gap flow between layer 3 & SciFi
G3T	gap flow between layer 3 & tile detector
Part A	Upstream layers 3 & 4
Part B	Center layers 3 & 4
Part C	Downstream layers 3 & 4

The fluid geometries shown in this chapter have all been constructed based on the Computer-aided design (CAD) geometry. The flow geometry was designed by Silvan Streuli from PSI who has also designed most of the detector construction. Some parts were later adapted as non negligible simplifications were found. Solid geometry as the silicon chips or some of the polyimide layers have been simplified to reduce the complexity of the model.

4.1.1 Goals

Goal of the Computational Fluid Dynamics (CFD) simulation is to investigate the cooling behaviour of the MuPix chips and verify the results already obtained by previous theses of Tormann [6], Ng [4] and Herkert [5]. For the gap flow between layers 1 & 2 Tormann [6] found a back-flow-regions which caused higher temperature as warmed up helium flowed back to the inlet. The cause of this back-flow-regions should be analysed and if possible optimise the geometry to reduce the chip temperature. Simulation for the outer layers were also carried out and showed less critical temperatures. But this simulations had several simplifications (geometrical and physical) which could have an effect on the flow behaviour and also temperature distribution. The previous simulations also simplified the heat dissipation as a constant heat load on the fluid walls without regarding the heat conduction in the chips and the polyimide. During the project the heat load specification changed from a constant heat load in the whole chip to a higher heat load in the periphery and a lower one in the detector part (see section 4.1.5).

The previous projects all used a constant heat load onto the fluid walls. Thus heat conduction in silicon chips and a polyimide which appeared as important at section 3.6.2 is neglected. To obtain reliable results it is crucial to model the MuPix chips as some parts are better cooled than others. This is especially required for layers 3 & 4 where several flows are cooling the MuPix chips. The percentage from total cooling rate of each flow is not known and can only be obtained in a CFD simulation considering all flows and solids parts.

4.1.2 Optimisation possibilities

One goal of the simulation is the optimisation of the helium cooling system. Many parts of the system are already defined and can hardly be changed. Still there are some options to optimise the cooling which are discussed here.

Heat transfer enhancement

Different methods to enhance the heat transfer between the wall and the fluid have been investigated. A rougher surface which can be achieved with corrugated or ribbed surface mostly increases the heat transfer. Other methods that significantly increase the turbulence and thus the mixing of the fluid are pulsating or swirling flows. A drawback of these methods is mostly a higher pressure loss. [17, 18]

Unfortunately these methods are not suitable for the application in the Mu3e experiment. Pulsating or swirling flows would cause even more irregular flows which could cause undesired

movement of the layers. Higher pressure drop would aggravate the pressure difference between the gap flows and the global flow and finally the surface of the MuPix chips can hardly be modified.

Inflow geometries

For several flows like G12, gap flow between layers 3 & 4 (G34) or V34 the inflow geometry which leads to the MuPix chips have not been designed in regards of a regular mass flow and cooling. Changes of the inflow geometry are generally no issue as this only influences the cooling and no parts of the detector. Most of these geometries are constructed in the largest possible dimensions so the optimisation consists of diminishing some inflow sections. This is applied to reduce the flow at positions where there is a too high mass flow. The result of it are higher pressure losses of the inlet parts.

For gap flow between layer 3 & SciFi (G3S) the inflow does not consist of slots like the other flows. Some guidance plates could be mounted after the inflow which can be used to optimise the mass flow distribution and therefore the cooling behaviour.

4.1.3 Simplifications

Several general simplifications have been made to enable simulation of the cooling of the chips in an acceptable time. They are mostly based on the estimation made in section 3.5 and are listed below.

Natural convection	Natural convection to the environment has been neglected.
Heat radiation	Heat radiation to the flow and environment has been neglected.
Incompressible	As the Mach number is under 0.3 the flow is considered as incompressible for the simulation. The other criteria for incompressible flow, such as low frequencies, differences in elevation and dissipation, also point to a non-compressible flow.
Ideal gas	The reduced temperature in the range of the Mu3e experiment is for helium $T_r \approx 68$ and for air $T_r \approx 2.3$ so following Y. A. Cengel [19, p. 139] both can be assumed as ideal gas. This is also neglecting the Joule-Thomson effect which has been seen during the helium measurement (see section 5.3.11).
Inflow tubes	The flow through the in- & outflow tubes has been assumed to be constant per area. In the experiment the flow could differ due to the distribution system of the flow.

Leakage	The layer and V-folds are not completely airtight and some helium can flow to other flows or the environment. This leakage flow has been neglected for simulations.
Layer	The layer are modelled as fixed walls but are quite flexible and are bending due to pressure gradient.
Stationary	The flow and heat transfer is assumed to have stationary results.

4.1.4 Boundary conditions

Inlet

The inlet mass flow was defined respecting table 2.3. The inlet temperature has been set to 0°C which is quite colder than the planned temperature of 4°C in the experiment. The small difference of temperature is not affecting the cooling behaviour of the helium and simplifies the comparison with Tormann [6] and others.

For the simulation of part A, B & C the G34, gap flow between layer 3 & tile detector (G3T) and G3S are merging into the global flow. For part B & C the outlet conditions of part A & C have been used which lead to higher mass flows and higher temperatures.

Outlet

The outlet is set to 0 Pa relative pressure which corresponds to 1 bar absolute pressure. In the experiment an underpressure at the outlet of V34 and G12 will probably be set to minimise the leakage flow.

Walls

For velocity treatment at the walls a no slip condition has been used.

The wall heat transfer was defined as adiabatic to environment and conservative heat flux for the interface between MuPix chip and flow.

For layers 3 & 4 a turbulence model is used with a y^+ which is mostly under 1 which can be seen in figure 4.2. Therefore, no wall function was needed for the simulation.

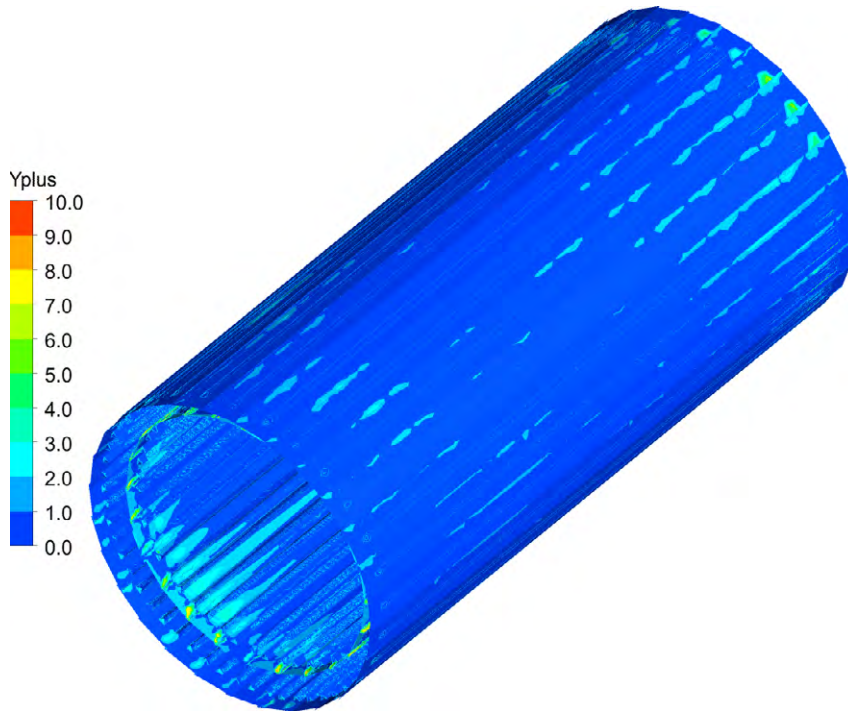


Figure 4.2: Dimensionless wall distance y^+ for original geometry.

Heat dissipation

The heat dissipation in the MuPix chips has been defined as a volumetric source in the whole chip. This is further discussed at table 4.1.

4.1.5 MuPix chips

The MuPix chips which have already been described in section 2.3.2 are the parts which have to be mainly cooled by the helium flow. At the beginning of the project the heat dissipation was specified as constant with 250 mW/cm^2 which is the expected specification and 400 mW/cm^2 as worst case scenario. Since the chips are modelled in the simulation, the heat production was defined volumetrically, which represents also the situation in reality.

After presenting the first simulation results of the G12, the heat dissipation was changed as there are two parts with different heat dissipations. The integral heat dissipation stayed constant over the whole chip but is only half of the specified production in the detector part of the chips and the remaining comes from the periphery. Figure 4.3 shows one chip with the detector and periphery part.

The heat dissipation per volume used for the simulation are shown in table 4.1. For the simulation which were compared with the measurements, the constant heat per volume was used.

The simulation representing the conditions of the Mu3e experiment were performed with the unequal heat load per volume.

As shown in figure 2.4 the temperature increase is linear with the heat dissipation and not influenced by the changing of material properties. Therefore, only the higher heat dissipation is simulated to efficiently use the computational resources.

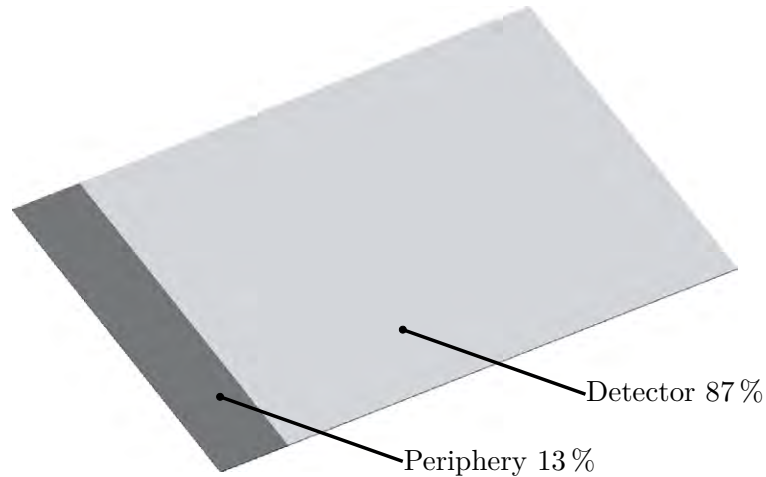


Figure 4.3: MuPix chip with different heat input sections.

Table 4.1: Heat dissipation per area and volume for periphery and detector part.

	Heat load		Units
	Detector	Periphery	
Constant heat per surface	400		[mW/cm ²]
Constant heat per volume		$8 \cdot 10^7$	[W/m ³]
Unequal heat per volume	$4 \cdot 10^7$	$34.6 \cdot 10^7$	[W/m ³]

4.1.6 Modelling

The simulations were performed using Ansys CFX 18.2. The modelling was first performed with the layers 1 & 2 and then adapted onto layers 3 & 4.

Time stepping

For the steady state simulations in Ansys CFX a physical time step was defined. To obtain an accurate result the time step should lay in a similar region than

$$\Delta t = \frac{l_{\text{Mesh}}}{w}. \quad (4.1)$$

Therefore, one fluid particle passes one cell per time step. The used physical time step was around $1 \cdot 10^{-4}$ s with helium and $1 \cdot 10^{-3}$ s for air due to lower velocities. The time step was set to a higher value at the beginning of the simulation to rapidly obtain an approximate start solution and later constantly decreased to the levels shown above.

Convergence criteria

As convergence criteria, the mass and heat balance as well as the temperature of the fluid and solid domain were used. These values were strongly dependent on the current time step and had large fluctuations with high steps and thus decreased with lower time steps. Once these values reached a stable level and the mass and heat balances showed a relative deviation of $> 0.2\%$ for the mass flow and $> 0.5\%$ for the heat, the simulation was considered converged and was stopped.

4.1.7 Mesh

The mesh has been computed with Ansys Workbench 18.2. For the flow regions a tetrahedral mesh has been used as there was no possibility for a structured mesh because of the complex geometry and several iteration steps which were performed for the optimisations. On all flow parts prism layers have been established. For the solid parts hexahedron sweep meshes were used.

Layers 1 & 2

A mesh size study has been realised to evaluate the needed mesh size for an adequate result. A too fine mesh requires high computational power and also takes longer per iteration step of the optimisation. Four different mesh sizes were simulated. Figure 4.4 shows the maximal MuPix temperature as well as the pressure drop dependent on different meshes. The temperature as well as the relative pressure at the inlet are increasing with smaller meshes. This is probably due to the finer grid which is better resolving the flow and heat transfer. As the results between 0.3 and 0.5 mm are showing only small differences, a mesh size of 0.5 mm has been used as it is more time efficient and delivers quite similar results compared to the finer mesh. For the high velocities parts and heat transfer walls a refinement with 0.4 mm was used.

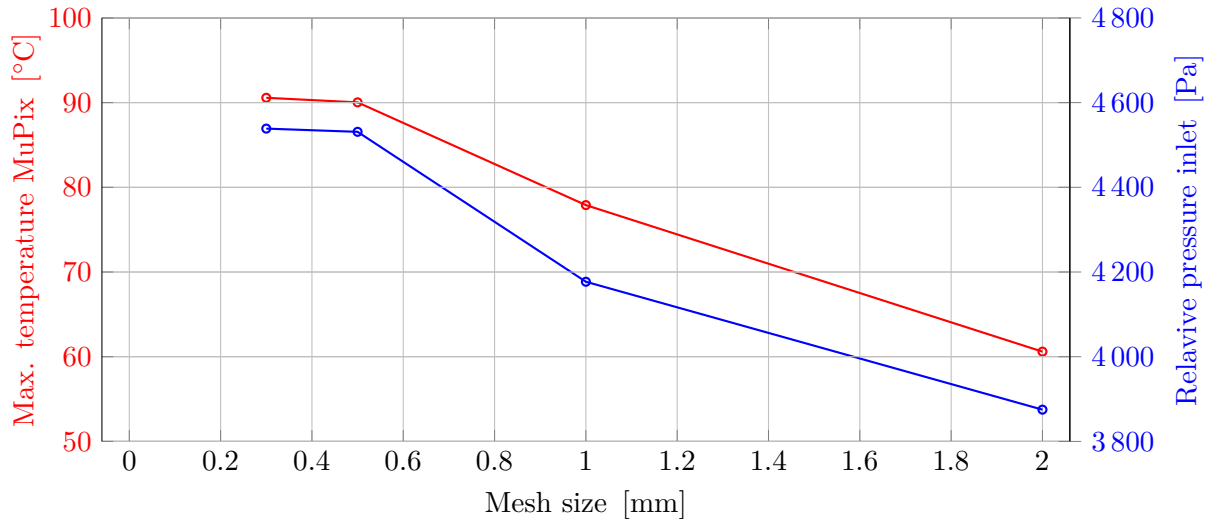


Figure 4.4: Maximal MuPix temperature and pressure drop from in- to outlet dependent on the mesh size.

Table 4.2 shows the mesh sizes used for the different flow and solid parts. In the gap, where the heat transfer occurs the mesh of the flow was refined. The prism layer were applied on all walls and have growth rate of 1.2.

Table 4.2: Mesh size of gap flow between layers 1 & 2 of different volumes and solid.

Region	Size [mm]	Cell over thickness
G12	0.5	
Refinement gap	0.4	
Prism layer (first layer)	0.05	7
Silicon	0.2	3

The mesh used had around $11.7 \cdot 10^6$ fluid elements and $0.4 \cdot 10^6$ solid cells which required a CPU time of ~ 650 h downscaled on one CPU.

Layers 3 & 4

The meshing of the all parts of all five flows together with the solid parts was quite a challenge. Firstly, the geometry needs to be designed very precisely to ensure that the right interfaces are found. The definition of all flow parts which require a prism layer and the control of interfaces are quite time consuming. The finest mesh which could be computed has the configuration showed in table 4.3. This restriction is due to Ansys Workbench 18.2 which did not manage to compute finer meshes. But also the maximal memory of 252.2 GB of the largest nodes on the

computing cluster were nearly reached with 220 GB. A finer mesh would therefore be possible, but this would be soon restricted by the computing cluster. The CPU time to simulate one part is around 2500 h downscaled on one CPU. With the largest available node which has 28 CPU the simulation took around four days.

A mesh study as carried out for the G12 has not been performed. Compared to the mesh size of G12 with 0.5 mm, a mesh dependency of the results for layers 3 & 4 is still expected, as the length scale, velocity and heat dissipation are quite similar. A mesh with a size of 1 – 1.5 mm showed in the mesh study of G12 a temperature which was around 10 – 15 K lower.

Table 4.3: Mesh size of different volumes and solid of layers 3 & 4.

Region	Size [mm]	Cell over thickness
G3S, G3T, G34	1.5	
V3, V4	1.0	
Refinement	0.7	
Prism layer (first layer)	0.05	5
Global	3.0	
Polymide	1.0	3
Silicon	1.0	3

A mesh of one part consists of about $62 \cdot 10^6$ elements whose portion is shown in figure 4.5. This large mesh requires a long time to be computed with the Workbench. Other software as ICEM were also tested but did not manage to create all interfaces between the different parts. Maybe there are better suited software for this purpose. Due to time constraints no further tests were performed.

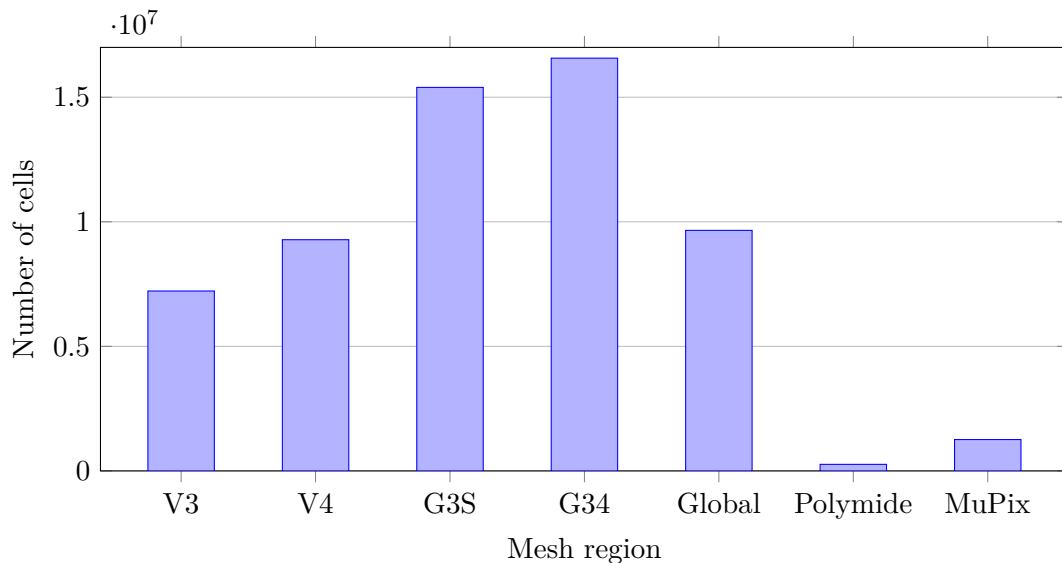


Figure 4.5: Number of elements per mesh region.

4.2 Layers 1 & 2

The gap flow between layers 1 & 2 (G12) is only present in the centre part and is placed over the target (see figure 2.2). Both layers have 6 chips over their length. Layer 1 is build as an octagon compared to layer 2 which is a decagon. Figure 4.6 shows the fluid geometry in beige with the in- and outlet. Additionally, the layers 1 & 2 with the silicon chips are also partly displayed. For layers 1 & 2 there is only one cooling flow intended between them.

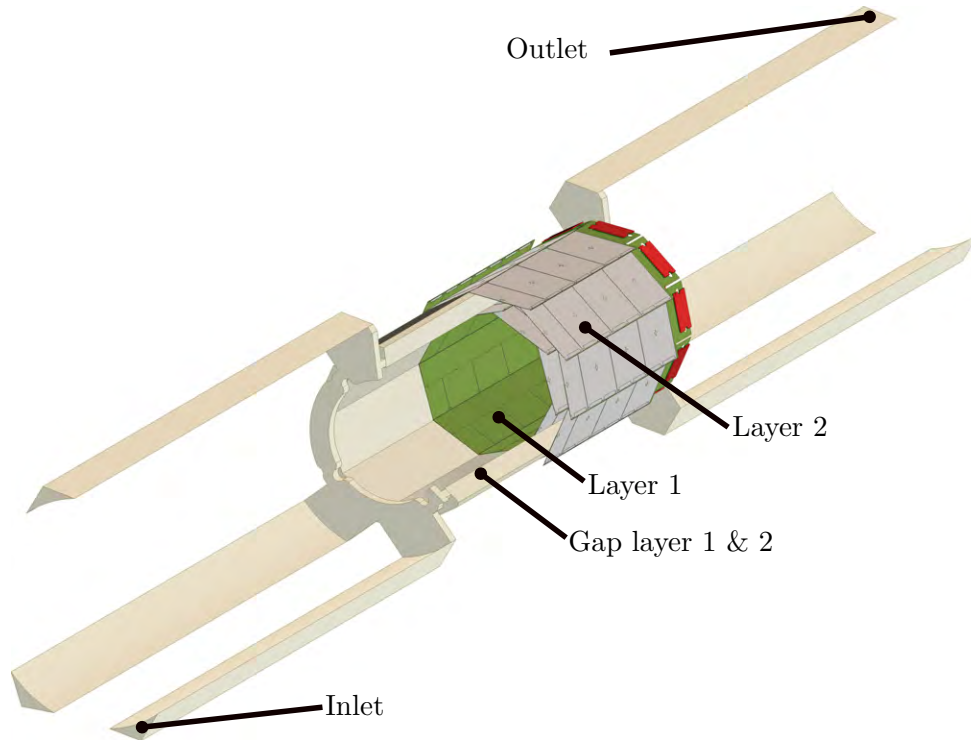


Figure 4.6: Geometry of gap flow between layers 1 & 2.

4.2.1 Geometry

The geometry of G12 has been mostly remodelled as there were some major simplifications which have an influence onto the helium flow and therefore the cooling behaviour. Main simplifications used by Tormann [6] are shown in figure 4.7. The overlaps of the chips which are indicated with ① & ② were not modelled which causes a reduction of the chip area of around 20%. Additionally, the overlap of layer 1 ① is located in the gap flow and has an influence on the flow behaviour. Figure 4.7b shows the cables which are closing a part of the inflow slots and have also been neglected until now. Finally, the carbon parts which are directly behind the inflow slots were also not considered.

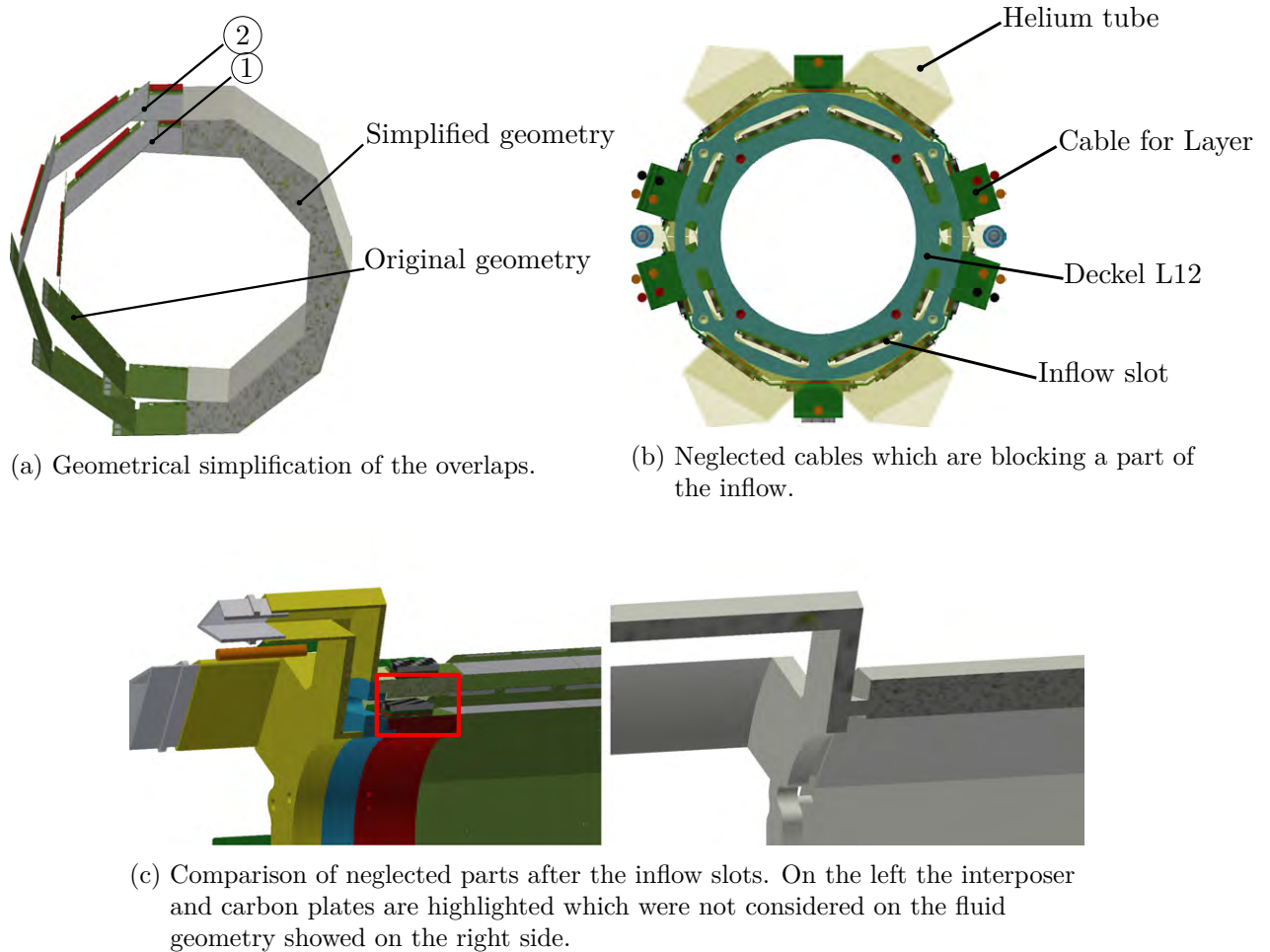


Figure 4.7: Geometrical simplifications made on gap flow between layers 1 & 2 from Tormann [6].

The geometry used for the simulation of G12 considered all the described elements to obtain a more accurate flow simulation.

4.2.2 MuPix chips on layers 1 & 2

Figure 4.8 shows the orientation of the MuPix chips on the layers 1 & 2. The gap flow is passing between them. It can be seen that for layer 2 there are parts which are not directly cooled by the flow. On layer 1 there is also an overlap, but it is less critical since it is located within the cooling flow. The overlap on the outer layer is mainly cooled by heat conduction which is later taken up by the coolant.

The red area is showing the periphery with the high heat dissipation and in yellow the detector part with the low heat dissipation. If a constant cooling of the helium flow is assumed, it is therefore clear that the periphery on layer 2 will have the highest temperature as it has a high heat dissipation and no direct cooling of the helium.

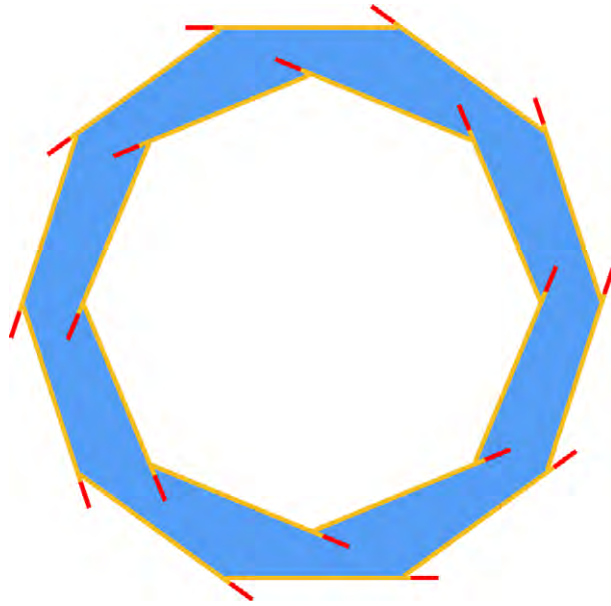


Figure 4.8: Orientation of the MuPix chips on layers 1 & 2 with the detector in yellow, periphery in red and blue cooling flow.

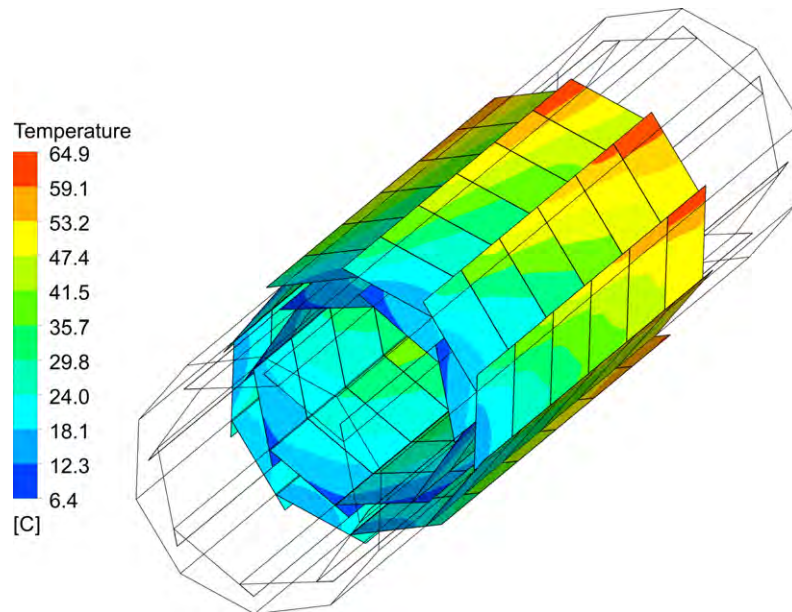
4.2.3 Results

The results obtained from the simulation of G12 are discussed in this section. All results showed here are with helium as coolant and silicon as chip material. Firstly, results obtained with a simplified geometry are discussed which are used as Benchmark for the further simulations and optimisation. Then, the results from the original geometry is shown, analysed and optimisation potential discussed. At the end the results obtained from the optimisation are shown.

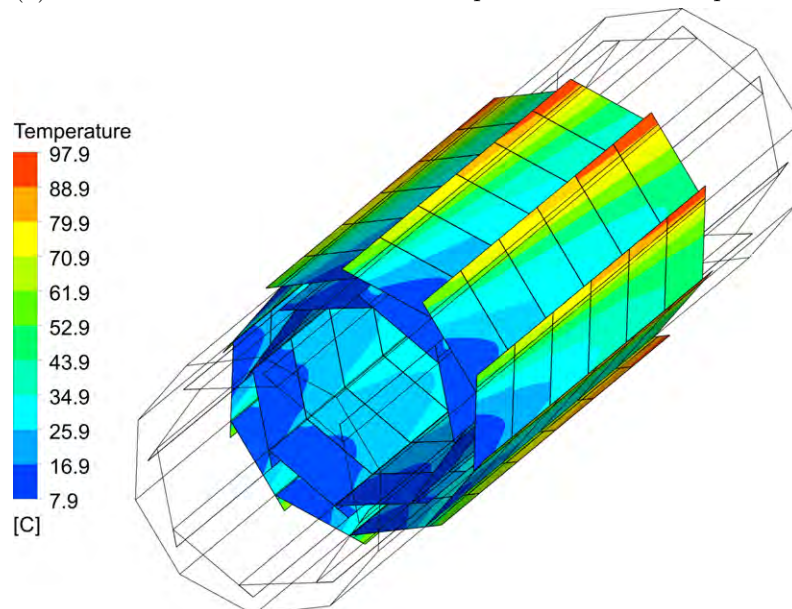
Benchmark results

As the in- & outflow of the G12 has a large influence on the results, a simplified geometry was used to estimate the possible temperature of the chips with straight in- & outlet. It is also useful to compare the influence of the unequal heat dissipation in the MuPix chip. Figure 4.9 shows the temperature of the MuPix with constant and unequal heat dissipation. With the equal heat dissipation the maximal temperature is $\sim 65^\circ\text{C}$ compared to $\sim 98^\circ\text{C}$ with the higher heat in the periphery. The main issue with the periphery is on layer 2 as there is no cooling flow directly over this overlap. Therefore, the heat has to be transferred by conduction to other cooled parts of the chip which is causing high temperature.

A change in the orientation would decrease the performance of the particle tracking and is therefore not suitable. It has still been tested with the Benchmark geometry and showed a major decrease of the maximal temperature. The temperature decreased from 98°C to 69°C .



(a) Benchmark with constant heat dissipation on MuPix chip.



(b) Benchmark with unequal heat dissipation on detector and periphery of MuPix chip.

Figure 4.9: Temperature of the MuPix chips with the Benchmark geometry.

Original geometry results

The results in this section are with constant heat dissipation on the detector and periphery. Figure 4.10 shows the temperature distribution on the MuPix chips. It can be seen that the maximal temperature is occurring in the overlap of layer 2 which are not directly cooled by the helium. But this high temperature is not on all of the overlaps like it has been seen for the Benchmark case. This is due to irregular flow distribution in the gap caused by the inlet

geometry. Figure 4.11a shows the velocity of the flow w in the z direction, where there are some high velocity regions and some backflow regions. The reason for this backwards flow is an unequal flow through the inlet slots. The slots just behind the tubes have a high mass flow compared to the one on the outside. Behind the slots with low mass flow a backflow region is occurring which leads to less cooling and therefore high temperatures.

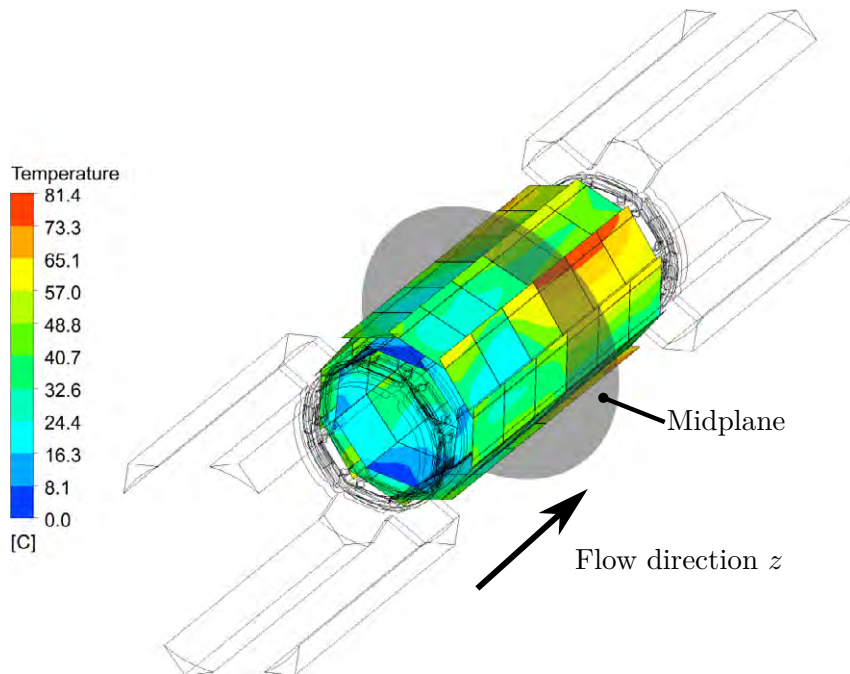


Figure 4.10: Temperature of the MuPix layer with the original geometry.

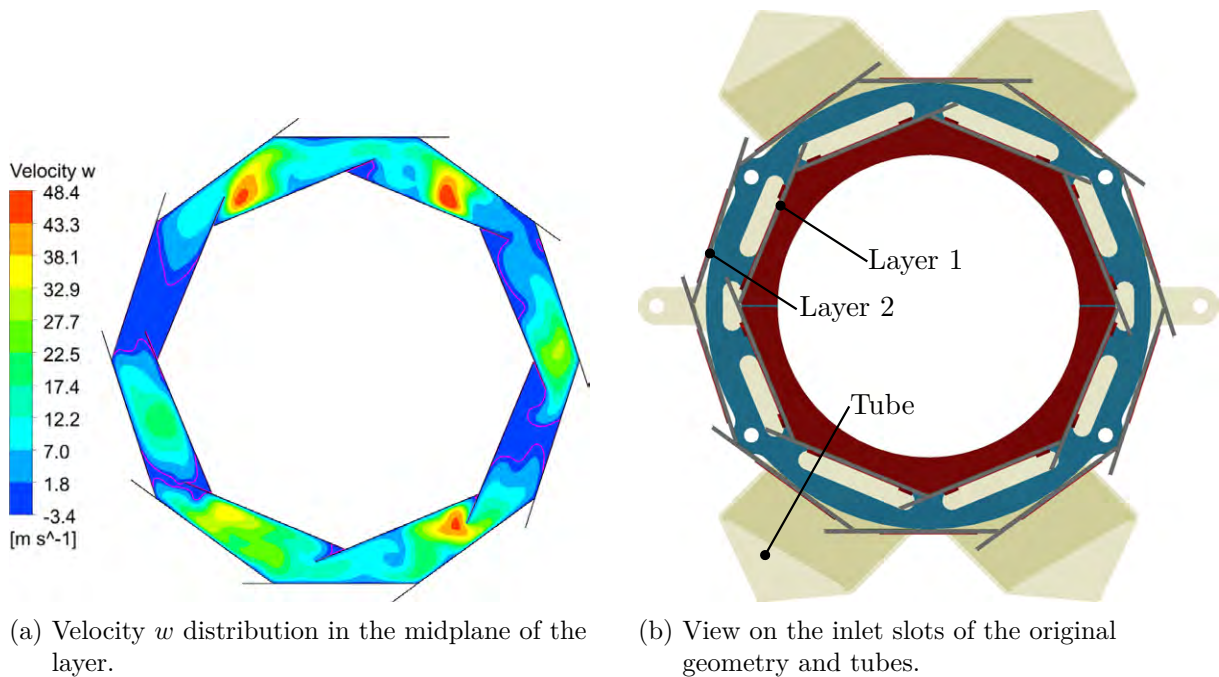


Figure 4.11: Original geometry and flow distribution in the midplane of layers 1 & 2.

4.2.4 Optimisation potential by mass flow

Increasing the helium mass flow is decreasing the layer temperature but it is inversely proportional. So a change of the mass flow at a low mass flow causes a high temperature change whereas at high mass flows the same change has nearly no effect. Figure 4.12 shows the maximal temperature of the MuPix chips and the helium with a constant heat dissipation and different mass flows. With a mass flow of 2 g/s the potential to increase the mass flow is quite small. A doubling of the mass flow would decrease the temperature by around 30% but increase the pressure drop and also helium requirement.

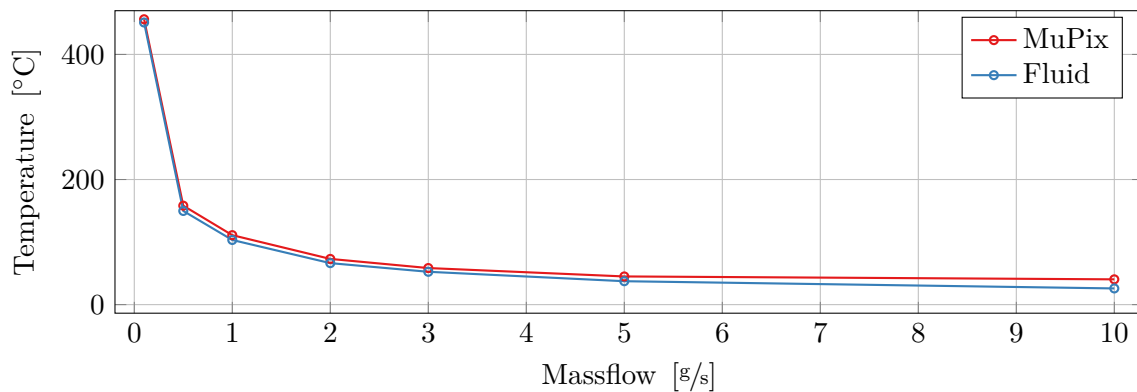


Figure 4.12: Maximal temperature of the layer depending on different helium mass flow with a constant heat dissipation of 400 mW/cm^2 .

Optimisation of slots

The cause of the higher temperature of some overlaps of layer 2 is due to irregular mass flow through the inlet slots. Figure 4.13 shows the inlet slots and which were divided into eight groups corresponding to the volume above each of the layer 1. The mass flow which comes into each of the volumes should be regular to prevent major back flow regions. Figure 4.14 shows the mass flow per group for the original geometry. It can be seen that the flow through the groups 1, 4, 5 & 8 is around 230% higher than the others. The theoretical optimal distribution would be 0.25 g/s per group.

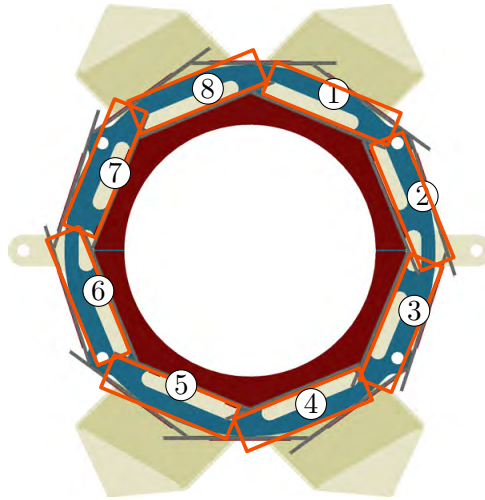


Figure 4.13: Original inflow slots of layers 1 & 2 with division into 8 sections corresponding to layer 1.

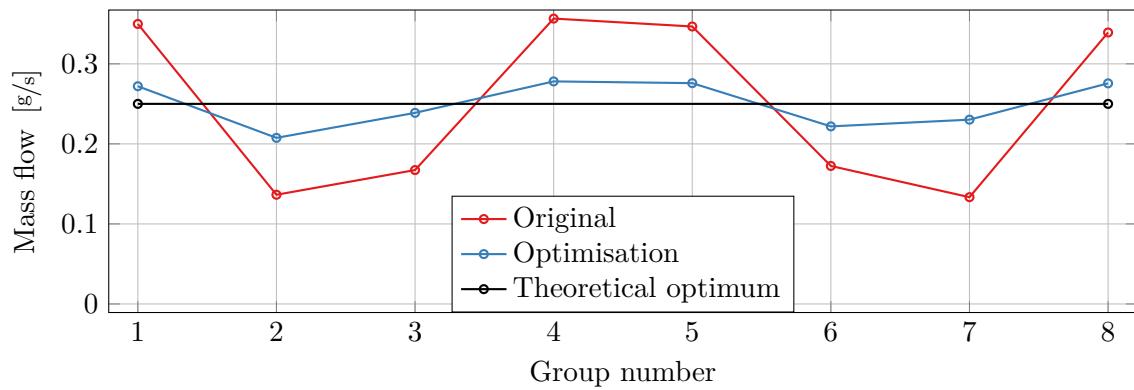


Figure 4.14: Mass flow of each group in G12.

To realise a more regular flow the best opportunity is to change the size of the slots, which is basically increasing the pressure drop of the slots in the high mass flow groups. The mass flow per area has been assumed as constant and based on this the new area of the slots has been computed. Several iterations were made as the assumption is not regarding the pressure level changes and interactions between the size of the slots. From five different optimisation the one with the lowest temperature is shown in figure 4.15 compared to the original one. The mass flow per group of the optimisation is shown in figure 4.14 which shows an improvement towards the theoretical optimum compared to the original one.

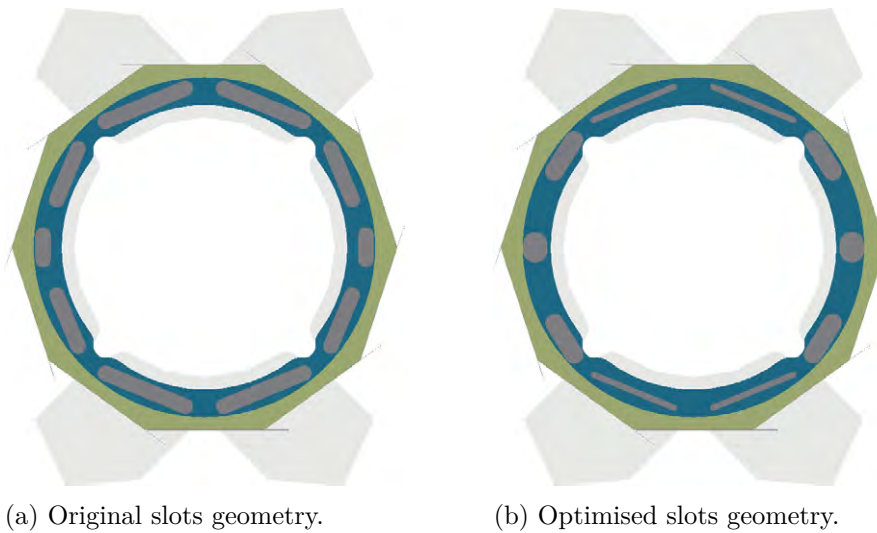


Figure 4.15: Comparison between original and optimised inlet slots of G12.

Figure 4.16 shows the temperature of the MuPix chips with the optimised slots. Compared to the original slots the temperature is around 10 K lower and there is not one specific part which has the maximal temperature but is more equalized, similar to the results of the benchmark. This can also be seen comparing the w velocity of figure 4.17 which has less backflow regions compared to the original case.

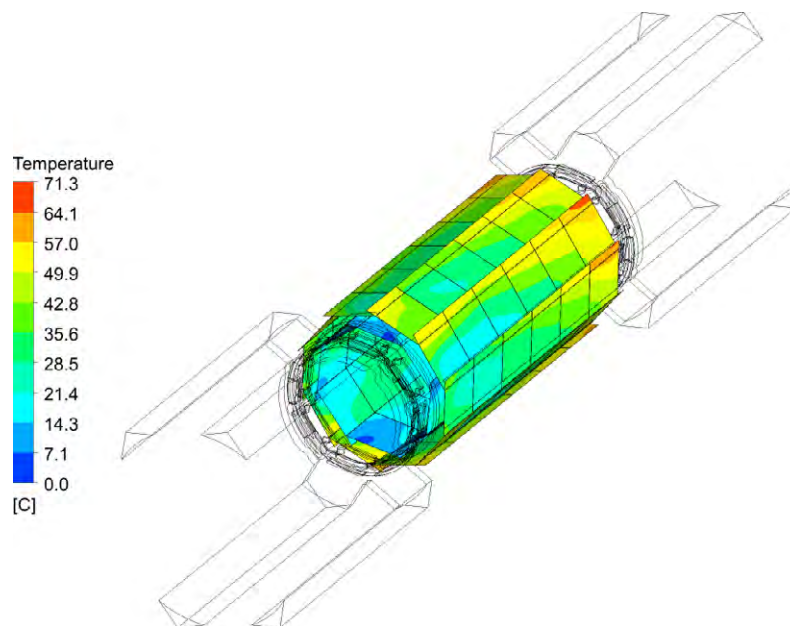


Figure 4.16: Temperature of the MuPix layer with the optimised geometry.

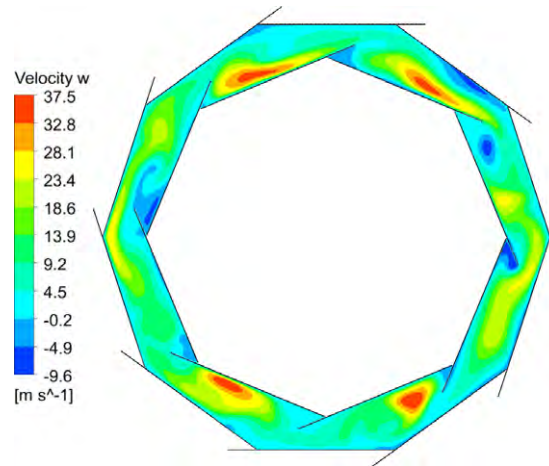
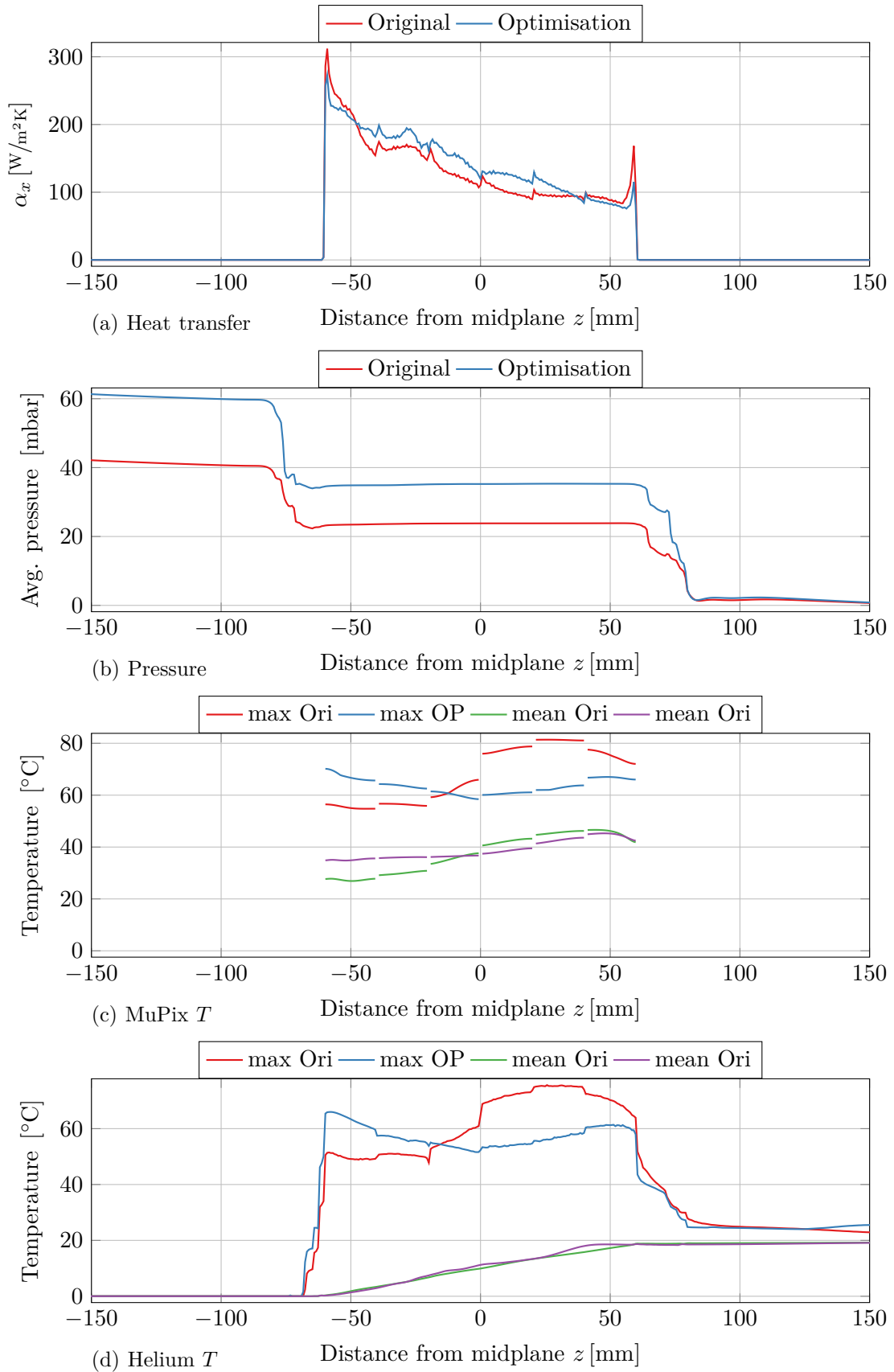


Figure 4.17: Velocity w distribution for optimisation in the midplane of the layer.

Development along the flow

Figure 4.18 shows the wall heat transfer coefficient, average pressure and temperature along z ¹ for the original and optimised slots. The wall heat transfer coefficient of the original part is higher at the in- & outlet but lower over the most range. Comparing the pressure development it can be seen that the pressure drop of the optimisation is 50 % higher than the original which is caused by the slots which are at $z = \pm 75$ mm. The higher heat transfer coefficient in the beginning can also be seen at the temperature of the MuPix. At the beginning the temperature of the original case is lower but along z is increasing compared to the optimisation which stays nearly constant over the length.

¹Distance from the midplane which has been defined in figure 2.2 on page 10.

Figure 4.18: Heat transfer coefficient, pressure and temperature of MuPix and flow along z .

Further optimisation

Due to the high temperature on the periphery of layer 2, especially with the unequal heat dissipation which reached temperatures over 90 °C (see table 4.5), further optimisations were considered. These optimisations would include not only the adjustment of existing parts but also consider new flows. An increase of the mass flow to enhance the cooling is possible but with 2 g/s the potential is small and would increase the pressure drop. Therefore several possibilities have been developed which are shown in figure 4.19. Three options were found from which two are requiring additional mass flows.

The mylar elongation of the layer 1 would lead the helium inside of the gap and prevent the exchange of mass flow between the groups defined earlier. This option also has potential drawbacks as there are additional walls causing slower velocities near layer 2 and decreasing cooling capacity. The advantage is that no additional flow is required and it is easy to be implemented into the current design.

Mylar tubes enable additional flows outside of the layer, which is beneficial for layer 2 which has no cooling flow on the overlap which leads to the highest temperatures. This would require a design change of the inlet tubing and helium distribution system.

The overlap flow is similar to the mylar elongation but on layer 2. They are inspired by the V-folds on layers 3 & 4 which will be explained later. Every overlap of layer 2 would have a flow which would ensure a cooling of the most critical part. Due to the design of the layer which consists of half shells which have to be disassembled for maintenance, this overlap flow is difficult to implement.

The outer mylar tube and the mylar elongation of layer 1 have been chosen to be further investigated. The outer mylar tube was chosen because of the possibility of implementation and providing a cooling flow at the most critical part. The mylar elongation was chosen as no additional flow is required and is quite easy to implement into the current setup. For the outer mylar tube an additional helium mass flow is needed which has the same flow velocity as the inner flow. The dimension as well as the mass flow are shown in table 4.4.

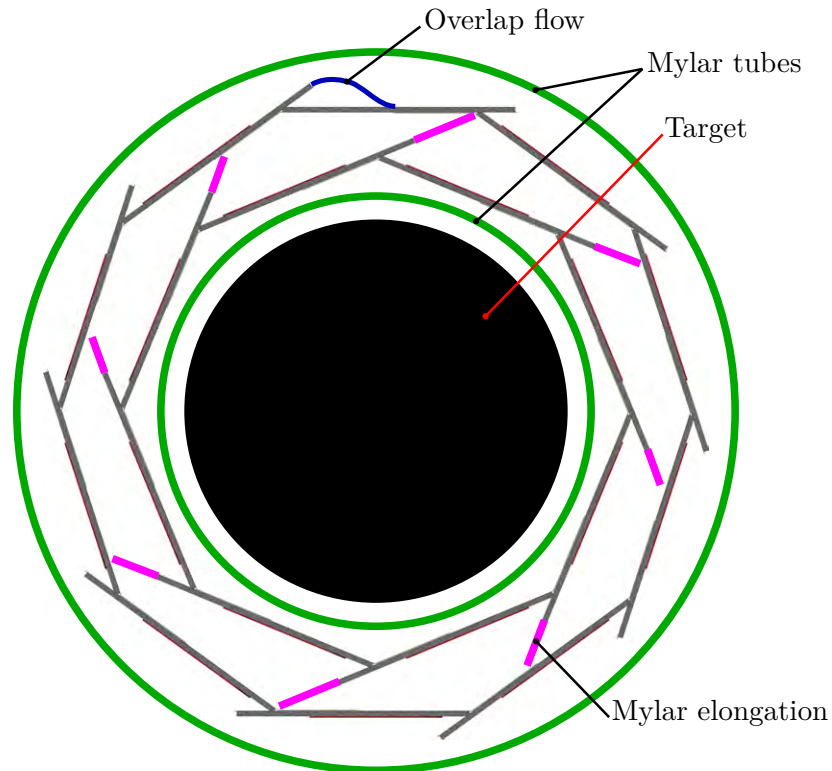


Figure 4.19: Further possible adjustment of gap flow between layers 1 & 2.

Table 4.4: Dimension of the outer flow created with a mylar tube.

Property	Value	Unit
Area	686	[mm ²]
Mylar tube diameter	67	[mm]
Diameter of overlap layer 2	59	[mm]
Flow velocity	10	[m/s]
Mass flow	1.1	[g/s]

Results of mylar elongation

The mylar elongation had some positive aspects, but also drawbacks. The simulation showed an increase of the temperature compared to the simulation with optimised slots. This is due to the lower velocity near the walls of layer 2. The elongation is therefore not a suitable optimisation.

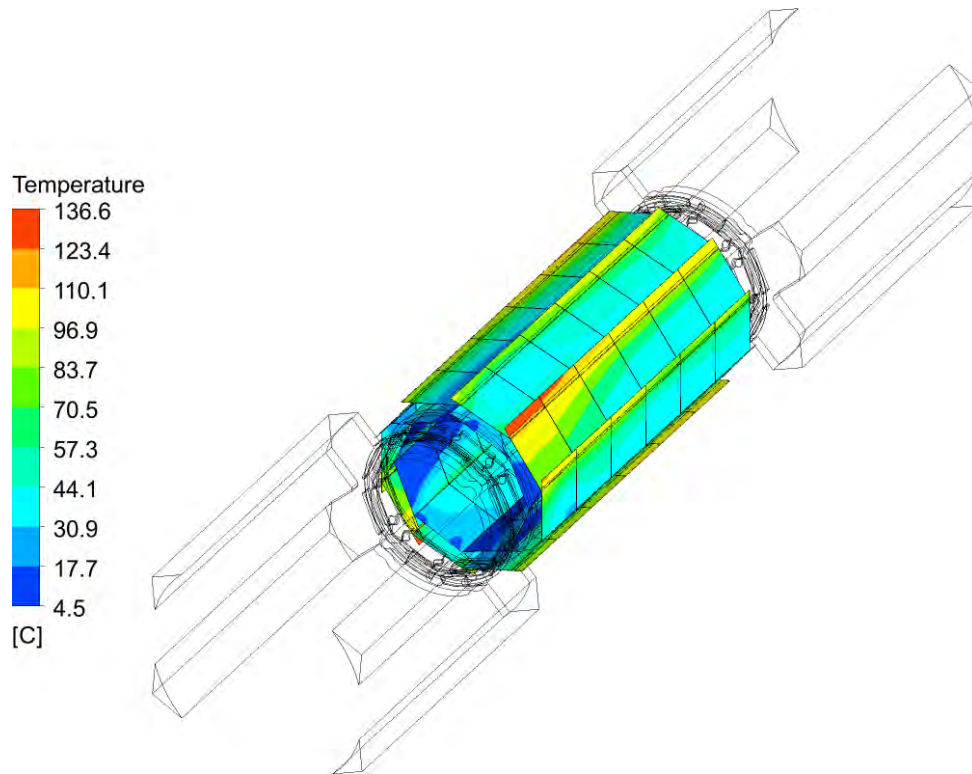


Figure 4.20: MuPix temperature with the mylar elongation of layer 1.

Results of outer mylar tube

The outer mylar tube which is cooling the overlap of layer 2 showed very good results. The overlap which was only cooled due to conduction over the material is now directly cooled by helium. Figure 4.21 shows the temperature distribution of the MuPix chips and the additional geometry. The temperature which was over 90°C could be decreased to a maximal value of 52°C .

The implementation of this additional mass flow into the CAD has not been designed and would require some additional adjustments. Maybe the existing tubes could be used with a higher mass flow. Also, the montage and de-montage of the mylar tube has to be envisaged to enable maintenance.

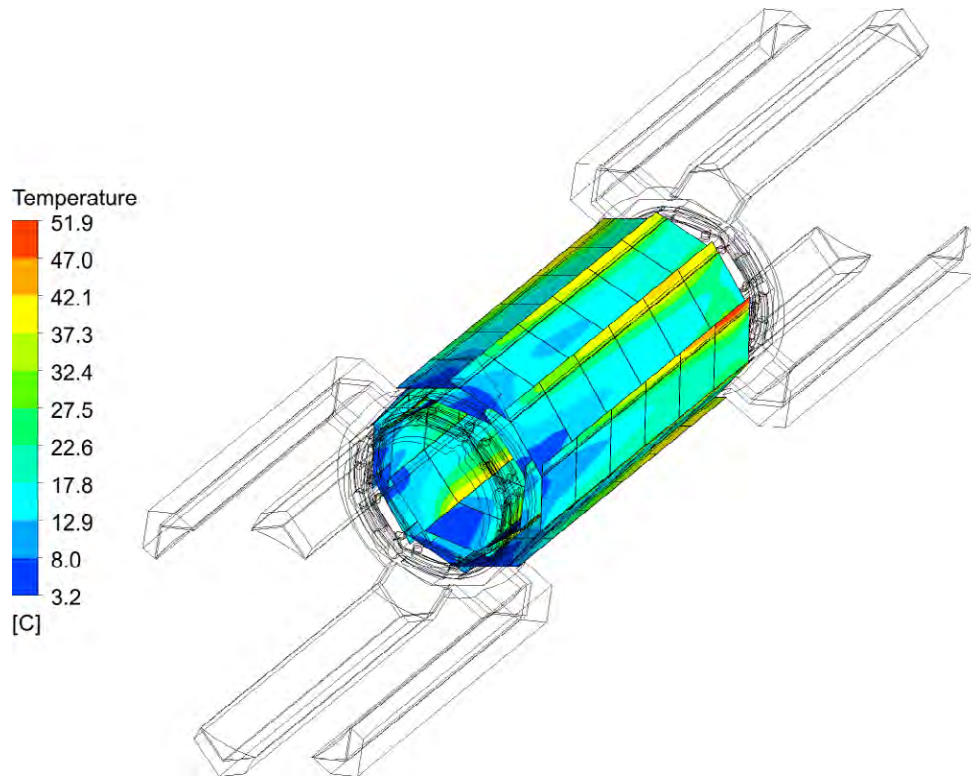


Figure 4.21: MuPix temperature with outer mylar tube.

Summary of results of G12

Table 4.5 shows the summary of all relevant results obtained for the gap flow between layers 1 & 2. The solid column is indicating the defined material of the MuPix chip. Unequal heat dissipation indicates if the MuPix chip was divided into two parts with different heat dissipation or set to the equal value of 400 mW/cm^2 (see section 4.1.5). The Benchmark was used to compare the heat transfer with the estimation and to provide a benchmark for the further simulations. It shows that the higher heat dissipation in the periphery is causing an increase of around 30 K. For the original and optimised version the increase is lower but in a similar range.

The optimisation is also decreasing the temperature of the MuPix by around 10 K both with and without the higher heat dissipation in the periphery.

The elongation and outer tube showed different effects in terms of cooling. The elongation increased the temperature by approximately 40 K which is not suitable. On the other hand the outer tube decreased the maximum temperature by 40 K which is far below the maximum of 70°C .

Table 4.5: Results with different configurations of gap flow between layers 1 & 2.

		Geometry	Heat load [mW/cm ²]	Unequal heat dissipation	Max. solid temp. [°C]
Bench	Benchmark		400	No	64.9
	Benchmark		400	Yes	97.9
Optimisation	Original slots		400	No	81.4
	Original slots		400	Yes	106.6
	Optimised slots		400	No	71.3
	Optimised slots		400	Yes	93.6
add. OP	Elongation & Optimised slots		400	Yes	136.5
	Outer tube & Optimised slots		400	Yes	51.3

4.3 Layers 3 & 4

Layers 3 & 4 have been treated differently than layers 1 & 2 as several flows are used for the cooling of the 912 silicon chips. There are three nearly identical layers 3 & 4, which are arranged upstream (A), centrally (B) and downstream (C). As the complete model is quite complex with four internal flows and one global flow, the internal flows have first been optimised to be more uniform and to have less backflow areas. This has been done for part B and then applied to the parts A and C. A scheme of the flows of part B is shown in figure 4.22.

4.3.1 Modelling

The geometry of the flow has been analysed to detect if any symmetries could be used to lower the mesh size. No useful symmetries were found and therefore a simulation of the whole geometry is necessary.

4.3.2 Internal flows

The internal flows through layers 3 & 4 are composed of two V-folds and two gap flows. Both V-folds have a similar design with the difference that layer 3 has 24 segments compared to 28 on layer 4. Because of this similarity the optimisation of the V-folds has been carried out for V-fold of layer 3 (V3) and applied onto V-fold of layer 4 (V4). The gap flows G34 and G3S on the other hand are not directly comparable and had to be analysed separately. The optimisation possibilities are discussed directly in the corresponding section. The flow G3T which is present in part A & C was not optimised up to this point.

4.3.3 Global flow

The global flow has been planned to flow between layer 4 and the inner walls of the magnet with an average velocity of 0.5 m. The global flow has two main purposes which are the outside cooling of layer 4 and the transport of the helium blown out into its volume. As the mass flow requirement inside of the magnet would be immense due to the large area, a mylar tube of 300 mm is proposed as explained in section 2.3.3.

The flow at the inlet is set to 4 g/s which are 0.5 m/s. The gap flows from part A, B & C are merging into the global flow resulting into a global mass flow at the outlet of 45.1 g/s. If such a flow is feasible with a mylar tube was not investigated.

4.3.4 Estimation

The estimation of the global cooling system is quite complex due to several flows with different flowing directions which are influencing each other. The physical modelling is the same which has been used for layers 1 & 2 and was compared to estimations and measurement results. As there are no measurement results until now for these layers 3 & 4 a comparison with them is not possible.

The Reynolds number of the flows of layers 3 & 4 are shown in table 4.6 and were computed for the in- & outlet and the cooling section. As the Reynolds numbers are higher than the critical Reynolds number, turbulence effect could occur at the in- & outlets. First simulations were carried out without a turbulence model but showed instabilities and did not converge. The SST turbulence model was then used which lead to more stable and converging simulations.

Table 4.6: Reynolds number of the flows of layer 3 & 4.

Flow	In- & outlet			Cooling section		
	D_h [mm]	w [m/s]	Re [-]	D_h [mm]	w [m/s]	Re [-]
V34	4.2-5.2	64	2800	2.3	20	400
G34	12.9	50	6600	24	10	2000
G3S	12.9	45	4600	21.4	10	1800

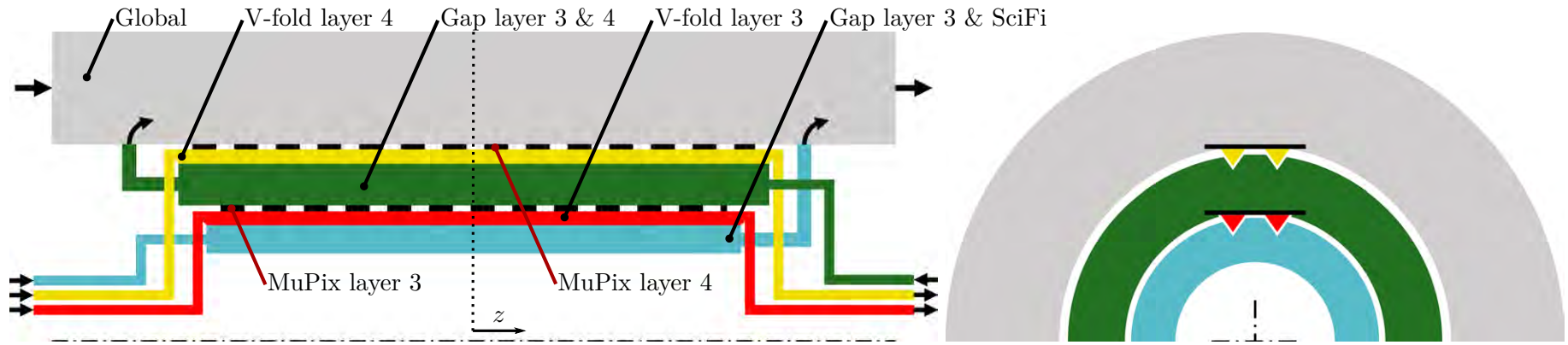


Figure 4.22: Scheme of the flows for cooling the centre part B of layer 3 & 4.

4.4 V-folds layer 3 & 4

The V-folds of layers 3 & 4 are quite similar and will be treated together. The V-folds have been designed to obtain more stability in layers 3 & 4 as for a length of around 350 mm the thin construction is unstable. Another benefit of the V-folds are the direct cooling possibilities on the MuPix chips. Figure 4.23 shows the V-folds fluid geometry of layer 3 in orange and layer 4 in yellow. For both layers there are 3 in- and outlets and 48 V-folds for layer 3 and 56 for layer 4 which are bundled into clusters of 8 folds. The mean velocity in the V-folds was set to 20 m/s , resulting in a mass flow of 1.3 and 1.5 g/s respectively for layers 3 & 4.

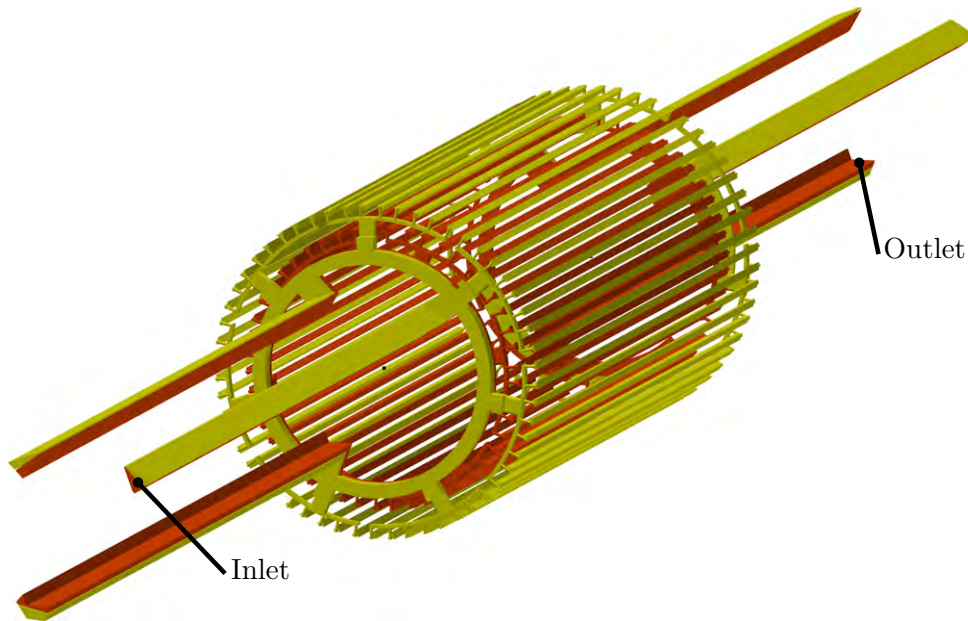


Figure 4.23: Fluid geometry of the V-folds of layer 3s (orange) & 4 (yellow).

4.4.1 Original geometry

Figure 4.24 shows one cluster of V-folds which have all the same inlet diameter of 1.5 mm . The inlet of this cluster is coloured in yellow. This configuration will result in different mass flows through the different V-folds.

Figure 4.25 shows the V-folds of both layers with the velocity in the midplane. In magenta the interfaces between the inlet geometry and the V-fold clusters are shown. One can see that the V-fold nearer of the interface show larger velocities as the one further away.

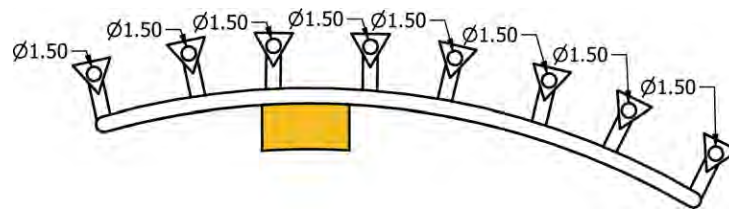


Figure 4.24: V-fold cluster with inflow diameter of original geometry.

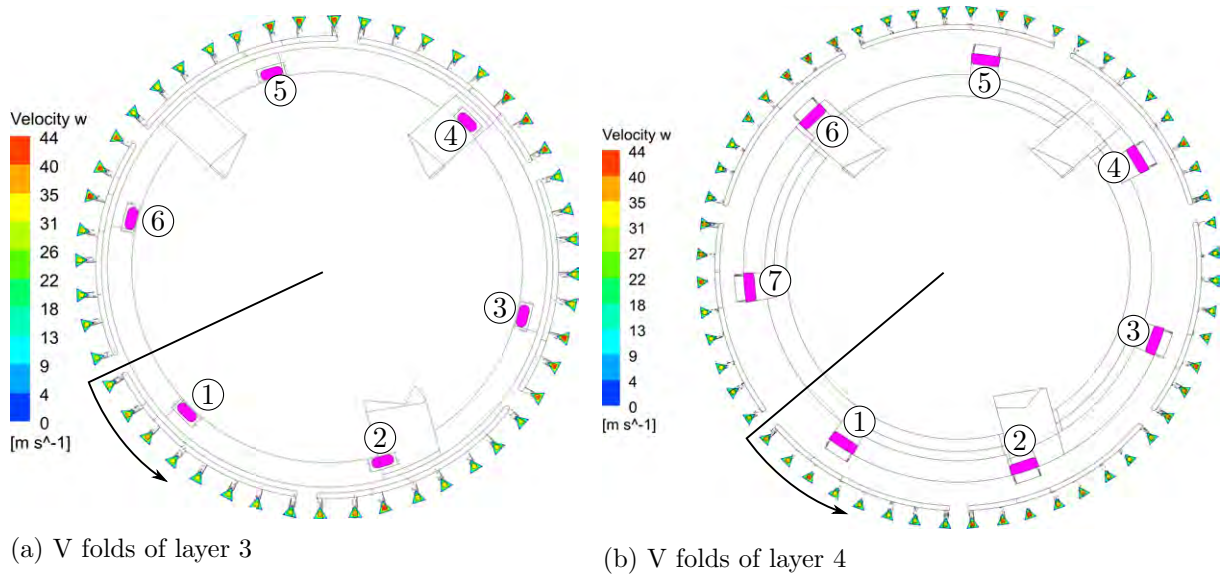


Figure 4.25: Velocity of the V-folds with interface numbering.

The mass flow through each of the V-folds is represented in figure 4.26 and shows a large difference of mass flow, especially within a cluster. The first three V-folds have a higher mass flow compared to the last ones. The mass flows between the different clusters are quite similar and do not require an optimisation. As indicator for the quality of the optimisation the variance of all V-folds was used which is indicated in the plot.

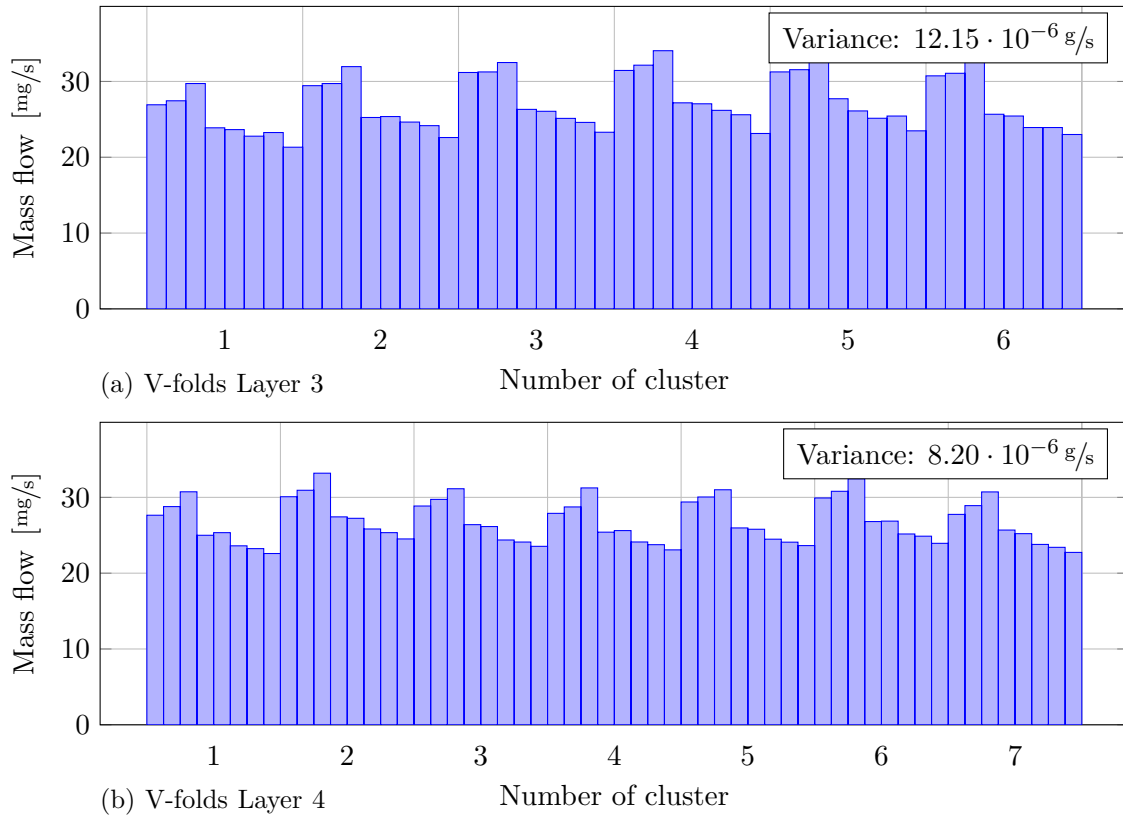


Figure 4.26: Flow through all V-folds of original geometry grouped by clusters.

4.4.2 Optimised geometry

The best approach to optimise the V-folds of layers 3 & 4 is a modification of the diameter of the inflow diameter at the beginning of the V-fold. A change at the interface of each cluster is not necessary as the flow only varies around 10%. The mass flow difference between the V-fold in one cluster are around 30%. This has also been analysed by Tormann [6]. The diameters in the original case have been set all to 1.5 mm. Tormann [6] proposed the use of smaller diameters following figure 4.27a.

With the mass flow data of one segment from original geometry (see figure 4.26) the diameters have been optimised. The mass flow per area for each of the eight V-fold has been assumed as constant and the available diameters for the optimisation were defined from 1.1 – 1.5 mm with an increment of 0.1 mm. The variance between the eight V-fold was then minimised using a brute-force algorithm which computed all combination and searched for the one with the lowest variance. This approach ignores the interaction between the different diameters and the resulting pressure levels which do not seem to be relevant. The obtained diameters are shown in figure 4.27b.

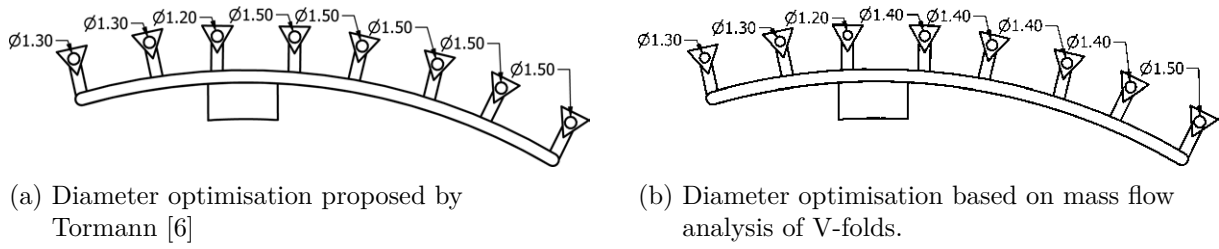


Figure 4.27: Optimisation of feeding diameter for V-folds.

The mass flow through the different V-folds is shown in figure 4.28 for both layers. The mass flow is more regular with the optimised inlet diameters and has therefore a variance that is five times lower. The same optimisation algorithm has again been applied to the optimised mass flow data. The second optimisation has led to the same diameters which means that the optimal geometry was found for this integer optimisation problem.

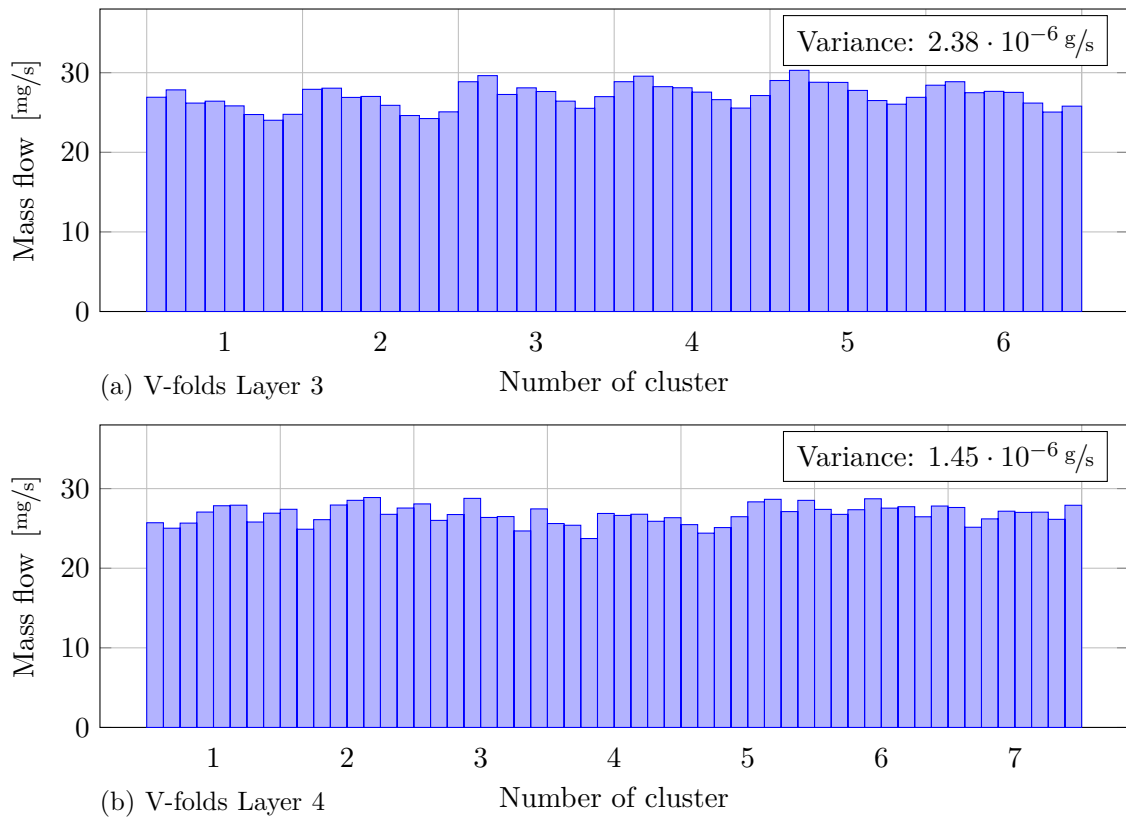


Figure 4.28: Flow through all V-folds grouped by interfaces of optimised geometry.

4.5 Gap layer 3 & 4

Figure 4.29 shows the geometry of the gap flow between layers 3 & 4. For part B there is a long inlet section which is not present for part A & C. The inner MuPix layer 3 is displayed in grey. This flow is cooling the layers 3 & 4 and flows in the opposite direction of V34, G3S and also the global flow for part B.

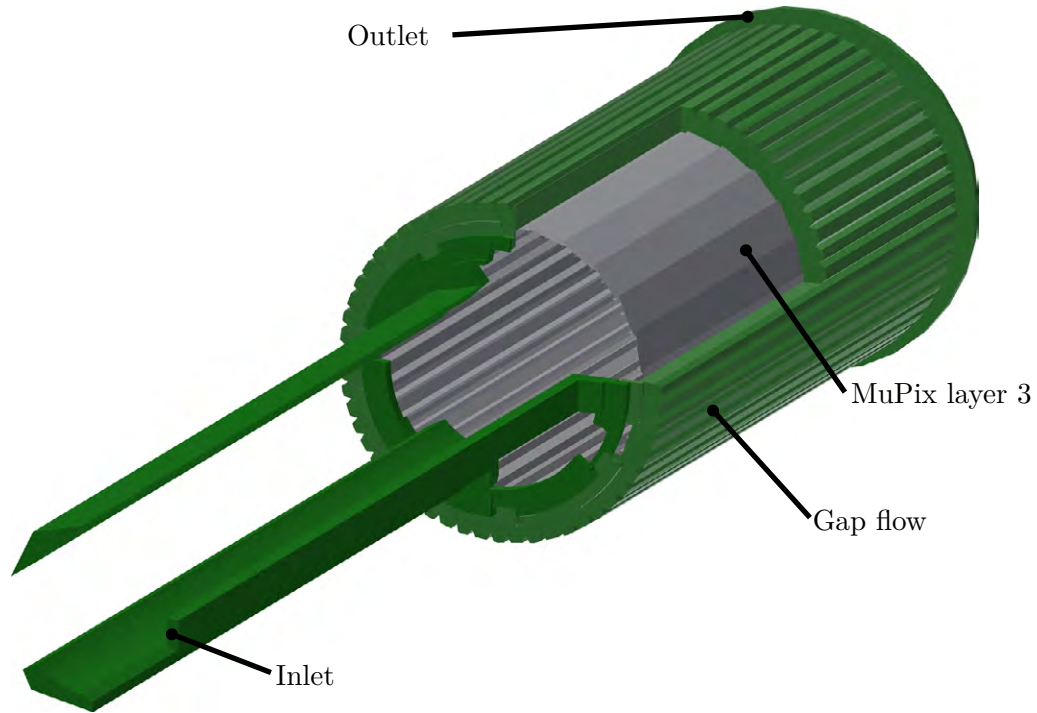


Figure 4.29: Geometry of the gap flow between layer 3 & 4 part B.

4.5.1 Original

Figure 4.32 shows the velocity w on the midplane of the main flow direction. In magenta the 14 inflow slots are highlighted which are the connection between the inlet ducts and the gap flow. The midplane velocity shows that there are different velocity magnitudes over the circumference with parts where there is a low flow velocity and therefore also a bad cooling rate. The mass flow over the circumference is shown in figure 4.31 with slices having an angle of 2° . The angle definition is shown in figure 4.32. The mass flow over the circumference has large differences which influences the cooling at this specific angle. A more uniform flow over the circumference would enhance the cooling behaviour.

4.5.2 Optimisation options

The inlet of the gap flow is passing through 14 inflow slots similar to the one for layers 1 & 2. These slots can be downsized to obtain a more regular flow which can be easily implemented. A major change of the geometry is not suitable as this would require a large redesign of the involved parts.

4.5.3 Optimisation

As described in the last section, the most reasonable optimisation involves varying the inflow slots to get a more uniform velocity distribution. Figure 4.33 shows the optimised geometry with smaller inflow slots (magenta) and the midplane velocity. The flow is more uniform over the circumference and has less parts with very low velocities. Figure 4.31 shows the original and optimised mass flow through the midplane with slices of 2° . One can see that the flow is more uniform which is also confirmed by the variance as quality criteria.

Several variants to optimise the flow have been designed to lower the variance of the flow. First the same approach as for G12 was used, which was to optimise the flow through every of the 14 inflow slots. As they have different areas the mass flow in figure 4.30 shows a zigzag pattern for the optimum. The original slots have a large deviation from the theoretical optimum case in terms of mass flow. The slots have been optimized to achieve a flow similar to the optimum case. Optimisation 3 achieved a very similar pattern, but the analysis of the flow showed that the variance worsened compared to the original case as more reflux regions were present. The reason for this was that parts of the inlet slots were blocked by layer 3 cables and the flows were then deflected to other regions. Finally, the slots were optimized by analysing the behaviour of the original case and optimisation 3, which finally led to optimisation 5. The variance of optimisation 5 is lower than that of the original geometry and therefore more regular.

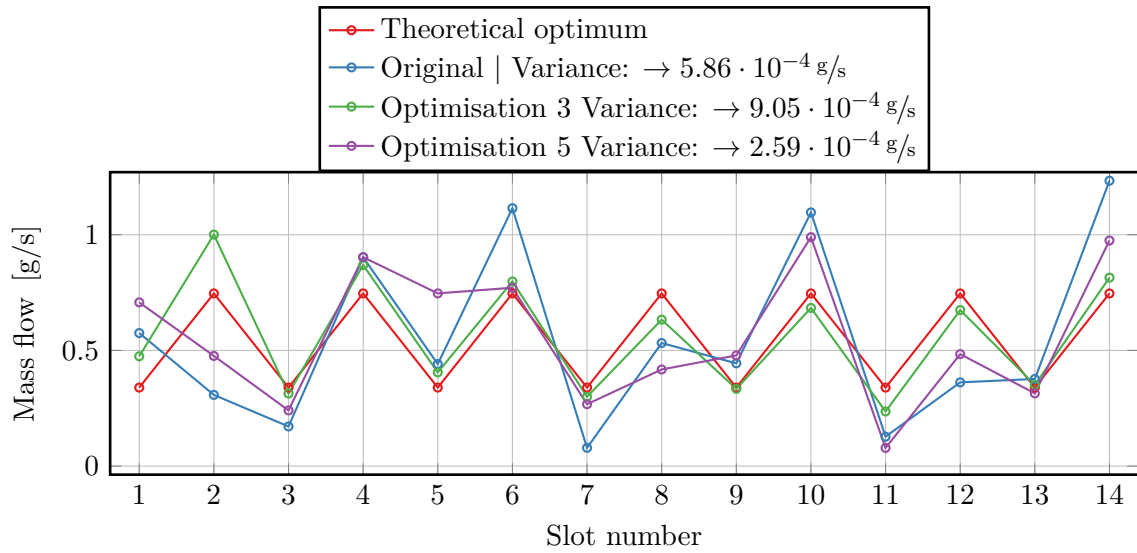
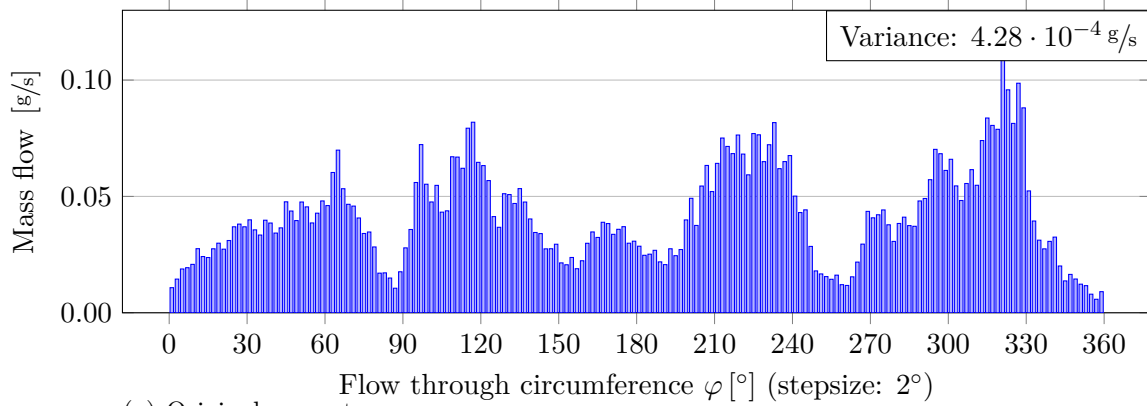
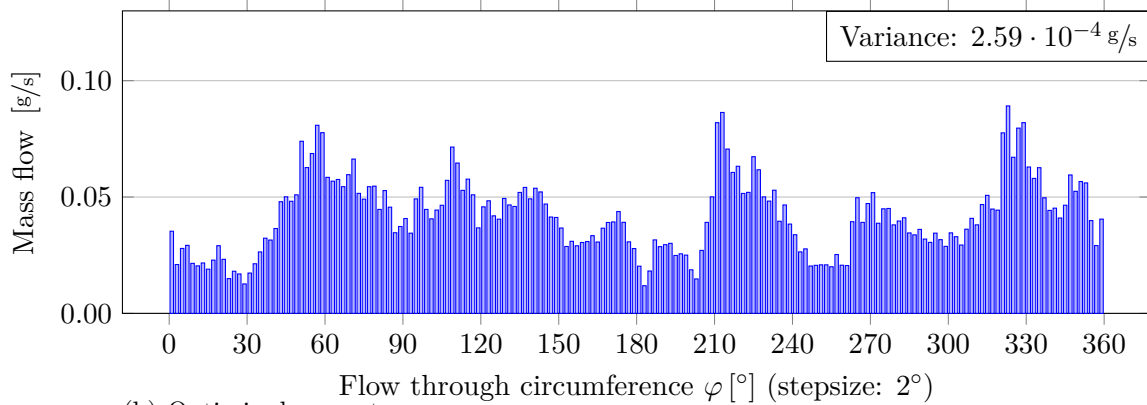


Figure 4.30: Flow through interfaces of gap layers 3 & 4.



(a) Original geometry



(b) Optimised geometry

Figure 4.31: Flow over the whole circumference of gap flow between layers 3 & 4.

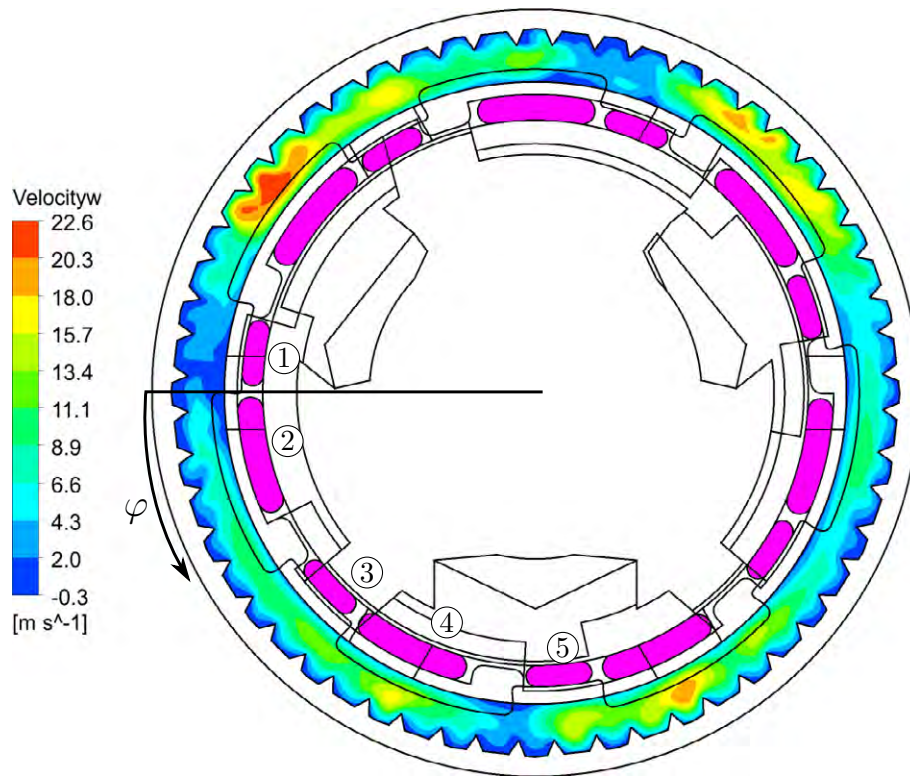


Figure 4.32: Original inflow geometry of gap flow between layers 3 & 4 and velocity distribution in the midplane.

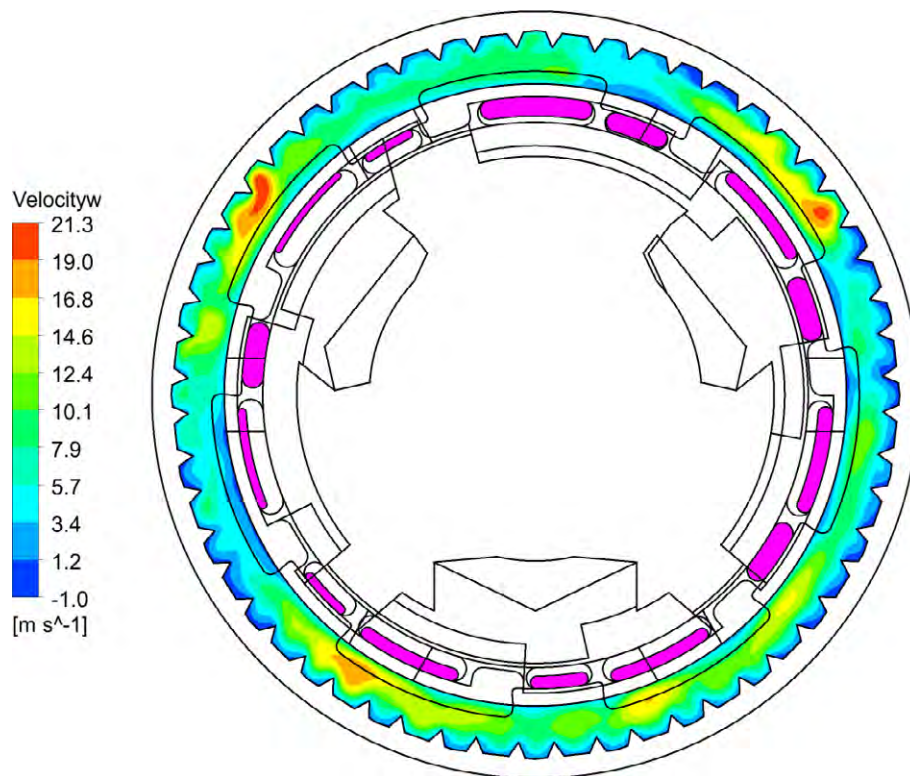


Figure 4.33: Optimised inflow geometry of gap flow between layers 3 & 4 and velocity distribution in the midplane.

4.6 Gap layer 3 & SciFi

The gap flow between layer 3 & SciFi is mainly intended to cool the MuPix layer 3 of part B. On the inside of the gap is the SciFi detector, for which no heat dissipation by the helium is specified, so this has been assumed to be an adiabatic wall. Figure 4.34 shows the flow and a part of the MuPix layer 3. The flow is merging into the global flow at the outlet.

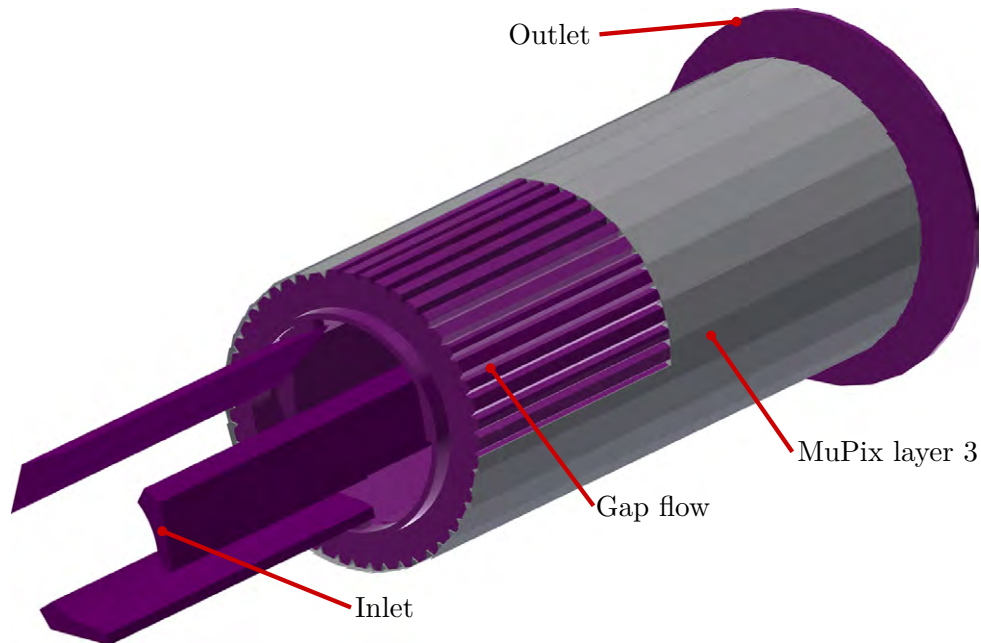


Figure 4.34: Geometry of the gap flow between layer 3 & SciFi.

4.6.1 Original

The original geometry has been simulated and the velocity in the midplane is shown in figure 4.36. There are areas with high velocity just after the three inlet tubes. Between them there are backflow regions at $\phi = 0^\circ$ & 180° which can also be seen in figure 4.38, where the mass flow distribution of the circumference is showed in slices of 2° .

4.6.2 Optimisation

Options

Compared to the G12, G34 and V34, the G3S has no slots at the inlet that could be modified. Two different options were proposed to change the inflow and obtain a more homogeneous flow. Figure 4.35 shows the inlet geometry, support plate of the SciFi and the MuPix layer 3. Two options for the distribution of the flow over the circumference are shown, one of which is within

the 3D-printed inlet to guide the flow, which is represented by orange curves. Another option is to use guidance plates, which can also be mounted on the grey support part of the SciFi and are represented by the blue curves. It has been decided to continue with the guidance plate on the support as there are more possibilities which can be realised. The required number of guide plates and their shape and length were difficult to estimate. This was done by trial and error until a satisfying flow distribution was reached.

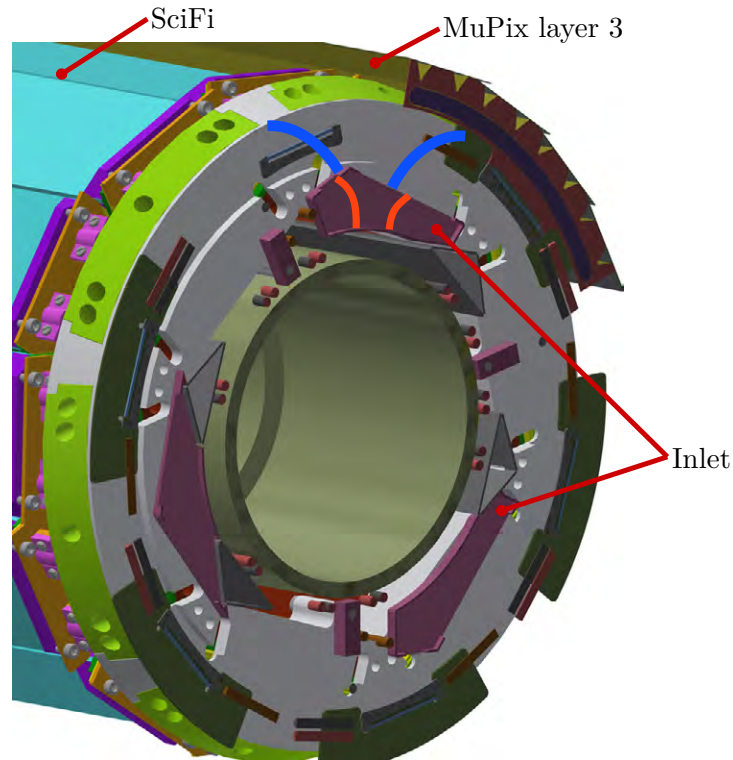


Figure 4.35: Cut through the inlet of gap flow between layer 3 & SciFi and other parts.

Results

After several iteration steps with more and more guidance plates, a satisfactory geometry was found, that is characterised by a regular flow field in the gap, and is shown in figure 4.33. The variance decreased by around 65%. Compared to the velocity in the original case there is a more regular flow over the circumference which is also confirmed by figure 4.38.

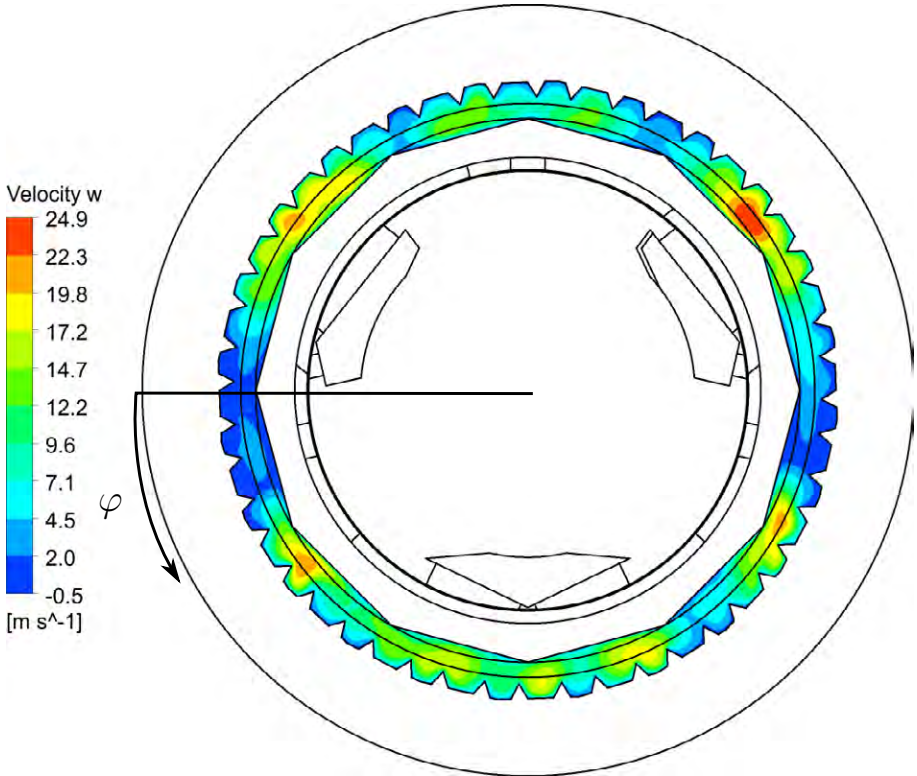


Figure 4.36: Original geometry of gap flow between layer 3 & SciFi with velocity distribution in the midplane.

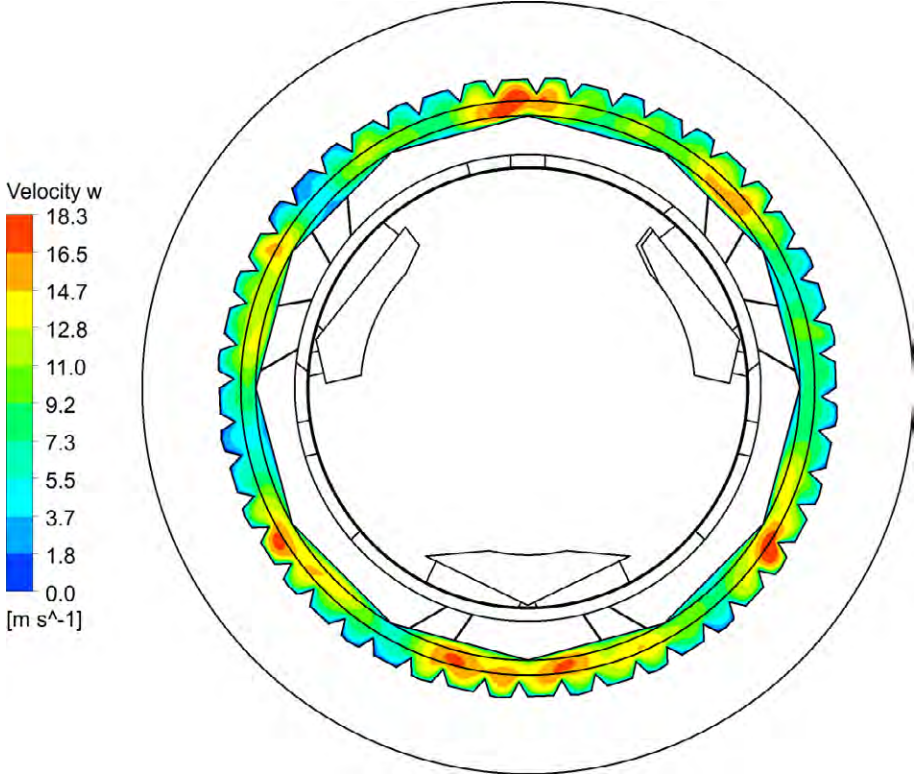


Figure 4.37: Optimised geometry of gap flow between layer 3 & SciFi with velocity distribution in the midplane.

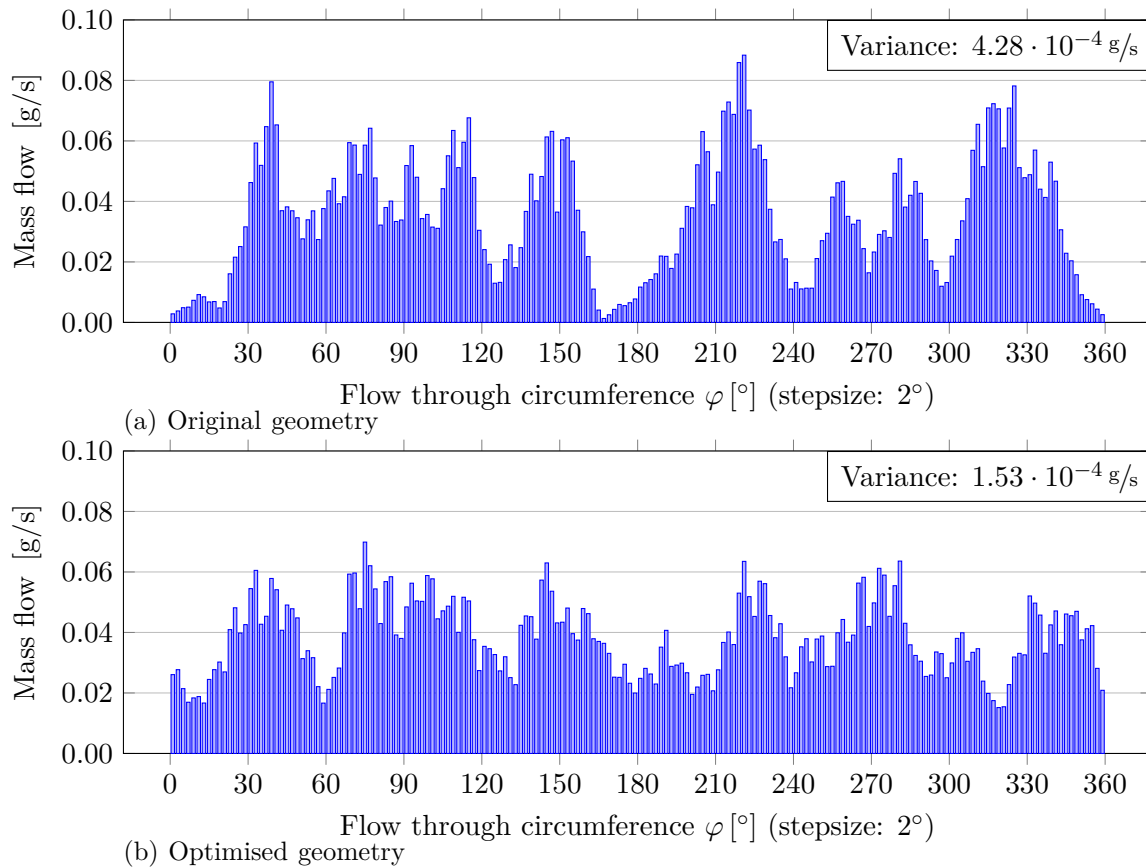


Figure 4.38: Flow over the whole circumference of gap flow between layer 3 & SciFi.

4.7 Layers 3 & 4 coupled

The last three sections showed the optimisation made on the geometry of the flow of layers 3 & 4. An optimisation with the full geometry and heat transfer would not have been possible due to the long simulation duration. The comparison between the original geometry and the optimised geometry is shown first, which was done only on the part B. Then a simulation of part A, B & C with optimised geometry is shown.

4.7.1 Global flow

The global flow was not discussed or optimised in the previous sections. The global flow goes along the inside of the magnet with the purpose to cool layer 4 from the outside and be the outlet of the G34, G3S and G3T. The proposed average velocity was set to 0.5 m/s . Since such a velocity would require a huge mass flow right inside of the magnet, a mylar tube with a diameter of 300 mm was introduced. The dimension of the tube was chosen so that a moderate mass flow is needed. Other dimensions were not tested and might be more advantageous.

For the combined simulation of parts A, B & C, each part was simulated sequentially. The outlet conditions (temperature and mass flow) of the upstream part were used as inlet conditions in the next part. The whole simulation could not be computed due to high computational time and memory requirements.

Table 4.7: Mass flow and temperature of the global flow between the part A, B & C.

Part	Inlet [g/s]	Outlet [g/s]	Inlet temperature [°C]	Merging flows into global
A	4.0	17.3	0	G34 & G3T
B	17.3	31.8	14.5	G34 & G3S
C	31.8	45.1	17.6	G34 & G3T

4.7.2 Model

The complete model of layers 3 & 4 of all parts is quite complex. Each part has four internal flows that were already discussed before and the global flow. Additionally, there are also 912 MuPix chips and around 150 polyimide parts. To model the heat transfer between the parts, interfaces must be created which could be identified by the Workbench using a tolerance and distance. In total over 10000 interfaces were present in every of the three parts. Unfortunately, some interfaces were not identified and caused higher MuPix chips temperatures. Figure 4.39 shows the temperature of the MuPix with original geometry. At the end of each layer there is a row of chips which have higher temperatures due to the missing interface between the MuPix chips and the flow underneath. These chips are therefore only cooled from below and show higher temperatures. This was a major problem for part B and is included in all data displayed later.

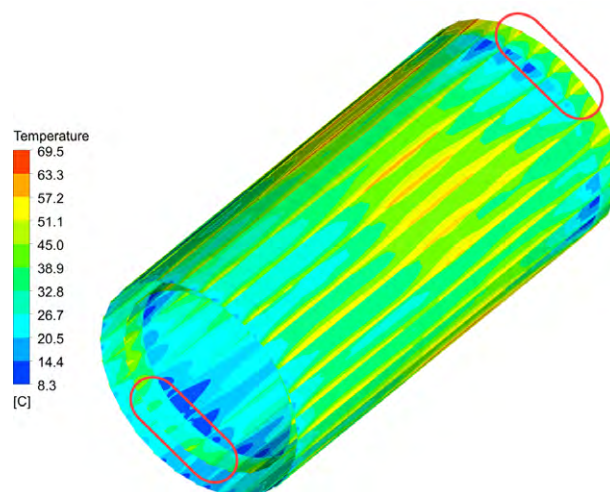


Figure 4.39: Increased temperature of one MuPix row due to failed interface.

4.7.3 Error of coupled flow

A lot of efforts have been put into the simulation of layers 3 & 4, but the results still have some remaining issues, which are explained in the following list:

- Outlet** Since the velocity profile has a recirculation zone at the outlet, an inflow had to be allowed, otherwise the solver would place walls into the backflowing area. Therefore, an opening had to be placed at the outlet. This is different from the characteristics of the Mu3e experiment, as it would also influence the downstream flow of the global flow. The coupling of the three parts and the global flow was not possible with the present resources. One possibility would be to take the velocity profile at the outlet and define it as inlet, but the downstream part has also an influence on the upstream parts.
- Interfaces** The interfaces between the fluid and the solids were difficult to define and failed frequently. To create and test a new mesh was quite time consuming. In the results shown here, there are some interfaces which could not be included. These missing interfaces are affecting the results.
- Mesh** A mesh study, as it was carried out for the G12, could not be performed with the available resources. Therefore, the results could have great temperature errors. To estimate the error, a mesh study could be performed with the individual flow sections. With these errors the quality of the whole simulation could be estimated.
- Turbulence model** For layers 3 & 4 a turbulence model was used because the laminar simulation was unstable. Nevertheless, it is assumed that the flow through the gaps is laminar, so the turbulence model affects the heat transfer at the wall and also the pressure loss.

4.7.4 Results

Three results of the heat transfer simulation of the layers 3 & 4 will be discussed in this section. The first one is comparing the temperature change obtained by the optimisation which is only performed on part B. Then the temperature and velocity profiles of part A are shown. This is followed by the results of all three parts which were simulated one after the other.

Part B: Original - Optimisation

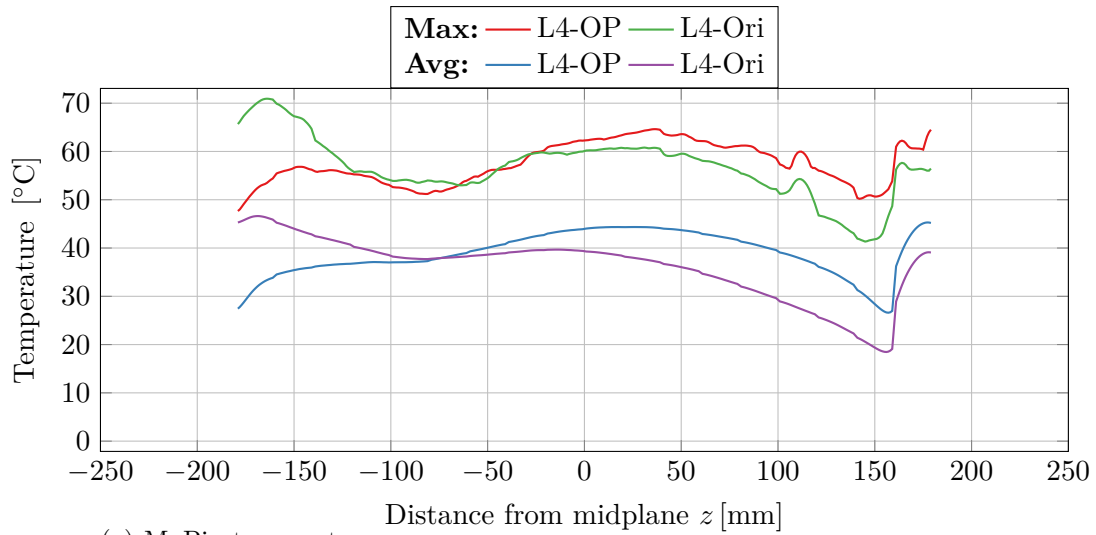
Part B was simulated with the original and optimised geometry and will be compared in this section. However, both simulations have the same failed interfaces. The results are still shown

here as some conclusion can be made from them. Figure 4.40 shows the average and maximal temperatures of the MuPix chips and the average temperature of the flows dependent on the distance from the midplane defined in figure 4.22.

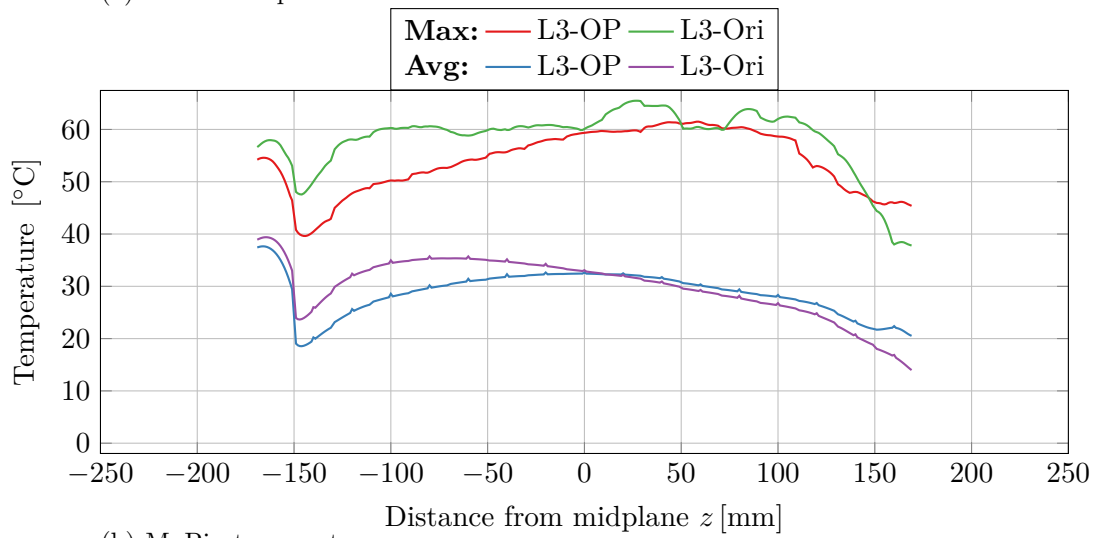
Figures 4.39b and 4.39a are showing the average and maximal temperature of the MuPix chips along z . At $z = \pm 160$ mm there is a sudden increase of the temperatures which is resulting from the missing interfaces. As these interfaces are missing for both cases, the results can be compared. The original geometry seems to have higher temperatures at the $Z = -150$ mm and lower temperature at $z = 150$ mm compared to the optimised geometry. The maximal temperature of the optimisation is around 5 K lower than the original case. The high temperature of the original case at the beginning could be decreased with the changes made. For layer 3 the optimisation shows overall lower temperatures as the original geometry but the influence is quite small.

The flow temperature shown in figure 4.39c has interesting behaviour due to the counterflow direction of G34. The flows V34 and G3S are cooling the MuPix at the beginning. At around $z > 50$ mm the flow temperature decreases which can be seen most clearly for V4. The counterflow G34 is coming with a temperature of 0°C and is cooling down the MuPix chips but also the other flows. This heat exchange cannot be prevented with the current configuration. The global flow has two abrupt temperature changes that are at $z = -200$ mm where G34 and at $z = 180$ mm where the flow G3S is blown out.

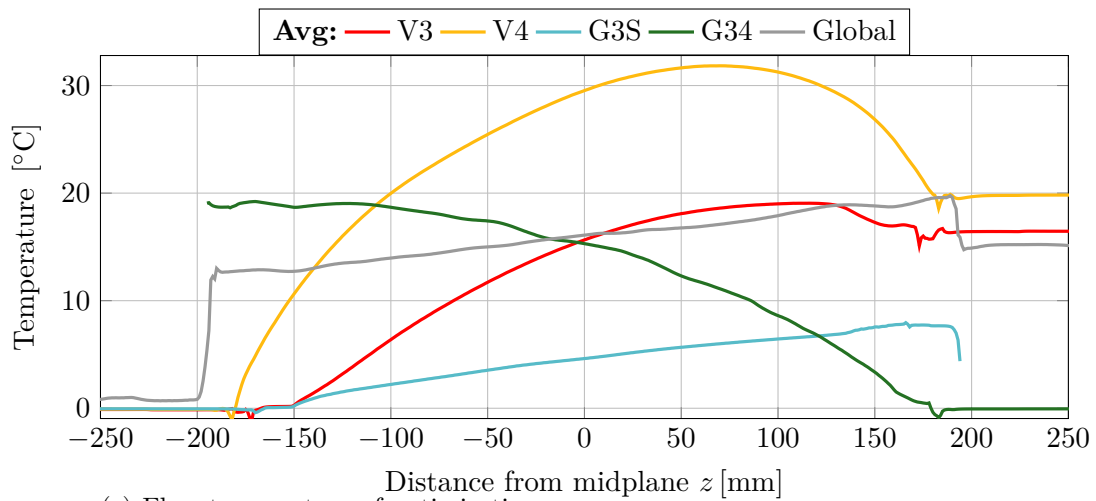
In appendix B.1 additional results of the simulation of part B are shown. The temperature of the layer as well as the flow velocity and temperature are displayed.



(a) MuPix temperature



(b) MuPix temperature



(c) Flow temperature of optimisation

Figure 4.40: Average pressure, temperature and velocity of part B along layers 3 & 4.

The cooling capacity of the flows have been evaluated for part B and are shown in figure 4.41. The highest cooling rate was reached by G34 which cools up to 40% of the heat dissipation. Compared to their mass flow the V34 have an excellent cooling rate. The share is only considering the changes between in- & outlet but as explained before the temperature of some flows are recooled by the counterflow G34 which is modifying the resulting cooling share. Also, the G34 is preheated by the other flows.

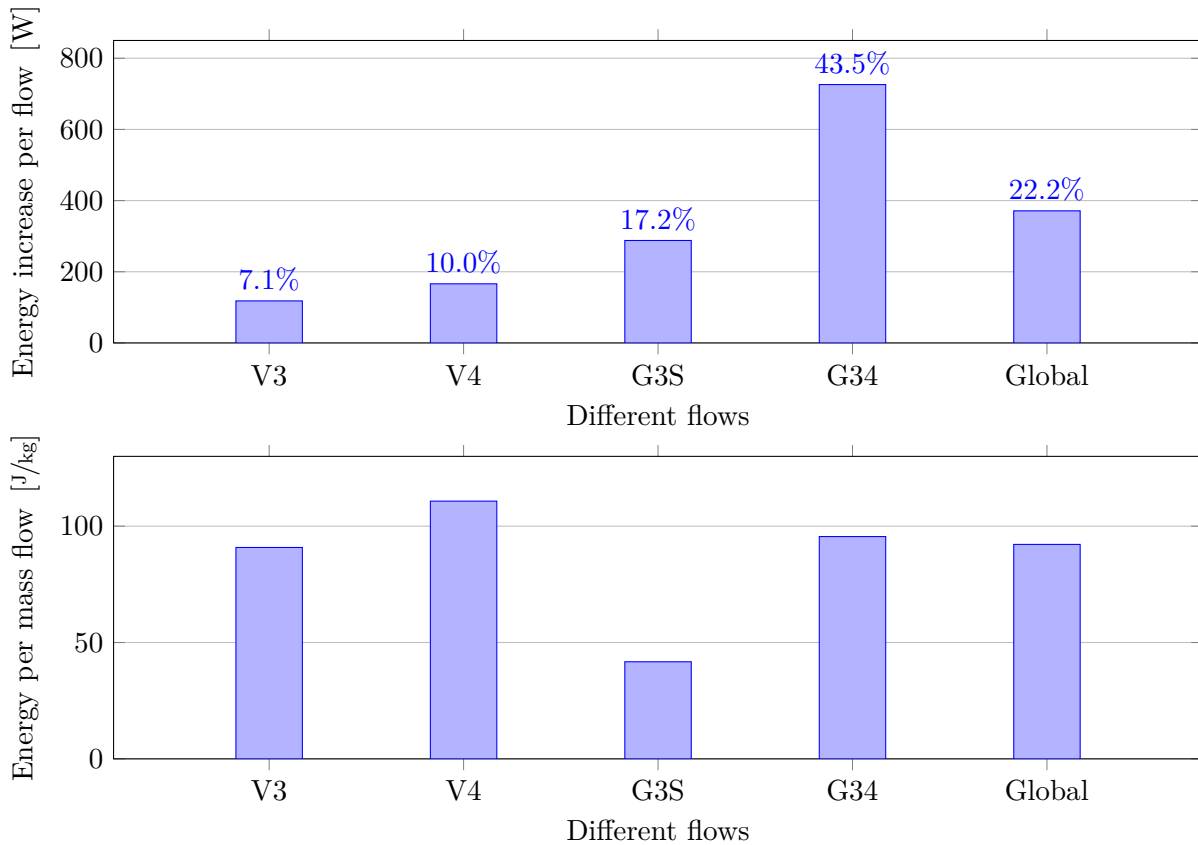


Figure 4.41: Cooling capacity of the flows of layer 3 & 4 with percentage share for part B.

The pressure at the outlets of the global flow, V3 and V4 were set to 1 bar. The flows G3S and G34 are merging to the global flow. V3 and V4 each have a separate outlet intended to have an adjustable underpressure to achieve a low pressure gradient from the V-folds to the gap flows.

For G3S, G3T and G34 an underpressure is not possible as the flows are merged into the global flow. This causes a pressure gradient over the MuPix layer which could affect the tracking of particles as the layers are inflated. The inflation would cause a leakage flow which would change the cooling behaviour simulated here. Along the layer the pressure drop is quite small, but the outlet geometry causes some pressure drop. To reduce this pressure drop the geometry would require a redesign. A simulation of the inflation caused by the pressure gradient across the layer is highly complex because a higher pressure drop causes higher inflation, whereas a higher

inflation results in a pressure adjustment by a leakage flow.

Figure 4.42 shows the pressure development along z for all optimised flows of part B. It can be seen that the reduction of the slots and holes of G3S and V34 is causing an increase in the pressure drop. Whereas, G3S with the guidance plates is not causing a higher pressure drop.

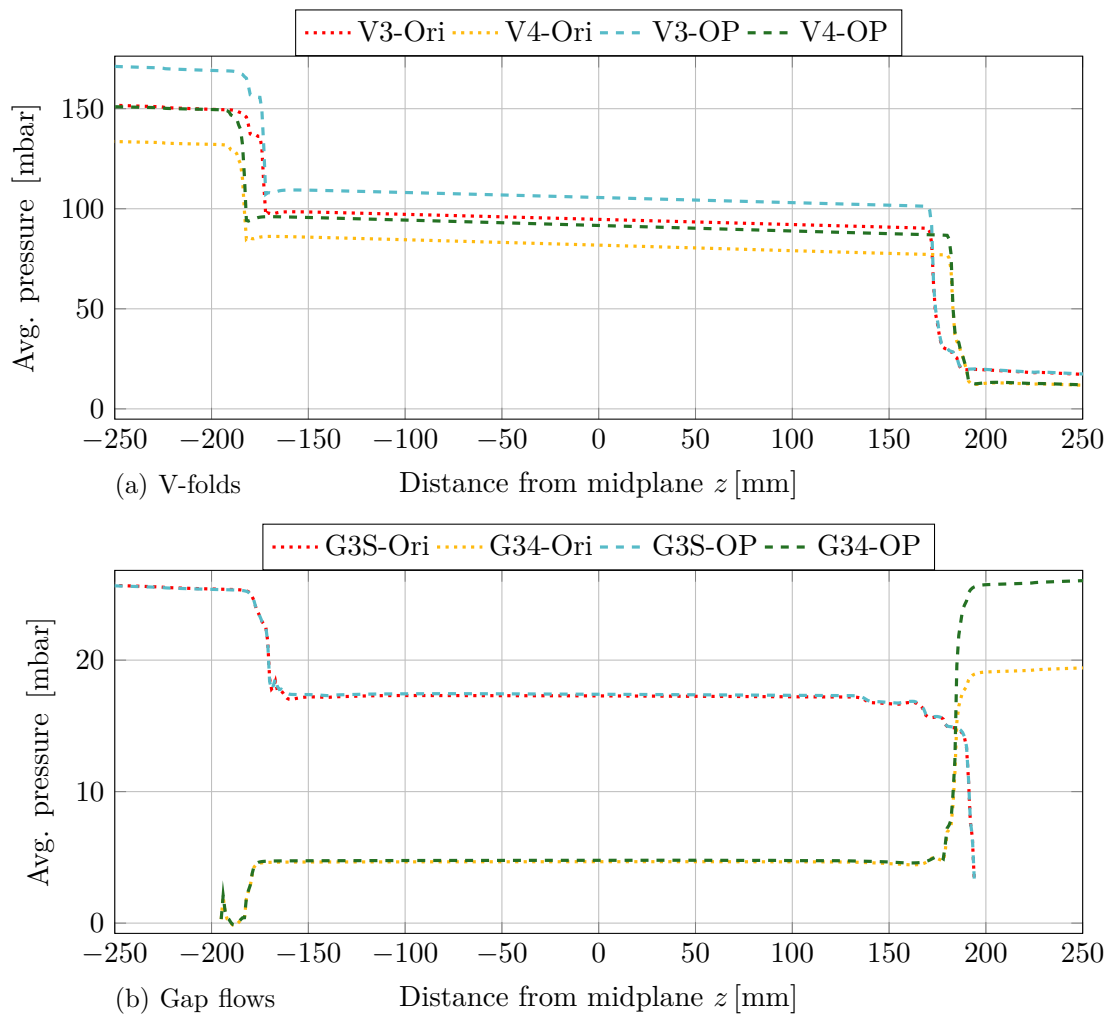


Figure 4.42: Pressure of the internal flows of layer 3 & 4 of part B.

Part A

Figure 4.43 shows the temperature and velocity profile of part A. These profiles are shown mainly for the temperature present over the tile detector, which represents the inner diameter. As with the SciFi detector, heating of the tile detector has not been defined yet. However, the developers of the detectors are interested in the temperatures of the helium flows. The helium flowing over the tile detector has a maximum temperature of 15°C .

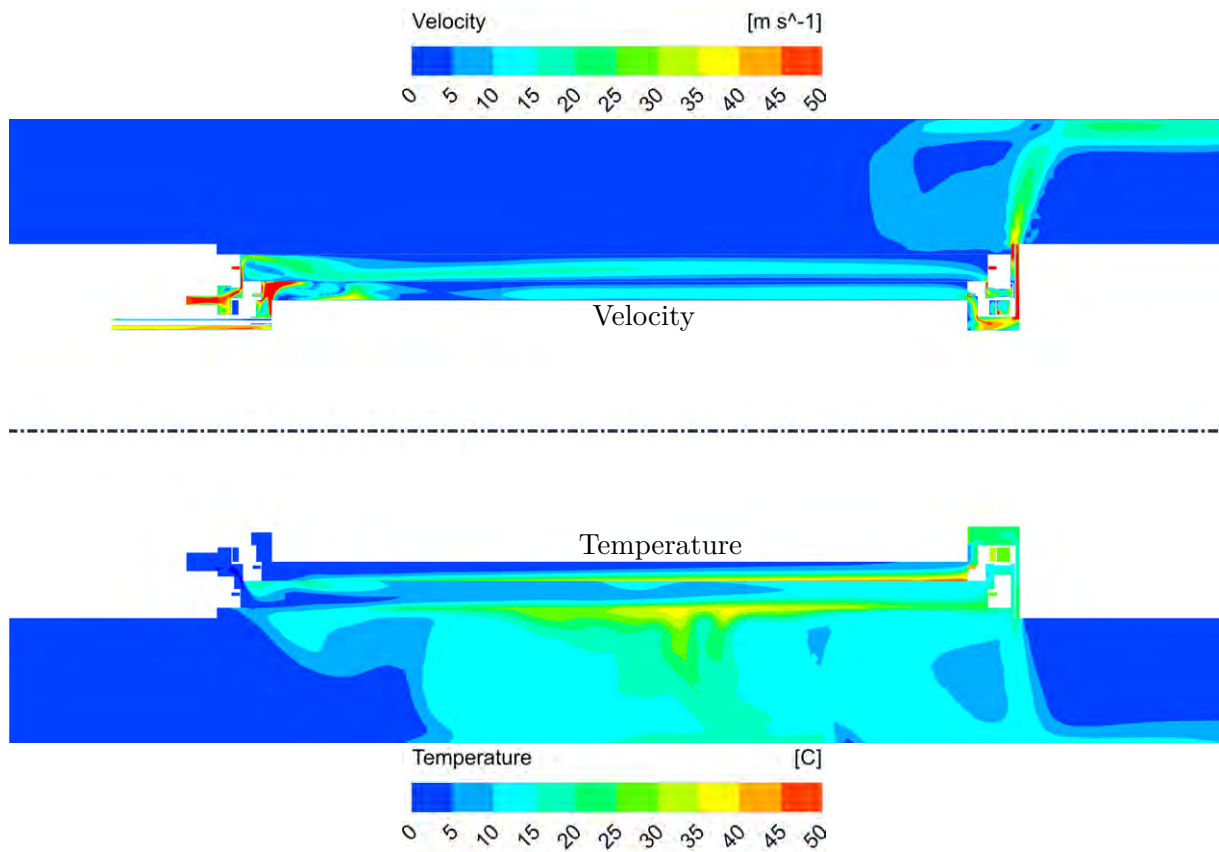


Figure 4.43: Velocity and temperature profile of part A with optimised geometry.

Part A-B-C

The results of the simulation with all three parts are shown in figure 4.45 with the MuPix and global flow temperatures. The MuPix of part B show again an increase in temperature resulting from the missing interface. All three parts show a different MuPix temperature behaviour, for part A the temperature increases with z , which can be expected, because the cold flow enters at $z = -580$ mm and flows along z where it gets heated up. Part B has flows coming from both sides resulting in a maximal temperature somewhere around $z = 0$ mm. Part C has the maximum temperature of layer 3 at low z because the inlet is at $z = 580$ mm and is heated up to $z = 200$ mm. On the other hand, layer 4 has the maximum temperature at higher z because the global flow is flowing in the opposite direction.

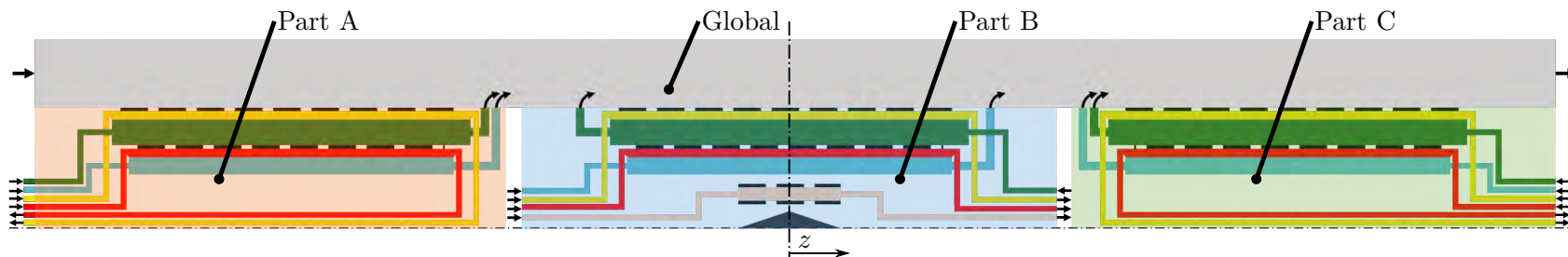


Figure 4.44: Scheme of the cooling flow and parts. (Different length scales)

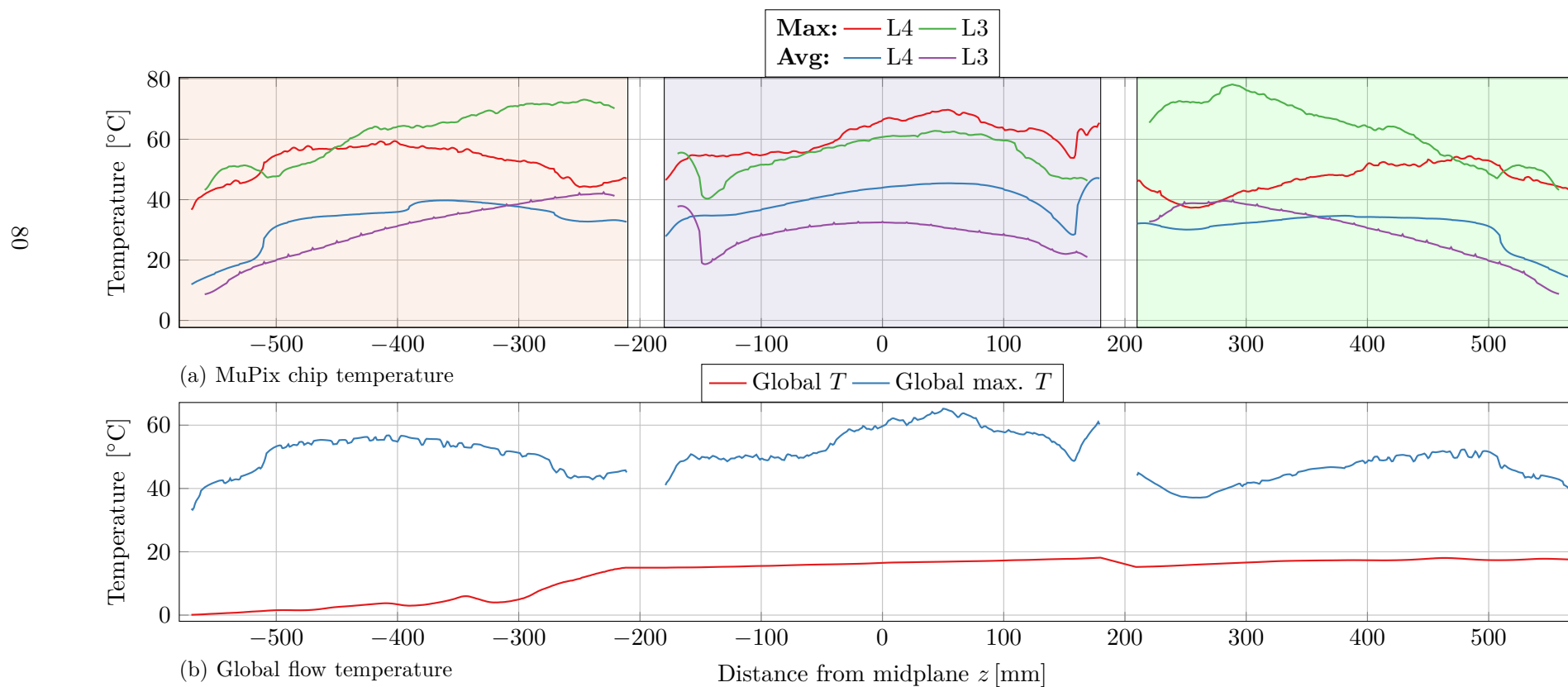


Figure 4.45: Results of the simulation with all three parts.

4.7.5 Summary of results of layer 3 & 4

The reliability of the simulation of layers 3 & 4 has already been discussed in section 4.7.3. There are several issues that may lead to large deviations from reality. Especially the mesh size, the turbulence and the behaviour of the layer towards a pressure gradient across them must be further investigated. Considering the mesh size compared to that of G12, the temperature could be around 15K higher. In the measurements of G12 the behaviour of the layer to a pressure gradient were investigated and showed a leakage flow of over 90% without a suction (also see section 5.5.2 on page 115). If the same is valid for layers 3 & 4, the model used does not represent the actual conditions.

Table 4.8: Results with different configurations of layers 3 & 4.

	Part	Geometry	Fluid	Solid	Heat input [mW/cm^2]	Periphery	Max. solid temp. [$^{\circ}\text{C}$]
Part B	B	Original	Helium	Silicon	400	Yes	69.5
	B	Optimisation	Helium	Silicon	400	Yes	64.4
3 sections	A	Optimisation	Helium	Silicon	400	Yes	73.1
	B	Optimisation	Helium	Silicon	400	Yes	69.7
	C	Optimisation	Helium	Silicon	400	Yes	78.1

5 Measurements

The goal of the measurements is to test the experimental cooling set-up and be compared with the simulated results. The simulation model implies several simplifications which are not present in the Mu3e experiment. However, there are also differences between the Mu3e experiment and the present mockup which are discussed later.

As the production of the mockup is not completely established, only a mockup of layers 1 & 2 was available for this project. With this mockup the simulation results can be partly compared and gives an idea about the challenges awaiting for the Mu3e experiment and also the measurement with layers 3 & 4.

In this chapter at first the measurement model, setup and design of experiment is developed, followed by the mockup, measurement equipment, diverse observations and finally the measurement results.

5.1 Measurement model

The used setup for the measurement is a mockup with some differences to the setup of the Mu3e experiment. The development of the measurement setup and modifications are described in this section.

The quantities which are measured have different priorities. The main goal is to measure the temperature of the layer dependent on the head load and mass flow. Additional quantities as the displacement of the layer, pressure differences and gas composition at the outlet are also measured as they can be used to analyse the behaviour of the mockup while cooled by a gas flow. At the beginning the measurement of the heat load was planned with a volt and current meter, but during the measurement and the data evaluation it was seen that the interposers and other parts of the electrical circuit caused higher additional resistances as expected. This is discussed in section 5.5.1, finally the worst case¹ heat load measurement was taken, which gives a safety factor to the temperature measurement.

¹Three different heat loads definition were compared and the one with the lowest heat load was used.

5.1.1 Setup

Figure 5.1 shows the measurement setup for the gap flow between layers 1 & 2. The gas inlet of the system is on the left followed by a pressure reducing valve. The mass flow at the inlet is measured and controlled using a valve. The flow passes through the mockup and is sucked out at the outflow from a vacuum pump. The outflow mass flow is also measured and controlled with a valve. This setup with a suction at the outlet is required as the layer are not leaktight and is planned to be realised in a similar way for the Mu3e experiment. The temperature is measured with several thermocouples which are measuring the flow and chip temperature. Also, a thermal camera is used to measure the temperature differences of the layers. Additionally, the gas composition at the outlet, pressure differences, current and voltage drop as well as the displacement of the layer are measured.

5.1.2 Modifications of the mockup

The present mockup has some modifications compared to the detector used in the Mu3e experiment which are described in the following list:

MuPix chips	The MuPix chips which will be used in the Mu3e experiment have been replaced by steel plates with the same dimensions. The stability with silicon will be a little smaller than with the steel plates. Also, the heat conduction of silicon is ten times higher than that of steel.
Heat source	The MuPix are the parts which will have to be cooled in the experiment. For the measurements an aluminium resistor is inside of the tape heater to simulate the heat dissipation of the MuPix. This aluminium resistor can only be heated constantly and therefore the difference of heat dissipation between the periphery and the detector parts are not present for these measurements. Also, the heat is not emitted directly inside of the chip but just below.
Temperature measurement	The aluminium resistor in the tape heater will be replaced with higher resistor with $\sim 1200\ \Omega$. This will enable a measurement of the averaged temperatures of all layers. The difficult assembly of the thermocouples, which is described later, will no longer be necessary.
In- & outlet	The adapter which connects the in- & outlet geometry with the tubing is different to the parts which will be used in the Mu3e experiment. Therefore, the pressure drop and also the leakage flow will be different.

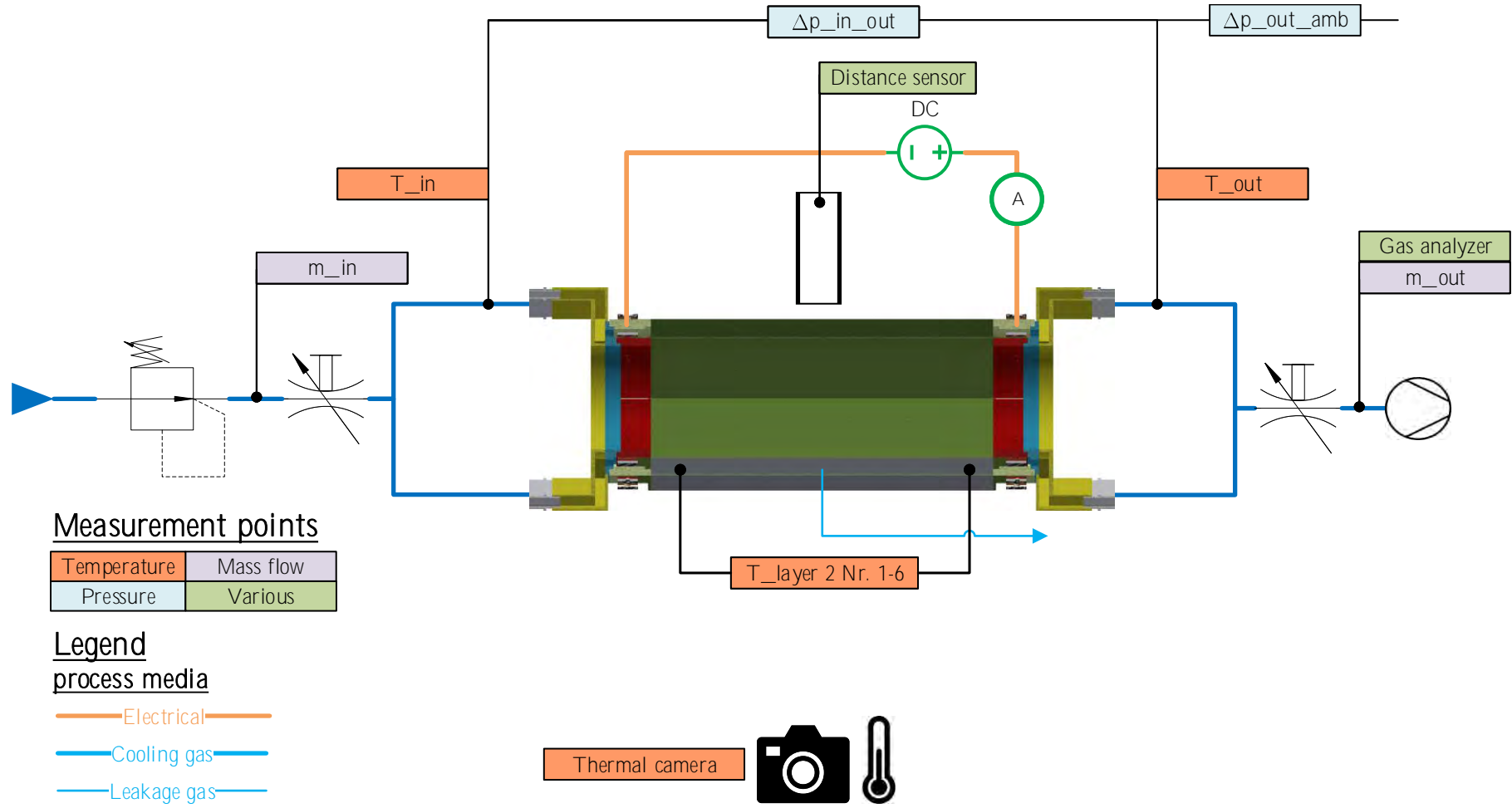


Figure 5.1: Measurement plan of gap flow between layers 1 & 2.

5.1.3 Design of experiment

Two different fluids were used for the measurements: firstly air which is available at negligible cost, secondly helium which costs around 15 CHF/min. Therefore, most measurements and tests of the measurements will be made using air, which should have similar conditions as helium to enable an easier comparing. The adaptation of the air parameter to have similar conditions as helium has already been made in section 3.6.1. These properties are shown again in table 5.1. The Reynolds number is held constant as well as the temperature increase of the fluid until the end of the heaters. With the lower mass flow and the lower total heat input, similar conditions can be achieved with air compared to helium.

Table 5.1: Experimental parameter for layers 1 & 2 with helium and air. Reynolds number and temperature increase of the cooling media are held constant to obtain similar conditions.

	Helium	Air	Unit	Source
Reynolds	1090	1090	[–]	
Velocity	10	1.28	[m/s]	
Massflow	2	1.87	[g/s]	
Temperature increase	19.1	19.1	[K]	
Nusselt	10.71	10.96	[–]	
Heat transfer coefficient	126.87	21.91	[W/m ² · K]	
Heat dissipation	400	72.1	[mW/cm ²]	
Heat dissipation	$8 \cdot 10^7$	$1.44 \cdot 10^7$	[W/m ³]	
Total heat	198.7	35.8	[W]	
Prandtl (20 °C)	0.66	0.71	[–]	
Pressure drop from in- to outlet	4000	500	[Pa]	CFD

5.2 Mockup of layers 1 & 2

Figure 5.2 shows the mockup of layers 1 & 2 with the tape heater and the gas in- & outlet. Only one half shell of layer 2 is mounted and is visible at the top. The mockup consists basically of 36 tape heaters which are described in the next section and some connection parts. On both sides there are the in- & outlet which consist of several parts. The gas distribution plate was optimised with simulations to ensure a better cooling and more homogenous temperature distribution. Measurements have been performed with both plates and are compared later.

The assembling process of the mockup is hand made by Thomas Rudzki and can be seen on https://youtu.be/1zDo_vx45cs.

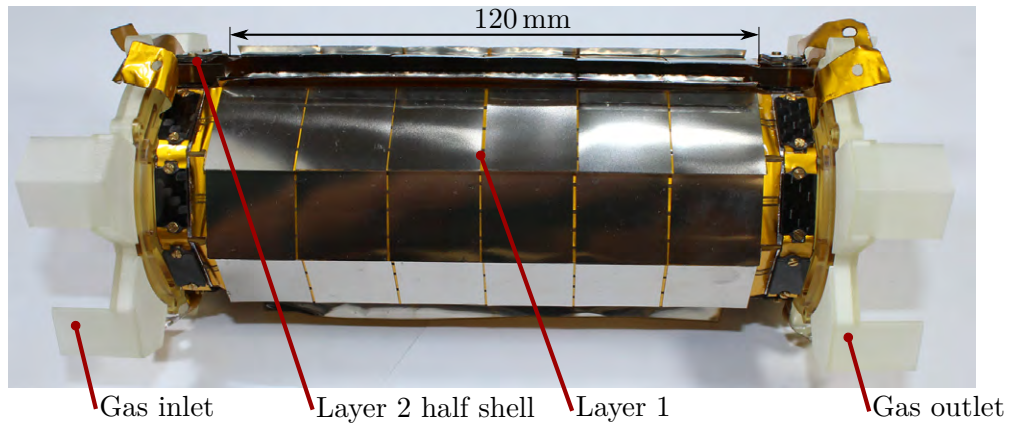


Figure 5.2: Mockup with both layer 1 half shells and one half shell of layer.

Figure 5.3 shows the mockup mounted into the frame with temperature and pressure measurement.

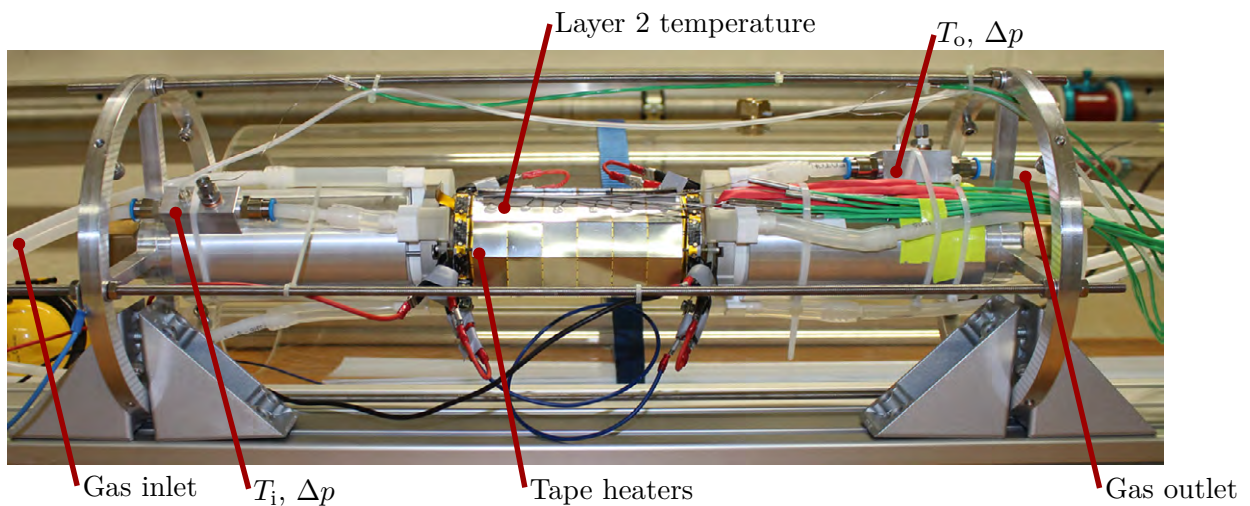


Figure 5.3: Mockup of gap flow between layers 1 & 2 with position of visible sensors.

5.2.1 Tape heater

The tape heaters are the key component of the experiment and consist of a thin aluminium and polyimide foil which have the heat resistors on one side. On the other side there are steel plates which are representing the silicon chips. On both sides there is an electrical connection to connect the resistor to the heating circuit. The resistance has been measured using a power supply, a voltage and a current meter. The voltage drop of the used connector cable has been subtracted from the measured value. Different currents have been used for the measurement which all resulted in a resistance of $0.110\ \Omega$. For all 36 layers this gives a total resistance of approximately $3.96\ \Omega$ which is later used to calculate the heat dissipation emitted by all layers. The measured value has also been compared with the theoretical resistance. Using

equation (5.1) the resistance can be calculated and equation (5.2) is considering the change of resistance depending on temperature. The obtained results are shown in table 5.2. The temperature increase of 50 K is increasing the resistance by 21.5%. The difference between the measured values and the theoretical could come from the contact resistance from the cable to the resistors, other material properties of the thin aluminium or little damages which are increasing the resistance.

$$R = \rho \cdot \frac{l}{A} \quad (5.1)$$

$$R(T) = R_{T_0} \cdot (1 + \alpha (T - T_0)) \quad (5.2)$$

Table 5.2: Theoretical and measured resistance of one tape heater side.

Property	Value	Unit	Source
Length l	280	[mm]	
Thickness	25	[μm]	
Width	4.5	[mm]	
Specific resistance Al. ρ	0.026	[$\Omega\text{mm}^2/\text{m}$]	[20, p. 267]
Temperature coefficient Al. α	$4.3 \cdot 10^{-3}$	[1/K]	[20, p. 267]
Reference temperature T_0	20	[$^{\circ}\text{C}$]	
Temperature T	70	[$^{\circ}\text{C}$]	
Resistance $R(T = 20^{\circ}\text{C})$	0.065	[Ω]	
Resistance $R(T = 70^{\circ}\text{C})$	0.0786	[Ω]	
Measurement R	0.110	[Ω]	

The measurement of the total resistance has a uncertainty as it was assumed that all tape heaters of the mockup have the same resistance as the one used for measurements. The total resistance has to be seen as a lower limit of the resistors which are heating up the flow. The heat load measurement has to be improved for further measurements which is discussed later.



Figure 5.4: Up- and downside of one tape heater with steel plate on top and aluminium resistor on downside.

Reparation of one tape heater

During the assembling of all half shells together and testing of the heating circuit a higher resistance (around $250\ \Omega$) of one half shell of layer 1 has been noticed. The source of the higher resistance was found on one of the tape heaters of the older half shell of layer 1. Figure 5.5a shows the tape heater which had some fissure which caused the high resistance. The fissure is probably due to the usage as sample object as it was the first one produced and the gluing of thermocouples could have enhanced them.

The first attempt to reconnect both sides of the fissure was with a conductive glue containing silver particles [21]. The gluing is shown in figure 5.5b with the lifted end of the tape heater with insulating tape to prevent a connection between both sides.

The gluing failed to fix the connection. The other option to repair the connection was to place two interposers with aluminium foil underneath the tape heater to connect both sides. The interposers are requiring some pressure to establish connection between the parts. On the left side ((A)) this is done with the carbon plates which are also connecting the normal interposer. In return on the right side ((B)) of the fissure something had to be built to apply some pressure. This is shown in figure 5.5c where the position of the underlying interposer is shown and also the construction to apply pressure on the second end of the interposer to establish the electrical contact. With this configuration the tape heater could be heated together with all others. Due to the additional interposers and pressure construction the resistance increased. The carbon plate and the pressure construction are heated more than normally. As the mockup can be flow through both sides, the part with this reparation was placed at the outlet. The advantage is that the flow is not preheated at the inlet and also the temperature at the outlet is measured in the four tubes. The repaired part is placed in front of one of outlets. The temperature

increase of one of the outlet temperature was handled as measurement or setup error of one outlet temperature.

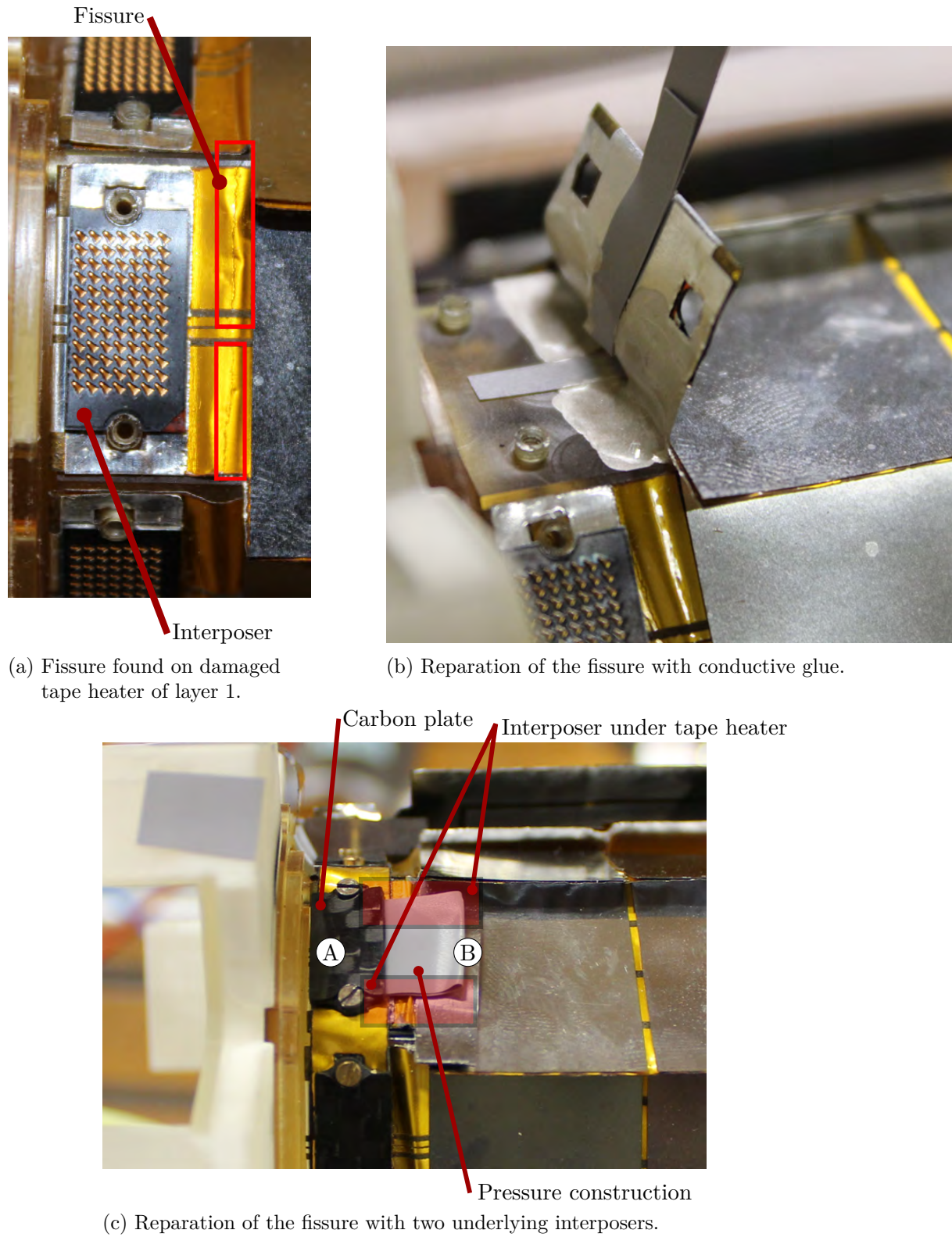
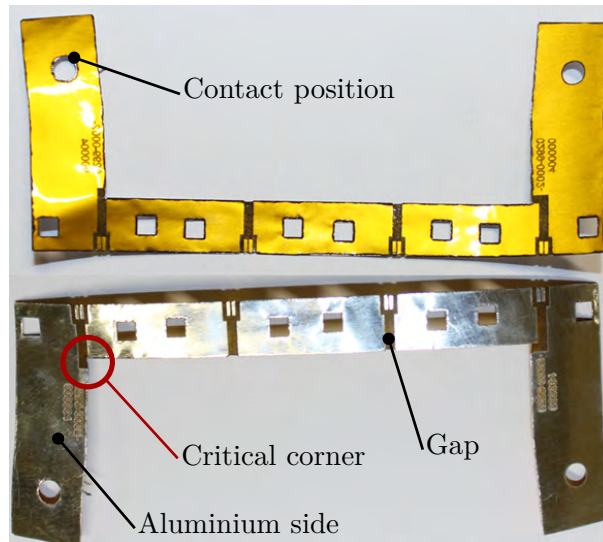


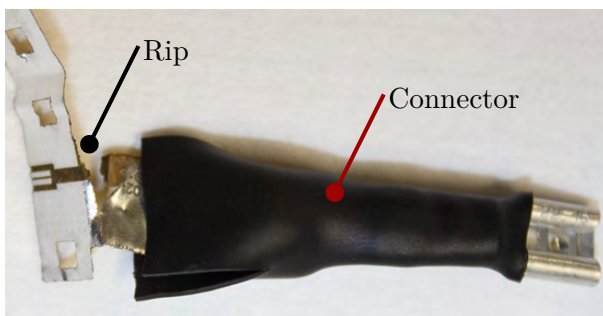
Figure 5.5: Repairation of the damaged tape heater of layer 1.

5.2.2 End piece flex

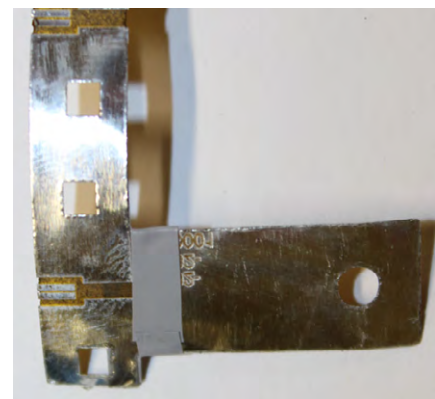
At the electrical contact between the tape heaters of every half shell there is one end piece flex which can be seen in figure 5.7. The flexes consist of a thin aluminium and a polyimide foil which are connected by an adhesive. The aluminium foil has some gaps to ensure the current is flowing through the tape heater. Figure 5.6 shows both side of the flex and indicates the gap. At the contact position some electrical contact with low resistance had to be build. These connectors are shown in figure 5.6b, which were fixed with a small screw. As the flexes have a thickness of only 0.1 mm and the connector had to be mounted and connected, the flexes were damaged. Most of the flexes ripped at the in figure 5.6a indicated critical corner which was then strengthened with insulating tape. This was still not enough so a connector plate was constructed which is described in the next section.



(a) Aluminium and plastic side of end piece flex.



(b) Rip of end piece flex and connector.



(c) Reinforcement of critical corner with insulating tape to prevent rupture of end piece flex.

Figure 5.6: End piece flex used to connect several tape heaters.

Connector plate

As the connector caused several failure of the end piece flexes, different options were considered as soldering a cable onto the aluminium side to lower the mechanical stress on the flexes or 3D print a connector plate on which the different cable could be connected. As soldering on aluminium is challenging, a connector plate has been designed. Figure 5.7 shows the connector plate and an end piece flex of layer 2 which has holes for the M3 screws. The end piece flex of layer 1 is contacted from the other side to prevent a short circuit between them. Two of the connector plates are used per side and are fixed together. With the connector plates the flexes can be easily fixed with minimising the stress. After mounting the connector plate, no damage was found at the flexes anymore.

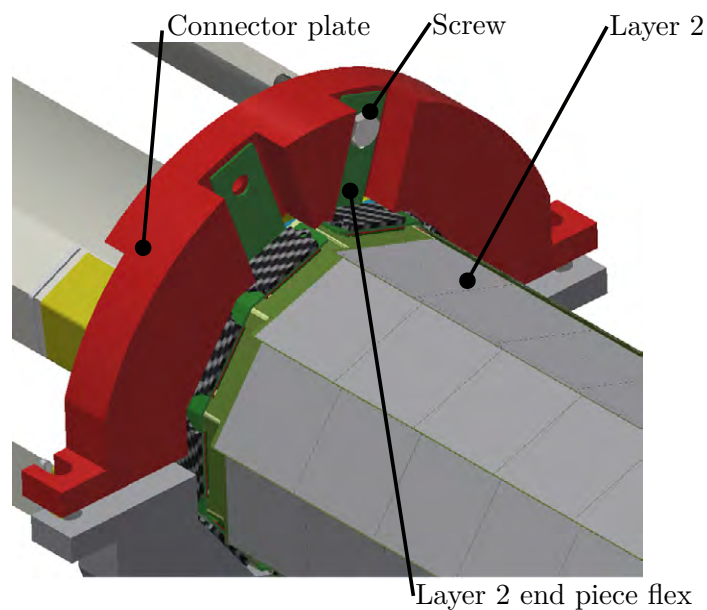


Figure 5.7: Connector plate for the end piece flex connection.

5.2.3 In- & outlet geometry

The in- & outlet geometry plates have been optimised during the CFD simulation which is shown in section 4.2.4 on page 48 and resulted in a lowering of the maximal temperature. This optimised plate has also been manufactured to investigate the effect onto the mockup. Figure 5.8 shows original and optimised inlet plate. The slots of the original geometry have all the same width which lead to irregular flow between the gap. The reason for this lies on the right and left side in the exiting end piece flex of layer 1, which closes a large part of the slots as can be seen figure 5.8b. This closed region has been minimised at the optimised plate. Also, the width of the slots was adjusted to ensure a more regular flow over the whole circumference.

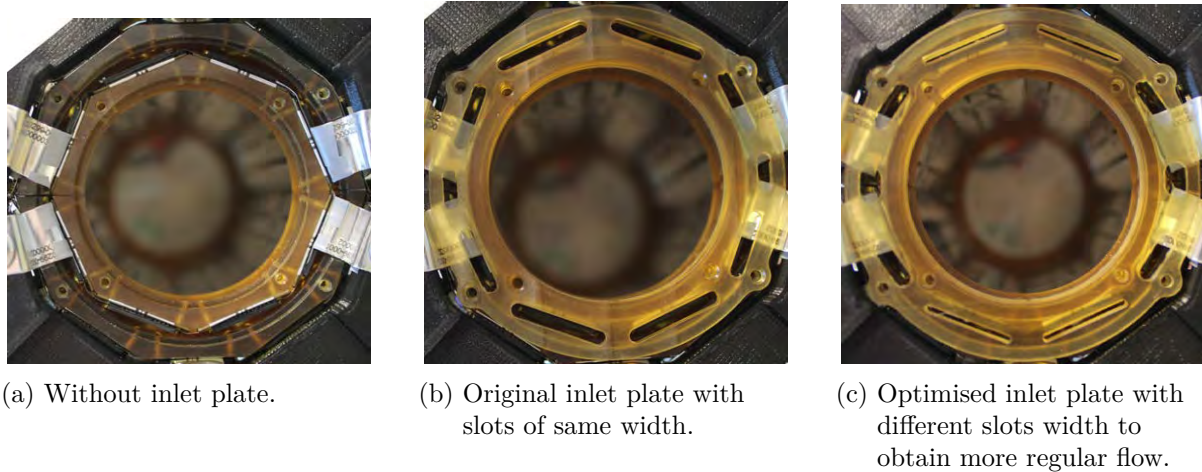


Figure 5.8: View of the inlet plate and inside of layer 1 which have all a inner diameter of 40 mm.

5.3 Equipment and setup

In this section the equipment used for the experiment and measurements is shown. Some equipment could only be used for air or helium as there are some difference between the cooling fluids. Firstly, a summary of all measurement devices is shown. Then, the main differences and challenges with helium compared to air are discussed followed by a more in-depth description of the devices.

5.3.1 Equipment list

The measurement equipment for the measurement is listed in table 5.3 with the device type, measurement principle, range and supplier. All available data sheets can be found in the digital appendix appendix D. Most of the equipment was available from the ITFE, only the thermocouples and the distance sensor were purchased for this thesis. The specialities of the measurement devices is explained further down in this section.

Table 5.3: Equipment used for measurements.

Description Code	Identifier	Principle Fluid	Range Output	Supplier
T-mass DN 15 m_in m_out	AT70F 65F15	Thermal flow Air 1 bar Air 1 bar	0 – 29 g/s 4 – 20 mA 4 – 20 mA	E+H
T-mass DN 25 m_out	65F25	Thermal flow Helium 1 bar	0 – 10 g/s 4 – 20 mA	E+H
Coriolis DN 4 m_in	83A04	Inertia of flow Helium 10 bar	0 – 6.5 g/s 4 – 20 mA	E+H
Distance sensor Distance	IPRM12I9505	Inductive	0 – 7 mm 4 – 20 mA	Baumer
Temperature T	IKT 05/10/2	Thermocouple K	–200 – 1150 °C	Electronic Sensor
Thermal imaging	SC7200M	Infrared radiation	320 × 256 Pixel	Flir
Pressure difference Δp	HCLA	Membrane	± 2.5 & ± 75 mbar 0.25 – 4.25 V	First Sensors
Gas composition Gas analyser	BGA244	Speed of sound	0 – 100 % 4 – 20 mA	SRS
Heating current A	M10S	Shunt resistor	0 – 10 A 0 – 60 mV	KnIck
Voltage drop I		Voltage divider	0 – 40 V 0 – 10 V	
Power supply	EA-PS 2342-10		2 × 160 W	EA
DAQ Voltage	NI-6211		± 10 V	NI
DAQ Thermocouple	NI-9213			NI
DAQ USB Carrier	NI-9162			NI
Vacuum pump	S100F	Rotary vane pump Helium	110 m ³ /h	Leybold
Vacuum pump	D16B	Rotary vane pump Air	16 m ³ /h	Trivac

5.3.2 Test rig modifications due to gas change

The density difference between air and helium is quite different which leads to different velocity to obtain the same Reynolds number. Because of these differences some measurement devices had to be changed.

Mass flow	<p>The mass flow of the air and helium are quite similar but with the difference in density the helium velocity is around 10 times higher than for air. With the Endress and Hauser applicator [22] the appropriate mass flow measurement devices have been chosen.</p> <p>For air a T-Mass DN15 is in appropriate range at ambient conditions. Helium requires a T-Mass DN25 due to higher volumetric flow. As only one T-Mass DN25 is available, a Coriolis DN4 was used at the high pressure inlet pipe.</p>
Pressure	<p>The simulated pressure drop is quite higher with helium and therefore other sensors are required which have a higher measurement range.</p>
Suction	<p>As the helium has a higher volumetric flow as well as a higher pressure drop, another suction device has to be used to obtain the required mass flow.</p>
Gas supply	<p>The air for the measurement has been taken from the compressed air network. Helium had to be taken from pressure bottles which were only lasting about 12 min with the full mass flow.</p>
Leakage	<p>The leakage flow is hardly measurable with air. With helium the gas composition at the outlet can be measured as it is in a surrounding of air. This gives an idea of the leakage flow for both cases, air and helium flows.</p>

5.3.3 Mass flow

The mass flow of the experiment has to be measured at the in- & outlet to adjust both flows to be equal which is resulting in a minimal leakage flow. Since no measuring instruments could cover the range of air and helium flow with an appropriate measurement uncertainty, different ones had to be used. Various devices were available from Endress + Hauser (E+H), of which the T-mass and Coriolis are best suited for the required gas flows. The devices have been chosen with the E+H applicator [22]. The measurement error of the different devices is shown in figure 5.9.

At the outlet due to the ambient pressure the T-mass is a better option than the Coriolis due to the low gas density. The Coriolis has further a high pressure loss compared to the T-mass which would require a larger vacuum pump at the outlet.

At the inlet both principles are possible. The pressure drop caused by the Coriolis is no issue as the pressure from the bottle and compressed air network has to be expanded anyway with a valve to regulate the mass flow.

Air

For air the best option at the outlet is a T-mass with a diameter DN15 which has for a mass flow over 1.5 g/s air an error of 1.5 %. For the inlet another T-mass DN15 was used as no Coriolis was available for a longer time and the measurement is then the same at the in- & outlet.

Helium

For helium outlet a T-mass DN25 has to be used which is already at its upper measurement range. As there is only one T-mass DN25 is available a Coriolis DN4 was used for the helium measurement which was operated at ~ 10 bar. The measurement error of the Coriolis is only 0.5 % compared to the T-mass which has an error between 1.5 – 2.5 %.

Error T-mass

According to the data sheet, the T-mass requires an inlet run of $50 \times DN$ if a valve is just placed in front of the valve. The outlet run has to be $2 \times DN$ which was always respected. If light gases as Helium or Hydrogen are used, the inlet run has to be doubled. With the DN15 used for air the distances were respected but the T-mass DN25 at the outlet with helium would require an inlet run of 2.5 m. The inlet run with the DN25 was only 0.6 m which is clearly under the requirements, which results in an unknown measurement error. The long inlet run would have lowered the mass flow of the vacuum pump due to higher pressure loss and was not reasonable as other errors as the gas composition were also present.

The measurements with helium the concentration at the outlet was between 65 – 85 % but the T-mass was set to pure helium. This led to a measurement error as the properties of helium and air are quite different. For T-mass there is an option to measure a gas mixture with an analogue input. This has not been used but for further measurement should be considered.

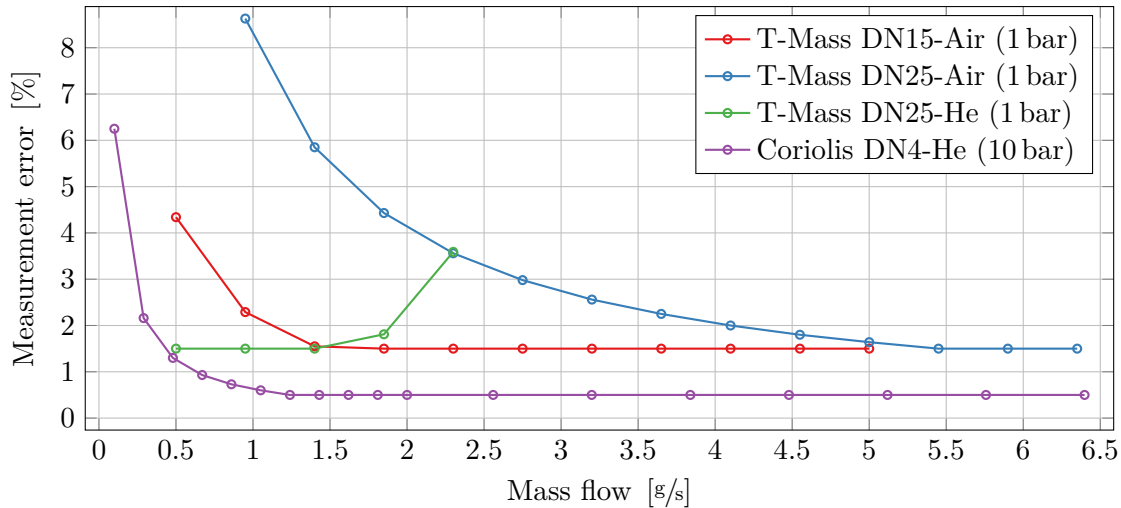


Figure 5.9: Measurement error of the T-Mass and Coriolis in the mass flow range used for the experiments. [22]

5.3.4 Distance

For the movement of layer 2 there are different options based on a laser triangulation measurement or inductive field change. An inductive sensor has first been tested and showed that the principle is working for 50 μm steel plates. As the inductive sensor is cheaper (~ 250 CHF) as the laser sensor (~ 1200 CHF) and showed the good accuracy for the required measurement, the low price option was chosen. The inductive sensor required a calibration as its linearisation of signal is only valid for thick material.

The distance sensor was placed at one steel plate at the end of a half shell where the movement of the layer is highest. The distance sensor showed only small displacements compared to the static case when the in- & outlet mass flows were regulated to the same flow. It is also a primitive pressure sensor for the pressure difference from inside the layer to the ambient.

Calibration

The inductive distance sensor has been calibrated as can be seen in figure 5.10. The sensor was placed in a mounting that was far from the guide plate and the moveable table to minimise the influence of the inductive field. A Polyoxymethylen (POM)-plate has been prepared on which the tape heater was fixed. POM has been used as it does not influence the inductive sensor.

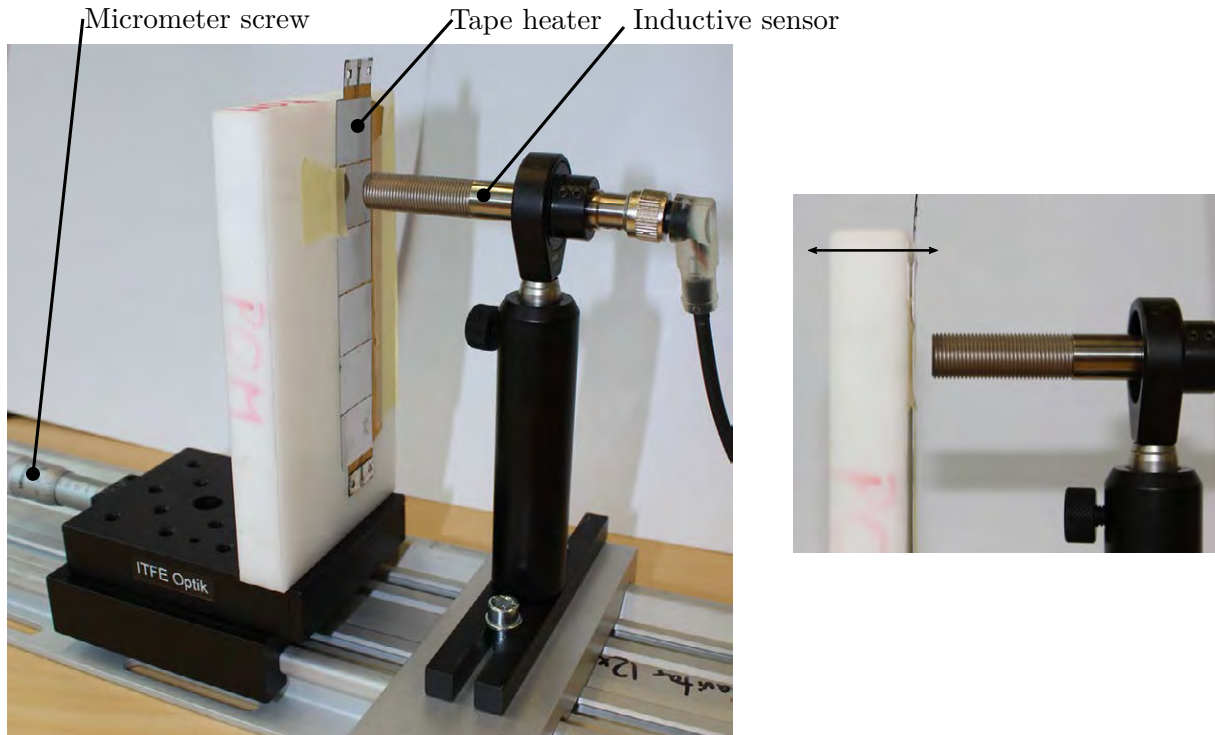


Figure 5.10: Calibration setup for inductive distance sensor for tape heater.

The distance between the sensor and the tape heater has been increased in steps of 0.1 mm from 0 up to 6.5 mm as illustrated in figure 5.11. Additionally, the signal was recorded only with the POM-plate, which shows no signal change over the whole range. The table with the micrometer screw has a moving precision of 0.005 mm and a spring mechanism which stopped the movement as soon as the sensor reached the plate. With the tape heater the distance goes down to -0.1 mm which is equal to zero, due to the spring mechanism. The signal is continuously increasing in the whole measurement range. The sensor's sensitivity is higher for little distances, which makes sense considering the measurement principle. Even at a maximal distance of 8.5 mm a difference could be measured with and without the tape heater. The sensor is linearised in the range between 0 – 2 mm for thick material with a signal range of 0 – 20 mA. As the tape heater is thin, the minimum signal which could be reached is from 10 mA up to 30 mA. This signal is converted into a voltage signal. Because of this linearisation no physical model can be fitted into the measurement data and a lookup table has to be used. The POM-plate has not influenced the measurement at all as expected.

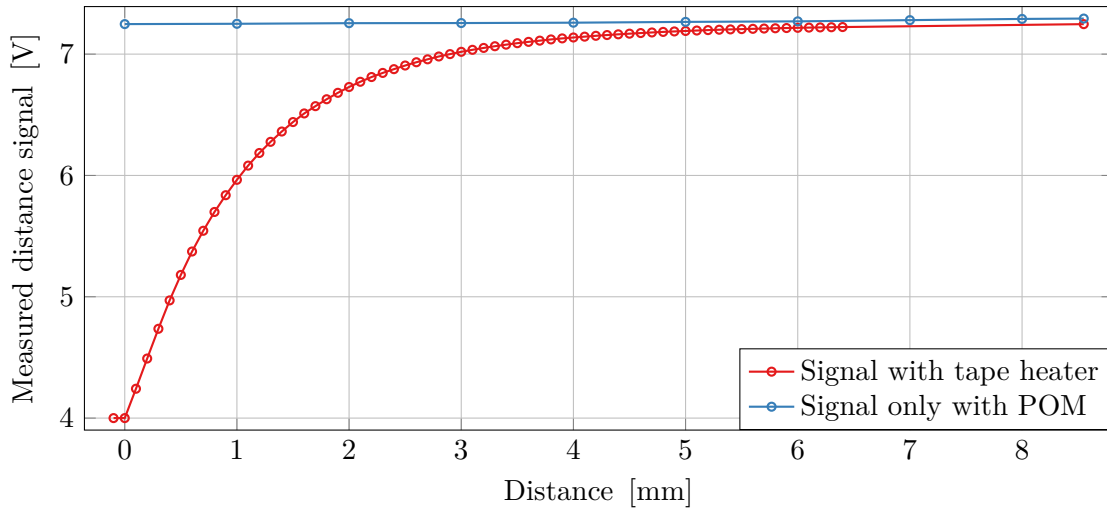


Figure 5.11: Calibration curve for the inductive distance sensor with tape heater.

In the results, the displacement is shown as the distance between the sensor and the layer, so that a positive value is a contraction and a negative value is an inflation. Figure 5.12 shows a sketch of the measured layer with the sensor.

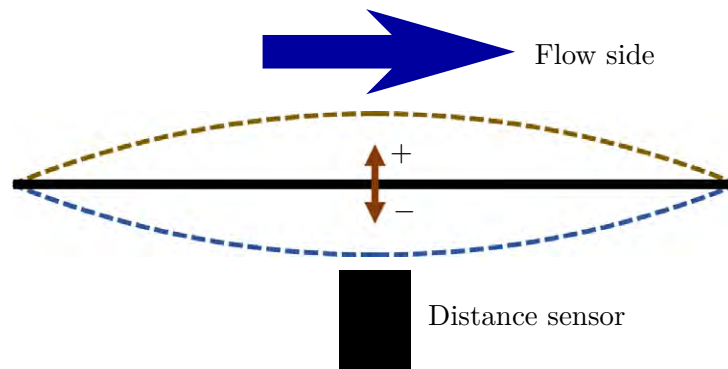


Figure 5.12: Displacement value sign treatment.

5.3.5 Temperature

The temperature is crucial for the cooling measurement. The temperature of the gas at the in- & outlet as well as the layer temperature must be monitored. Ideally the temperature of different layers would be measured as the CFD simulation showed that the temperature is not uniform over the circumference. Thermocouples were chosen for the measurement of the layer surface, inlet and outlet temperature. The mounting of the thermocouples on the layer is quite challenging and has only been made on one tape heater of layer 2. The differences over the circumference should be monitored with a thermal camera.

Thermocouple

The temperature of the in- and out-flowing gas has been measured as well as the surface temperature of the steel plates. For the gas measurement a block has been manufactured for temperature as well as the pressure measurement which is shown in figure 5.14. The thermocouple at the inlet has been placed in the middle of the flow. At the outlet all four flows have been measured as some differences were expected which were expected due to an modification of one tape heater resulting in a higher temperature (see section 5.2.1 for details). The thermocouples at the outlet have a slower reaction time than the one on the layer and have therefore be placed further upstream. This is falsifying the pressure drop measurement but on the other hand lowering the time until a stationary point is reached. This is crucial during the measurements with helium.

The diameter of the used thermocouple is 0.5 mm with a sheath length of 100 and 150 mm depending on the mounting position. SERTO adapters were used to insert the thermocouples leak tight into the measurement block.

The thermocouples which have been mounted on the layer required some preparation to ensure a solid bounding. Figure 5.13 shows the setup used for the gluing of the thermocouples on layer 2. A mounting block has been manufactured to fix the half shell of layer 2 and prevent damages. The green cables of the thermocouple are quite rigid and have therefore been fixed. The used adhesive is Hysol 9497 which is suited for high heat transfer application with a thermal conductivity of 1.2 W/mK [23]. The curing process was accelerated using a heat lamp. The temperature was directly monitored with the glued thermocouple. Three thermocouples have also been mounted on one tape heater of layer 1. The insertion into the whole structure is tricky. During the replacement of the inflow geometry, the inner thermocouples fell off.

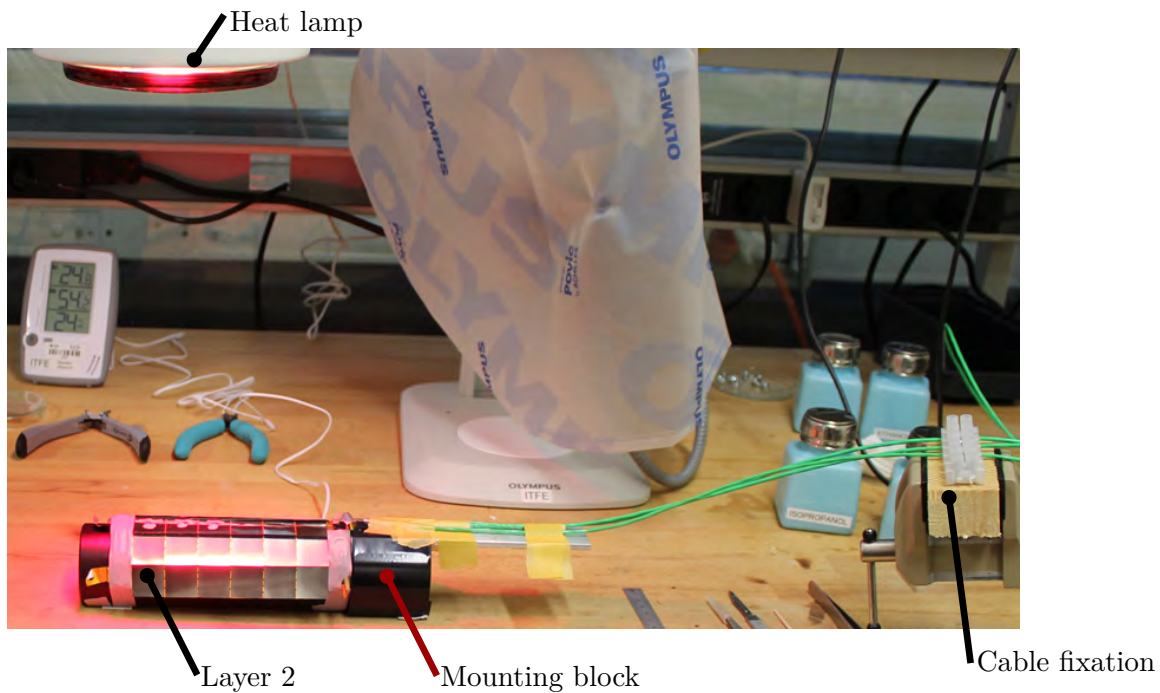


Figure 5.13: Setup for the mounting of thermocouples on the layer 2.

Thermal camera

The thermal camera has been placed such as the thermocouple of layer 2 could be seen as reference. The main focus is on the part which showed to have the highest temperature during the simulation. This high temperature is caused by the overlap which is not directly cooled and the cooling flow is slow or goes even backward. However, the imaging of the steel plate there is requiring some adjustment as the surface is reflecting the radiation of the environment. If the thermal imaging camera is used on this blank steel plates basically only reflected radiation is measured. Therefore, a coating has been applied onto one half shell of layer 2 with a specific emissivity. The black coating contains spherical pigments which are leading an angle independent emissivity of 98% [16]. This higher emissivity also leads to stronger thermal radiation which has already been estimated in section 3.5.4.

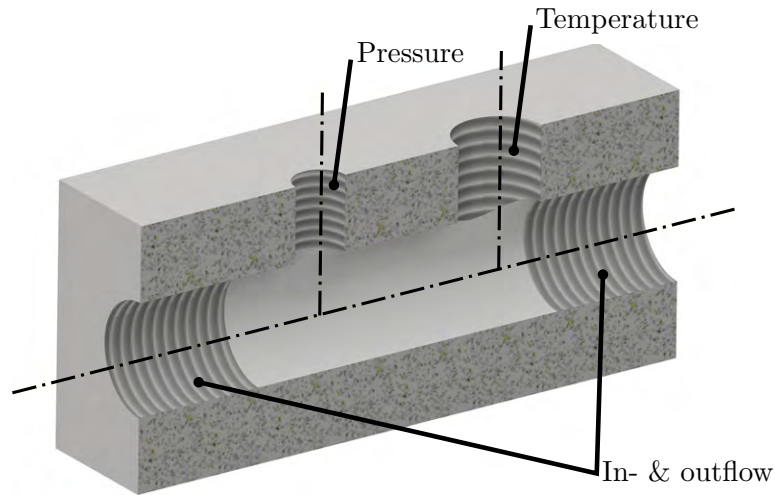


Figure 5.14: Measurement block for temperature and pressure at in- & outflow tubes.

5.3.6 Pressure

The pressure measurements on the mockup are supposed to be used for validation of the pressure resulting of the CFD simulations. The measurement points have been chosen in the in- and outlet tubes as these are easily accessible and do not affect the experiment. A measurement between the layers has been considered but this would influence the flow between the layers and has therefore not been realised.

From the simulation the occurring pressure drops have already been estimated which are shown in table 5.1. Since the absolute pressure differences are rather low, differential pressure sensor were chosen. As the pressure drop for helium and air are different at constant Reynolds number, sensors with different operating pressure were required. For the measurements with air and helium, sensors with an operating pressure of 12.5 mbar and 75 mbar respectively were selected.

Figure 5.14 shows the measurement block for the in- & outflow pressure as well as the temperature. The pressure sensor was connected with the auxiliary block using silicone tubes.

The pressure measurement had higher pressure drops compared to the simulations. First, the in- & outflow geometry are different between the mockup and the simulations. The geometric change from a round cross section into a triangle is surely causing some pressure losses. Also, the thermocouples at the outlet were placed inside of the tube to enable a faster response but are also causing a pressure drop. Therefore, the expected pressure drop of the measurement is probably higher.

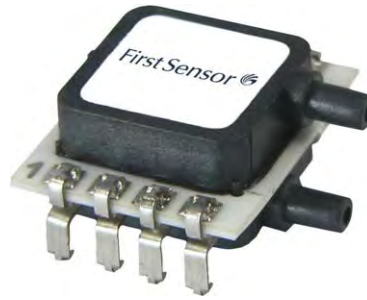


Figure 5.15: Differential pressure sensor (HCLA) from First Sensor. [24]

5.3.7 Gas analyser

The leakage flow in the experiments using air could not be evaluated. From the energy balance some discrepancy between the thermal and electrical energy were present. Some leakage flow could be felt near of the in- and outlet geometry. However, a quantitative measurement of the leakage is difficult. For the helium the concentration at the outlet can be measured using a gas analyser. With the amount of air during the helium measurement, the leakage flow could be quantified. These values are not totally representative for the Mu3e experiment as the ambient gas will later be helium. Due to the low partial pressure of the helium in the ambient air and vice versa there is also a higher exchange to be expected.

A BGA244 Binary Gas Analyser has been placed at the lowest of the four outlets, which would probably measure the highest concentration as the helium is rising in the air. The expected type of gases have to be entered before the measurement and with the speed of sound measurement the composition of the flowing gas can be exactly determined.

5.3.8 Power supply

The heating of the tape heaters requires a laboratory power supply. The used one has two separate output which maximal output of 160 W with can be connected serially which gives a maximum of 320 W.

5.3.9 Heating circuit

Figure 5.16 shows the electrical circuit which was used for the heating of the tape heater of layers 1 & 2. As source a laboratory power supply was used with voltage-control which lowers the current in case of a short circuit. The eight half shells with tape heaters were connected in series to have the same current through all of them. One resistor of the tape heater has a resistance of around $0.110\ \Omega$. For measurement of the current a shunt resistor with a resistance of $6\ \text{m}\Omega$

was used which produces a voltage drop of 0 – 60 mV for a current of 0 – 10 A. Additionally, the total voltage drop of the whole electrical circuit was measured using a self made voltage divider with two serial resistors. R_{d1} has 3.3 k Ω and $R_{d2} = 1$ k Ω which splits the voltage drop to a level which can be measured with the measuring board.

Per tape heater there are two circuits which can be seen in figure 5.4. These circuits are connected from different sides and in total there are 18 tape heater which gives 36 resistor and a total resistance of $\sim 3.96 \Omega$. The shunt resistance adds less than a thousandth which can be neglected. The voltage divider has a total resistance of 4.3 k Ω which is connected in parallel to the tape heaters. This is lowering the total resistance seen by the power supply of about 0.15 % which can also be neglected.

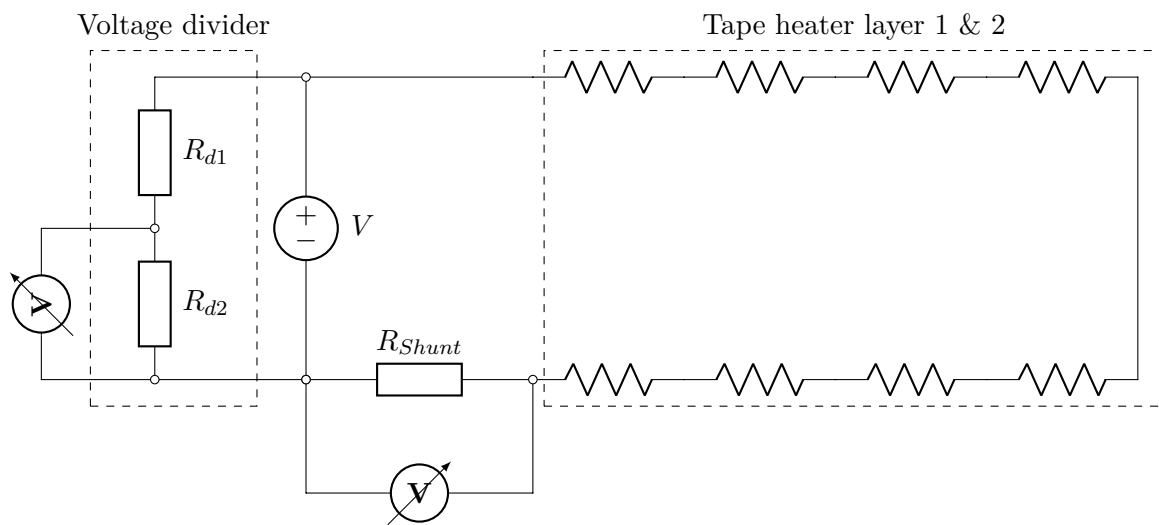


Figure 5.16: Heating circuit of the tape heater of layers 1 & 2 with the measurement of current and voltage.

Additionally, to the shunt and voltage divider, there are the connection cables and connector of the end piece flex which are additional resistors. The cable resistance is computed according to equation (5.1) on page 88 with a total length of 2m which consists of the cable from the power supply and between the half shells. All quantified resistors are shown in table 5.4. Some resistances were hard to quantify like the diverse contact resistances as well as micro fissures in the aluminium of the tape heater and the end piece flex.

Table 5.4: Components of the heating circuit and their resistance.

	Part	#	Value	Total	Unit	Source
Cables	Length	-	2.0		[m]	
	Area	-	1.5		[mm ²]	
	Specific resistance Cu. ρ	-	0.0173		[Ω mm ² /m]	[20]
	Resistance	1	23.1	23.1	[m Ω]	
	Shunt	1	6	6	[m Ω]	[25]
	Voltage divider	1	$4.3 \cdot 10^3$	$-12 \cdot 10^{-3}$ (parallel)	[Ω]	
	Connector	16	10	160	[m Ω]	Estimation
	End piece flex	8	40	320	[m Ω]	Calculation
	Tape heater	36	0.110	3.96	[Ω]	Measurement
	Total			~ 4.5	[Ω]	

5.3.10 Suction

For the G12 there is an in- & outflow which is used for the Mu3e experiment. At first it has been tested, if a suction is required at the outlet or if the mockup is leaktight. As described in section 5.5.2 the leakage flow without an underpressure at the outlet is nearly 100 %. Therefore, a vacuum pump is required combined with a mass flow measurement to set the same flow conditions at in- & outlet. It is then assumed that most of the fluid flows through the layer and is sucked in by the vacuum pump.

Since the outlet of the G12 consists of four tube with a diameter of 8mm, which results in significantly lower total cross section area compared to the vacuum pump, high losses were expected.

For air a vacuum pump with a specified volumetric flow of 16 m³/h was used. The maximal flow which has been achieved with it was around 6 m³/h.

For helium a higher volumetric flow is needed due to the higher velocity/lower density. The required volumetric flow is 43 m³/h for a mass flow of 2 g/s. A side channel blower as well as a bigger vacuum pump were tested. Both were tested with only the T-Mass DN25 to estimate the capability. The blower only achieved 30 m³/h (specified up to 200 m³/h) without even the reduction to the 8 mm tubes. The Leybold S100F vacuum pump provided a volumetric flow of 65 m³/h (specified up to 110 m³/h) with the same setup. Therefore, the vacuum pump was used. With the splitting into 4 tubes with a diameter of 8 mm, the resulting volumetric flow was around 30 m³/h with helium.

5.3.11 Gas supply

Air was used from the compressed air network with a decompression valve set to 1.5 bar in combination with a hand valve to adjust the mass flow to desired values. For helium measurements two bottles ($V = 50\text{ l}$, $p = 200\text{ bar}$) were available.

Air

The compressed air from network is cooled during the expansion from around 10 bar to atmospheric conditions which leads due to a positive Joule-Thomson coefficient to a decrease of around 2 K. As the temperature before the expansion was not measured, this could not be verified with the measurement data.

Helium

The bottle has a volume of 50 l at 200 bar which is approximately 9.2 m^3 helium gas at atmospheric pressure. One bottle has around 1.54 kg helium which gives a measurement time of around 12.8 min with a mass flow of 2 g/s . The fast expansion of the helium of the bottle leads to a temperature changes of the helium. Two main effects superimpose each other, leading to a temperature increase at the beginning and a decrease at the end.

The first effect is the adiabatic expansion of helium from 200 bar to atmospheric pressure. Helium has a negative Joule-Thomson coefficient (see section 3.1) at ambient temperature, which leads to a temperature increase of the helium while expanding from the gas bottle. The theoretical temperature increase with a pressure difference of 199 bar is around 12 K. This temperature increase could mainly be seen at the beginning of the measurement where high pressure differences are present. The maximal temperature increase measured at the inlet was around 5 K which is probably due to heat exchange between the helium and the tubing.

The second effect cools the helium inside the bottle and is caused by volume work exerted on the atmosphere. As the mass of helium is quite small compared to the mass of the bottle, the temperature of the helium does not fall below 0°C , which would otherwise be the case in an adiabatic system.

Figure 5.17 shows the inlet temperature during one measurement with helium. The pressure of the bottle at the beginning was around 100 bar as some measurements were performed some hours before. The bottle could at this point still have been colder than environment. As soon as the valve was opened the temperature at the inlet increased to a maximum of 23.5°C after 2 min. From then on the inlet temperature decreased to a minimum of 14°C . Since the Joule-Thomson

effect reduces heating with decreasing pressure drop and the helium in the bottle becomes colder over time, this explains the observed behaviour.

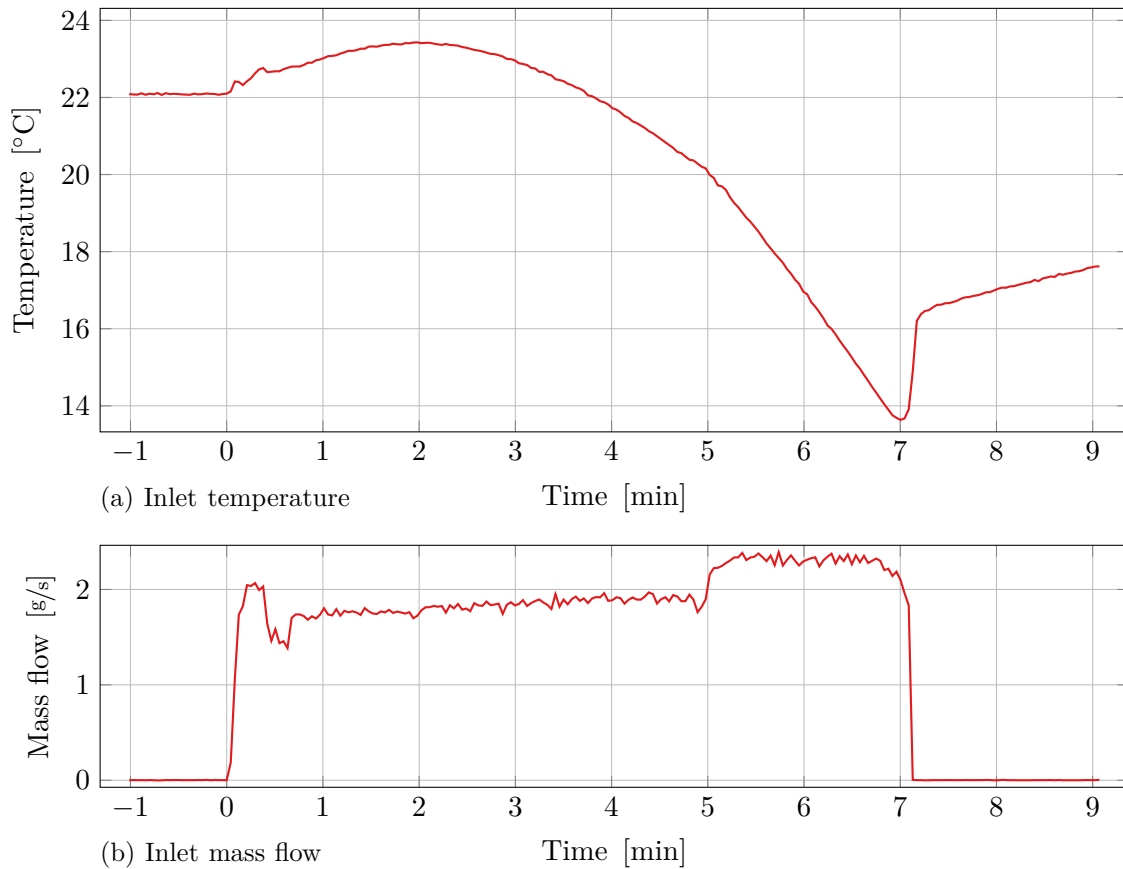


Figure 5.17: Inlet temperature of helium during measurement with around 100 bar and bottle below room temperature due to previous measurements.

5.3.12 Data acquisition

The Data acquisition for logging all measured values was performed with National Instruments (NI) measurement boards and processed with a LabView program, which was taken from a colleague and adapted. The measurement frequency was set to 87 Hz. These recorded data were then averaged over 30 points and logged in a file to reduce the signal noise. The thermal camera has its own software and was logged separately.

The NI-6211 voltage measurement board was used for all measurement excluding the thermocouples. Most sensors have an output of 4 – 20 mA which had to be transferred into a voltage signal for the measurement board. This was performed using precise $500 \Omega \pm 0.1 [\%]$ resistors. The conversion of the voltage signal into the physical value was performed in the LabView software. The only exception is the distance sensor which does not have a linear signal and was converted during data processing in Matlab.

The thermocouples were all connected to the measuring card NI-9213, which allows the connection of 16 thermocouples.

5.3.13 Measurement error

The measurement error of all measurements devices is discussed here. Most of the devices the measurement error has been taken from the data sheet which can be found in appendix D and are summarised in table 5.6. The error of the mass flow was already discussed in section 5.3.3 which considered the error of the devices and not of the whole chain. For the thermocouples the whole measurement chain was determined following to Guide to the Uncertainty in Measurement (GUM). The measurement error of the heat loads is discussed in detail in section 5.5.1.

Thermocouple

The measurement uncertainty of the whole chain was computed following the GUM which was summarised from Gossweiler [26]. For the thermocouples the uncertainty is computed following equation (5.3). The uncertainty consists of type A, which considers the random deviation, and type B, which includes all other uncertainties. For the errors assumed to be Gaussian, the uncertainty is multiplied by $1/2$ while for the other errors with a rectangular distribution, the factor is $1/\sqrt{3}$. The uncertainty has to be extended by the factor $k = 2$.

$$\Delta T_{TC} = k \cdot \left(\left(\frac{1}{2} \Delta T_{\text{typeA}} \right)^2 + \left(\frac{1}{2} \Delta T_{\text{inaccuracy}} \right)^2 + \left(\frac{1}{2} \Delta T_{\text{quantisation}} \right)^2 + \left(\frac{1}{\sqrt{3}} \Delta T_{\text{coldjunction}} \right)^2 \right)^{\frac{1}{2}} \quad (5.3)$$

The errors shown in table 5.5 were taken from the data sheet of the NI-9213 and norm for thermocouple type K. With those values the uncertainty of the thermocouple measurement is around ± 1.8 K.

Table 5.5: Computation of different measurement uncertainties for thermocouples typ K.

Uncertainty		Unit
Type A	$\frac{std(T)}{\sqrt{n}}$	[K]
Inaccuracy	± 1.5	[K]
Quantisation	$\frac{\text{Range}}{2^{\text{resolution}}}$	[K]
Cold junction	0.8	[K]

This range is quite high and has to be understood as upper limit of the possible deviation. Also, it gives the possible deviation of the absolute temperature. As the temperatures used here are relative temperatures to the inlet, the measurement has been further analysed by the deviation of the thermocouples to each other.

The temperature of the thermocouples was read on several days before starting the measurement². Figure 5.18 shows the temperature on different days. The shift of the temperature between the thermocouple of the layer is around ± 0.2 K. The temperature of the inlet thermocouple is shifted about 0.4 K compared to the one of the layer. The sensor at the inlet is from an older order and has probably due to it another offset. All thermocouples have been shifted in the data processing to the average temperature of the layer thermocouple to have the a lower offset to the inlet.

²This was done in the early morning before the laboratory was used. It is then assumed that the temperature of the thermocouples reached the same absolute temperature over night and the relative differences are constant offsets or small deviations of the thermocouples.

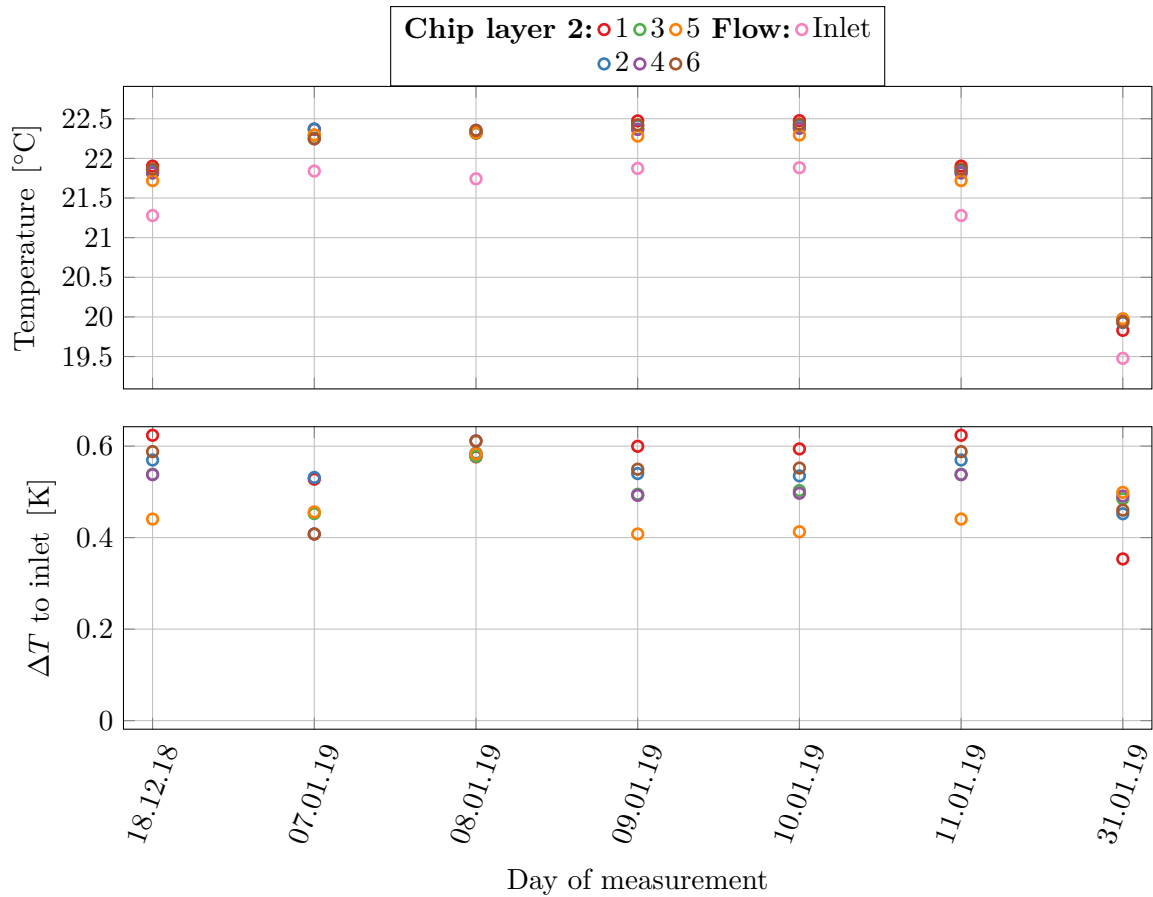


Figure 5.18: Temperature of thermocouple after long time without influence of surrounding.

As the thermocouples at the in - & outlet are placed in the middle of the flow, the measured temperature is the total temperature. The temperature increase due to the stagnation of the flow for air is approximately 0.05 K and for helium due to the higher flow velocity around 0.2 K. These effects are neglected in the results as the increase of temperature is neglectable compared to the one caused by the heating.

Table 5.6: Measurement error of the devices used.

Description Code	Identifier	Principle Fluid	Specified Error	Comment
T-mass DN 15 m_in m_out	AT70F 65F15	Thermal flow Air 1 bar Air 1 bar	$\pm 1.5\%$ $\pm 1.5\%$	Depending on mass flow.
T-mass DN 25 m_out	65F25	Thermal flow Helium 1 bar	$\pm 1.5 - 2\%$	Probably higher due to short inlet run.
Coriolis DN 4 m_in	83A04	Inertia of flow Helium 10 bar	$\pm 0.5\%$	
Distance sensor Distance	IPRM12I9505	Inductive	$< 0.012 \mu\text{m stat. } 10 \text{ Hz}$	For distance 0 – 2 mm, higher for steel plates.
Temperature T	IKT 05/10/2	Thermocouple K	$\pm 2.65 \text{ K}$	Relative error is smaller.
Thermal imaging	SC7200M	Infrared radiation	$\pm 1\%$ or 1 K	
Pressure difference Δp	HCLAXXX	Membrane	$\pm 0.25\%$ $\pm 2.0\%$	Non-linearity and hysteresis Thermal effects (-25 to 80°C)
Gas composition Gas analyser	BGA244	Speed of sound	$< 0.035\%$	Combination Helium/Air
Heating current A	M10S	Shunt resistor	$< 0.5\%$	
Voltage drop I		Voltage divider	$\sim 2\%$	Due to precision of resistors.

5.4 Data evaluation

The data obtained from the LabView and the thermal camera were processed using Matlab. At first the temperature shifts are corrected as explained in section 5.3.13. Different values are then computed with the present data as: different defined heat loads (see section 5.5.1) and the conversion of the voltage signal of the inductive sensor into a distance value. For the heat load \dot{Q}_{I2R} ³ based on the resistance and current, the temperature coefficient was considered.

The temperature temporal variation is then plotted and using a graphical input the sector for averaging a stationary point are chosen. In these sectors the mean values of all measured values are computed as well as the measurement uncertainty of the thermocouples. The error bars are only present for thermocouple. The other quantities were not computed due to time issues. Figure 5.29 on page 123 shows one measurement campaign with red areas which were chosen for the averaging.

5.4.1 Thermal imaging

The start of measurement of the thermal camera is not corresponding to the one of LabView and there is also another measurement rate of 1 Hz. The temperature curve from the camera were shifted and interpolated onto the time vector of the LabView data and showed no time shift.

The data from the thermal camera were imported into Matlab as tiff-file. The data were then processed to obtain the minimal, mean and maximal temperature. Additional animations were created which are showing the temperature during the measurement. Figure 5.19 shows one frame of the measured layer 2. The flow direction is from left to the right. The interposers have a high heat dissipation per surface and are not directly cooled. Therefore, the temperature of them is higher as the one of the tape heaters. For the results only the temperature of the layer is used which is inside of the frame. The minimal, mean and maximal temperature were taken from the indicated frame which was adjusted for each measurement as the camera view change by little.

³See equation (5.5).

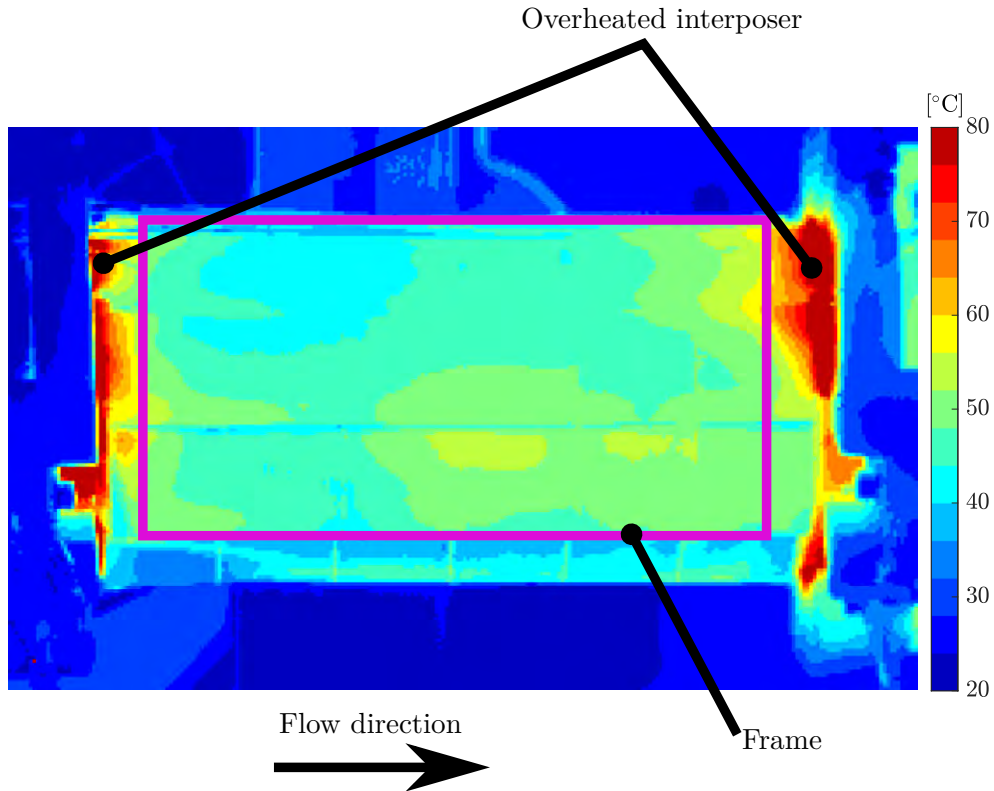


Figure 5.19: Example of one frame from the thermal camera measurement.

5.5 Diverse observations

During the assembly, testing, measurement and analysis of the data, observations were made which are described in this section. Some of them were unexpected, others were expected, but the quantification with estimates or simulations was not possible. Some effects are also documented in the setup, such as the increasing temperature of helium at the inlet caused by the Joule-Thompson effect described in section 5.3.11.

5.5.1 Heat load measurement

The measurement of the heat flux caused some issues as the heating circuit has uncertainties. In order to estimate the heat dissipation which is cooled by the flow, three different heat flux computations were compared:

$$\dot{Q}_{UI} = U \cdot I \quad (5.4)$$

$$\dot{Q}_{I2R} = I^2 \cdot R(T) = I^2 \cdot R_0 \cdot (1 + \alpha(T - T_0)) \quad (5.5)$$

$$\dot{Q}_{Th} = \Delta T_{i,o} \cdot c_p \cdot \dot{m}. \quad (5.6)$$

Equation (5.4) is considering the whole electrical input into the system which is certainly higher than the cooled heat flux from the flow, as there are losses in the cables, end piece flexes and interposers which are not in contact with the flow. Equation (5.5) is based on the current which is constant and the measured resistance of one new tape heater. This measured resistance is valid for a new tape heater but is probably higher for the tape heaters of the mockup. Equation (5.6) is computing the thermal energy increase of the cooling flow from the inlet to the outlet.

Figure 5.20 shows the three measured heat loads, which show large differences. The electrical energy based on the current and voltage drop is highest as there are additional elements in the heating circuit. The thermal heat is around 30% lower than $U \cdot I$. The electrical energy based on the current and the resistance is too small as there is more energy exceeding the system with the flow. To estimate the real heat flux which has been cooled from the MuPix is difficult to estimate. It is assumed to lay somewhere between the electrical curves. For the data evaluation the heat load based on the resistance and current was used as it is the worst case and can be understood as lower limit. The temperature dependency of the resistance was considered for the computation of \dot{Q}_{I2R} .

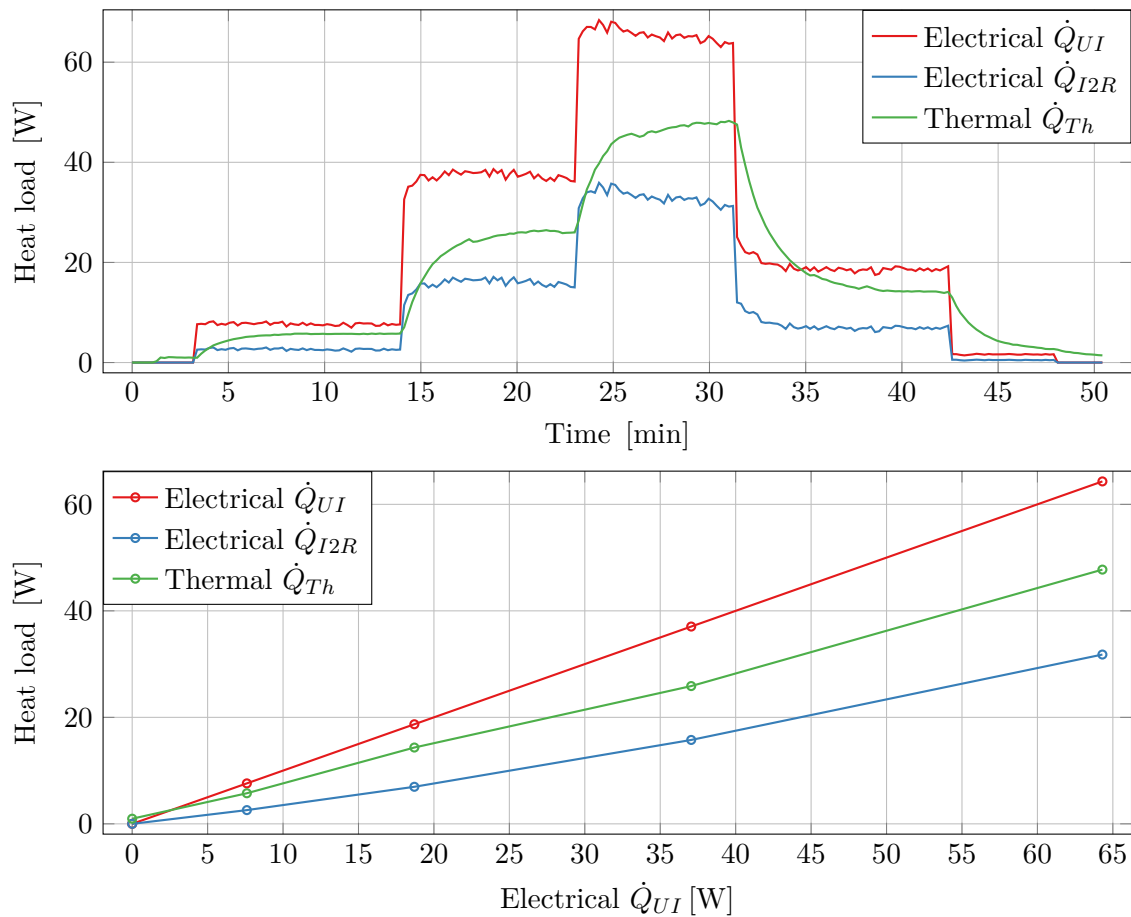


Figure 5.20: Different heat flux measurements.

5.5.2 Mass flow over layer

Before the cooling measurement were performed, the flow properties and behaviour of the layer were measured and analysed. The inlet mass flow was increased and the displacement of one tape heater of layer 2 was measured. The blow up of t layer was observable when the mass flow was increased. Figure 5.21a shows the distance between layer 2 and the inductive sensor depending on the mass flow at the inlet. The red and green measurements with an open outlet but without a vacuum pump are showing large displacement up to 1 mm. There is a hysteresis as the layers are retracting less when the mass flow is lowered. Both results are looking quite similar to the violet curve which was measured with a fully closed outlet. This means that the pressure drop through the outlet is higher than the pressure drop through the gap between the layers where the leakage occurs.

Figure 5.21b shows the mass flow at the in- & outlet. Up to 3 g/s of air mass flow there was no measurable flow through the outlet. Therefore, the leakage flow is nearly 100% which means that the experimental flow is not comparable with the simulation set-up and also the Mu3e experiment which will use an underpressure for the outlet of G12. In order to reproduce the same conditions a vacuum pump was installed at the outlet. The mass flow was then set to the same level as for the inlet. This led to a maximum displacement of layer 2 of about 0.05 mm and nearly diminished the leakage flow. Some fluid could still exit the gap along of the layer and be sucked in at the end. This leakage flow is assumed to be small and was measured to be around 15% with the helium measurement discussed in the following section.

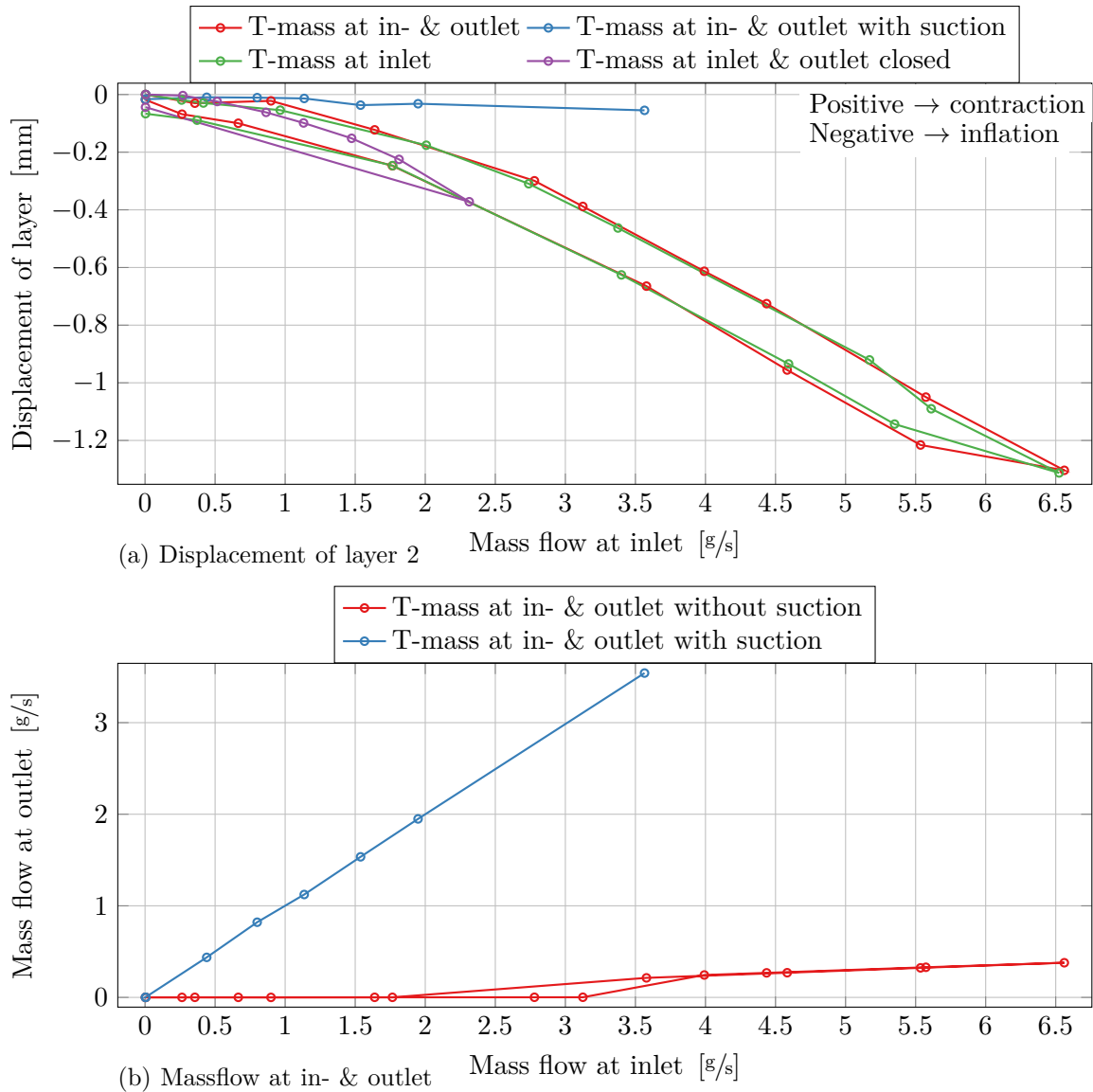


Figure 5.21: Distance of layer 2 and flow at outlet in dependence of inlet mass flow.

Leakage over layer

The leakage flow during could be estimated during helium measurement. The main focus during measurement lied on the cooling of the mockup, so the minimal leakage flow could not directly be estimated. Figure 5.22 shows the helium measurement with the in- & outlet mass flow, air-helium concentration and the displacement of the layer. At around 1 min the vacuum pump is turned on which is sucking only air at this moment. Later the valve of the helium is opened resulting in a mass flow at the inlet and moments later also at the outlet. At an inlet mass flow of 2 g/s a concentration of air of 25% is present at the outlet. The layer is contracted by 0.2mm with this conditions. With a higher inlet mass flow that was adjusted to obtain the same displacement as at the beginning, the concentration decreased further to 15%. The

mass flow at the outlet has some deviation as it is a mixture of helium and air but the T-Mass was only configured for helium. In the range of 7 – 8.5 min the displacement of the layer is approximately the same as without a flow, which means that the pressure drop between the gap and environment is small and not causing a displacement. Therefore, the mass flow at the outlet produces a similar pressure drop as the inlet and is assumed to have less deviation as measured.

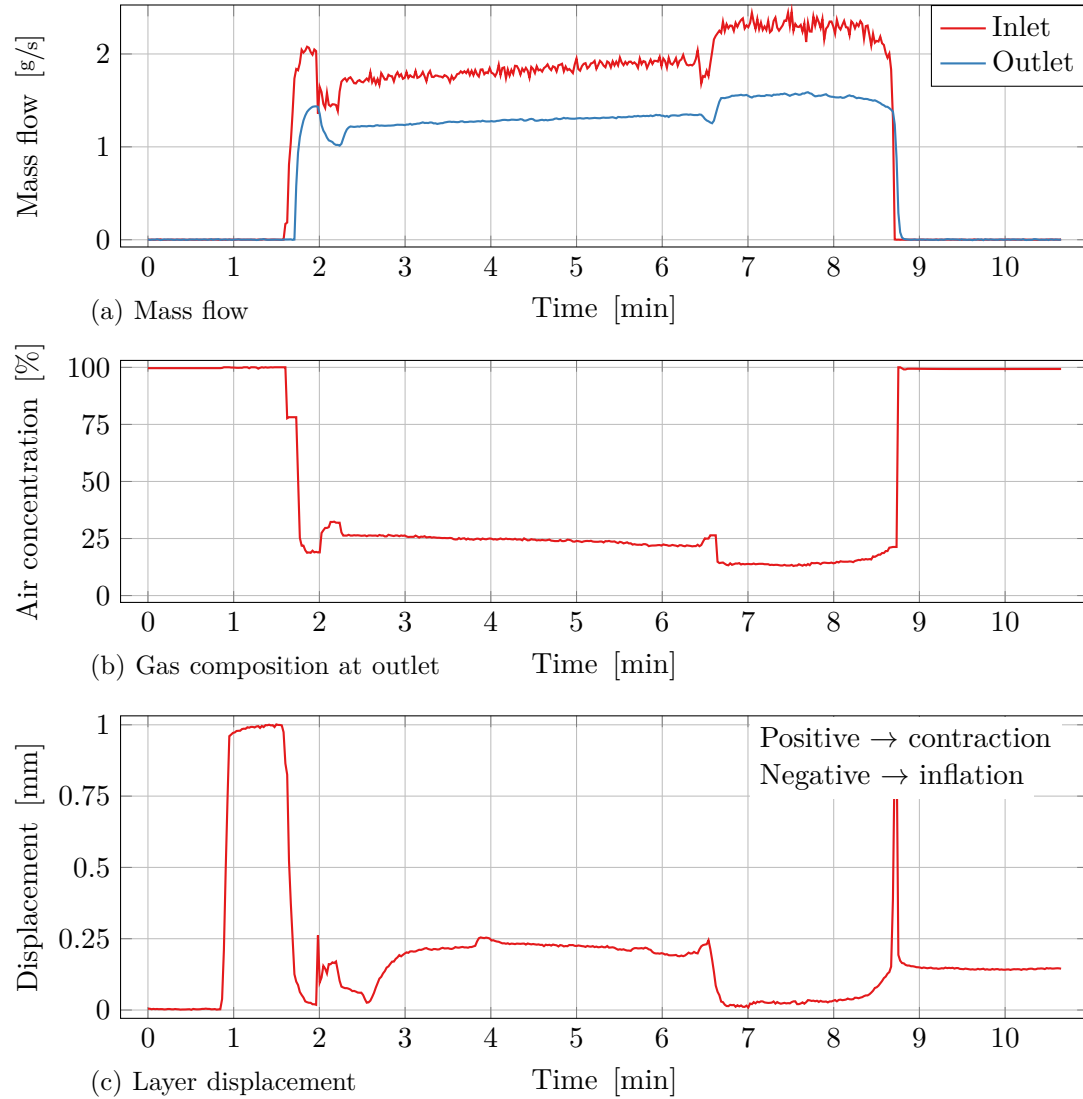


Figure 5.22: Helium measurement with different mass flows resulting in different gas concentration and displacements.

5.5.3 Movement of layer due to heating

The displacement of the layer was measured with the inductive sensor and showed some displacement with temperature changes. As it is also observable while no flow is present, it is probably due to the thermal expansion of the layer materials. The layer consists of aluminium-polymide foil with 6 steel plates on it. As polymide, aluminium and steel have different thermal expansion coefficient thermal gradients cause stresses which might lead to thermal bending which is known from bimetallic strip thermometer. The displacement could also occur from elongation of the layer which causes a bending due to a fixed length l . Figure 5.23 shows the layer in straight condition and with deflection s in both ways. If the bending is caused by the bimetallic strip effect or from expansion was not identified.

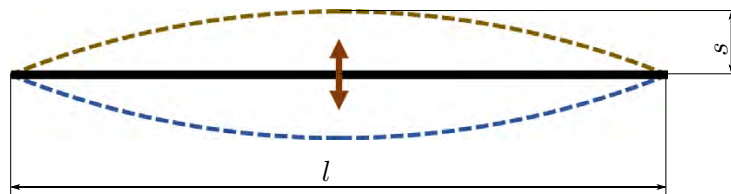


Figure 5.23: Displacement of the layer by increasing temperature as the material is expanding.

Figure 5.24 shows the layer displacement without a cooling flow and different heat loads. As the temperature of the tape heater is increasing, the distance between the layer and the inductive sensor is increasing. The displacement is occurring present just after the temperature increase.

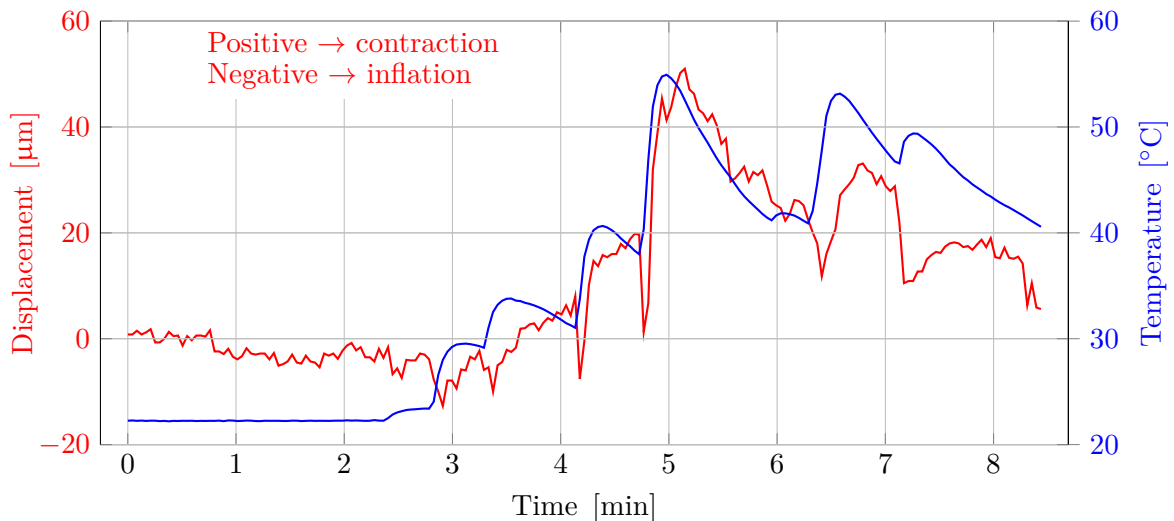


Figure 5.24: Displacement of the layer caused by heating of the tape heater without a cooling flow.

5.5.4 Readjustment of mass flow

During the experiment it was observed that the mass flow of the outlet increased with higher outlet temperatures. Therefore, the outlet mass flow for air was readjusted after the air heated up. This procedure was not applied for helium as the outlet valve was already completely open to obtain the maximum mass flow and the regulation was not possible in the short time of measurement.

Figure 5.25 shows a measurement performed to investigate the mass flow drift. Constant mass flows were set on in- & outlet and then the layers were heated. With the increase in temperature the pressure drop is increasing which is confirmed by the distance sensor which shows an inflation of layer 2. The explanation for the mass flow shift was not fully clarified. One possibility is the enlarged gap of the layer, where more air could be sucked in. The second possibility is a systematic measurement error of the T-mass at the outlet due to higher outlet temperature. The manufacturer company was contacted regarding the deviation in the event of temperature changes. The material data is defined and temperature dependent, which excludes this systematic error. The mass flow at the outlet should rather decrease with a higher pressure drop.

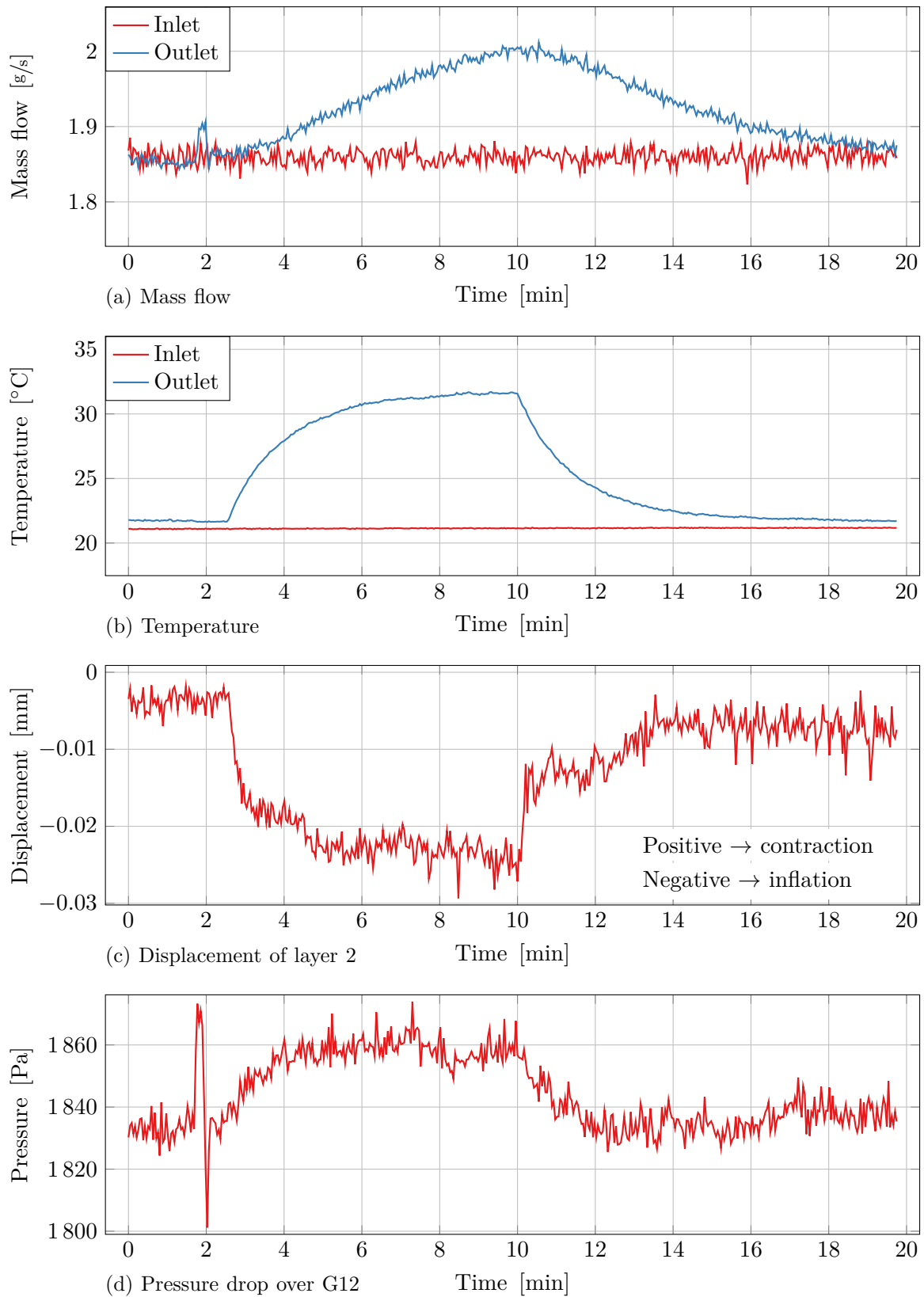


Figure 5.25: In- & Outlet mass flow over time with heating and resulting mass flow shift.

5.5.5 Shielded heat radiation

The heat radiation of the chips has been estimated in section 3.5.4 which is small compared to the total heat dissipation of the chips. In order to validate that the radiation can be neglected compared to the cooling by convection, an aluminium shield has been placed over the mockup which is reflecting the radiation. Figure 5.26 shows the mounting of the shield. The temperature along layer 2 is shown in figure 5.27 with approximately the same heat load on the layer. It can be seen that the temperature with the aluminium shield is higher by around 1 – 3 K with a heat load which is inferior by 0.8 W. The radiation observed with the measurement is making up to 5 – 7% of the cooling which is in the same range as obtained with the estimations.



Figure 5.26: Aluminium shield over the mockup to investigate the heat radiation.

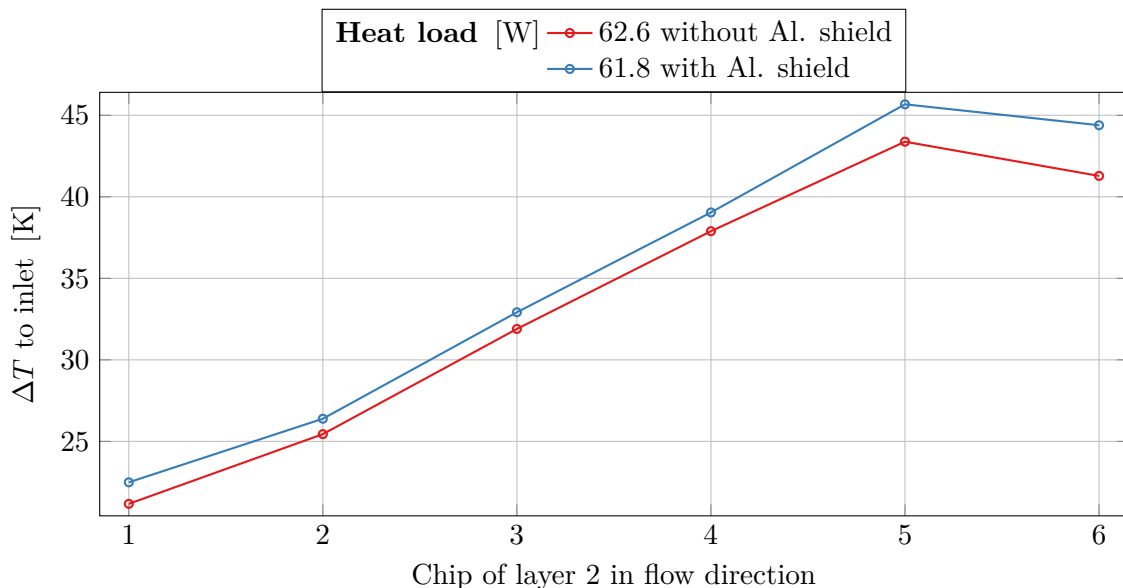


Figure 5.27: Temperature of layer 2 with and without aluminium shield.

5.5.6 Temperature at different mass flow

As already described in section 4.2.4 the temperature is approximately inversely proportional to the mass flow. Therefore, a doubling of the mass flow must not compulsory lead to half of the temperature. Figure 5.28 shows an experiment with increasing mass flow with a constant heat load of 10 W. The temperature decreases as expected with higher mass flow and is not linear.

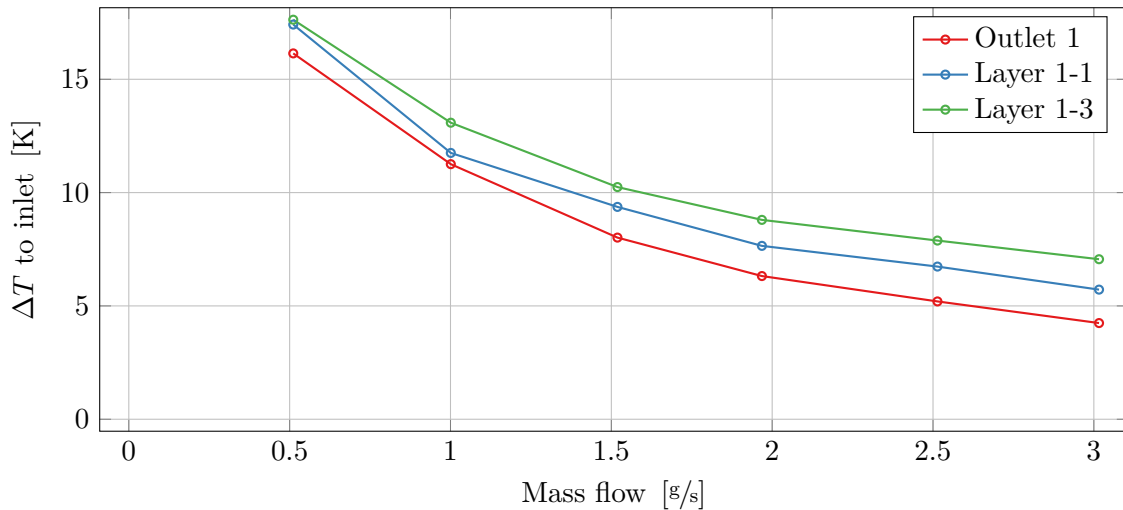


Figure 5.28: Different temperatures dependent on the air mass flow with constant a constant heat load of 10 W.

5.5.7 Measurement campaign and averaging

The data shown in figure 5.29 was one of the first runs in which no thermal camera was used. The in- & outlet mass flow was held constant whereas the heat load was in- & decreased as shown in figure 5.29b. The temperature of the in- & outlet and of layer 2 are shown. The inlet temperature does not change over time as it is not influenced by the heating. The thermal inertia of the layers and their thermocouples is judged to be low since steady-state conditions prevail after ~ 2 min. The outlet temperature has a higher time constant which leads to longer measurement times. Based on this observation the outlet temperature has later been changed to four thermocouples with better positioning.

The mass flow during the measurement time is nearly constant and has sometimes be adjusted. These adjustments are required as the outlet mass flow changes with different heat loads which was described in section 5.5.4.

The red areas shown in the temperature plot are the time slots, where the measurement have been averaged to be used for further analysis.

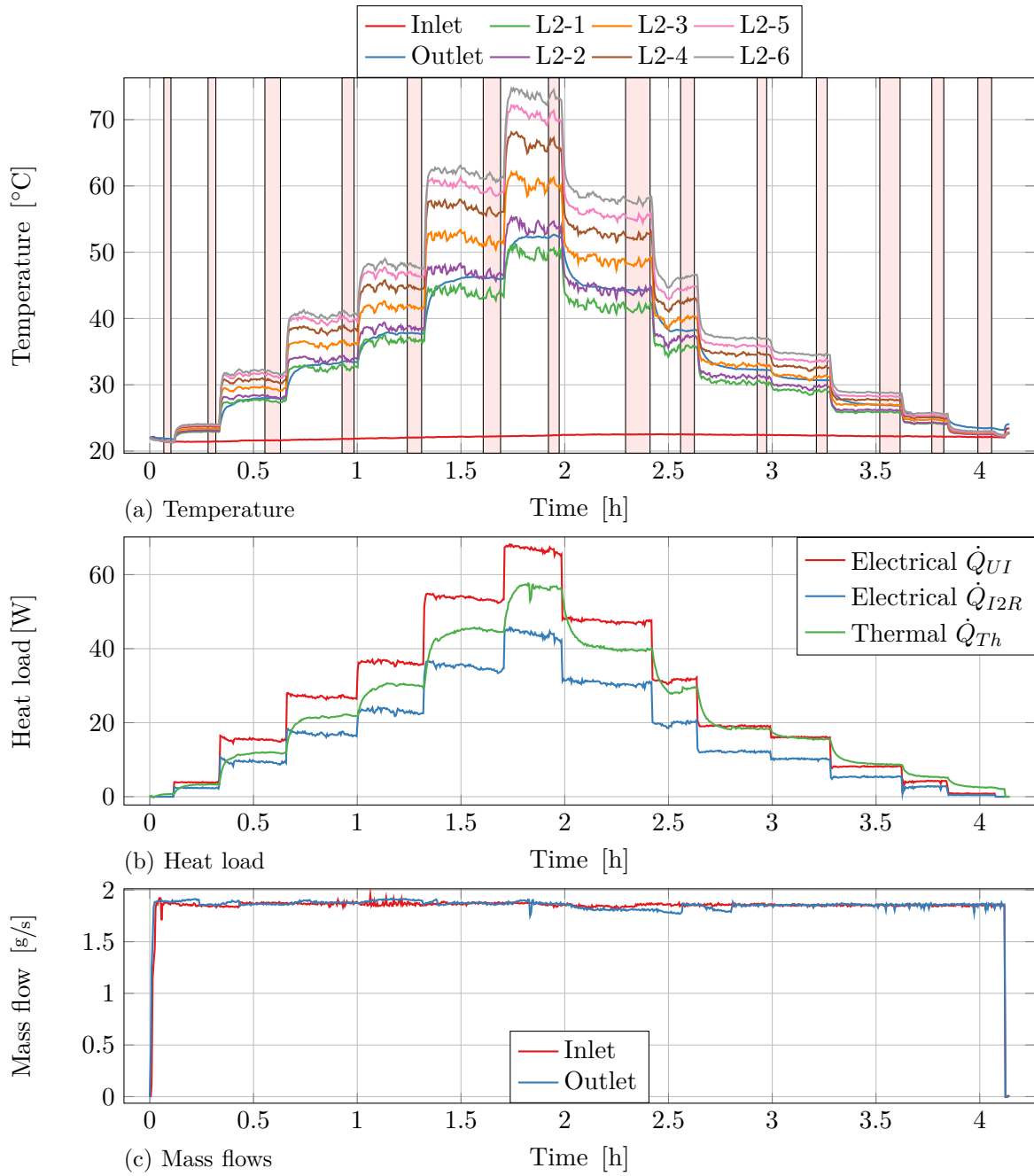


Figure 5.29: Measurement data with constant air flow and different heat loads. The heat load was increased stepwise until the maximum temperature reached 70°C and then decreased again. The red areas are showing the used sector for averaging.

5.6 Results

In this section the measurement results for air and helium are presented. The measurements have been performed with different in- & outlet geometry plates. In section 7.3 the results of the measurements and the CFD simulations are later compared.

From the air measurement there are a lot more data available which have been used for testing of the setup and to investigate different behaviours. Here only the final measurement with the thermal camera are shown. The temperatures of layer 1 are not displayed because the thermocouples fell off the layer during the change of the in- & outlet plates and therefore cannot be compared with the newer results. The temperature range and behaviour on layer 1 were similar to the one on layer 2.

The measurement setup has some deviation from the Mu3e experiment or major measurement errors which are summarised here:

- The leakage flow is estimated to be around 15%. This loosen hot fluid and recuperated cold fluid are affecting the measurement. But the conditions in the Mu3e experiment are quite similar which makes the results comparable.
- The heating is applied with tape heater and not directly inside of the MuPix chips. Also, the higher dissipation of the periphery could not be applied.
- The thermocouples are glued onto the layer and are changing their heat capacity. Which will slower the heating time of these chips and lead to lower temperatures.
- Three different heat loads measurements were defined, here only the heat load based on the current and resistance is shown. This heat load is probably 30% too low and is taken as worst case.
- One half shell was coated with a black colour with a high specific emissivity which is enhancing the radiation.

5.6.1 Thermal imaging

The results from thermal imaging were used to estimate the minimal, mean and maximal temperature present on layer 2. Here the temperature distribution on the layer are discussed. Figure 5.30 is showing the temperature of the measurement with air with the mass flow and similar heat load. The highest temperatures is at the beginning and end at the interposers. The original case shows a high temperature area in the middle of the displayed area. At this position a backflow region was detected in the CFD simulations. For the optimised geometry, this area is shifted further downstream and has also lower temperature. The difference achieved by the simulations between both geometries is a more uniform flow over the circumference for

the optimised part. This results in a more uniform cooling and less backflow regions. This behaviour can also be observed with this measurements.

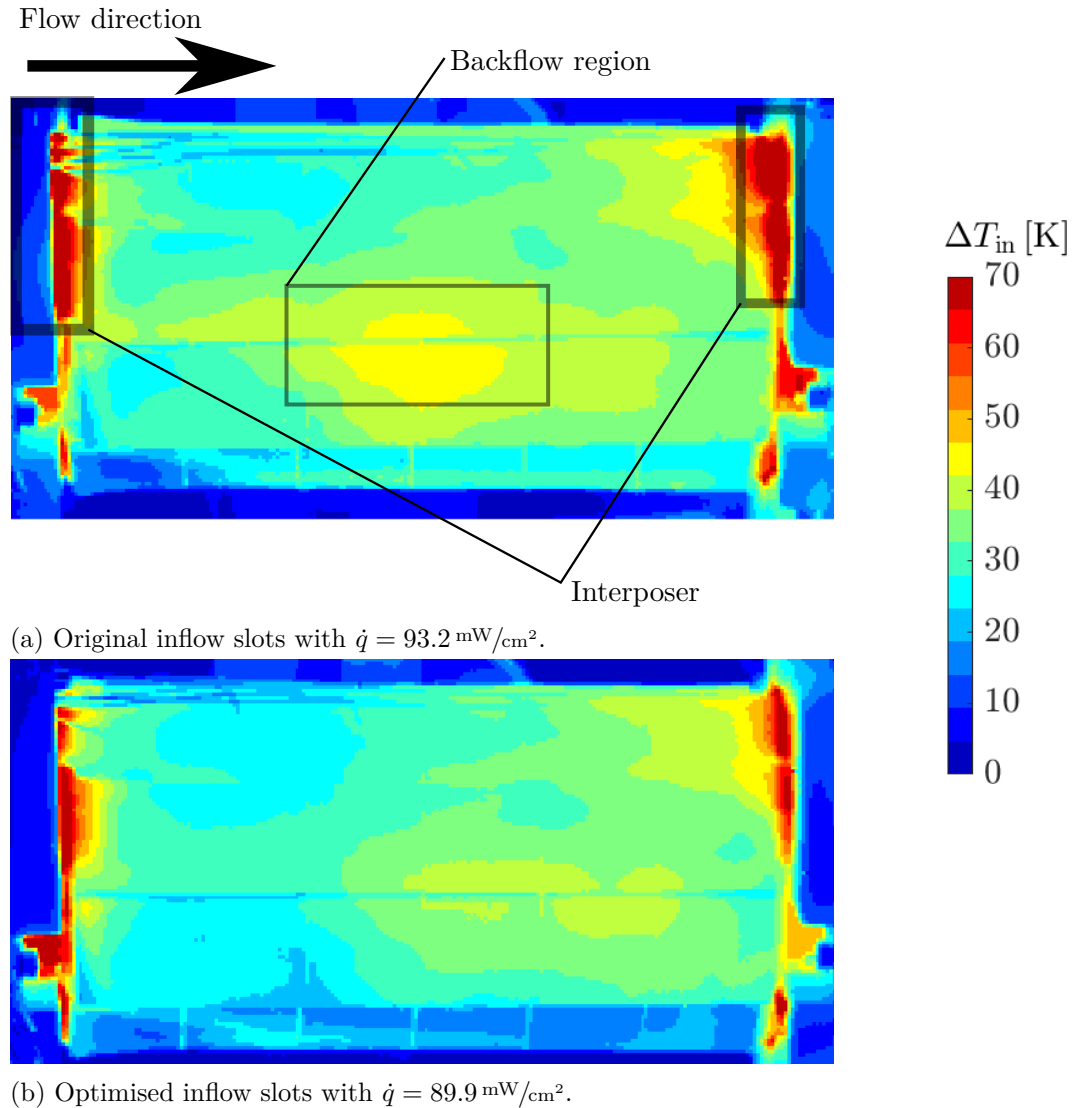


Figure 5.30: Comparison of temperature distribution on layer 2 with air.

The temperature profile measured with helium has some differences to the one of air. Firstly, the highest temperature of the layer is on the overlap as shown in figure 5.31. This difference is due to the different proportion between wall heat transfer and the heat conduction in the solid also known as Biot number. The wall heat transfer of the helium is around six times higher than the one of air for this case, whereas the heat conduction in the chips stays constant.

Another aspect is the temperature distribution over the circumference. Here three layers are fully displayed ((A), (B), (C)). (C) shows the highest temperatures which is probably due to

the backflow region which has also be seen with air.

The highest temperature difference to the inlet is in a range of $\Delta T \approx 75$ K with a heat dissipation of 390 mW/cm^2 . This would lead to a temperature in the Mu3e experiment for the worst case of $\sim 80^\circ\text{C}$ as the inlet will be set to 4°C .

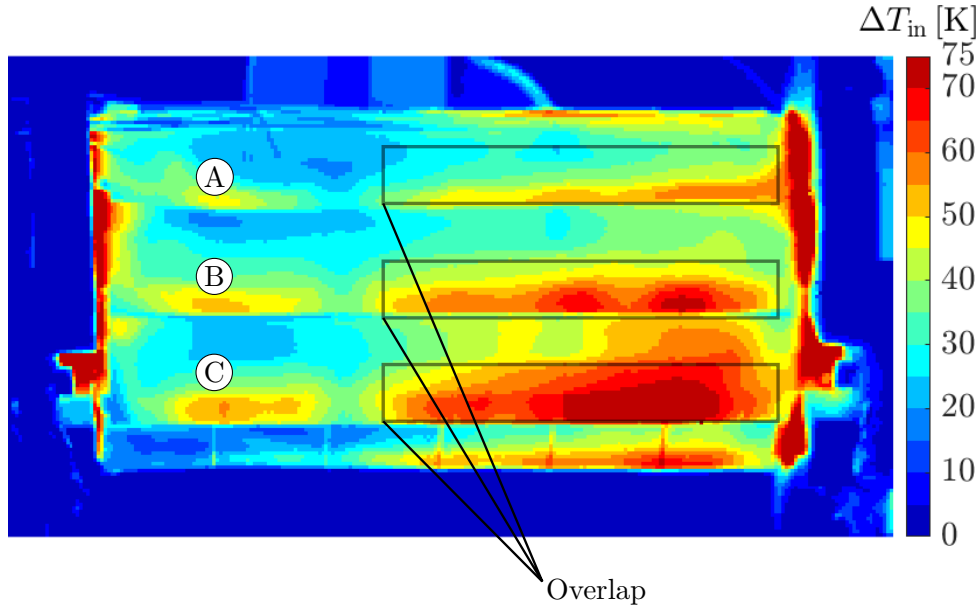


Figure 5.31: Temperature distribution on layer 2 with helium, optimised inflow slots and $\dot{q} = 390 \text{ mW/cm}^2$.

5.6.2 Temperature dependent on the heat load

Three measurement results are discussed here, whose differences can be seen in the following list:

- Air measurement with original geometry.
- Air measurement with optimised geometry.
- Helium measurement with optimised geometry.

Figures 5.32 to 5.35 are showing different temperatures dependent on the heat load. The equivalent heat load per surface is additionally showed as x-axis at the bottom. The temperatures are all relative to the inlet temperature (except the inlet temperature). The temporal change of the temperature and mass flow of the data used here is shown in the appendix C.2.

Figure 5.32 shows the measurement with air and the original inlet plate. It can be seen that the temperatures are increasing linearly which has also be seen in the CFD simulation. The measurement uncertainty of the thermal camera is specified in the data sheet and is constantly 1 K. For the thermocouples the measurement uncertainty of the whole measurement chain is

shown. The measurement uncertainty of the heat load was not evaluated, but the one showed here can be seen as worst case limit⁴. From the thermal camera the minimum, maximum and average temperature are plotted. It can be seen that the maximal temperature of the thermal camera exceeds the highest temperature measured on a layer about 30%. The temperature of the MuPix chips on layer 2 are increasing with their position number, which makes sense as the cooling flow temperature is increasing along the flow direction. Chip number 1 is deviating from this behaviour, which has also been seen in the CFD simulation and will be compared later on. From the outlet temperatures #2 deviates from the other which is due to the repaired tape heater explained in section 5.2.1 on page 89. The inlet temperature stays constant over the whole measurement time.

Figure 5.33 compares the measurement with the original and an optimised inlet plate. The full measurement of the optimised plate is shown in figure C.1 on page 193. The temperatures with the optimisation show the same behaviour as the original plate but with a slightly lower temperature for the same heat load. The measurements with the thermal camera are showing a difference of ~ 3 K at a heat load of 45 W. The chip temperatures show also a lower temperature for the optimised part which is smaller.

Figures 5.34 and 5.35 are showing the results obtained with helium. The first measurement had a mass flow of around 2 g/s compared to the second one with 1.5 g/s. The bottle for the second measurement had another valve as the first one and 1.5 g/s was the highest mass flow reached. The inlet temperature is varying compared to the air measurements which is due to the Joule-Thomson effect and the cooling of the bottle. The measurement points were sorted by the heat load and have been measured in another order. This also explains the jump in figure 5.34b as these two similar points were measured with different mass flows.

With both measurements the maximal heat load was around 200 W resulting in a heat load per surface of 400 mW/cm^2 which is the worst case. The maximal reached temperature is around $70 - 80^\circ\text{C}$ and was measured by the thermal camera.

⁴Compare with section 5.5.1.

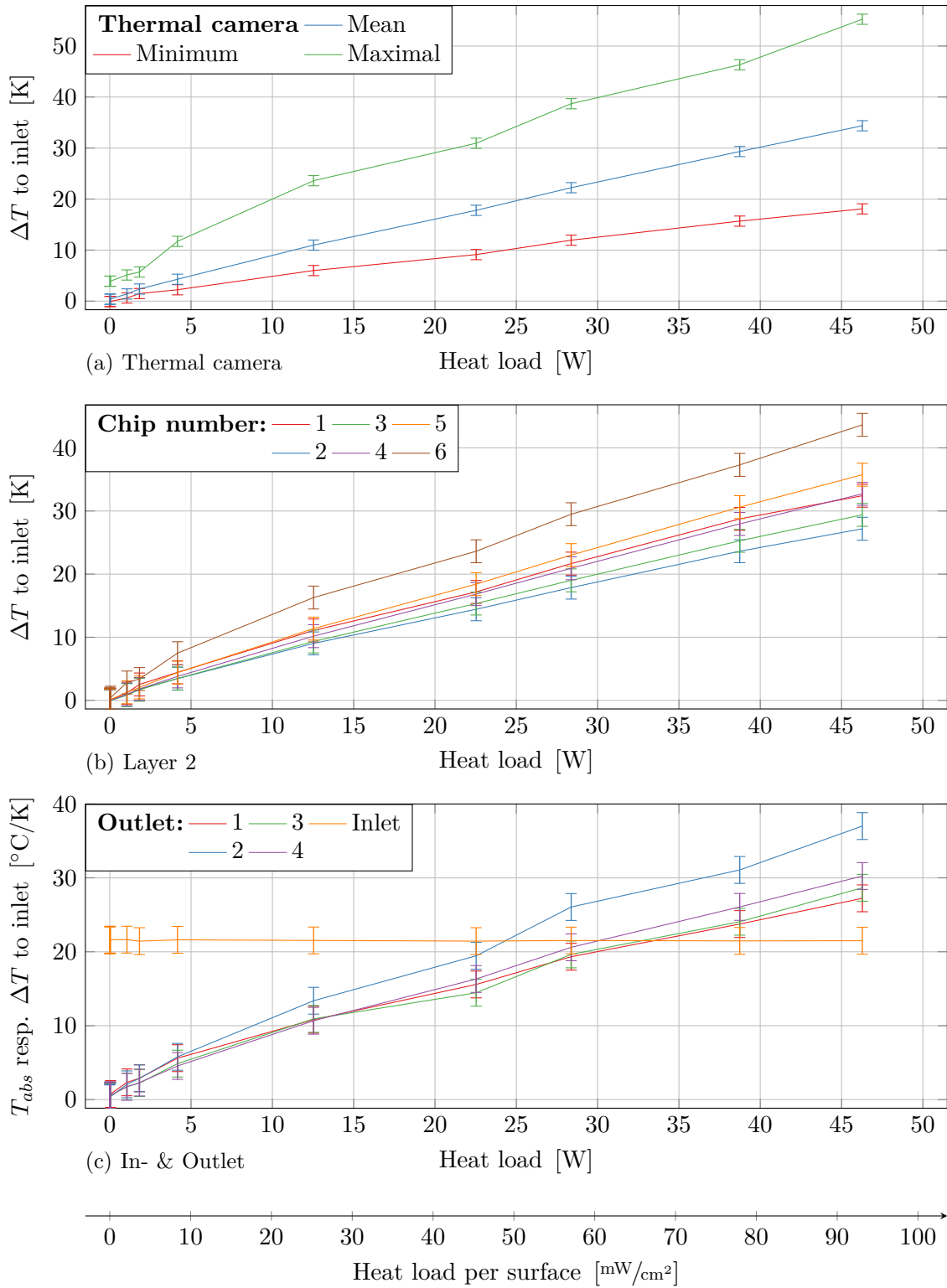


Figure 5.32: Temperature dependent on the heat load with an air mass flow of 1.87 g/s and original inlet plate.

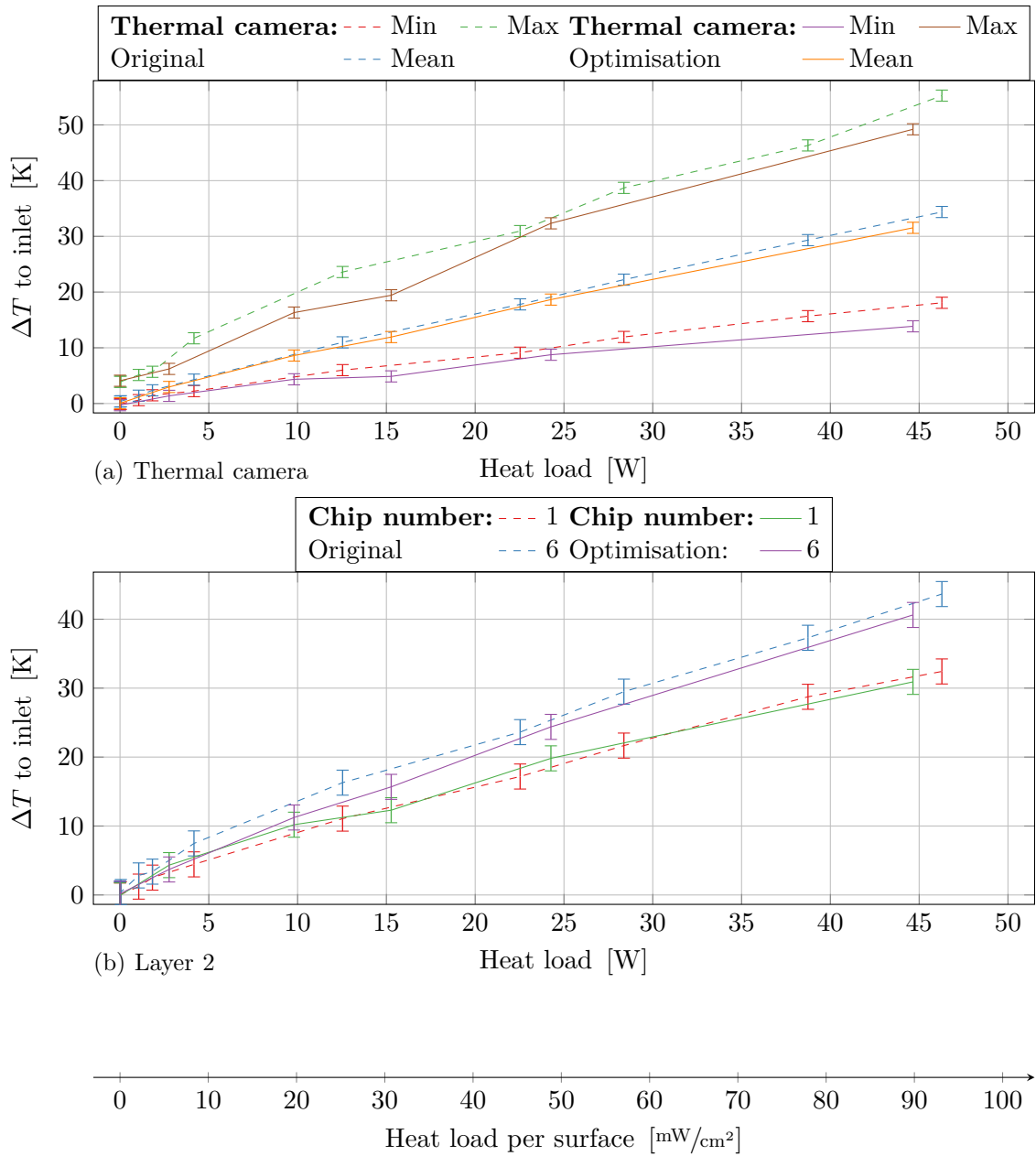


Figure 5.33: Temperature dependent on the heat load with an air mass flow of 1.87 g/s comparison of original and optimised inlet plate.

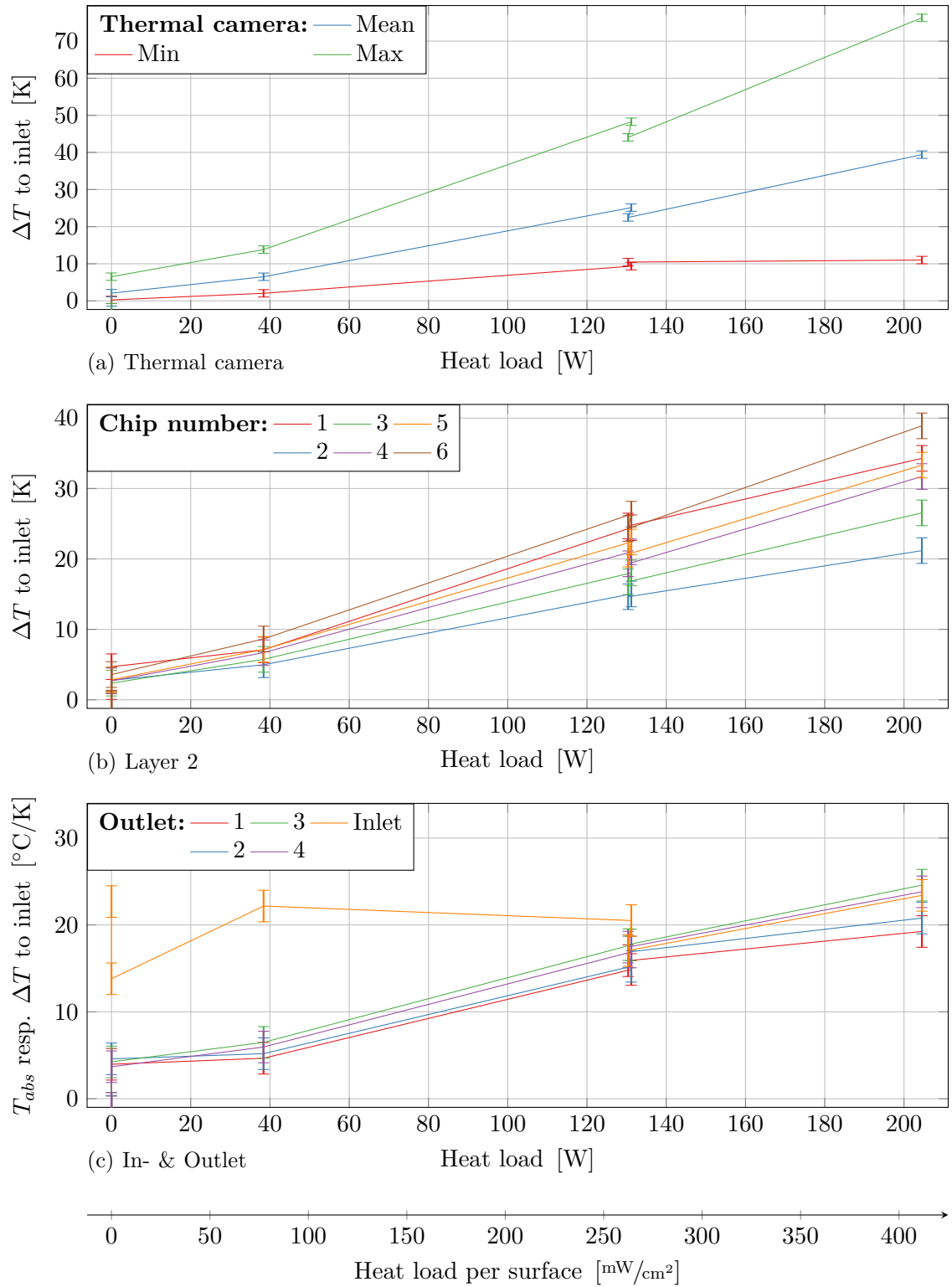
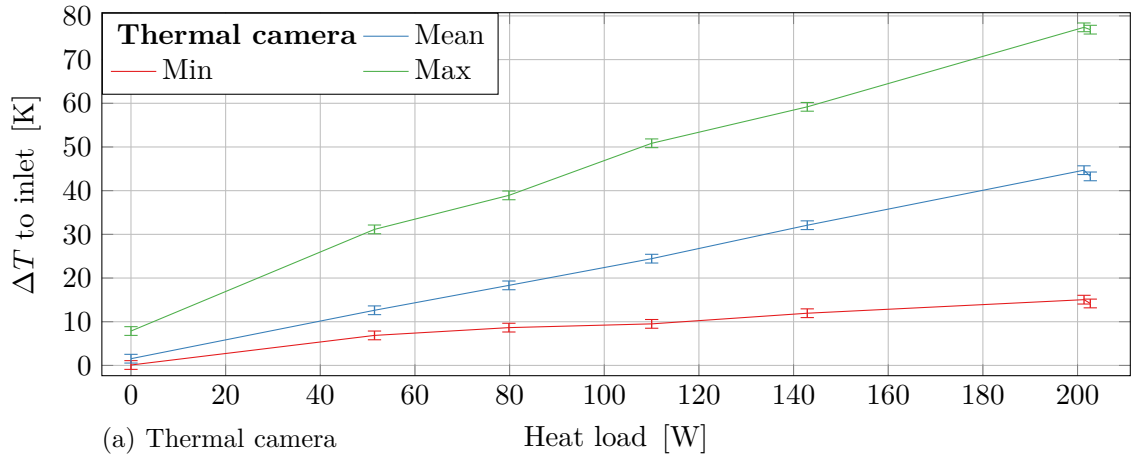
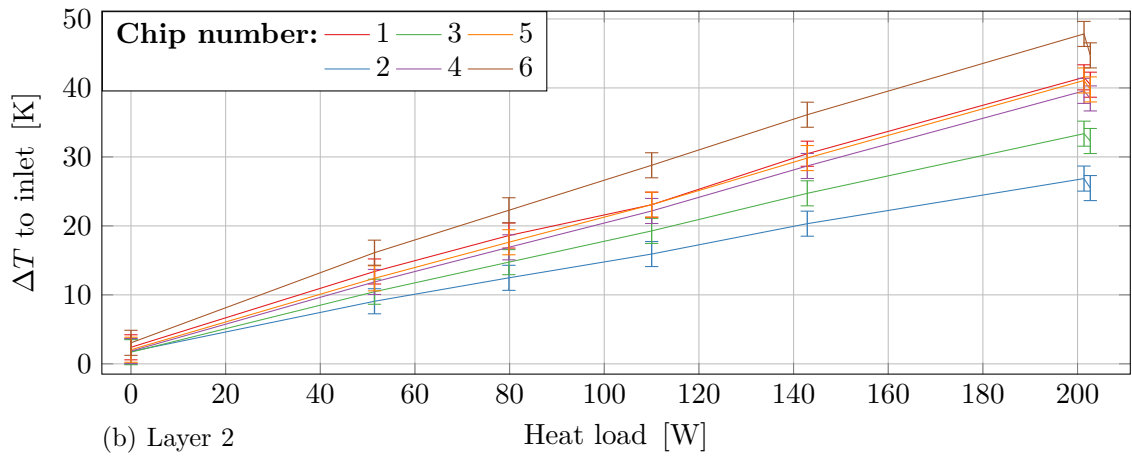


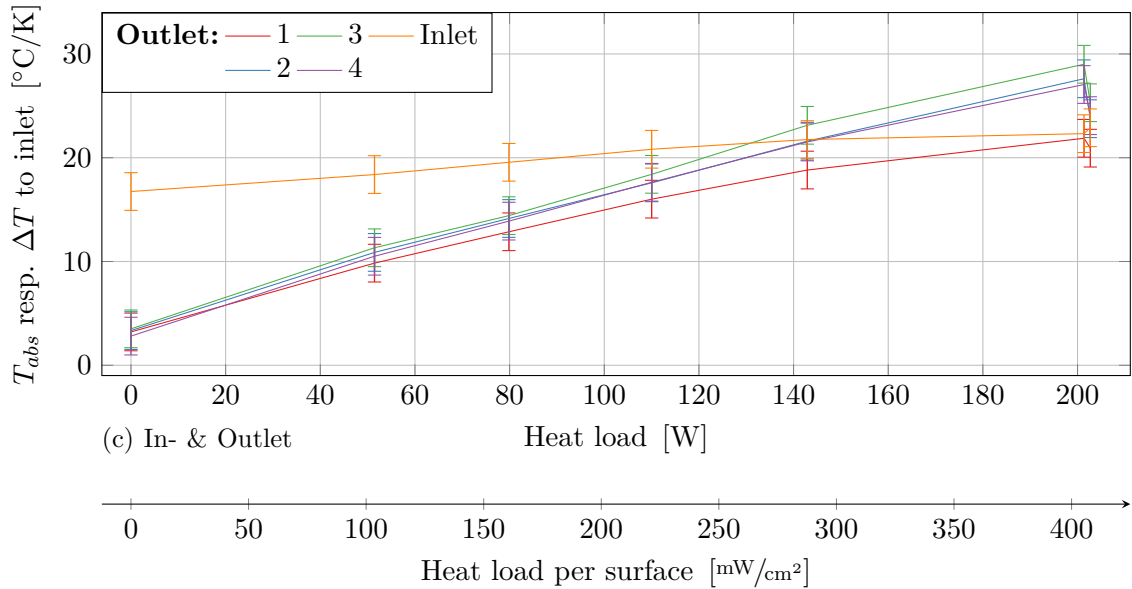
Figure 5.34: Temperature dependent on the heat load with an helium mass flow of $\sim 2 \text{ g/s}$ and optimised inlet plate.



(a) Thermal camera



(b) Layer 2



(c) In- & Outlet

Figure 5.35: Temperature dependent on the heat load with a helium mass flow of ~ 1.5 g/s and optimised inlet plate.

5.6.3 Discussion

In this chapter the measurement setup and instrumentation were shown in detail to facilitate further measurement which are planned for the layers 3 & 4.

The suction at the outlet of the mockup was a challenge with helium, as a volumetric flow of $45 \text{ m}^3/\text{h}$ had to be sucked away. Different vacuum pumps, side channel blowers were tested to obtain the required mass flow. The best option for air and also for helium was a vacuum pump. The mockup required also several modifications as one tape heater had a fissure and the end piece flex ripped due to large connectors. The fissure could be repaired after several attempts but caused higher heatings in front of one outlet. For the end piece flex a connector plate was constructed which prevented damages on the flexes.

The pressure measurement with helium was higher than the expected range obtained from the simulations and could therefore not be evaluated. The higher pressure drop is mainly caused by the outlet thermocouples which were placed inside of the tubes. From the measurement block the thermocouples were placed $\sim 50 \text{ mm}$ further upstream to fasten the reaction time. With the displacement sensor it was shown that the layer is not displaced while the mass flow at the in- & outlet is equal. The heat load measurement has still to be improved, as some larger differences are present between the used methods.

The results obtained not only showed that the optimised plates from the CFD simulations are decreasing the temperature but also that the intended cooling system is behaving similar to the simulations and expectations. The measured temperatures are showing that a cooling of the MuPix for the layers 1 & 2 is possible in the required range with a constant heat dissipation. The high heat dissipation of the periphery could not be tested, but according to the CFD simulation the temperature will exceed 100°C in the periphery of layer 2. Measurements with the unequal heat load should be performed with the proposed mylar tube over layer 2.

6 System simulation

The main goal of the system simulation is to investigate the transient behaviour of the helium cooling system, which could be extended to the pipes from and to the compressor and heat exchanger. The system simulation also serves the decision of whether the valves must be placed inside the magnet, which requires the selection of special valves that can be used in a strong magnetic field and must be controlled hydraulically or pneumatically. The control system of the valves will mostly be used during start-up and shut-down phase. During measurement the flows will be held constant to not disturb the measurements.

In a first step the flow through layers 1 & 2 is modelling the start-up of the flow. The time constant of the system should be analysed and eventual oscillation of the flow as well as the possibilities of modelling with Simscape. In further steps the whole cooling system could be modelled.

6.1 Approach

There are several approaches that can be used for this task, some of which are listed below:

- Transient CFD simulation with all tubes.
- Experiments with kinematic similarity or real dimensions.
- Physical modelling of the system.
- Estimations.

For this project the physical modelling has been the most suitable as it requires low computational power and can be extended to the complete cooling system.

The Matlab add-on Simscape™ was used for the system simulation which is based on Simulink®. Simscape enables the physically modelling of dynamic systems with physical units and different physical libraries as electrical, fluid and others which can be combined.

6.2 Layer 1 & 2

With the results obtained from the CFD simulation of gap flow between layers 1 & 2 a Simscape model was built to investigate the response time of the whole system. The heating of the layers could be modelled but was not necessary here.

Figure 6.1 shows the Simscape model with different blocks which are explained in the following list. The parts from the inlet to the outlet are representing different flow sections of gap flow between layers 1 & 2 which are also shown in figure 6.2.

Reservoir	At the beginning and end of the system there are two infinite gas reservoirs. The pressure and available mass flow are defined and has be set to 1 bar at the outlet. The inlet provides as much mass flow at every pressure level as required by the mass flow control.
Mass flow signal	The mass flow signal can be individually defined and is passed to a Simulink module which passes the signal to the mass flow control.
Mass flow control	The mass flow control has an infinite gas reservoir and the mass flow signal as input. The pressure at the mass flow control is computed regarding the pressure drops of the following elements and the pressure level of the outlet reservoir.
In- & outlet, Layer	The in- & outlet block are four similar tubes which have a defined length, hydraulic diameter, area, surface roughness and the transition Reynolds number. The layer gap flow is also modelled with the pipe block which is computing the pressure drop based on the moody diagram.
In- & out-flow	The in- & outflow geometry which consists of slots have been modelled using the block called Flow Resistance which has as input a nominal pressure drop, mass flow rate and density. The drop is then computed proportional to the square of the mass flow rate and inversely proportional to the density.
Gas properties	In the gas properties block the gas is defined as perfect, semiperfect or real gas. The properties can be provided as lookup tables or single values for perfect gases. The helium has been defined as perfect(ideal) gas.
Solver configuration	In the solver configuration different setting on the discretisation and memory use can be set. The standard settings have been used with an ode23 solver.

The dimensions were taken from the CAD data with the original in & outflow geometry. Material data are from section 2.4.1. For the in- & outflow a nominal pressure drop had to be defined. The data from the CFD simulation were used for the case with a mass flow of 2 g/s. The mass flow at the mass flow control has been defined with no mass flow at the beginning and a linear increase until the maximal mass flow which is shown in figure 6.3.

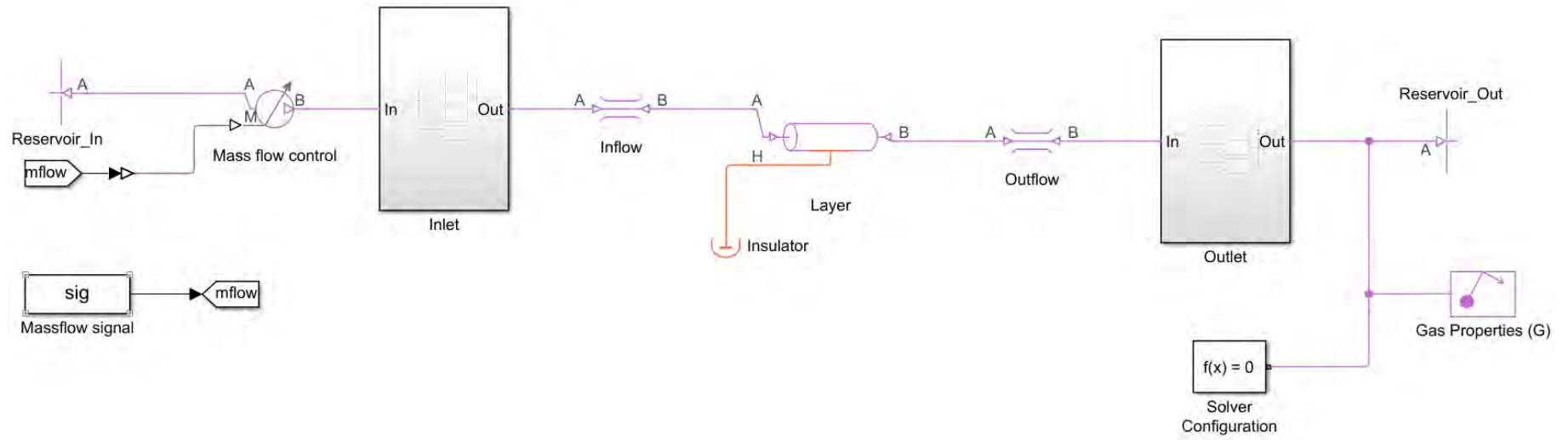


Figure 6.1: Simscape model of flow through gap flow between layers 1 & 2.

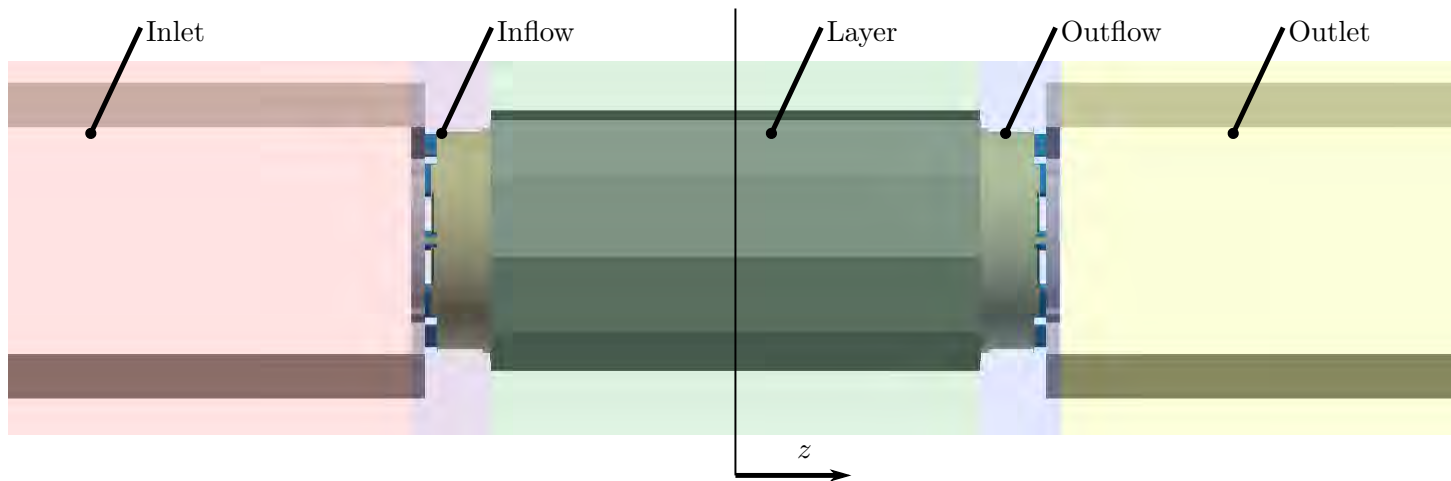


Figure 6.2: Side view of flow parts of Layer 1 and 2.

6.2.1 Results

Figure 6.3 shows the mass flow at the in- & outlet of the system. The inlet mass flow is the one defined by the mass flow control. As the helium is incompressible, the gas in the system is pressed out of the outlet as soon as the valve is opened. The difference between in- & outlet signal is around 0.3 ms which is the time which the velocity of wave propagation (speed of sound) needs to pass the system. The time constant of the system is very low which makes it easy to be controlled in terms of oscillation.

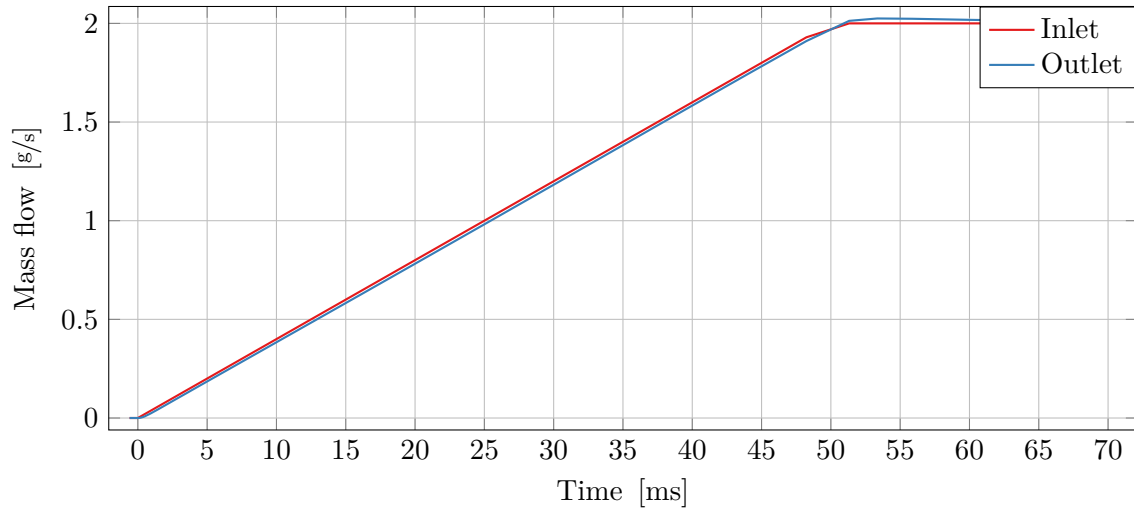


Figure 6.3: Mass flow time dependent at mass flow control and outlet of the system.

Figure 6.4 shows the pressure drop obtained from the CFD simulation with the five different sections which were also shown in figure 6.2. There is also the pressure drop obtained from the Simscape simulation. The pressure drop of the in- & outlet and layer has been simulated very well in comparison with the CFD simulation, as only the dimensional data were defined. The in & outflow are modelled with a block called Flow Resistance which requires a nominal mass flow and a nominal pressure drop. These pressure drops were taken from the CFD simulation so it is not surprising that their fitting very well. The nominal mass flow was set to 2 g/s .

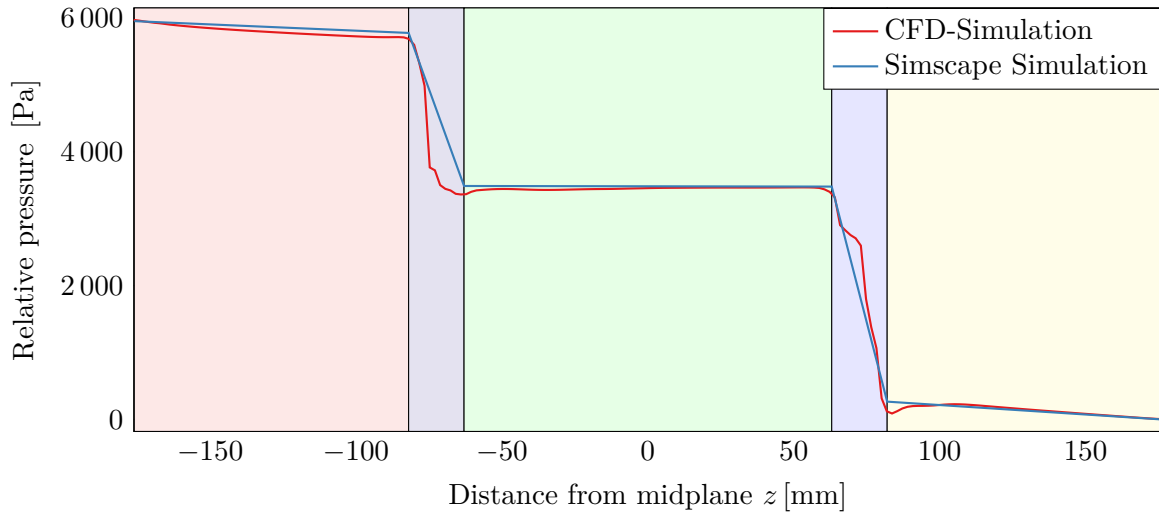


Figure 6.4: Pressure along flow direction from CFD- and Simscape-simulations with 2 g/s.

As data for different mass flows from the CFD simulations were available, those were compared to the one of Simscape to analyse if the modelling is predicting the pressure drops for different mass flows well. Figure 6.5 shows the pressure drops with lowest and highest mass flows compared to the simulated results. With a mass flow of 10 g/s the Reynolds number is in a transitional region and is influenced by turbulence. The pressure drop at low mass flow and laminar flow is predicted very well compared to the CFD data. For the higher mass flow there are some differences which could be due to the more complex computation of the pressure drop of a turbulent flow.

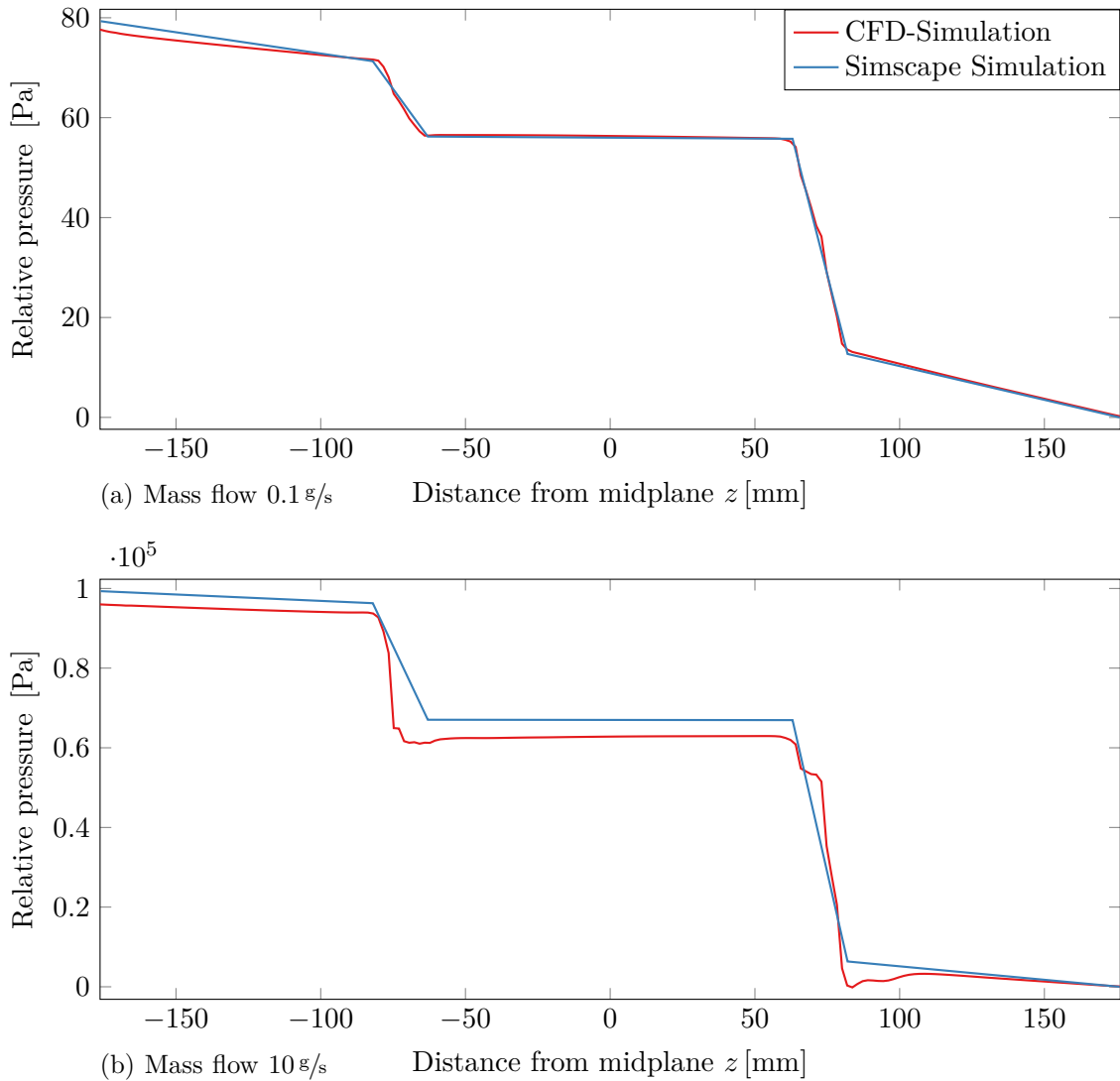


Figure 6.5: Pressure along flow direction from CFD- and Simscape-simulations with different mass flows.

The results obtained with the Simscape model show good agreement with the CFD results and are consistent in terms of pressure drop. The main goal to investigate the transient behaviour has been accomplished and showed that the control is not depending on longer tubes. The valve can easily be placed outside the magnet as the pressure change propagates at the speed of sound.

Simscape could also be used for a simulation of the whole cooling concept to investigate optimisation potential but first the whole cooling system had to be designed which is described in the next section.

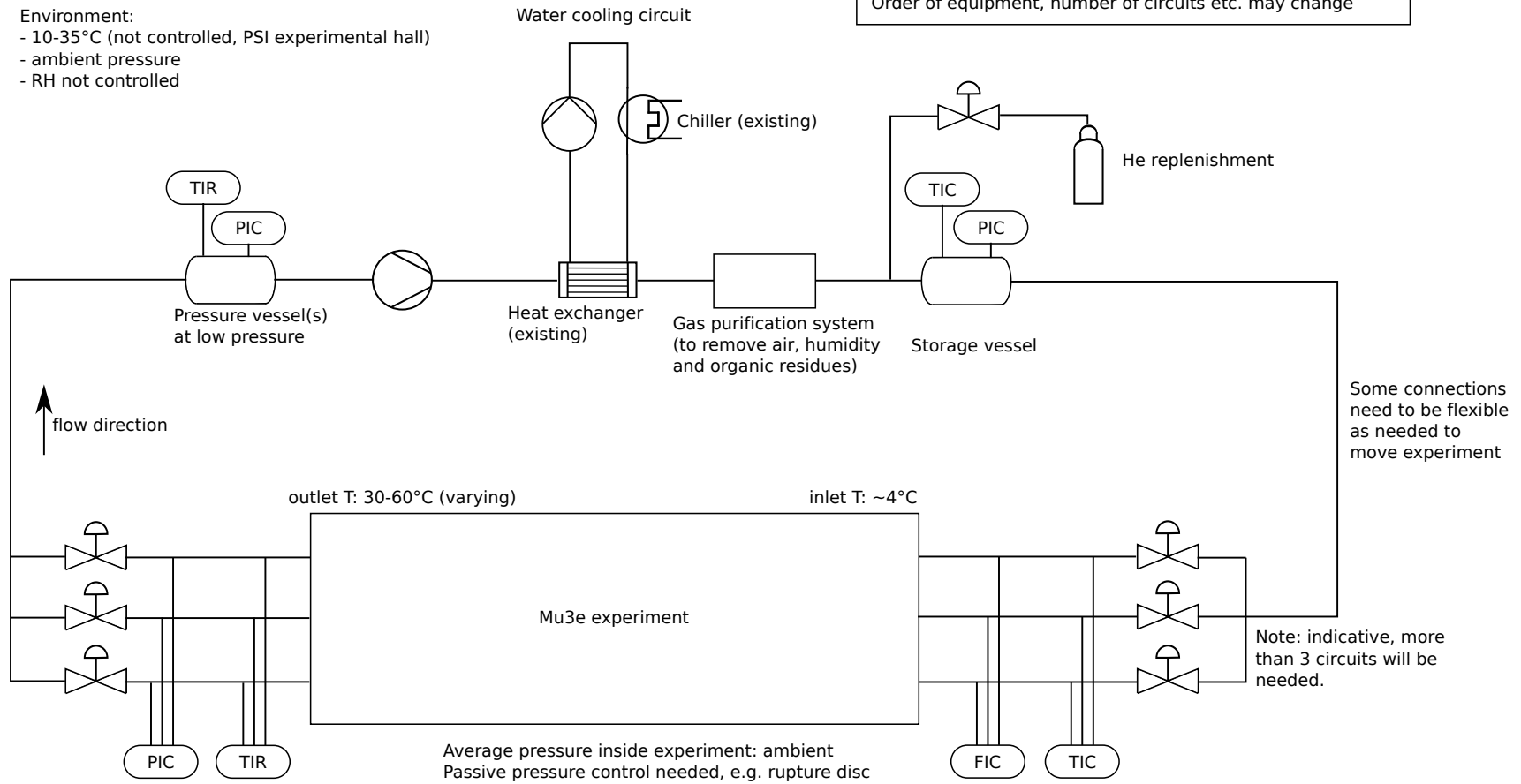
6.3 Cooling plant concept

The cooling concept has been developed by Frank Meier Aeschbacher with some inputs that came from the present thesis. Figure 6.6 shows the current system with the Mu3e experiment as black box with in- & outlet. Behind the experiment some low pressure vessel is foreseen for G12 and V34 followed by a compressor or ventilator. The helium is cooled by a water cooling circuit, purified and then refeed to the experiment. At the in- and outlet there are mass flow regulators for the different flows. The concept is not finalised and needs some further investigations.

Mu3e helium gas cooling system – concept

Environment:
 - 10-35°C (not controlled, PSI experimental hall)
 - ambient pressure
 - RH not controlled

Important note:
 This is a conceptual sketch to develop the full cooling system
 Order of equipment, number of circuits etc. may change



1.40

Figure 6.6: Gaseous cooling concept for the supply of cold helium with storage, over- and underpressure, chiller and regulation. [27]

7 Comparison of results

7.1 Simplifications

The different analysis of the cooling system necessitated simplifications to enable feasible approaches. Table 7.1 shows a comparison of the simplifications and for which analysis they were neglected. Most important is the comparison between CFD simulations and the measurements. The simulation mainly neglected the leakage current, the displacement of the layer and the tolerances of the geometry. On the other hand the measurements could not investigate the unequal heat load inside of the MuPix chips.

Table 7.1: Summary of simplifications of different analysis.

	CFD	Measurements	System	Heat transfer estimation
Leakage	×	✓	-	×
Unequal heat	✓	×	-	×
Silicon chip material	✓	×	-	×
Natural convection	×	✓	-	×
Heat radiation	×	✓	-	-
Ideal gas	✓	×	✓	-
Stationary flow	✓	×	×	×

7.2 Wall heat transfer coefficient

The local wall heat transfer coefficient was first computed with correlations from the VDI-Wärmeatlas [14]. From the CFD simulations the coefficient could also been analysed in dependence of the position along x . At very low x -values the coefficient is high due to the lack of thermal boundary layer. This is displayed in figure 7.1. The simulation results show the average coefficient value of a slice at the specific x and have also a decrease of the coefficient along x . The original geometry has lower values than the benchmark case due to the irregular flow inside the gap. Both simulations are showing some jumps whenever one chip finishes and another begins, which is also only an effect of the thermal boundary layer, as the inner walls are perfectly flat.

The similarity of the benchmark case to the optimisation shows quite well, that the heat transfer modelling is accurate. The dependency of the heat transfer coefficient on the mesh size was not investigated but due to the differences seen by the mesh size study, a dependence is also expected.

The wall heat transfer obtained by the measurements was not investigated but will show a similar behaviour and magnitude as the occurring temperatures are also in good accordance.

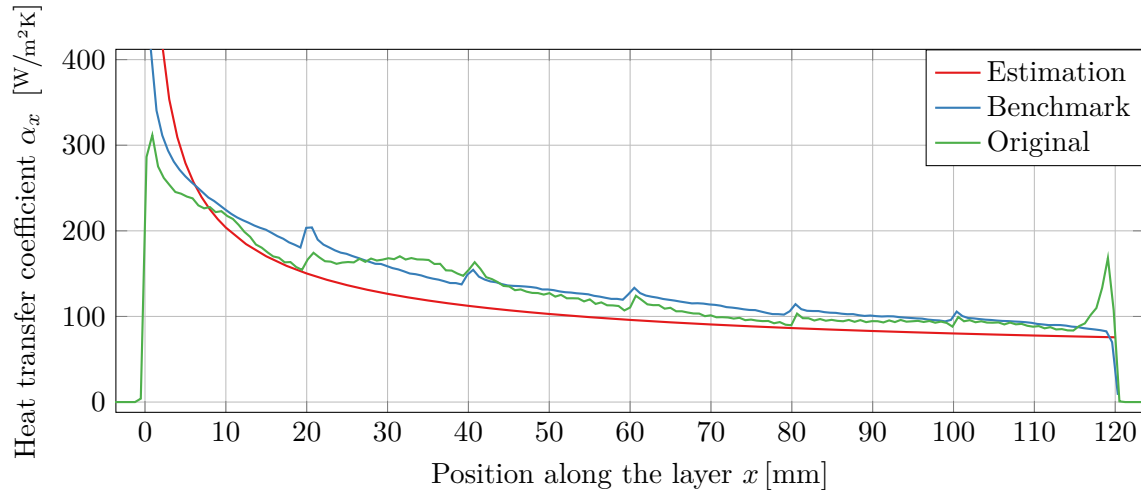


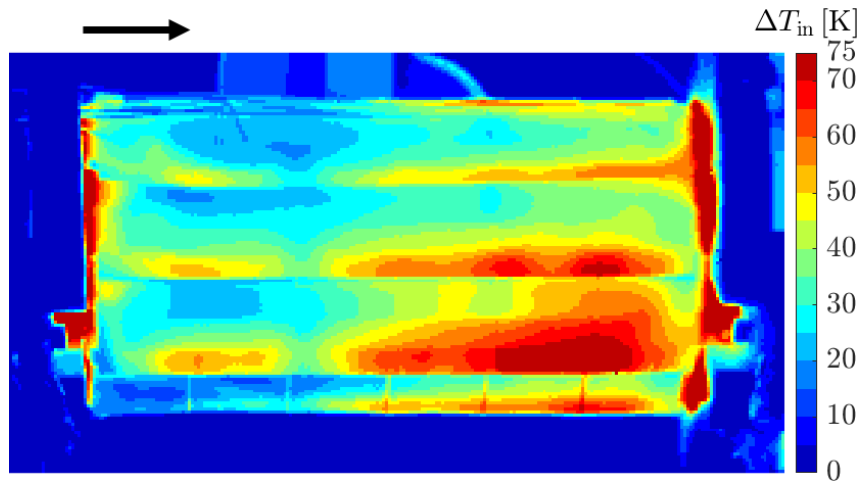
Figure 7.1: Local wall heat transfer coefficient from estimation and CFD simulations of G12.

7.3 Temperature distribution

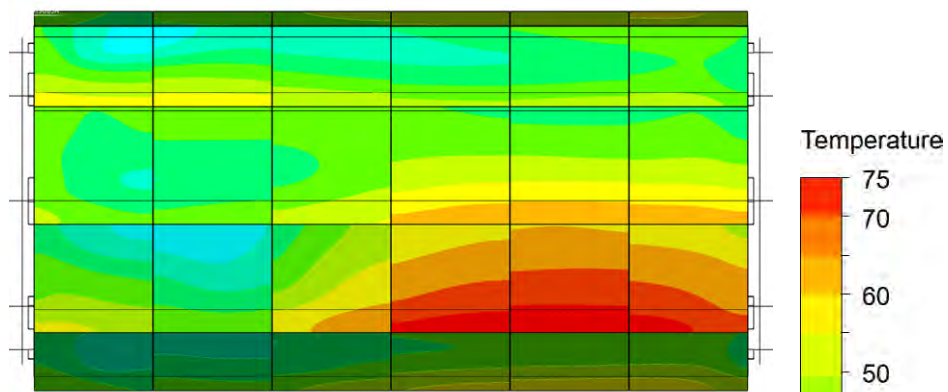
Figure 7.2 shows the same view on layer 2 obtained from measurement and CFD simulations. The measurement shown in figure 7.2a has high temperatures in the overlap which is also present in figure 7.2b. The temperature range of both cases are matching quite well, but there are two differences between those results. Firstly, the measurements was performed with optimised inflow plates compared to the original one in the first simulation. Secondly, the heat load is very well defined for the simulation but lacks of precision for the measurements and could be up to 30 % higher.

Comparing the results from measurement with the optimised simulation, the simulation has lower temperatures and also less overheated overlaps. As the measurement has a leakage flow and uncertain heat load measurement, a direct comparison is difficult. The temperature range of the simulation is around 15 K lower than for the measurement.

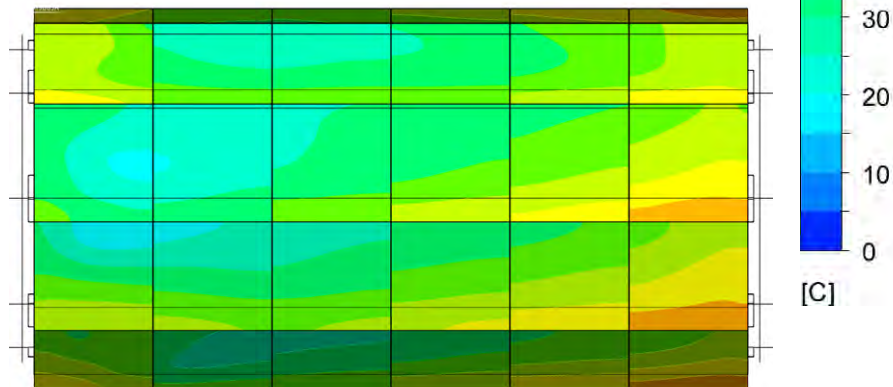
A measurement with the original inflow geometry with helium was not performed due to the high costs, so a comparison of the temperature profile is not possible. For air the temperature distribution could be compared between both geometries and showed a lower temperature for the optimised case which is shown in section 5.6.1 on page 124.



(a) Measurement - optimised inflow geometry.



(b) CFD - original inflow geometry.



(c) CFD - optimised inflow geometry.

Figure 7.2: Comparison of temperature distribution obtained from CFD simulations and measurement with a helium mass flow of 2 g/s and a constant heat load of 400 mW/cm^2 .

7.4 Dimensionless temperature

To enable a comparison of the measurements with air and helium, a dimensionless temperature has been defined following

$$\Pi_{TQ} = \frac{\Delta T \cdot \dot{m} \cdot c_p}{\dot{Q}}. \quad (7.1)$$

Figure 7.3 shows the dimensionless temperature of the chips of layer 2 measured with the thermocouples. The dimensionless temperature is heat load dependent and decreases with higher heat loads. This could be due to higher radiation losses. At high heat loads the curves seem to reach a constant level. To compare the different measurement and simulation results, the dimensionless temperature at high heat loads were compared.

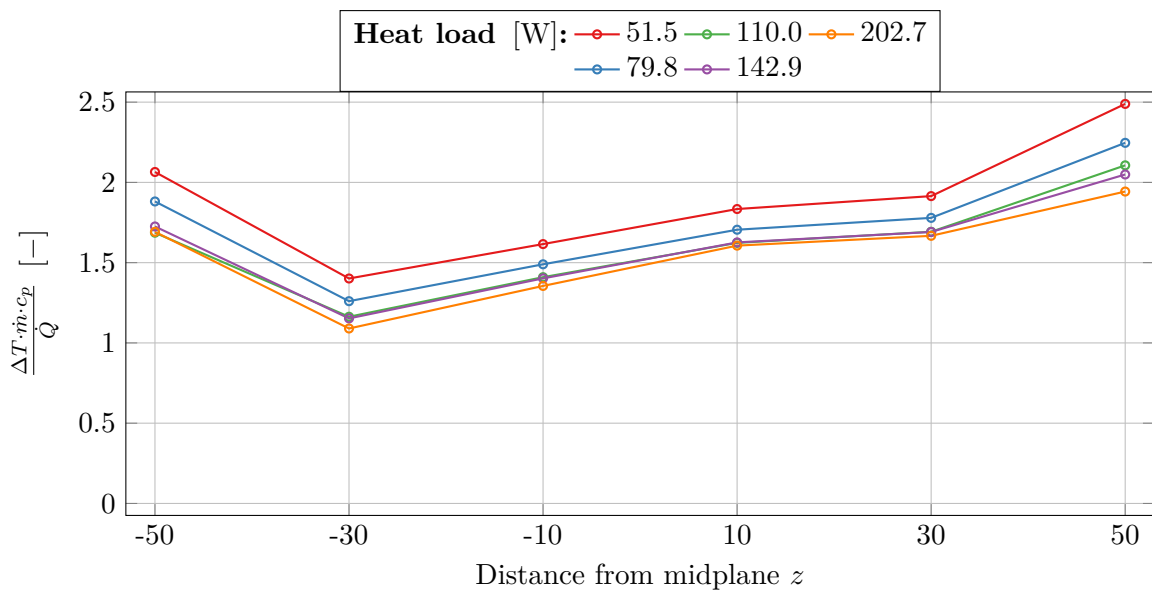


Figure 7.3: Example of different heat loads for the helium measurements.

In figure 7.4 the dimensionless temperature of all the air and helium measurement and simulation are shown. The highest heat loads were used for this comparison because the data seems to converge to one curve at high heat loads which were around 45 W for air and 200 W for air. The measurement data are showing a similar temperature profile over the length of layer 2. The temperature at the beginning is higher due to the irregular flow from the flow slots and increasing from $z = -30$ mm again. Same behaviour was also obtained by the simulations. The air measurement with a higher mass flow differs to the end of the layer which is due to the worse cooling per mass flow. This dimensionless temperature is showing that the design of experiment worked quite well as the data of air and helium are consistent.

Between the curves of the simulation and measurement there are some deviations, explained in the following list:

- The original plate shows higher temperature to the end of the layer compared to the optimised plate. This difference is not present in the dimensionless temperature of the measurement.
- The dimensionless temperature of the measurement is also higher than for the simulations. This could be due to the changed heat capacity of the chips with the glued thermocouples on it.

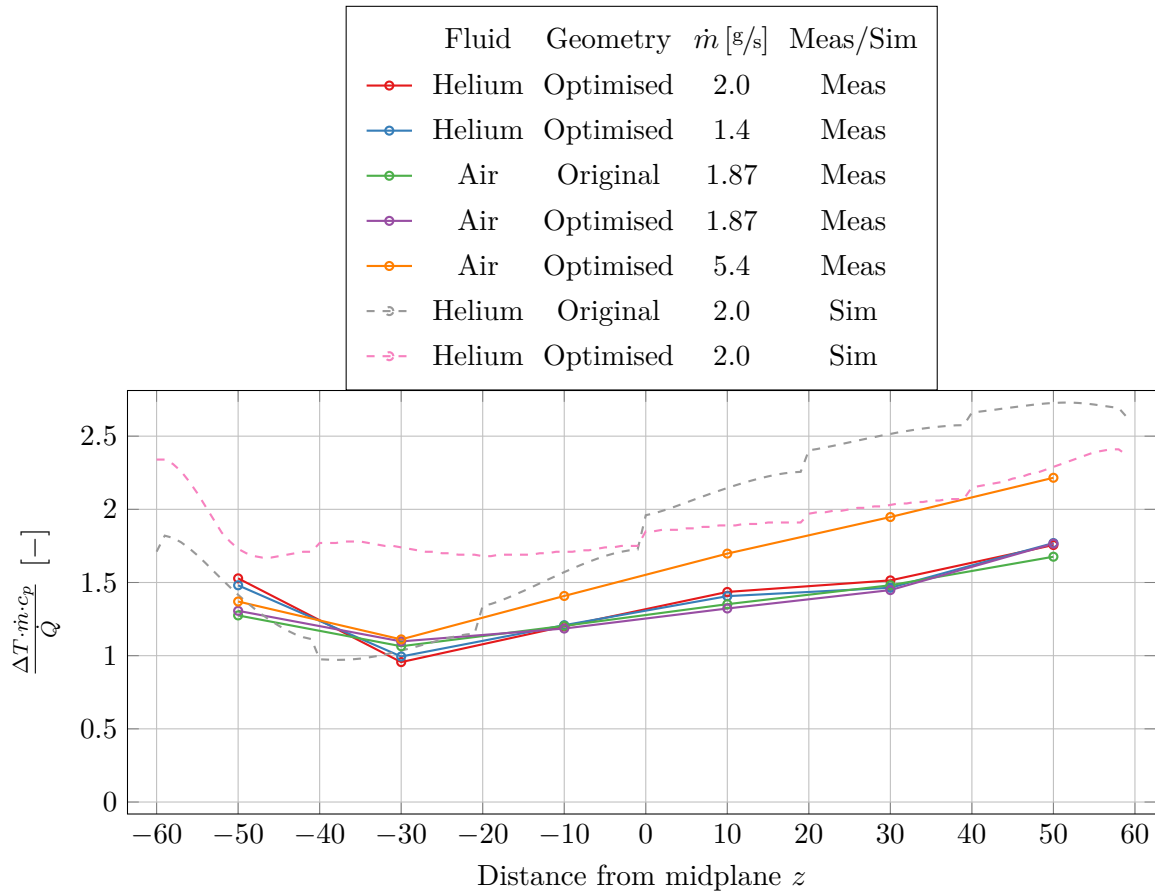


Figure 7.4: Dimensionless temperature of different measurement setups and simulations.

7.5 Discussion

The comparison shows that the simulation and measurement have quite similar behaviour and temperatures. The simulation shows good agreement with the estimation of the wall heat transfer coefficient and also the temperature profile of layer 2. This is enhancing the trust into the results of the simulation.

8 Summary and Outlook

The helium cooling system of the Mu3e experiment has been analysed in this thesis. The cooling system is required to cool thin MuPix detectors under 70°C with a heat dissipation up to $400\text{ mW}/\text{cm}^2$. Overall a maximal thermal heat of 5 kW must be cooled in the entire detector.

At first the cooling system was analysed with an analytical study of the flow between layers 1 & 2. The estimations have shown that such a heat dissipation in an annular gap flow could be cooled under 70°C with helium. It was also shown that the MuPix chips should be modelled in the CFD simulation as parts of the MuPix chips are not directly cooled which results in a higher temperature. Additionally, the periphery part of the MuPix has a higher heat dissipation than the detector part, which is also emphasising the modelling of the whole chips.

Based on the estimations a CFD simulation model was built for layers 1 & 2 and also the more complex layers 3 & 4. Layers 1 & 2 were first investigated as results from previous work were available from Tormann [6] which used a simplified geometry. The flow behaviour observed by Tormann could be reproduced and showed good agreement. The backflow region which leads to higher temperatures of the layers have been reduced by adjusting the inflow plate geometry. The unequal heat dissipation leads to high temperature in the overlap of layer 2, which could not be lessened in the required range by changing the present flow. An additional flow outside of layer 2 showed promising results to cool the periphery.

The cooling of layers 3 & 4 is more complex since 13 flows are involved in total. As the setup of one simulation is time consuming, the flows were optimised separately to obtain more regular flow over the circumference and prevent backflow regions. A mesh study as performed for layers 1 & 2 could not be performed and therefore the results of the heat transfer and the obtained temperatures are more qualitatively trustful than quantitatively. A finer mesh could lead to higher temperatures, but the temperature distribution and flow behaviour will probably not change significantly. Of part B, the optimised and original geometry were simulated and a decrease of the temperature of the MuPix chips for the optimised part was seen. Finally, a simulation of the parts A, B & C was performed sequentially and showed that the highest temperatures are occurring in part C.

A thermo-mechanical mockup of the layers 1 & 2 has been used for the measurement. The mockup has thin steel plates instead of the MuPix silicon chips. Additionally, there is an aluminium resistor inside the tape heaters to imitate the heat dissipation of the MuPix chips. The mockup was equipped with thermocouples on several chips and coated to enable the temperature measurement with a thermal camera. An inductive distance sensor was calibrated with one tape heater and then used to estimate the displacement while a mass flow passed to gap flow. Additionally, the mass flow, pressure and temperature were measured at the in- & outlet. The optimised and original inflow geometry were used to validate the effect of the simulation. The measured temperatures showed to be lower with the optimised plates but could only be measured with air, as there was only short helium measurement time available. The measurement with helium showed that cooling of the layers with a heat dissipation of 400 mW/cm^2 caused a temperature increase of around $70 - 75 \text{ K}$ compared to the inlet temperature, which is slightly exceeding the required range. Additionally, several unexpected effects were described which will presumably be present in the Mu3e experiment and could help in the further development.

As there were some concerns about the control system of the whole helium flow, a system simulation was performed to estimate whether the control valves should be placed in- or outside of the magnet. The results showed that the valves can be placed outside of the magnet, as a change of pressure at the inlet is propagated quickly through the system. In addition it was seen that the pressure drop can be estimated quite well compared to the CFD simulations.

Results of the different analysis were compared and showed similar behaviour but also some differences. It can be concluded that the measurements using air can be compared to the one with helium to some extent. But the costly helium measurements were crucial to test the mockup with higher heat dissipations and higher flow velocities. It was also seen that the high temperature of the overlap is mainly present for helium and not for air. The CFD simulations are a powerful tool to analyse the occurring effects and improve the cooling but cannot replace completely measurements. The measurements have only few simplifications compared to the Mu3e experiment and are therefore more trustworthy than the simulations.

The main difference between the Mu3e experiment and the mockup measurement is the higher heat dissipation in the periphery. The simulation showed that the periphery temperature exceeds $70 \text{ }^\circ\text{C}$ due to the higher heat dissipation. Therefore, the mylar tube is proposed, which enables a flow outside of layer 2, resulting in a maximum temperature of $51 \text{ }^\circ\text{C}$. This has to be implemented to ensure an effective cooling and therefore a good functionality of the MuPix chips.

8.1 Outlook

This thesis worked on several aspects of the cooling system and performed optimisation of cooling components as well as measurements with the mockup of layers 1 & 2. Despite of the progress made, there are still open points which should be further improved. All these tasks are summarised in this section together with the proposed modifications. The tasks within a group are sorted by priority.

8.1.1 Measurements

Heat load

The heat load measurement has been underestimated and showed major differences between the different measurement approaches. The estimation of the losses in the cables, interposers and contact resistances are uncertain and are partly contributing into the heating of the flow. A more precise measurement should be elaborated for further measurements.

Measurement Error

The measurement error was only analysed for the measurement device. Only for the thermocouple measurement the whole measurement chain was analysed. In further research the whole measurement uncertainty should be evaluated following Guide to the Uncertainty in Measurement (GUM).

Leakage

The measurement with the mockup of layers 1 & 2 have shown, that without a suction at the outlet, the leakage over the layer is high. This was expected and was now firstly measured on a mockup. For the gap flows of the layers 3 & 4 no suction can be applied at the outlet, which will cause an inflation of the layers and a leakage flow. The pressure drops of the outlet geometry of the gap flows of the layers 3 & 4 are around 5 mbar for G34 and around 17 mbar for G3S. Compared to the pressure drop of G12 which is around 25 mbar, the drops of the layers 3 & 4 are lower, but will certainly also cause a certain leakage. To reduce this leakage, the outlet geometry into the global flow can be improved, which will result in a lower pressure drop and therefore less leakage flow. Another option is to lower the mass flow, which will decrease the pressure drop but also the cooling capacity. All these pressure drops were obtained from CFD simulation.

Pressure measurement

The differential pressure sensors used for the experiment with helium, which had a range of ± 75 mbar were saturated during the helium measurements. Therefore, the occurring pressure drop could not be evaluated. A measurement of the occurring pressure drops should be performed in regards of the helium cooling plant design.

Helium measurement layers 3 & 4

Measurements with the outer layer will firstly have to be realised with air as coolant. The helium mass flow required can only be provided with a recirculating flow. For this a cooling plant is required, which will have to be allocated for the Mu3e experiment.

Mass flow measurement

The mass flow measurement of helium in an air atmosphere lead to false mass flow measurement at the outlet. If it is intended to use a T-Mass for helium measurement in a air atmosphere, the T-mass should be coupled with a gas analyser to enable the measurement of the real mass flow.

Helium atmosphere

The current measurement setup with helium was performed in an air atmosphere, which lead to an air leakage flow and also false outlet mass flow measurements. This leakage causes lower cooling capacity and does not represent the conditions present during the Mu3e experiment. A measurement in a helium atmosphere will only be reasonable as soon as the helium cooling plant is available.

8.1.2 Simulation

Layers 3 & 4 - optimisation

The optimisation of the layers 3 & 4 were performed on part B and then adopted onto parts A & C. For the flow G3T no optimisation was performed. Therefore, this flow could still be improved to obtain a better cooling.

Different domain turbulence model

For the flows of layers 3 & 4 only one turbulence model was defined over the whole range as Ansys CFX has not a direct option to apply different turbulence models in one model. Later on, it was found that different turbulence modelling can be chosen for different fluid domains in the Advanced environmental variables. For V34 the Reynolds number is so low that it could be defined as laminar. For G34, G3S & G3T a turbulence model lead to more stable results, but as the Reynolds number is partly under the critical value, a transition model should be considered.

Leakage

The SciFi detector has gaps between each of the detector parts, which will cause a leakage flow into the volume between layer 2 and the SciFi detector. A simulation could be used to estimate the magnitude of this leakage flow. But the leakage flow over layer 3 is not known either, and will influence the leakage over the SciFi. Therefore, a simulation of the SciFi leakage will be difficult.

CFD simulation of the leakage flow over layers 3 & 4 is a huge challenge and will take a lot of resources and the results will be uncertain. This is due to the coupling of layer movement of a very thin construction which is movable depending on the pressure of the flow. To estimate the amount of leakage flow, a measurement with a mockup will lead to better results.

Real gas

The gas behaviour was assumed as ideal gas. During the measurement the Joule-Thompson effect was observed with helium. The helium could be defined as real gas in further simulations to consider the Joule-Thompson effect.

8.1.3 Helium cooling plant

Pressure drops

The pressure drops of the simulation shown are smaller than the one measured with the mockup, which is partly due to the thermocouples placed into the flowing tube. The pressure drop should be investigated with a measurement on a mockup with preferably full inlet tube length and also the connectors and tubes leading out of the magnet. This pressure drop are crucial for the development of the cooling plant and also for the regulation.

8.1.4 Proposed modifications

The proposed modifications are described here. The geometry used for the simulation can be found in appendix D. Those changes will have to be implemented into the current design.

- Mylar tube global flow
- Mylar tube over layer 2
- Inflow slots of layers 1 & 2
- Inflow slots of gap flow between layers 3 & 4
- Guidance plates of gap flow between layer 3 & SciFi
- Inlet diameters of V-fold of layers 3 & 4

8.2 Goal

■ **Goal:** Temperature

Comment: The temperature of the MuPix chips has been evaluated with simulations and measurements. For the simulation of layers 1 & 2 optimised parts were developed to ensure a temperature level well below the defined maximum. The measurement shows a similar temperature level, but the crucial heat load measurements are not reliable and should be improved. Optimised parts were also proposed for the layers 3 & 4 which also decreased the temperature in the simulations. This effect could not be measured with a mockup.

■ **Goal:** Verification

Comment: The results found in previous thesis could be verified and similar behaviour of the flow were observed.

■ **Goal:** Validation

Comment: The results of the simulation have been compared with the one obtained from the measurements. The obtained temperature levels and flow behaviours from the CFD simulations could also be observed to some extent in the measurements. The simulation and measurements could still be improved to reach a better consistency.

■ **Goal:** Optimisation

Comment: The flows of the layers 1 & 2 and layers 3 & 4 have been analysed and changes to enhance the cooling were proposed.

■ **Goal:** Instrumentation

Comment: The mockup of the layers 1 & 2 has been instrumented for measurements with focus on the temperature measurement. However, different issues were found and changes for the further ongoing have been proposed. The instrumentation was documented extensively to simplify the instrumentation for the layers 3 & 4.

■ **Goal:** Thermal deformation

Comment: The thermal deformation was not directly investigated as there was no layer with silicon chips available. Still some measurements were performed with the mockup. These measurements showed that the layers are very sensitive on pressure levels and also to the temperature.

■ **Goal:** Flow system

Comment: A system simulation of the flow through layers 1 & 2 has been performed and showed that the system behaviour in terms of controllability is good and that the control valves can be placed outside of the magnet. Therefore, no special valves which can be used inside of a strong magnetic field are required. The full system simulation with all flows and heat exchanger was not performed.

■ **Goal:** Control concept

Comment: With the results obtained from the flow system analysis and findings from the project partner, the control concept development was not further followed in this thesis. The focus was put on the CFD simulations and measurements.

8.3 Review

The investigation of the Mu3e cooling system was a very interesting, challenging and fascinating project to work on. The broad range of aspects studied allowed me to gain a broad know-how. Until the complete cooling system is ready, many challenges have to be mastered.

Due to time issues several tasks could not be performed to the planned extent. The obtained measurement data could not fully be analysed. The complete mockup of the layers 1 & 2 was only available by mid December 2018, which left little time to finalise the measurement setup and collect data. With more time, the measurement uncertainties of the heat load and other quantities could have been further assessed. The present heat load measurement has a high uncertainty, which makes a comparison with the simulation difficult. Still the obtained results are showing good accordance between simulation and measurement and emphasise that the cooling of the layers 1 & 2 is realisable with some modifications. For the layers 3 & 4 the mockup was not available until now and therefore only simulation were performed.

Personally I enjoyed this versatile project and I was able to improve my skills in various areas such as measurements, data analysis, CFD simulations and also project management. I was grateful that the communication with the project partner was excellent and led to many helpful suggestions.

Declaration of independence

I hereby declare that I have done the present work independently and have not used any tools other than those indicated. All used text excerpts, quotations or contents of other authors, in particular also contents of the internet were expressly marked as such.

Windisch, 4th March, 2019



Marin Deflorin

Bibliography

- [1] U. Bellgardt et al. “Search for the decay $\mu^+ \rightarrow e^+e^+e^-$ ”. In: *Nuclear Physics B* 299.1 (1988), pp. 1–6.
- [2] Marco Zimmermann. “Cooling with Gaseous Helium for the Mu3e Experiment”. Bachelor Thesis. University of Heidelberg, 2012.
- [3] Lukas Huxold. “Cooling of the Mu3e Pixel Detector”. Bachelor Thesis. University of Heidelberg, 2014.
- [4] Yanwing Ng. “Finite Element Analysis of the Cooling System for the Mu3e Experiment”. MA thesis. University of Applied Science Jena, 2015.
- [5] Adrian Herkert. “Gaseous Helium Cooling of a Thin Silicon Pixel Detector for the Mu3e Experiment”. MA thesis. University of Heidelberg, 2015.
- [6] Constantin Tormann. “Thermal Analysis of the Silicon Pixel Detector for the Mu3e Experiment”. Bachelor Thesis. Department of Physics and Astronomy University of Heidelberg, 2018.
- [7] Andre Schöning et al. *Technical design of the Phase I - Mu3e Experiment*. Tech. rep. 2019.
- [8] E. W. Lemmon, M. L. Huber, and M. O. McLinden. *NIST Standard Reference Database 23: Reference Fluid Thermodynamic and Transport Properties-REFPROP, Version 9.1, National Institute of Standards and Technology*. 2013. URL: <https://www.nist.gov/srd/refprop>.
- [9] John A. Dean. *Lange’s Handbook of Chemistry*. McGraw-Hill Professional, 1998.
- [10] *Datasheet Kapton*. 2017. URL: <http://www.dupont.com/products-and-services/membranes-films/polyimide-films/brands/kapton-polyimide-film.html/> (visited on 10/22/2018).
- [11] *Datasheet 1.4310*. URL: https://www.notzgroup.com/media/wysiwyg/PDF/NME/Datenblaetter/Werkstoffdatenblatt_1.4310_def..pdf (visited on 10/22/2018).
- [12] *Datasheet Araldite AW 106 Resin*. URL: [http://adhesive.leaderseal.com/download/TDS-A106-953\(US\).pdf](http://adhesive.leaderseal.com/download/TDS-A106-953(US).pdf) (visited on 10/22/2018).
- [13] M. Tanabashi et al. “Review of Particle Physics”. In: *Phys. Rev. D* 98 (3 Aug. 2018), p. 030001.

- [14] *VDI-Wärmeatlas (VDI-Buch) (German Edition)*. VDI-Wärmeatlas. Springer Vieweg, 2013.
- [15] Sarang V. Muley and Nuggehalli M. Ravindra. “Emissivity of Electronic Materials, Coatings, and Structures”. In: *JOM* 66.4 (Mar. 2014), pp. 616–636.
- [16] *NEXTEL Velvet-Coating 811-21*. 2nd ed. Mankiewicz. Georg-Wilhelm-Str. 189; 21107 Hamburg, Germany, Oct. 2017.
- [17] Yunus Cengel. *Heat and Mass Transfer*. Fifth Edition. MHS, 2014.
- [18] Sayed Ahmed E. Sayed Ahmed, Osama M. Mesalhy, and Mohamed A. Abdelatif. “Flow and heat transfer enhancement in tube heat exchangers”. In: *Heat and Mass Transfer* 51.11 (Nov. 2015), pp. 1607–1630.
- [19] M. A. Boles Y. A. Cengel. *Thermodynamics: An Engineering Approach*. McGraw-Hill Education - Europe, Jan. 7, 2014. 1024 pp. URL: https://www.ebook.de/de/product/21995048/yunus_a_cengel_michael_a_boles_thermodynamics_an_engineering_approach.html.
- [20] *Handbuch Elektrotechnik: Grundlagen und Anwendungen für Elektrotechniker (German Edition)*. Vieweg+Teubner Verlag, 2008.
- [21] *Datasheet Electrodag 1415m*. URL: http://www.agarscientific.com/media/import/AGG3648_&_9,AGG3692_Jan14.pdf (visited on 12/20/2018).
- [22] *E+H Applicator*. 2018. URL: <https://portal.endress.com/webapp/applicator10/> (visited on 11/20/2018).
- [23] *Datasheet Hysol 9497*. Feb. 2008. URL: http://www.silitech.ch/upload/fiche_technique_D/467.pdf (visited on 11/12/2018).
- [24] First Sensor. *Drucksensoren*. URL: <https://pages.first-sensor.com/differenzdruck-sensor> (visited on 10/22/2018).
- [25] *Datasheet Shunt*. URL: <https://www.knick-international.com/de/products/proline/transducers-for-shunt-applications/maconic/index.html> (visited on 11/10/2018).
- [26] Christoph Gossweiler. *Einführung in die Bestimmung der Messunsicherheit, v17*. Vorlesungsskript.
- [27] Frank Meier Aeschbacher. Personal communication. 2019.

List of Figures

1.1	Task structure diagram.	5
2.1	Detectors of the Mu3e experiment.	8
2.2	Helium cooling system of the silicon chips with detail of the centre part.	10
2.3	One segment of MuPix chips of layers 1 & 2 with 6 Mupix chips.	11
2.4	Temperature of MuPix chips depending on different heat dissipations.	12
3.1	Joule-Thomson coefficient of different gases.	18
3.2	Quantities used for multiple Coulomb scattering.	18
3.3	Inflow geometry and gap flow between layers 1 & 2.	20
3.4	Simplified cross section of gap flow between layers 1 & 2 for analytical study.	20
3.5	Annular flow considered for the analytical study.	21
3.6	Local heat transfer coefficient and resulting temperature from uniform wall heating.	27
3.7	Heat generation inside the MuPix chip and heat transfer.	29
3.8	Temperature profile through the MuPix chip.	29
3.9	Estimation of the temperature increase in the overlap.	31
4.1	Fluid geometries of layer 1 to 4 in the centre part.	34
4.2	Dimensionless wall distance y^+ for original geometry.	38
4.3	MuPix chip with different heat input sections.	39
4.4	MuPix temperature and pressure drop depending on mesh size.	41
4.5	Number of elements per mesh region.	42
4.6	Geometry of gap flow between layers 1 & 2.	43
4.7	Geometrical simplifications on G12 from previous projects.	44
4.8	Orientation of the MuPix chips on layers 1 & 2.	45
4.9	Temperature of the MuPix chips with the Benchmark geometry.	46
4.10	Temperature of the MuPix layer with the original geometry.	47
4.11	Original geometry and flow distribution in the midplane of layers 1 & 2.	47
4.12	Maximal temperature of the layer depending on mass flow with constant heat.	48
4.13	Original inflow slots of layers 1 & 2.	49
4.14	Mass flow of each group in G12.	49
4.15	Comparison between original and optimised inlet slots of G12.	50
4.16	Temperature of the MuPix layer with the optimised geometry.	50
4.17	Velocity w distribution for optimisation in the midplane of the layer.	51
4.18	Heat transfer coefficient, pressure and temperature of MuPix and flow along z	52
4.19	Further possible adjustment of gap flow between layers 1 & 2.	54

4.20	MuPix temperature with the mylar elongation of layer 1.	55
4.21	MuPix temperature with outer mylar tube.	56
4.22	Scheme of the flows for cooling the centre part B of layer 3 & 4.	60
4.23	Fluid geometry of the V-folds of layers 3 & 4.	61
4.24	V-fold cluster with inflow diameter of original geometry.	62
4.25	Velocity of the V-folds with interface numbering.	62
4.26	Flow through all V-folds of original geometry grouped by clusters.	63
4.27	Optimisation of feeding diameter for V-folds.	64
4.28	Flow through all V-folds grouped by interfaces of optimised geometry.	64
4.29	Geometry of the gap flow between layer 3 & 4 part B.	65
4.30	Flow through interfaces of gap layers 3 & 4.	67
4.31	Flow over the whole circumference of G34.	67
4.32	Original inflow geometry of G34 and velocity distribution in the midplane.	68
4.33	Optimised inflow geometry of G34 and velocity distribution in the midplane.	68
4.34	Geometry of the gap flow between layer 3 & SciFi.	69
4.35	Cut through the inlet of G3S and other parts.	70
4.36	Original geometry of G3S with velocity distribution in the midplane.	71
4.37	Optimised geometry of G3S with velocity distribution in the midplane.	71
4.38	Flow over the whole circumference of gap flow between layer 3 & SciFi.	72
4.39	Increased temperature of one MuPix row due to failed interface.	73
4.40	Average pressure, temperature and velocity of part B along layers 3 & 4.	76
4.41	Cooling capacity of the flows of layer 3 & 4 with percentage share for part B.	77
4.42	Pressure of the internal flows of layer 3 & 4 of part B.	78
4.43	Velocity and temperature profile of part A with optimised geometry.	79
4.44	Scheme of the cooling flow and parts. (Different length scales)	80
4.45	Results of the simulation with all three parts.	80
5.1	Measurement plan of gap flow between layers 1 & 2.	85
5.2	Mockup with both layer 1 half shells and one half shell of layer.	87
5.3	Mockup of gap flow between layers 1 & 2 with position of visible sensors.	87
5.4	Up- and downside of one tape heater.	89
5.5	Reparation of the damaged tape heater of layer 1.	90
5.6	End piece flex used to connect several tape heaters.	91
5.7	Connector plate for the end piece flex connection.	92
5.8	View of the inlet plate and inside of layer 1.	93
5.9	Measurement error of T-Mass and Coriolis in used flow range.	97
5.10	Calibration setup for inductive distance sensor for tape heater.	98
5.11	Calibration curve for the inductive distance sensor with tape heater.	99
5.12	Displacement value sign treatment.	99
5.13	Setup for the mounting of thermocouples on the layer 2.	101
5.14	Measurement block for temperature and pressure at in- & outflow tubes.	102
5.15	Differential pressure sensor.	103
5.16	Heating circuit of the tape heater of layers 1 & 2.	104
5.17	Inlet temperature of helium during measurement.	107

5.18	Temperature of thermocouple after long time without influence of surrounding.	110
5.19	Example of one frame from the thermal camera measurement.	113
5.20	Different heat flux measurements.	114
5.21	Distance of layer 2 and flow at outlet in dependence of inlet mass flow.	116
5.22	Measurement of the leakage flow occurring with helium.	117
5.23	Displacement of the layer by increasing temperature as the material is expanding.	118
5.24	Displacement of the layer caused by heating.	118
5.25	In- & Outlet mass flow over time with heating and resulting mass flow shift.	120
5.26	Aluminium shield over the mockup to investigate the heat radiation.	121
5.27	Temperature of layer 2 with and without aluminium shield.	121
5.28	Temperature dependent on the air mass flow at constant heat.	122
5.29	Measurement data with constant air flow and different heat loads.	123
5.30	Comparison of temperature distribution on layer 2 with air.	125
5.31	Temperature distribution on layer 2 with helium.	126
5.32	Temperature dependent on the heat load with air.	128
5.33	Temperature dependent on the heat load with air comparison.	129
5.34	Temperature dependent on the heat load with helium.	130
5.35	Temperature dependent on the heat load with helium.	131
6.1	Simscape model of flow through gap flow between layers 1 & 2.	135
6.2	Side view of flow parts of Layer 1 and 2.	135
6.3	Mass flow time dependent at mass flow control and outlet of the system.	136
6.4	Pressure along flow direction from CFD- and Simscape-simulations with 2 g/s.	137
6.5	Pressure along flow direction with different mass flows.	138
6.6	Gaseous cooling concept for the supply of cold helium.	140
7.1	Local wall heat transfer coefficient from estimation and CFD simulations of G12.	142
7.2	Comparison of temperature obtained from CFD and measurements.	143
7.3	Example of different heat loads for the helium measurements.	144
7.4	Dimensionless temperature of different measurement setups and simulations.	145

List of Tables

2.1	Dimensions of the different layers and segments.	11
2.2	Absolute heat load per layer.	12
2.3	Helium mass flow through different cooling sections.	14
2.4	Properties of helium and dry air used for simulations and estimations.	15
2.5	Properties of silicon, polyimide, steel and araldite.	15
3.1	Data used for the estimation of non-dimensional number.	22
3.2	Data used for the heat radiation estimation.	24
3.3	Data used for the estimation of the G12.	26
3.4	Properties of the conjugated heat transfer of the silicon chip.	30
3.5	Properties for temperature increase in the overlap of layer 2.	31
4.1	Heat dissipation per area and volume for periphery and detector part.	39
4.2	Mesh size of gap flow between layers 1 & 2 of different volumes and solid.	41
4.3	Mesh size of different volumes and solid of layers 3 & 4.	42
4.4	Dimension of the outer flow created with a mylar tube.	54
4.5	Results with different configurations of gap flow between layers 1 & 2.	57
4.6	Reynolds number of the flows of layer 3 & 4.	59
4.7	Mass flow and temperature of the global flow between the part A, B & C.	73
4.8	Results with different configurations of layers 3 & 4.	81
5.1	Experimental parameter for layers 1 & 2 with helium and air.	86
5.2	Theoretical and measured resistance of one tape heater side.	88
5.3	Equipment used for measurements.	94
5.4	Components of the heating circuit and their resistance.	105
5.5	Computation of different measurement uncertainties for thermocouples typ K.	109
5.6	Measurement error of the devices used.	111
7.1	Summary of simplifications of different analysis.	141

A Project management

A.1 Project task

Vertiefungsausbildung

Modulbeschreibung

P9 Master-Thesis im Herbstsemester 2018

Institut: **Institut für Thermo- und Fluid-Engineering (ITFE)**

Projekttitle: **Verifizierung und Regelung des Helium-Kühlsystems für das Mu3e-Experiment**

Thema:
(Kurzbeschreibung) Das so genannte Mu3e-Experiment sucht nach dem sehr seltenen Zerfall eines Müons in drei Elektronen bzw. Positronen. Es wird derzeit am Paul Scherrer-Institut in Villigen aufgebaut und soll über die nächsten Jahre in Betrieb genommen werden.

Kernelement des Experiments ist ein Pixeldetektor, der aus Siliziumchips besteht, auf denen der Sensor und die Auslese-Elektronik integriert sind. Aus diesen Chips werden Module gebaut, so dass mehrere konzentrische Zylindermäntel entstehen. Die Sensorflächen der Module sind mit ca. 100 µm sehr dünn und bestehen lediglich aus den Flexprints und den Chips. Für die Kühlung ist gasförmiges Helium vorgesehen (4°C).

In dieser Arbeit geht es um die Weiterentwicklung der Heliumgaskühlung und einige Aspekte der Steuerung. Die Kühlung hat in den vorherigen Arbeiten noch einige Schwachstellen aufgezeigt, welche mittels Simulationen und eventuell Experimenten ausgebessert werden sollen.

Der Kühlkreislauf besteht aus sieben unabhängigen Kühlkreisläufen, welche einzeln gesteuert werden müssen. Der Differenzdruck über einer Sensorlage darf eine Schadenschwelle nicht übersteigen (während Hochfahren, Betrieb und Herunterfahren der Kühlung).

Da das Experiment in einem kryogenen, supraleitenden Magneten (1 T Feldstärke) durchgeführt wird, dürfen keine magnetischen Materialien benutzt werden. Spulengetriebene Stellorgane wie Motoren und Magnetventile sind auszuschliessen.

Bislang wurden erfolgreiche Konzeptstudien mit Simulationen und Labormessungen durchgeführt, die zeigen, dass die He-Kühlung der Si-Pixelsensoren prinzipiell funktioniert. Die finale Geometrie der Mechanik ist ebenfalls bekannt.

Nun steht die Umsetzung an, was bedeutet, dass die korrekte Funktionsweise der Kühlung am finalen Modell erfolgen muss. Dazu gehört die Evaluation geeigneter Steuerkomponenten, wobei die Platzverhältnisse sehr beschränkt sind.

Derzeit entstehen beheizbare Module (L1/2 und L4) mit korrektem Materialaufbau. Diese gilt es im Labor zu überprüfen. So ist insbesondere das Verhalten des dünnen Schichtaufbaus bei mehreren Chips noch unbekannt und konnte bislang nicht befriedigend modelliert werden. So muss etwa der Einfluss sich wölbender Oberflächen auf die Strömung und Kühlleistung abgeklärt werden.

Es müssen weiter alle Zu- und Rückleitungen, Wärmetauscher wie auch der Kompressor einbezogen werden. Die Eigenschaften der Regelstrecke müssen untersucht werden, um daraus Anforderungen an die Regelung abzuleiten.

Ziel ist ein Entwurf des Gesamtsystems und ein Vorschlag zur Umsetzung am PSI, wobei zu Steuerungsfragen das Institut für Automation der FHNW beratende Unterstützung zugesagt hat.

Projektteam:

Auftraggeber: Dr. Frank Meier Aeschbacher
Universität Heidelberg, Physikalisches Institut

Student/-in Marin Deflorin

Experte/-in Dirk Büche

Betreuer (extern): Dr. Frank Meier Aeschbacher /
PD Dr. Olaf Steinkamp

Betreuer (intern): Prof. Dr. Beat Ribi /
Prof. Dr. Peter Stuber /
Prof. Dr. Daniel Weiss

Fragestellungen:
(erwartete Arbeiten)

Schwerpunkt Simulation und Optimierung:

- Reproduzieren und verifizieren der bisherigen Ergebnisse
- Optimierungen (bekannt: L1/2 sowie aus Verifikation erkanntes Potential)
- Untersuchen des dynamischen Verhaltens (Hoch-/Runterfahren, thermische Verformung)
- Einbezug der relevanten Volumina bis zur Kühl- und Kompressorgruppe
- Einfluss der Verformung der Pixeldetektor durch den Temperaturanstieg

Schwerpunkt System:

- Auslegung Gesamtsystem, relevante Simulationen nach Bedarf
- regeltechnische Kenngrößen ermitteln, Formulierung einer Regelstrategie
- Umsetzungsplan
- Konzept Steuerung und Regelung

Ergänzende Veranstaltungen:

- Orientation Center (1 ECTS)
- «Zum Mu3e-Experiment, auf der Suche nach einem seltenen Teilchenzerfall.» (1 ECTS)
- «Einarbeitung in LabView» (1 ECTS)

Starttermin: 17.09.2018

Projektphasenaudit: Voraussichtlich in 12/2018, Termin noch zu bestimmen

Abgabetermin: 31.03.2019

Ort, Datum: Windisch, 02.10.2018

Windisch, 02.10.2018

Unterschriften:




Student/Studentin

Advisor

A.2 Project clarification

Helium cooling of Silicon Pixel Detector for Mu3e Experiment

Project 9 - Clarification



University of Applied Sciences and Arts Northwestern Switzerland
Institute of Thermal and Fluid Engineering, ITFE

Master of Science FHNW in Engineering

Focus in Energy and Environment

Masterthesis, FS2018

October 17, 2018

Student

Marin Deflorin

marin.deflorin@students.fhnw.ch

Project supervision

Beat Ribi

Peter Stuber

Daniel Weiss

Project partner

Mu3e

Frank Meier Aeschbacher

Olaf Steinkamp

Contents

- Acronyms** **ii**

- 1 Introduction** **1**

- 2 Goals** **2**

- 3 Resources** **3**
 - 3.1 Supervision 3
 - 3.2 Infrastructure 3
 - 3.3 Financial resources 3

- 4 Planning** **4**
 - 4.1 Task structure diagram 4
 - 4.2 Tasks 6
 - 4.3 Milestones 11
 - 4.4 Schedule 11

- 5 Risk management** **13**

- 6 Declaration of consent** **15**

- A Project task** **16**

Acronyms

FHNW University of Applied Sciences and Arts Northwestern Switzerland

PSI Paul Scherrer Institut

IA Institute of Automation

CFD Computational Fluid Dynamics

1 Introduction

The Mu3e-Experiment is searching for a rare decay of the muon into two positrons and one electron. The experiment has been planned for several years already and is going into the set-up at the Paul Scherrer Institut (PSI) in Villigen. A decay into three particles, which is extremely unlikely in the Standard Model of particle physics, would give evidence that some suggested extended model could be valid.

The experiment consists mainly of a muon-beam (see Figure 1.1) which is shot onto a target where the muons are decaying. Around the target several layers of pixel detectors are arranged which are tracking the particles. The pixel detector is mainly out of silicon with a flexprint out of kapton holding the chip at the specific position. Helium with a temperature of 4°C is intended for the cooling mainly because of the reasonable compromise between radiation length and cooling potential. The whole experiment is in a strong magnetic field which does not allow the use of ferromagnetic materials inside of the main component.

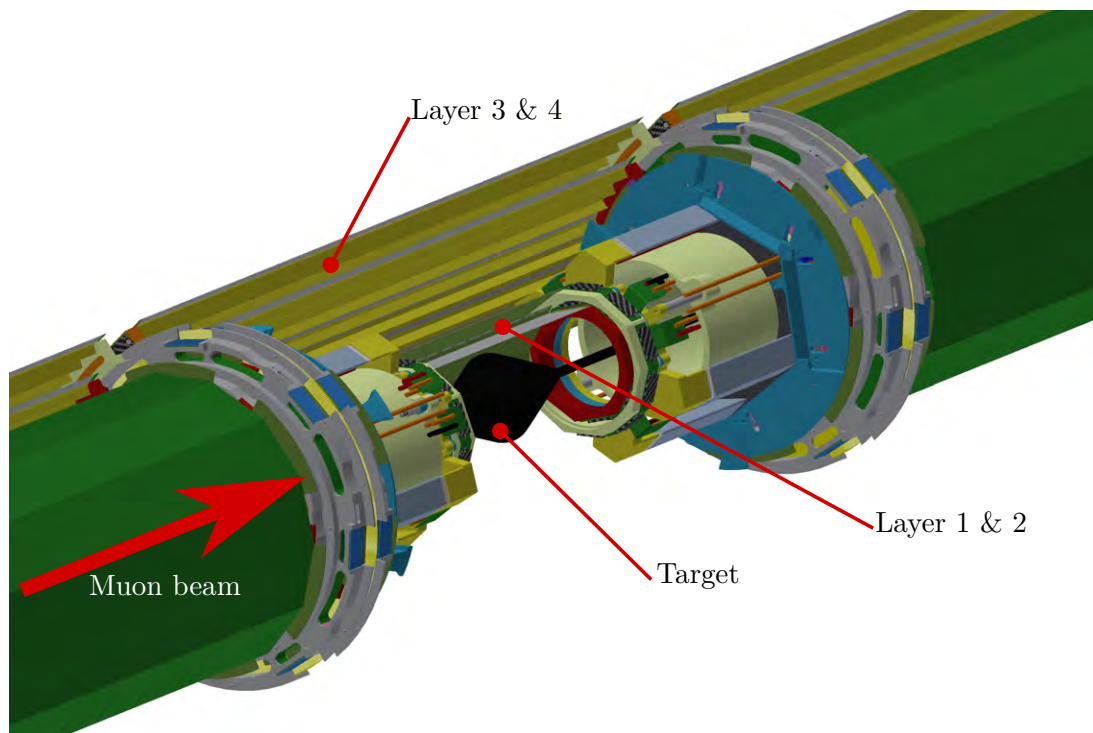


Figure 1.1: CAD model of beam line with Target and different detector Layers

2 Goals

Main goal of the project is to analyse the whole helium cooling of the silicon chips, optimize parts which could affect the experiment and create a concept for the control and regulation system.

The silicon chip used for the Mu3e-Experiment have a heat load of around 250 to 400 mW/cm². The temperature of the chip should not exceed 70 °C as the Araldite glass transition temperature is in this region. Slow oscillations (under ≈ 5 Hz) of the flow and the chip is also not suitable, as the chips should stay at a specific position.

Another aspect that should be covered is the system behaviour of the helium circuit. Especially in the start-up and shut-down phase the pressure between the Layer has to be controlled to prevent a damaging of the Layers.

The sub-goals of the project can be found in following list:

Verification	Verification of the cooling results of the Layer 1/2 and 3/4 obtained in previous works.
Instrumentation	Instrumentation of the mock-up for validation of the Computational Fluid Dynamics (CFD)- and flow system-simulations.
Validation	Validation of the simulation results with measurements on the mock-up.
Optimisation	Optimize the cooling of the Layer 1/2 and 3/4 if the temperature is too high or if other unacceptable states occur, e.g. oscillations that may trigger mechanical vibrations or stress.
Thermal deformation	Thermal deformation of the flexprint has to be investigated and the influence of it onto the cooling behaviour.
Flow system	Characterisation of helium flow through the whole system with the pressure drop and system behaviour.
Control concept	Develop control concept for the helium cooling circuit with a focus on start-up and shut-down phase.

3 Resources

3.1 Supervision

As supervision from the project partner from the Mu3e-experiment team there are Frank Meier Aeschbacher and Olaf Steinkamp. From the University of Applied Sciences and Arts Northwestern Switzerland (FHNW) there are Beat Ribi, Peter Stuber and Daniel Weiss. Additionally Daniel Binggeli from the Institute of Automation (IA) could give some support for the regulation of the flow system.

3.2 Infrastructure

From the FHNW a place in the laboratory will be provided for the experiments and also licences for different software packages. Computational resources on the Cluster can be used for the simulations. Different measurement devices are available but are part of the inventory and should be returned at the end of the project. If some devices should be transferred to the PSI for some experiments they have to be returned soon.

Firstly the experiment will be carried out with air as cooling fluid. In a latter step Helium from a gas container could be used.

3.3 Financial resources

Financial resources for the experimental set-up has to be discussed with the client.

4 Planning

4.1 Task structure diagram

Figure 4.1 shows the task structure diagram with the different work tasks of the project, which are split into four groups. First task package are the CFD simulations which can be performed directly from the beginning. The order between the optimisation and the validation has been set in this order as the mock-up is not available right from the beginning of the project. Second package are the measurements which are partly depending on the delivery of the different layer. Some part of the instrumentation can start from the beginning but some knowledge of the whole system is needed for it. The measurements are used as verification for the cooling behaviour that has been simulated and also to examine the system behaviour. In the package System the whole flow system from the compressor through the Layers and back to the chiller should be considered. The last package is the documentation and the defense.

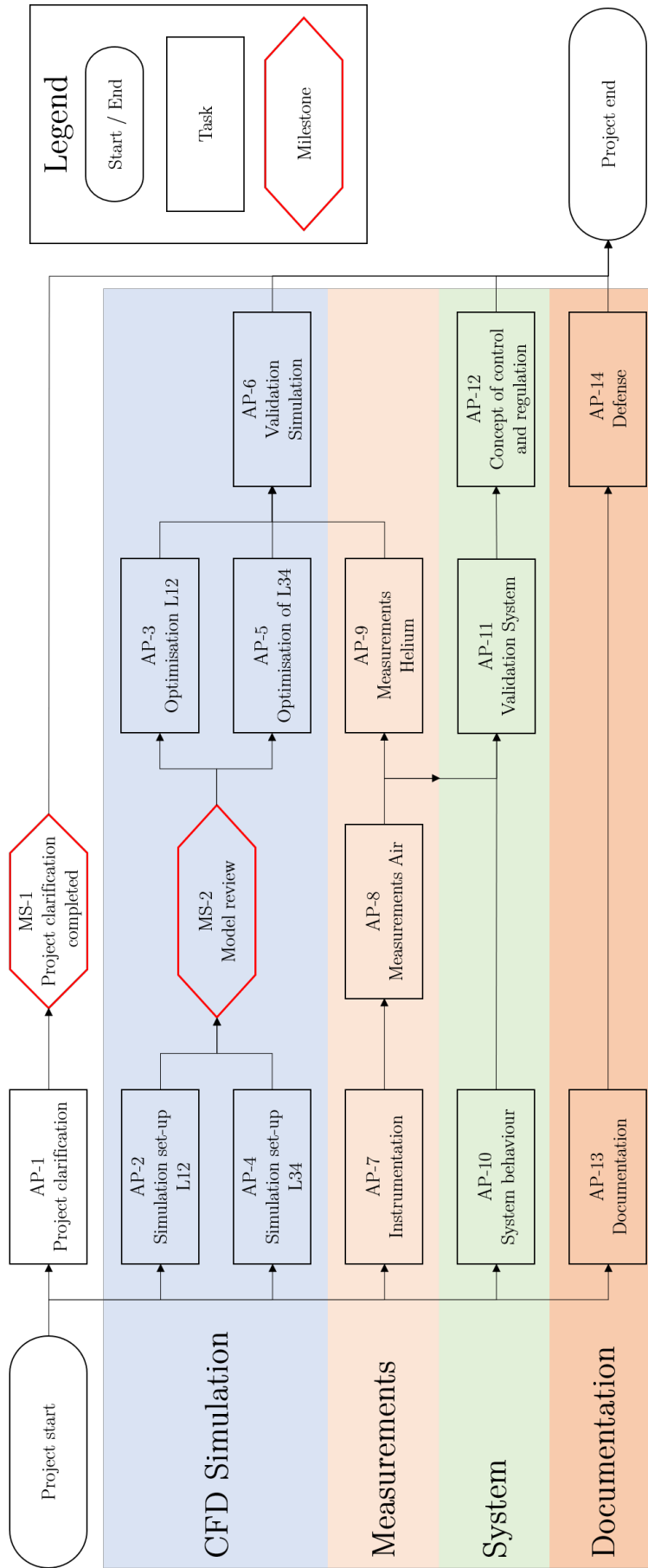


Figure 4.1: Task structure diagram

4.2 Tasks

AP-1 Project clarification

Goal Work tasks, risk management, time plane and project goals are defined and signed.

- Goals of the project are defined
- Work tasks are defined
- Time plane with deliverables and milestones
- Risk management
- Resources

Work time: 15 h

Deliverable: Project clarification

AP-2 Simulation set-up L12

Goal Set-up of the simulation of the gap flow between Layer 1 and 2. Evaluation and verification of the results, comparison with previous works and documentation of the present cooling condition.

- Estimation of the occurring phenomena
- Preparation of the geometry for meshing
- Meshing of the geometry and mesh study
- Examination of different parameter on the result
- Determine issues which could affect the cooling behaviour or the Mu3e-experiment

Work time: 80 h

AP-3 Optimisation L12

Goal Optimisation of the gap flow between Layer 1 and 2 to improve the cooling behaviour.

- Estimation of the optimal possible cooling
- Investigate the part which can be optimized
- Propose the optimized part

Work time: 30 h

Deliverable: Geometry of optimised part

AP-4 Simulation set-up L34

Goal Set-up of the simulation of the gap- and V-flow between Layer 3 and 4. Evaluation and verification of the results, comparison with previous work and documentation of the present cooling condition.

- Estimation of the occurring phenomena
- Preparation of the geometry for meshing
- Meshing of the geometry
- Verification of the conjugated heat transfer results
- Examination of different parameter on the result
- Determine issues which could affect the cooling behaviour of the Mu3e-experiment

Work time: 80 h

AP-5 Optimisation L34

Goal Optimisation of the gap- and V-flow between Layer 3 and 4 to improve the cooling behaviour.

- Estimation of the optimal possible cooling
- Investigate the part which can be optimized
- Propose the optimized part

Work time: 30 h

Deliverable: Geometry of optimised part

AP-6 Validation Simulation

Goal Validation of the simulation results of Layer 1-4 with air and helium measurements.

- Validate the simulation model with measurements
- Compare the occurring phenomena

Work time: 30 h

AP-7 Instrumentation

Goal Instrument the mock-up of the Mu3e-experiment with different sensors to enable the measurement of the cooling and system behaviour. It also includes the data collection with LabView or another software.

- Define which quantities should be measured
- Choose sensor which will be used
- Modifications or extension of the mock-up to fix the sensors
- Data collection software to collect measurement data
- First functionally test of the measurement system

Work time: 85 h

AP-8 Measurements with Air

Goal Measurement at the FHNW with equipment available. The used cooling fluid will be air.

- Measurement of the cooling with air
- Measurement of the system behaviour with air

Work time: 80 h

AP-9 Measurements with Helium

Goal Measurements with helium.

- Measurement of the cooling with helium
- Measurement of the system behaviour with helium

Work time: 55 h

AP-10 System behaviour

Goal Analyse the system behaviour of the cooling circuit. This will probably be done with a Simscape model.

- Analyse the system behaviour of the entire cooling system
- Oscillation of the mass flow should be prevented
- Pressure inside the Layers have to be controlled to prevent inflation and damaging of the Layers
- Time constant for the start-up and shut-down have to be determined
- Define if control units of the flow can be placed outside of the magnet or have to be inside
- If the control units have to be inside the magnet, appropriate units have to be chosen which are adapted to the condition

Work time: 70 h

AP-11 Validation System

Goal Validate the system behaviour with measurement on the mock-up. This could be done with air or helium as fluid.

- Validate the system behaviour with the mock-up system
- Adapt the Simscape on the occurring phenomena

Work time: 40 h

AP-12 Concept of control and regulation

Goal Establish a concept for the control and regulation system for implementation.

- Assemble all findings which are relevant for the control of the system

Work time: 40 h

AP-13 Documentation

Goal Work tasks are documented, the results presented and the further procedures specified.

- Documentation of all relevant work tasks done
- Define next steps which should follow

Work time: 160 h

Deliverable: Documentation

AP-14 Defense

Goal Presentation of the project and following discussion.

- Prepare presentation for defense

Work time: 15 h

Deliverable: Presentation of the project

4.3 Milestones

MS-1 Project clarification completed

Goal The project clarification is finalised and signed by all parties.

MS-2 Model review

Goal Check of the simulation model with the simulation set-up document with an additional person to ensure an error-free model.

Delivery documentation & presentation

Goal Documentation is finalised and presentation is prepared for the defense. Poster of the project is prepared.

4.4 Schedule

On the next page the schedule of the project with the work tasks and the milestones is displayed.

5 Risk management

In Table 5.1 the risks of the project are specified and classified after there danger (D) for the project and the probability (P) to occur. The scale goes from 1 – 4 (low-high) and the two values are multiplied with each other. If a risk has a high value there should be more measures intended and this risks should also be monitored during the task.

Table 5.1: Risk management

AP	Risk	D	P	D · P	Measures
1	Misjudgement of time for tasks	2	3	6	Tracking of the work time and adjust planning if there are large deviations.
1	Important work tasks are forgot	3	1	3	Generate new work tasks in agreement with project team.
2-12	A work task is too time consuming and interferes with other tasks	2	3	6	Discuss with the client and supervisors which tasks to focus on and which can be neglected.
2 & 4	Simulation is not feasible because of modelling constraints	2	2	4	Try new software, discuss with CFD experts or evaluate if a measurement would be more helpful.
2 & 4	Simulation is not feasible because of computational constraints	2	1	2	Evaluate if fine mesh is necessary.
3 & 5	Optimisation is too time consuming	3	2	6	Evaluate the importance of the optimisation for the whole system. If the optimisation is crucial shift more resources onto work task.
6	Simulation results does not show same behaviour as the measurements	3	2	6	Examine where the differences could come from and adapt simulation or measurement model.
7-9	Instrumentation and measurements are too time consuming	3	2	6	Focus on main measurement tasks. Take time resources from other tasks.
10	Simscape model does not show the expected results.	2	2	4	Discuss with other experts of system modelling or examine the system behaviour with measurements.

6 Declaration of consent

Client

FM Aeschbacher

Frank Meier Aeschbacher

Bregg 26.10.18

Place & Date

Supervisors and advisor

D. Weiss

Daniel Weiss

Windisch, 30 Oct 2018

Place & Date

B. Ribi

Beat Ribi

Windisch, 31. Oct. 2018

Place & Date

P. Stuber

Peter Stuber

Windisch 26.10.2018

Place & Date

Student

M. Deflorin

Marin Deflorin

Windisch, 31.10.2018

Place & Date

A Project task

Vertiefungsausbildung

Modulbeschreibung

P9 Master-Thesis im Herbstsemester 2018

Institut: **Institut für Thermo- und Fluid-Engineering (ITFE)**

Projekttitle: **Verifizierung und Regelung des Helium-Kühlsystems für das Mu3e-Experiment**

Thema:
(Kurzbeschreibung) Das so genannte Mu3e-Experiment sucht nach dem sehr seltenen Zerfall eines Müons in drei Elektronen bzw. Positronen. Es wird derzeit am Paul Scherrer-Institut in Villigen aufgebaut und soll über die nächsten Jahre in Betrieb genommen werden.

Kernelement des Experiments ist ein Pixeldetektor, der aus Siliziumchips besteht, auf denen der Sensor und die Auslese-Elektronik integriert sind. Aus diesen Chips werden Module gebaut, so dass mehrere konzentrische Zylindermäntel entstehen. Die Sensorflächen der Module sind mit ca. 100 µm sehr dünn und bestehen lediglich aus den Flexprints und den Chips. Für die Kühlung ist gasförmiges Helium vorgesehen (4°C).

In dieser Arbeit geht es um die Weiterentwicklung der Heliumgaskühlung und einige Aspekte der Steuerung. Die Kühlung hat in den vorherigen Arbeiten noch einige Schwachstellen aufgezeigt, welche mittels Simulationen und eventuell Experimenten ausgebessert werden sollen.

Der Kühlkreislauf besteht aus sieben unabhängigen Kühlkreisläufen, welche einzeln gesteuert werden müssen. Der Differenzdruck über einer Sensorlage darf eine Schadenschwelle nicht übersteigen (während Hochfahren, Betrieb und Herunterfahren der Kühlung).

Da das Experiment in einem kryogenen, supraleitenden Magneten (1 T Feldstärke) durchgeführt wird, dürfen keine magnetischen Materialien benutzt werden. Spulengetriebene Stellorgane wie Motoren und Magnetventile sind auszuschliessen.

Bislang wurden erfolgreiche Konzeptstudien mit Simulationen und Labormessungen durchgeführt, die zeigen, dass die He-Kühlung der Si-Pixelsensoren prinzipiell funktioniert. Die finale Geometrie der Mechanik ist ebenfalls bekannt.

Nun steht die Umsetzung an, was bedeutet, dass die korrekte Funktionsweise der Kühlung am finalen Modell erfolgen muss. Dazu gehört die Evaluation geeigneter Steuerkomponenten, wobei die Platzverhältnisse sehr beschränkt sind.

Derzeit entstehen beheizbare Module (L1/2 und L4) mit korrektem Materialaufbau. Diese gilt es im Labor zu überprüfen. So ist insbesondere das Verhalten des dünnen Schichtaufbaus bei mehreren Chips noch unbekannt und konnte bislang nicht befriedigend modelliert werden. So muss etwa der Einfluss sich wölbender Oberflächen auf die Strömung und Kühlleistung abgeklärt werden.

Es müssen weiter alle Zu- und Rückleitungen, Wärmetauscher wie auch der Kompressor einbezogen werden. Die Eigenschaften der Regelstrecke müssen untersucht werden, um daraus Anforderungen an die Regelung abzuleiten.

Ziel ist ein Entwurf des Gesamtsystems und ein Vorschlag zur Umsetzung am PSI, wobei zu Steuerungsfragen das Institut für Automation der FHNW beratende Unterstützung zugesagt hat.

Projektteam:

Auftraggeber: Dr. Frank Meier Aeschbacher
Universität Heidelberg, Physikalisches Institut

Student/-in: Marin Deflorin

Experte/-in: Dirk Büche

Betreuer (extern): Dr. Frank Meier Aeschbacher /
PD Dr. Olaf Steinkamp

Betreuer (intern): Prof. Dr. Beat Ribi /
Prof. Dr. Peter Stuber /
Prof. Dr. Daniel Weiss

Fragestellungen:
(erwartete Arbeiten)

Schwerpunkt Simulation und Optimierung:

- Reproduzieren und verifizieren der bisherigen Ergebnisse
- Optimierungen (bekannt: L1/2 sowie aus Verifikation erkanntes Potential)
- Untersuchen des dynamischen Verhaltens (Hoch-/Runterfahren, thermische Verformung)
- Einbezug der relevanten Volumina bis zur Kühl- und Kompressorgruppe
- Einfluss der Verformung der Pixeldetektor durch den Temperaturanstieg

Schwerpunkt System:

- Auslegung Gesamtsystem, relevante Simulationen nach Bedarf
- regeltechnische Kenngrößen ermitteln, Formulierung einer Regelstrategie
- Umsetzungsplan
- Konzept Steuerung und Regelung

Ergänzende Veranstaltungen:

- Orientation Center (1 ECTS)
- «Zum Mu3e-Experiment, auf der Suche nach einem seltenen Teilchenzerfall.» (1 ECTS)
- «Einarbeitung in LabView» (1 ECTS)

Starttermin: 17.09.2018

Projektphasenaudit: Voraussichtlich in 12/2018, Termin noch zu bestimmen

Abgabetermin: 31.03.2019

Ort, Datum: Windisch, 02.10.2018

Windisch, 02.10.2018

Unterschriften:




Student/Studentin

Advisor

A.3 Project plan

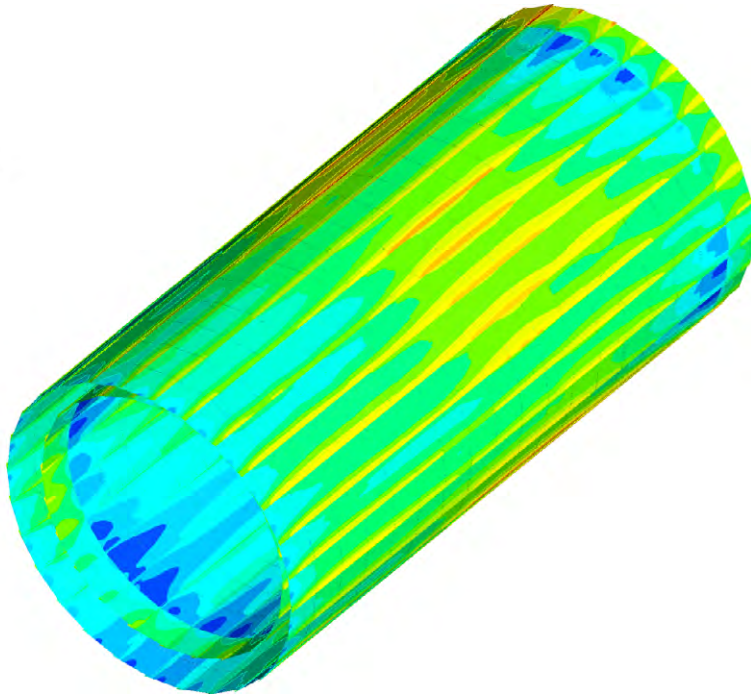
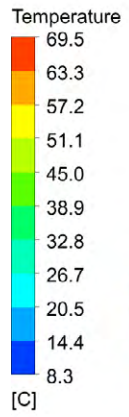
Tasks		Time	Weeks																				Special Periods						
			KW 37	KW 38	KW 39	KW 40	KW 41	KW 42	KW 43	KW 44	KW 45	KW 46	KW 47	KW 48	KW 49	KW 50	KW 51	KW 52	KW 53	KW 2	KW 3	KW 4	KW 5	KW 6	KW 7	KW 8	KW 9	KW 10	
			10. 9.	17. 9.	24. 9.	01. 10.	08. 10.	15. 10.	22. 10.	29. 10.	05. 11.	12. 11.	19. 11.	26. 11.	03. 12.	10. 12.	17. 12.	24. 12.	31. 12.	07. 1.	14. 1.	21. 1.	28. 1.	04. 2.	11. 2.	18. 2.	25. 2.	04. 3.	
Planning	AP-1 Project clarification	15 h	Target							Actual																			
	MS-1 Project clarification completed									Planned milestone																			
CFD Simulation	AP-2 Simulation set-up L12	80 h	Target							Actual																			
	AP-3 Optimisation L12	30 h	Target							Actual																			
	AP-4 Simulation set-up L34	80 h	Target							Actual																			
	AP-5 Optimisation L34	30 h	Target							Actual																			
	AP-6 Validation Simulation	30 h														Target				Actual									
	MS-2 Model review															Planned milestone				Effective milestone									
Measurements	AP-7 Instrumentation	85 h	Target							Actual																			
	AP-8 Measurement Air	80 h	Target							Actual																			
	AP-9 Measurement Helium	55 h	Target							Actual																			
System	AP-10 System behaviour	70 h	Target							Actual																			
	AP-11 Validation System	40 h	Target							Actual																			
	AP-12 Concept of control and regulation	40 h	Target							Actual																			
Documentation	AP-13 Documentation	160 h	Target							Actual							Auxiliary tasks							Target					
	AP-14 Defense	15 h																								Target		Actual	
	Delivery documentation & Defense																									Planned milestone	Effective milestone		
Work time per week			5	30	30	40	40	40	40	40	40	40	40	40	40	35	30	0	0	30	40	40	40	40	40	40	40	5	5
Total time			5	35	65	105	145	185	225	265	305	345	385	425	465	500	530	530	530	560	600	640	680	720	760	800	805	810	

Total time planned: 810 h

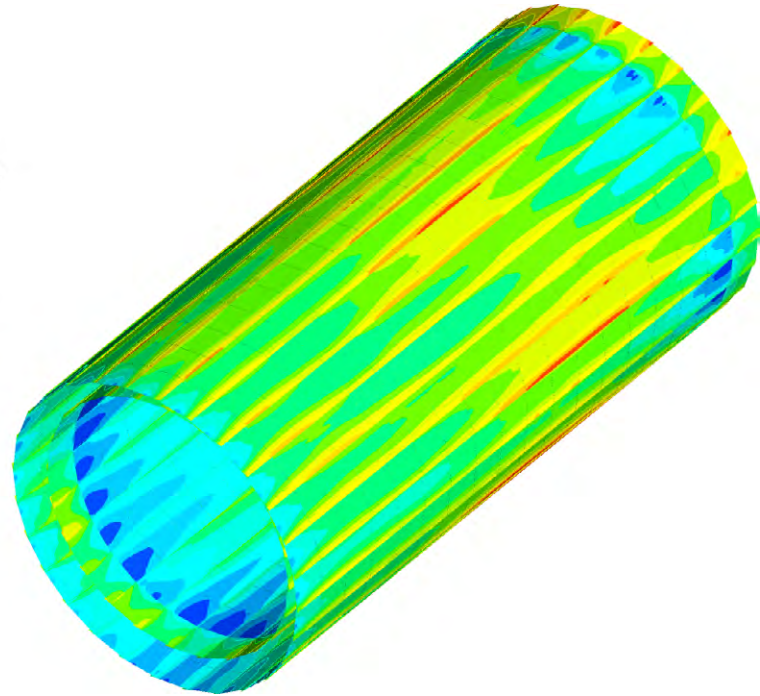
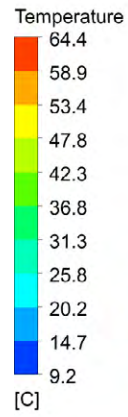
Legend: ■ Target ■ Actual ■ Auxiliary tasks ◆ Planned milestone ◆ Effective milestone

B Simulation

B.1 Layers 3 & 4 part B



(a) Original



(b) Optimisation

Figure B.1: Comparison of temperature between original and optimised geometry of part B.

Figures B.2 and B.3 show a comparison of the velocity and temperature profile of both cases. The influence of the opening defined at the outlet can clearly be seen. On the right side low temperature fluid is flowing back into the global volume. The temperature profile of the optimisation shows lower temperatures along the SciFi detector, which is due to the optimisation that leads to a more regular flow.

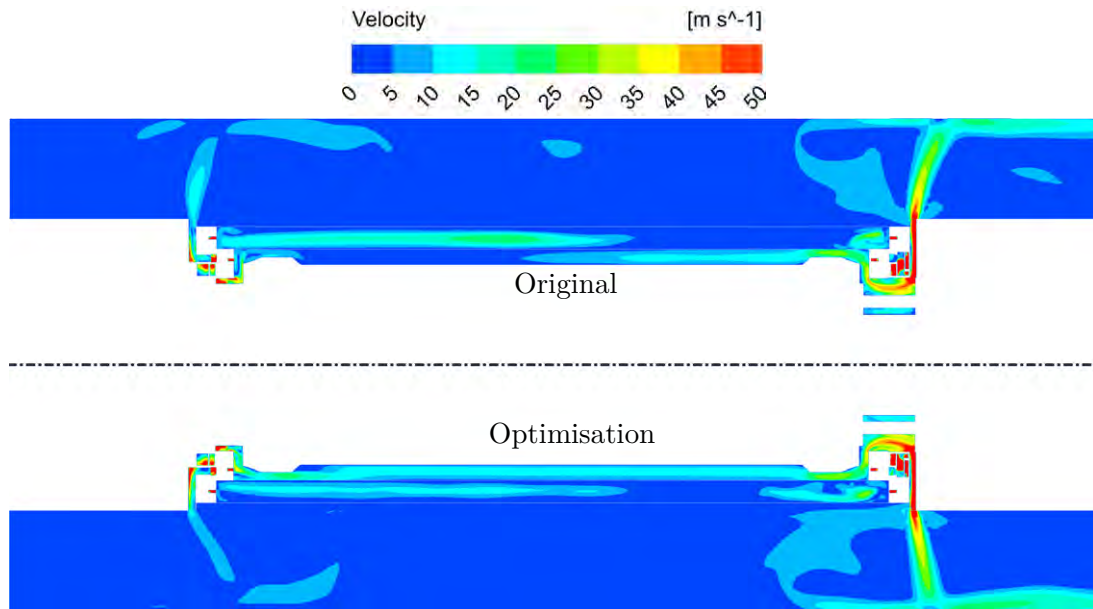


Figure B.2: Velocity and temperature profile of part B with original geometry.

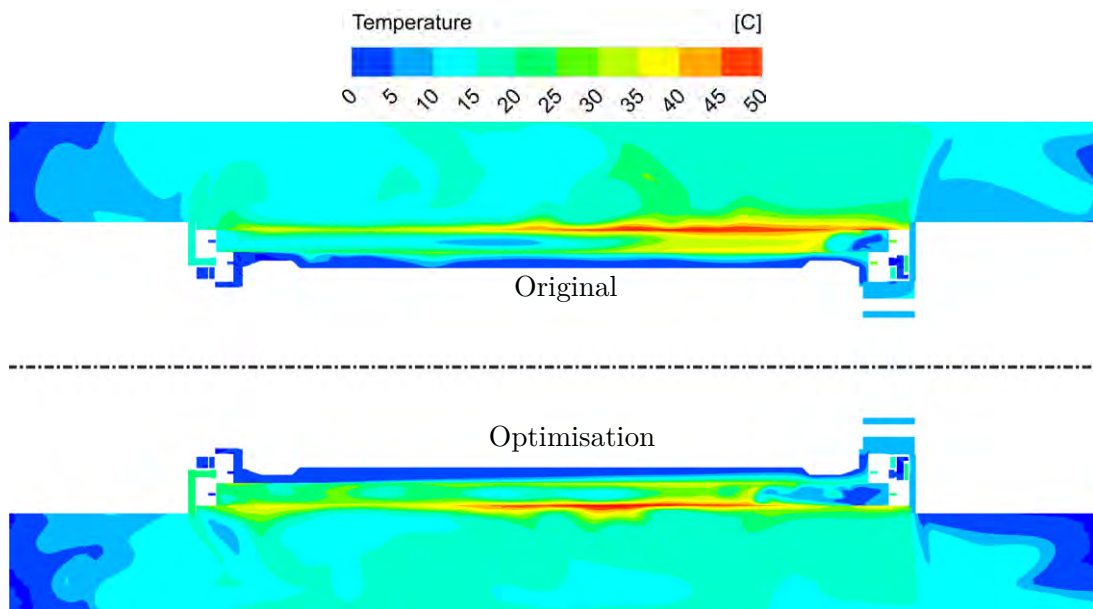


Figure B.3: Velocity and temperature profile of part B with optimised geometry.

C Measurements

C.1 Air

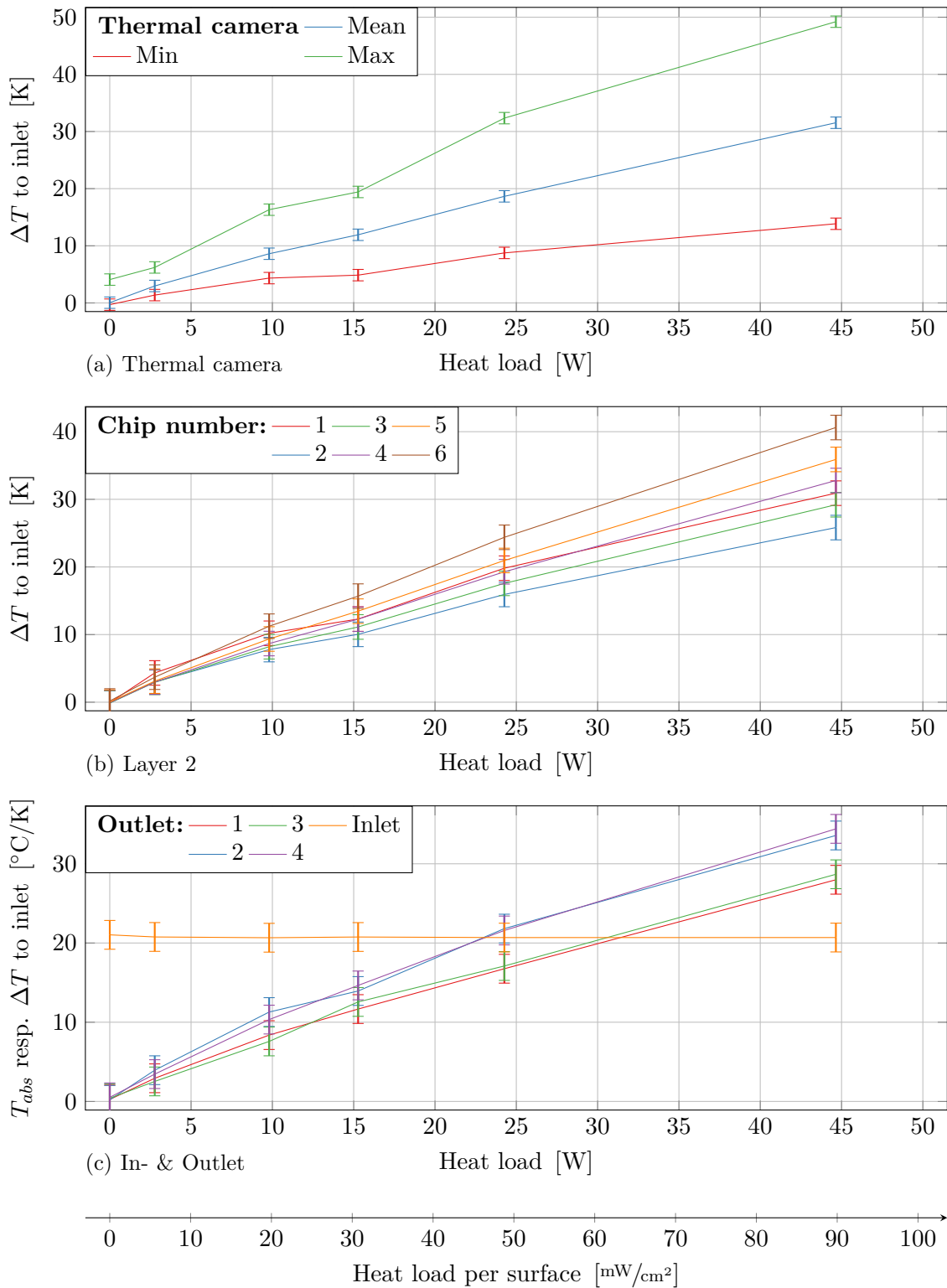


Figure C.1: Temperature dependent on the heat load with an air mass flow of 1.87 g/s and optimised inlet plate.

C.2 Raw measurement data

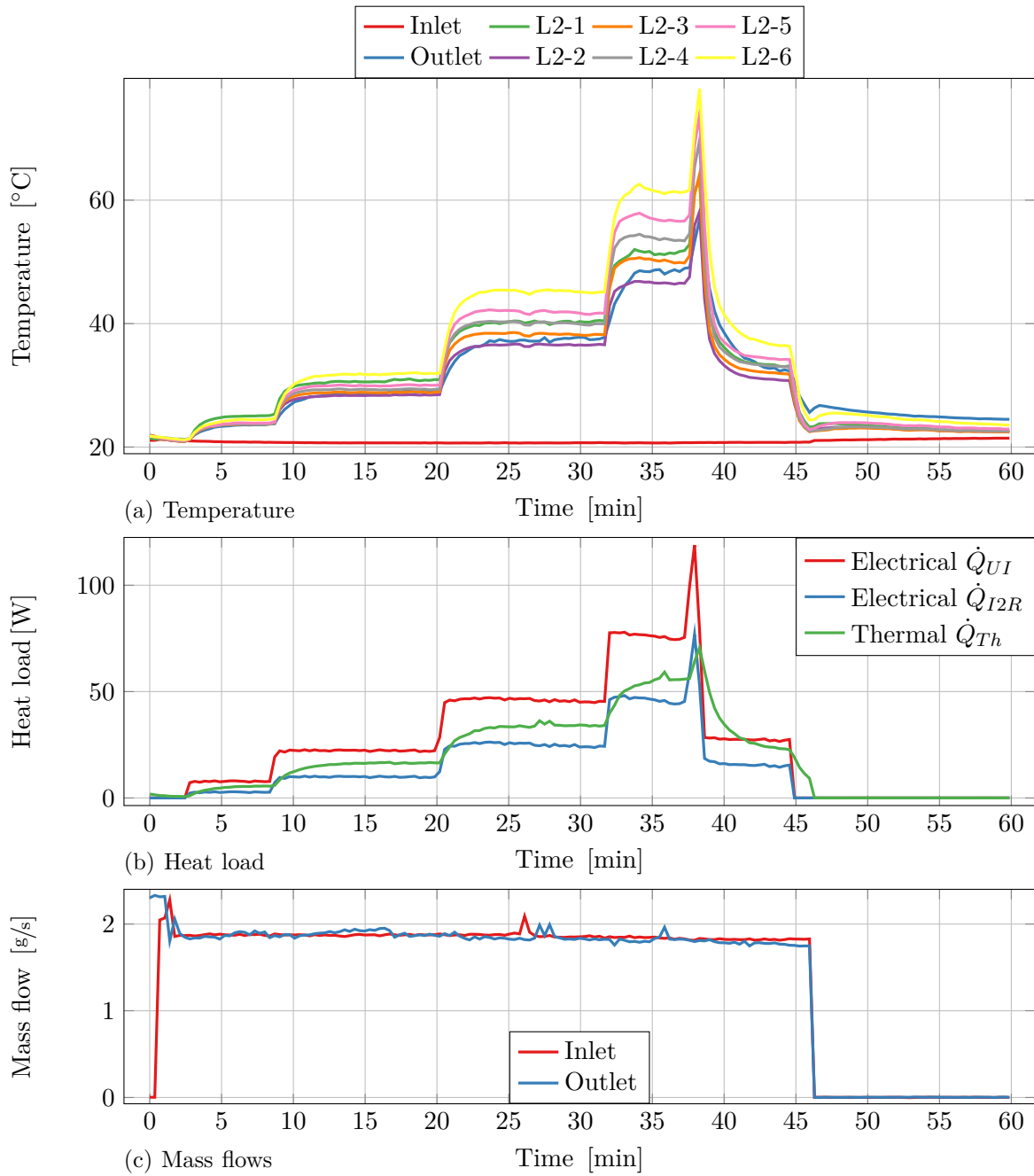


Figure C.2: Raw measurement data of air with original inlet plate.

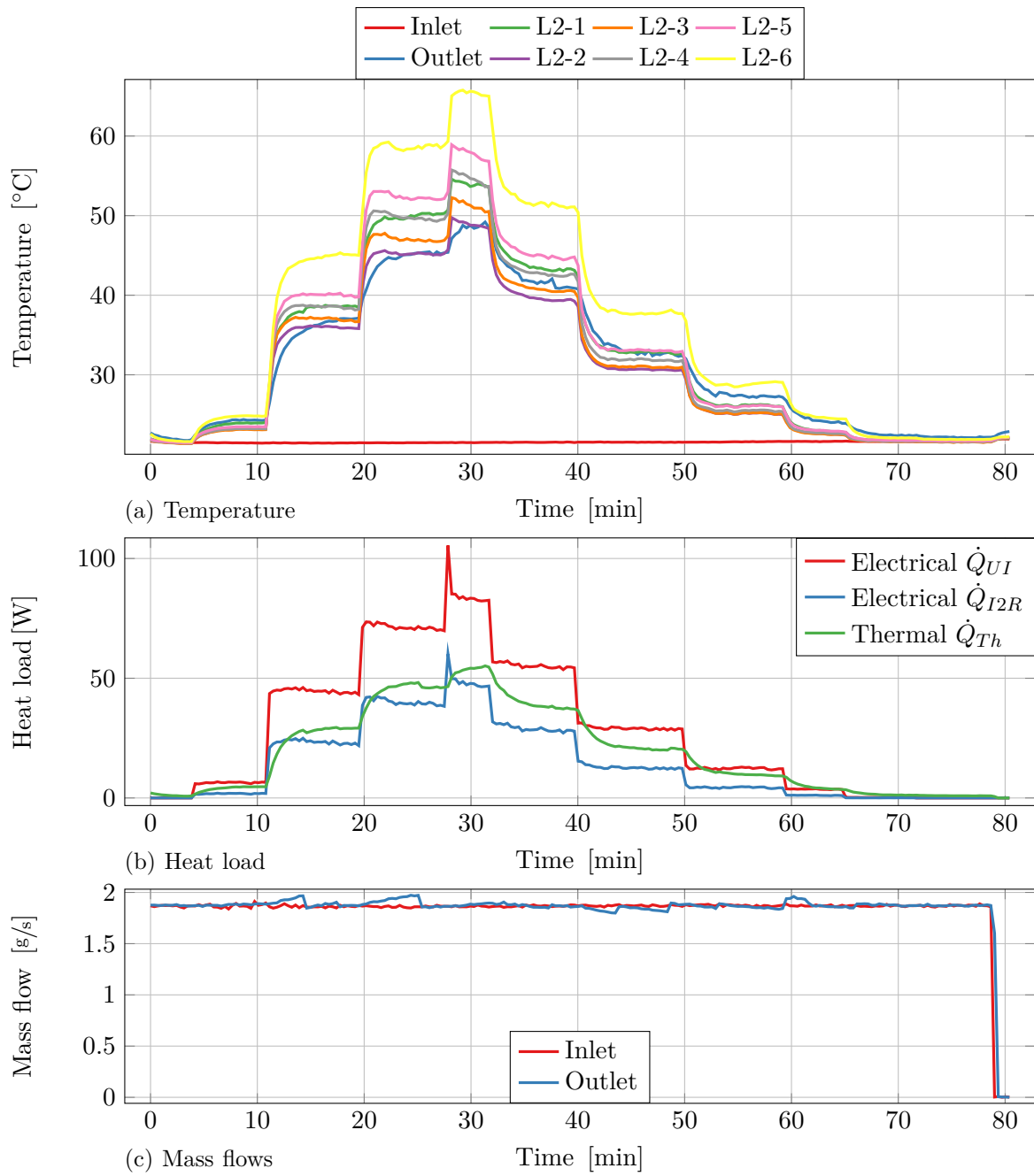


Figure C.3: Raw measurement data of air with optimised inlet plate.

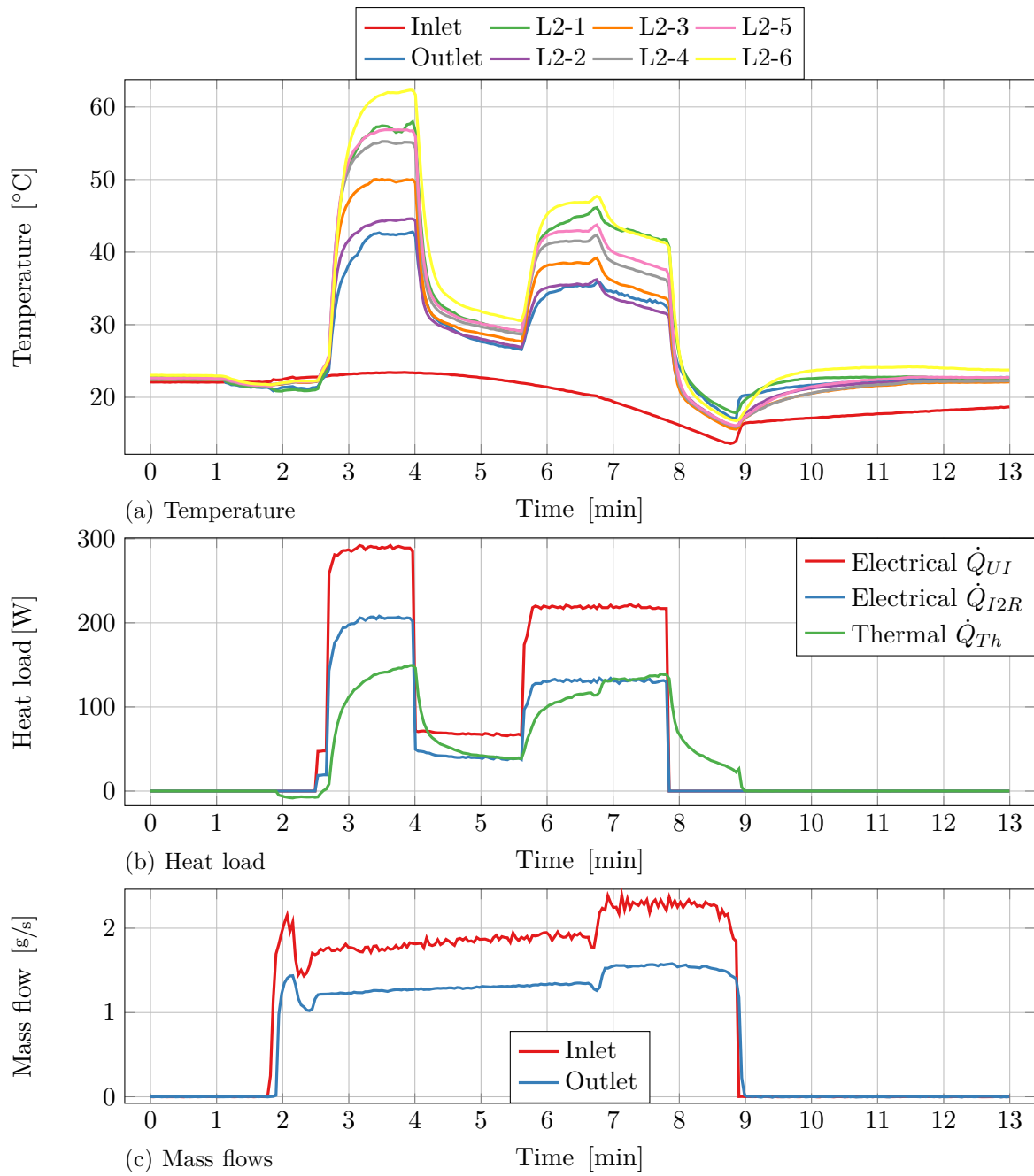


Figure C.4: Raw measurement data of helium measurement 1.

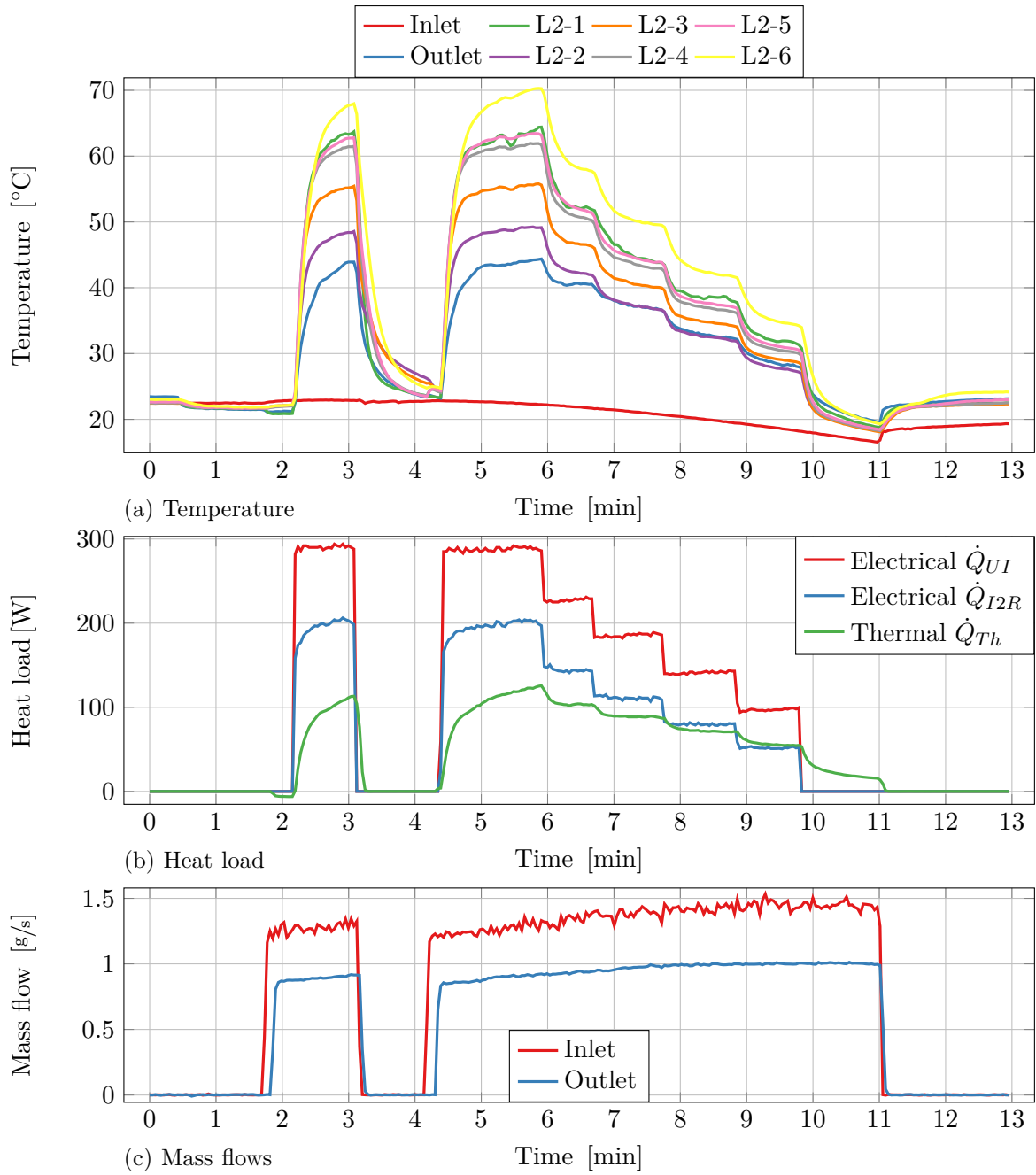


Figure C.5: Raw measurement data of helium measurement 2.

D Digital appendix

- 📁 01_Project_management
 - 📄 Project_task_P9_Deflorin
 - 📄 Project_clarification_P9_19_Deflorin_Mu3e
- 📁 02_CAD
 - 📄 G12_OP
 - 📄 G34_OP
 - 📄 G3S_OP
 - 📄 V34_OP
 - 📄 Connector_plate_endpieceflex
 - 📄 Measurement_block_T_P
- 📁 03_Measurements
 - 📁 Datasheets
- 📁 04_Literature
 - 📄 Previous thesis
 - 📄 Presentation
 - 📁 Weekly reports
 - 📄 Weekly reports
 - 📄 Wengen workshop presentation
 - 📄 Projektphasenaudit presentation
 - 📄 Collaboration meeting presentation
- 📁 05_Diverse
 - 📄 Scheme and other drawings
 - 📁 Pictures of the experiment
- 📄 Doku_P9_HS18_Deflorin_Mu3e